

High Frequency Spin Dynamics Investigation of Quantum Critical Matters by Metallic Coplanar Resonators

Von der Fakultät Mathematik und Physik der Universität Stuttgart
zur Erlangung der Würde eines Doktors
der Naturwissenschaften (Dr. rer. nat.) genehmigte Abhandlung

vorgelegt von

Mojtaba Javaheri Rahim

geboren in Teheran, Iran

Hauptberichter:	Prof. Dr. Martin Dressel
Mitberichter:	Prof. Dr. Jörg Wrachtrup
Prüfungsvorsitzender:	Prof. Dr. Maria Daghofer

Tag der mündlichen Prüfung: 17.12.2018

1. Physikalisches Institut der Universität Stuttgart 2018

Contents

Motivation (English)	A
Motivation (Deutsch)	a
1. Introduction.....	1
1.1. Electron Spin Resonance; an Overview of the Phenomena	5
1.2. ESR Spectrometers	11
1.3. ESR Experiments via Coplanar Waveguides	13
2. Metallic Coplanar Waveguides; Introduction and Theory.....	17
2.1. Loss and Attenuation	17
2.2. Quality Factor	18
2.3. Characteristic Impedance.....	21
2.4. The Effect of Geometrical Parameters.....	25
2.5. The Effect of Ground Planes Size.....	27
2.6. The Effect of Metallization Thickness	29
2.7. The Effect of Shielding; Box Effects	31
2.8. The Effect of Constituents' Materials and Substrate Thickness	32
2.9. Coupling of the Lines.....	35
2.10. Briefing Table.....	36
3. Studied Systems and Materials	37
3.1. 2,2-diphenyl-1-picrylhydrazyl; DPPH	37
3.2. Heavy Fermion Metals.....	39
3.2.1. YbRh ₂ Si ₂	45
3.2.2. YbNi ₄ P ₂	50
3.3. Spin Liquid System; κ -(BEDT-TTF) ₂ Cu ₂ (CN) ₃	53
4. Metallic Coplanar Waveguides; Developments and Measurements....	59
4.1. Material Selection	59
4.2. Fabrication and Packaging	62
4.3. Designs and Geometrical Structures	68
4.4. Microwave Measurements at Cryogenic Temperatures	74
4.5. Transmission Lines Measurements.....	76

4.6.	Resonator Measurements	77
4.6.1.	High Q Achievement	81
4.6.2.	Low Fundamental Achievement	91
4.6.3.	Straight Line Resonators	91
4.6.4.	Double Resonators.....	91
4.6.5.	Golden Resonators.....	92
4.7.	Numerical Analysis of the Quality Factor Loss Background for Superconducting CPW Resonators	93
5.	Primary ESR Measurements	95
6.	Heavy Fermion Metals; YbRh_2Si_2 and YbNi_4P_2	100
6.1.	YbRh_2Si_2	101
6.1.1.	ESR of YbRh_2Si_2	101
6.1.2.	Non-ESR Measurements on YbRh_2Si_2	115
6.2.	ESR of YbNi_4P_2	118
7.	Spin-Liquid System.....	124
8.	Summary and Outlook.....	137
8.	Zusammenfassung und Ausblick	142
	Appendix I	148
	Appendix II.....	178
	Appendix III.....	180
	References	184
	Acknowledgements	201

Motivation (English)

Investigation in physics needs developing new methods and devices to be able to provide new understandings and uncover interesting phenomena. This includes the both of optimizing the current procedures to obtain cleaner data and establishing totally new procedures to reach so far unreachable ranges and scales. In condensed matter physics, depending on the focused properties of the under-study matter, the challenging or problem making parameters could be temperature, magnetic and electric fields, frequencies etc. In this work, new devices were developed and applied to investigate electron spin resonance (ESR) in some exotic materials at low temperatures. The devices were metallic coplanar resonators and the exotic materials were quantum critical matters which include quantum critical phase transition(s) in their phase diagrams.

Coplanar resonators (or generally all planar resonators) for ESR studies is a reasonable and appropriate choice since the multiple resonance frequencies with the same (microwave) magnetic field direction give us the possibility of analyzing the materials at various (external) magnetic fields. This means probing the phase diagrams and finding new observations in different phases and at phase transitions are easily achievable. On the other hand, studying the matters at very low temperatures, since coplanar resonators are small compared to conventional cavity resonators, is feasible due to high compatibility of them with dilution refrigerators. This is a big advantage and has a high importance since many materials have interesting physics only at temperatures near to absolute zero.

The functionality of planar structures (microstrip, stripline and coplanar) for ESR studies is already proven as will be mentioned later in text in section 1.3 of chapter 1. In this work, the coplanar configuration was chosen because of their advantages in comparison with other possible structures as will be elaborated in section 1.3. The conductive materials used in the fabrication of planar resonators, depending on the

desired application, could be normal high conductive metals like copper or superconducting materials (for enough low temperatures).

In an ESR experiment, exerting external magnetic field is inevitable; if not a zero-field measurement. On the other hand, a superconductor has always critical magnetic fields approaching which the superconductivity starts to become lost in limited areas (vortices) and by further increasing the field it will totally disappear. So, the functionality of a superconducting coplanar resonator in a magnetic ambient will be affected and each kind of output signal will be affected as well. Therefore, an ESR spectrum out of a superconducting resonator will be affected by distortions, and, intensive and extensive regression analysis are required to remove the distortions as will be introduced and discussed with details in section 4.7 and Appendix I. In addition, of the other unfavorable issues of superconducting materials in a coplanar resonator is the repelling of the magnetic field by superconductors. This leads to some deviations between the sensed field intensity by the sample and the supposed (ordered) amount. Hence, in this work, particular metallic (non-superconducting) coplanar waveguides for ESR experiments were developed to study the materials with new and not-fully understood physics at low temperatures.

Certainly, when a new tool or device is introduced for a kind of measurement, it cannot be used without any validation process and without making sure if the data obtained by this device are reliable. Thus, it must be tested in a way that we can verify the reliability of the data. The functionality of the developed coplanar resonators in this work were checked in two different processes.

The first part of validation process was measuring the resonances of the resonators. It was done under various conditions like sweeping the temperature and magnetic field. In addition, the dependence of the resonators performance on changing the structural and geometrical parameters of the resonators' component, as shown and described in chapters 2 and 4, observed and analyzed. Albeit, another purpose of several designs was achieving high quality resonators. Utilizing the results in other theoretical and experimental studies and based on the already existing experiences in PI1 department, each time a number of resonators were designed, fabricated, tested and the data were analyzed and used for further designing to improve the quality and performance of the resonators.

The fabricated resonators were measured each time at different temperatures and the evolution/alteration of the resonances were monitored and analyzed. Some resonators were tested in magnetic fields up to 7 T. Beside the resonators some transmission line structures were also fabricated and measured (chapter 1, section 1.3) to characterize

exclusively the resonators' metallization and to find any probable abnormal signature in temperature dependence of the metal line properties; chapter 4, section 4.5.

The second part of validation process was measuring the ESR signals of a well-known calibration material for ESR measurement and comparing the obtained data with the already in other sources introduced data.

In order to check the ability of the resonators to yield reliable results in ESR, the widely used ESR calibration material 2,2-diphenyl-1-picrylhydrazyl, abbreviated as DPPH, was employed. The free radical DPPH has a stable chemical structure and narrow ESR linewidths. In this work a powder form sample was measured several times with different sample position configurations down to 1.6 K. Very sharp and clear ESR signals were obtained from the DPPH measurements. The g -factors and signal intensities were compared with the data in the literatures; chapters 3 and 5.

After reaching a high confidence level in the ESR functionality of the designed resonators, the materials of interest were measured by placing them in the adjacency of the resonator surface. At the following a short introduction of the studied materials is offered which shows the importance and necessity of ESR studies for them.

At the time when the Landau Fermi Liquid theory/method was a widely accepted to model any strongly correlated materials, some new observations like the deviation of electron heat capacity, C_{elec} , at around 100 mK from the linear expression for ^3He or the dependence of the electron effective mass on temperature in some studied systems showed the shortcomings of this theory. The number of such observations raised continuously. Heavy fermion metals (HFs) showed such properties as well so that very rich phase diagrams were mapped for them. Interesting phenomena like anomalies in electric and thermal conductivity, quantum phase transition (QPT) or non-Fermi-liquid (NFL) phase could be observed in HFs. The name of "Heavy Fermion Metals" is attributed to them since in HFs, due to the strong electron-electron correlations, mobile electrons (at low temperatures) behave as if their masses were hundred times the mass of a "free" electron in a simple metal. This means the effective mass of the quasiparticles in HFs is hundreds of times higher than the ones in normal metals.

HFs are intermetallic compounds containing rare earth elements with open $4f$ and $5f$ orbitals. In these orbitals the electrons have a very narrow band and thus experience strong Coulomb repulsions. When the system temperature is enough low the conduction electrons and unpaired $4f/5f$ become hybridized with each other through Kondo effect and form a Kondo singlet. At even lower temperatures the interactions of the spins and charges of the mentioned electrons (the Kondo singlet electron and mobile electrons as well) are very sensitive to small variations of an external parameter like pressure,

magnetic field or doping. These external excitations can therefore have a tuning role so that the state of the material changes by changing e.g. the magnetic field through a quantum phase transition. Quantum phase transitions are second order phase transitions which can occur even at $T = 0$ K by a tuning parameter like magnetic field. The point at which a QPT happen are called as quantum critical point (QCP). A typical QCP is shown in Figure M-1 [1]. This phase diagram belongs to YbRh_2Si_2 which is one of the most studied HFs.

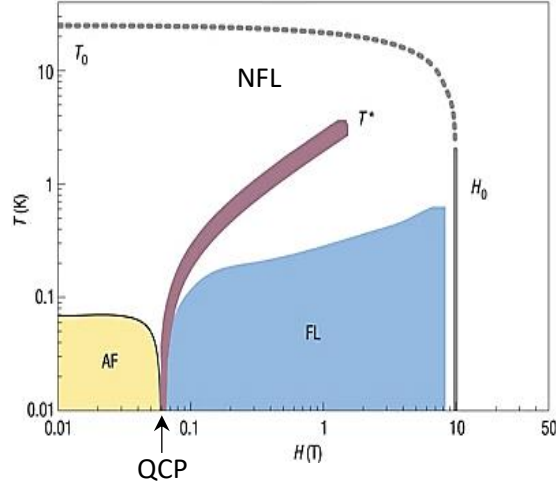


FIG. M-1. The $T - B$ phase diagram of YbRh_2Si_2 [1].

The hybridization of conduction electrons and the $4f/5f$ electrons is explained by Kondo effect. HFs form a Kondo lattice since Kondo effect is happening in the whole of lattice at each lattice point of the rare earth element. A QPT tunes the strength of the $4f/5f$ and conduction electron hybridization. A continuous ESR measurement at different magnetic fields can be helpful to represent any evolution or alteration of this hybridization. Furthermore, ESR measurements could yield valuable facts in another aspect which is in fact the type of the quantum phase transition.

One explanation for a QPT (and NFL behavior) is vanishing the quasiparticles and appearing an infinite correlation length in the material. In contrast to this, another interpretation of QPTs is that the quasiparticles exist on the both sides of the QCP, and the magnetic orders are a result of them. In other words, these two theoretical discussions describe a QCP by: 1) a spin density wave scenario and, 2) a localized moment scenario or Kondo breakdown. In the former, known as spin density wave QCP, the spin polarization of the Fermi surface is the origin of magnetic order, in the latter, known as Kondo breakdown QCP, the hybridized (heavy) electrons disintegrate at the QCP and form well-defined quasiparticles. The formation of Kondo singlets intuitively implies that the (hybridized) f electrons must not be able to show any ESR signal since the screening conduction electrons occupy the otherwise empty states on

the magnetic atom. In another view, the typical spin fluctuation rate of the Kondo ions, causes a large ESR linewidth beyond of detection. If nevertheless a HF system like YbRh_2Si_2 is showing a very significant and relatively narrow ESR signal, a very interesting mechanism for it is expected. The HF candidates which were studied in this work were YbRh_2Si_2 and YbNi_4P_2 with anti-ferromagnetic (AFM) and ferromagnetic (FM) orders in their phase diagrams respectively.

J. Sichelschmidt et al. [2] surprisingly detected a very sharp and significant ESR signal around 1.5 K at the X- and Q-band frequency range. Regarding the high Kondo temperature of this compound, the ESR linewidth must be $\frac{k_B T_K}{\mu_B} \approx 37$ T which, however, it was found to be in the range of 10 to 150 mT with the corresponding g -factor of ≈ 3.47 to ≈ 3.60 ; chapter 3, section 3.2.1.

This sharp Dysonian ESR signal was interpreted as the suppression of the Kondo effect in proximity to the QCP and reinforced the idea of a Kondo breakdown QCP in YbRh_2Si_2 . Other experiments have also shown similar results. HF compounds of Ce have also detectable ESR signals.

The observation of ESR signal in HFs at even down to ≈ 0.5 K and up to very high magnetic fields of 8 T (360 GHz) brought up the idea that a sharp ESR can happen not just by the local magnetic moments, but it could be a collective response of the ferromagnetic (FM) fluctuations of f -spins. FM fluctuations, which are mediated by RKKY interaction, could facilitate the translational diffusion of quasilocalized f -electrons from one site to the next by providing the similar local fields for the spin. This is feasible if the RKKY interactions are FM. This mechanism for the narrow ESR signals in a Kondo lattice ($T < T_K$) is called motional narrowing.

Experimental works could yield more complementary data and shed light on this discussion whether the ESR of the Kondo lattices are of localized moments or are due to the collective responses. A useful experiment to prove the validity of FM fluctuations hypothesis is measuring the ESR response of a Kondo lattice with proven FM correlations like YbNi_4P_2 which as stated above has an FM order next to its QCP.

YbNi_4P_2 is introduced as a quasi-one-dimensional compound because of Yb ions arrangement in its crystalline structure as shown in Figure M-2 [3].

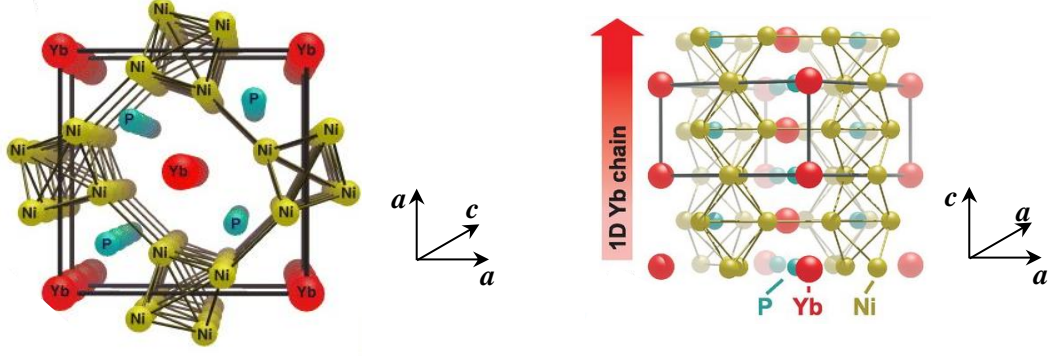


FIG. M-2. The crystalline structure of YbNi_4P_2 at different orientations [3].

The FM ordering in the ordered phase is perpendicular to c -direction. The anisotropy in YbNi_4P_2 is significant, although the symmetry on each Yb ion site is identical. This is due to the dissimilar crystalline electric fields which Yb ions experience in one chain compared the neighboring chains since the chains have a shift of $\frac{c}{2}$ relative to each other. This leads to a geometrical frustration between Yb ions next to each other which are in adjacent chains. This together with typical and various strong electron-electron correlations in this compound favors a quantum phase transition. Analysis the ESR behavior of YbNi_4P_2 is expected to provide beneficial data for the theoretical discussion about FM fluctuations among the f -spins since this HF compound has long-range FM order and FM polarized-phases in its magnetic lattice.

The NFL phase in HFs is a consequence of the strong correlation among the electric charges of the electrons. However, it is not always the interaction among the electric charges which lead to exotic behavior, but the spins and strong magnetic correlations could also cause phenomena like quantum phase transitions.

A quantum spin liquid (QSL) state gets formed by highly correlated spins whose frustration avoid a well-defined ground state down to even 0 K. In other words, quantum fluctuations in these materials avoid a well-defined ordered ground state. In fact, the ground state is the superposition of various possible states. The interesting question is now what could be the response of such a system to an electron spin excitation? In some HF Kondo systems, a significant ESR signal could be observed although the magnetic moments were screened by the surrounding charges (conduction electrons). Can an ESR signal be obtained from a spin frustrated system?

A practical example of a QSL system is the layered molecular structure: κ -(BEDT-TTF) $_2\text{Cu}_2(\text{CN})_3$ as shown in Figure M-3 [4] [5] [6]. The BEDT-TTF (bis(ethylenedithio)-tetrathiafulvalene) molecules can be located beside each other with different orders. Their molecular orbitals overlap and make the electron transfer from one molecule to the other possible. BEDT-TTF molecules form charge-transfer salts.

In a charge-transfer salt, j molecules of BEDT-TTF jointly donate one electron to another type of molecule, labeled with X, to form a $(\text{BEDT-TTF})_j\text{X}$ compound. In case of $j = 2$, dimers form. X is an anion because of its gained negative charge from $(\text{BEDT-TTF})_j$.

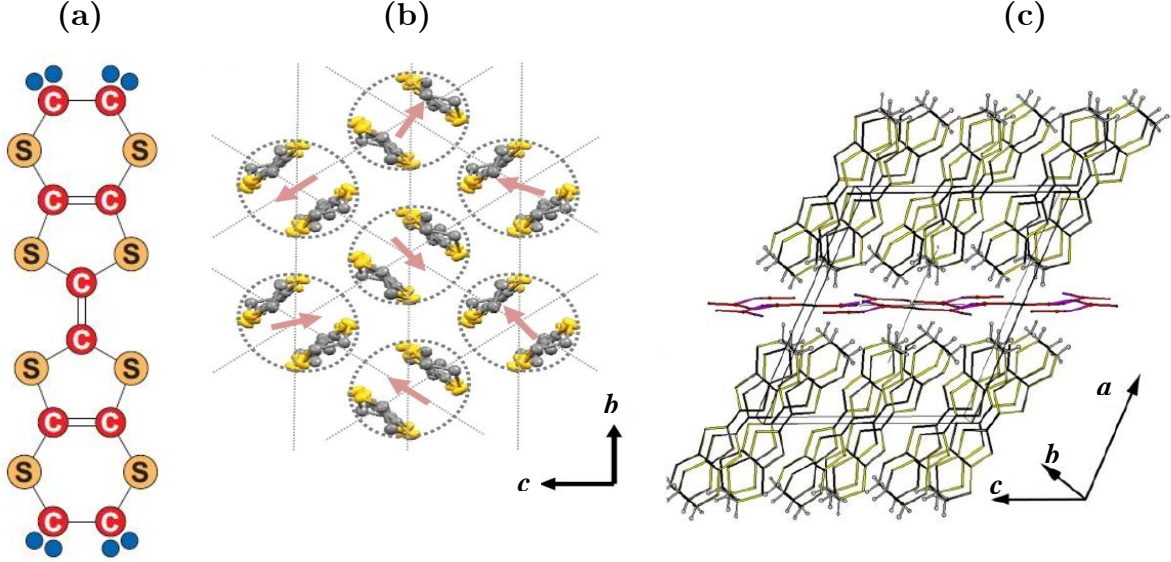


FIG. M-3. (a) BEDT-TTF molecule sketch [4], (b) The top view of the BEDT-TTF layer in which the BEDT-TTF dimers (spinons) are signified by the dashed circles [5] and (c) The layered structure of κ -(BEDT-TTF)₂Cu₂(CN)₃ [6].

κ -(BEDT-TTF)₂Cu₂(CN)₃ is a Mott insulator with the antiferromagnetic spin- $\frac{1}{2}$ BEDT-TTF dimers ($(\text{BEDT-TTF})_2^+$) with a triangular magnetic lattice; chapter 3, section 3.3. κ is the sign for the standing up arrangement of adjacent BEDT-TTF dimers. κ -(BEDT-TTF)₂Cu₂(CN)₃ is a suitable candidate for studying the QSL state, because of much less possible diffusing impurities (during the sample growth) than the other similar compounds. ESR measurements of κ -(BEDT-TTF)₂Cu₂(CN)₃ will definitely yield interesting data for comprehending the correlations among the quantum entities in a frustrated system.

The represented method in this work offers several opportunities for low temperature spectroscopic microwave measurements. The presented data and results can provide new insights in the comprehension of charge and spin correlations which are existing in highly correlated systems. In addition, they highlight some appropriate ways for future experiments in the studies similar to this work.

Motivation (Deutsch)

Forschung in der Physik bedarf der Entwicklung neuer Methoden und Instrumente, um neue Sichtweisen zu ermöglichen und interessante Phänomene aufzudecken. Damit ist sowohl die Optimierung der bereits genutzten Prozesse zur Gewinnung aussagekräftigerer Daten als auch völlig neue Verfahren gemeint, um bislang unerreichbare Bereiche und Skalen zu erforschen. In der Physik der kondensierten Materie kann der herausfordernde Parameter, je nachdem welche Eigenschaften der Materie untersucht werden, die Temperatur, das elektrische oder magnetische Feld, die Frequenz etc. sein. In dieser Arbeit wurden neue Module entwickelt und bei der Untersuchung der Elektronenspinresonanz (ESR) in außergewöhnlichen Materialien bei Tiefsttemperaturen angewendet. Die Module waren metallische koplanare Resonatoren und die außergewöhnlichen Materialien waren quantenkritische Materien, die in ihren Phasendiagrammen quantenkritische Phasenübergänge enthalten.

Koplanaren Resonatoren (oder allgemein alle planaren Resonatoren) sind für ESR-Untersuchungen ein geeignetes Instrument, da ihre vielfältigen Resonanzen mit den gleichen Magnetfeldrichtungen die Analyse von Materialien bei verschiedenen Magnetfeldstärken ermöglichen. Damit ist die Untersuchung der Phasendiagramme sowie neue Beobachtungen in unterschiedlichen Phasen und bei Phasenübergängen einfacher. Außerdem wird das Erforschen der Materie bei Tiefsttemperaturen möglich, da die koplanaren Resonatoren im Vergleich zu den konventionellen Hohlraumresonatoren deutlich kleiner sind und deshalb gut mit den Mischungskryostaten kompatibel sind. Das ist ein großer Vorteil und ist von hoher Bedeutung, weil viele Materialien ihre interessanten Eigenschaften erst bei Temperaturen in der Nähe des absoluten Nullpunkts enthüllen.

Die Funktionalität der planaren Resonatoren (Microstrip, Stripline und Koplanar) für ESR-Untersuchungen ist bereits bewiesen und wird in dieser Arbeit im Abschnitt 1.3

des ersten Kapitels dargestellt. Für die vorliegende Forschungsarbeit wurde die koplanare Konfiguration aufgrund ihrer Vorteile im Vergleich mit anderen möglichen Konfigurationen ausgewählt, wie ebenfalls im Abschnitt 1.3 erläutert. Die leitfähigen Materialien, welche bei der Herstellung der koplanaren Resonatoren benutzt werden, können, abhängig von der Anwendung, normal leitfähige Metalle wie Kupfer oder supraleitende Materialien (bei ausreichend tiefen Temperaturen) sein. In einem ESR-Experiment ist das Anlegen eines externen Magnetfeldes unabdingbar, falls die Messung keine Nullfeldmessung ist. Jedoch hat ein Supraleiter immer ein kritisches Magnetfeld. Wenn dieses erreicht wird, fängt die Supraleitfähigkeit an in begrenzten Bereichen (Vortexes) verloren zu gehen. Bei einer weiteren Erhöhung des Feldes verschwindet sie vollkommen. Deshalb ist die Funktionalität eines supraleitenden koplanaren Resonators in einer magnetischen Umgebung beeinträchtigt und jedes Ausgangssignal wird verzerrt. Demzufolge ist ein ESR-Spektrum eines supraleitenden Resonators immer von Verzerrungen betroffen und umfangreiche Regressionsanalysen sind nötig, um diese Verzerrungen zu eliminieren, wie im Abschnitt 4.7 und Annex I ausführlich vorgestellt und diskutiert wird. Ein weiterer ungünstiger Aspekt von supraleitenden Resonatoren ist die Abstoßung des Magnetfeldes von Supraleitern. Das führt zu Abweichungen zwischen der am Versuchsstand eingestellten Feldstärke und der Feldstärke an der Probe. Daher wurden in dieser Arbeit spezifische metallische (nicht-supraleitende), koplanare Wellenleiter für ESR-Experimente entwickelt, um die Materialien mit neuen und noch nicht vollständig erforschten physikalischen Eigenschaften bei Tiefsttemperaturen zu untersuchen.

Selbstverständlich kann ein neues Messinstrument oder eine neue Apparatur für eine Untersuchung nicht ohne Validierung und ohne Sicherstellung, dass die gewonnenen Daten zuverlässig sind, eingesetzt werden. Daher muss das neue System in einer Weise geprüft werden, dass die Zuverlässigkeit der Daten bestätigt wird. Die Funktionalität der im Rahmen dieser Forschungsarbeit entwickelten koplanaren Resonatoren wurde durch zwei unterschiedliche Prozesse geprüft.

Im ersten Schritt der Validierung erfolgte die Messung der Resonanzen der Resonatoren. Diese wurden unter verschiedenen Bedingungen wie schrittweisen Temperatur- und Magnetfeld-Änderungen beobachtet. Darüber hinaus wurde die Abhängigkeit der Resonatoren-Leistungsfähigkeit von strukturellen und geometrischen Parameteränderungen der Resonatoren-Komponenten, wie in den Kapiteln 2 und 4 beschrieben wurde, beobachtet und analysiert. Ein weiteres Ziel der unterschiedlichen Konfigurationen war, einen höheren Resonatoren-Gütefaktor zu erzielen. Unter Nutzung der Ergebnisse von anderen theoretischen und experimentellen Untersuchungen und anhand der bereits vorliegenden Erfahrungen am

1. Physikalischen Institut der Universität Stuttgart wurden mehrere Resonatoren ausgelegt, hergestellt und getestet. Die gemessenen Daten wurden ausgewertet und zur weiteren Verbesserung der Gütefaktoren und der Leistungsfähigkeit der Resonatoren genutzt.

Die hergestellten Resonatoren wurden jedes Mal bei unterschiedlichen Temperaturen gemessen und die Resonanzentwicklungen und -veränderungen wurden überwacht und analysiert. Manche Resonatoren wurden im Magnetfeld bis zu 7 T getestet. Neben den Resonatoren wurden auch einige koplanare Breitband-Wellenleiter (Transmission Line) hergestellt und gemessen (Kapitel 1, Abschnitt 1.3), um ausschließlich die Resonatoren-Metallisierung zu charakterisieren und Abweichungen beziehungsweise Auffälligkeiten der Temperaturabhängigkeit der Metallbahnen festzustellen; Kapitel 4, Abschnitt 4.5.

Im zweiten Teil des Validierungsprozesses wurde die Zuverlässigkeit der Resonatoren im Hinblick auf die Datenqualität geprüft. Dazu wurde das häufig zur Kalibrierung von ESR-Anlagen eingesetzte Material 2,2-Diphenyl-1-Picrylhydrazyl, abgekürzt DPPH, verwendet. Das freie Radikal DPPH hat eine stabile chemische Struktur und schmale ESR-Linienbreiten. In dieser Arbeit wurde eine pulverförmige Probe mehrfach mit verschiedenen Probenposition bis zu einer Temperatur von 1,6 K gemessen. Bei den DPPH-Messungen wurden scharfe und klare ESR-Signale erhalten. Der g -Faktor und die Signalstärke wurden mit den Daten in der Fachliteratur verglichen; Kapitel 3 und 5.

Nachdem die Zuverlässigkeit der entwickelten Resonatoren bestätigt werden konnte, wurden die Materialien von Interesse in unmittelbare Nähe der Resonatoren-Oberfläche positioniert und gemessen. Im Folgenden erfolgt eine kurze Vorstellung dieser Materialien und der Notwendigkeit sie näher zu untersuchen.

Obwohl die seit Langem bekannte Landau-Fermi-Flüssigkeits-Theorie/-Methode weithin zur Modellierung der stark korrelierten Materialien anerkannt ist, zeigten manche neue Beobachtungen wie die Abweichung der Elektronen-Wärmekapazität, C_{elec} , von rund 100 mK von der linearen Regression für ^3He oder die effektive Elektronenmasse-Abhängigkeit von der Temperatur in einigen untersuchten Systemen die Mängel dieser Theorie auf. Die Zahl derartiger Beobachtungen stieg ständig. Schwere-Fermionen-Metalle (HFs) zeigten auch solche Eigenschaften, so dass sehr umfangreiche Phasendiagramme für sie dargestellt wurden. Interessante Phänomene wie Anomalien der elektrischen und thermischen Leitfähigkeit, Quantenphasenübergänge (QPT) oder nicht-Fermi-Flüssigkeitsphasen (NFL) wurden in HFs beobachtet. Den Namen „Schwere-Fermionen-Metalle“ erhielten diese Materialien, da sich in HFs aufgrund der starken Elektronen-Korrelationen, die beweglichen Elektronen bei Tiefsttemperaturen so verhalten, als ob ihre Masse

hundertfach schwerer als die Masse eines „freien“ Elektrons in einem einfachen Metall wäre. Das bedeutet, dass die effektive Masse der Quasiteilchen in HFs hundertfach höher als die der Elektronen in normalen Metallen ist.

HF's sind intermetallische Verbindungen, die Seltene-Erde-Elemente mit offenen $4f$ - und $5f$ - Orbitalen enthalten. In diesen Orbitalen haben die Elektronen ein sehr schmales Band und erfahren daher eine starke Coulomb-Abstoßung. Wenn die Systemtemperatur tief genug ist, werden die Leitungselektronen und ungepaarte $4f/5f$ -Elektronen durch den Kondo-Effekt miteinander hybridisiert und bilden ein Kondo-Singulett. Bei noch tieferen Temperaturen sind die Wechselwirkungen zwischen den Spins und den Ladungen der erwähnten Elektronen (sowohl des Kondo-Singulett-Elektrons als auch der beweglichen Elektronen) sehr empfindlich gegen geringfügige Änderungen eines externen Parameters wie Druck, Magnetfeld oder Dotierung. Diese externen Anregungen haben folglich eine regelnde Rolle, dass die Phase des Materials sich z.B. bei der Änderung des Magnetfelds durch einen Quantenphasenübergang ändert. Quantenphasenübergänge sind Phasenübergänge zweiter Ordnung, welche sich sogar beim absoluten Temperaturnullpunkt $T = 0$ K bei Einwirkung eines Parameters wie dem Magnetfeld einstellen können. Der Punkt, an dem ein QPT stattfindet, wird Quantenkritischer Punkt (QCP) genannt. Ein typischer QCP ist im Bild M-1 [1]. Dieses Phasendiagramm gehört zu YbRh_2Si_2 , welches eines der am meisten untersuchten Schwere-Fermionen-Metalle ist.

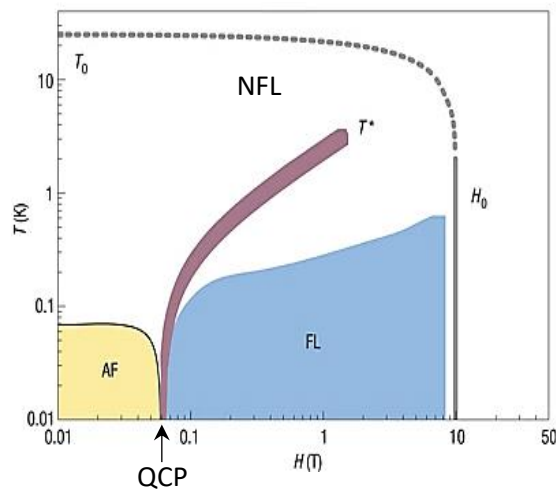


Bild M-1. Das $T - H$ - Phasendiagramm von YbRh_2Si_2 [1].

Die Hybridisierung von Leitungselektronen und $4f/5f$ -Elektronen ist durch den Kondo-Effekt erklärt. HF's bilden ein Kondo-Gitter, da der Kondo-Effekt im gesamten Gitter an jedem Gitterpunkt des Seltene-Erde-Elements eintritt. Ein QPT regelt die Hybridisierungsstärke der $4f/5f$ - und Leitungselektronen. Eine kontinuierliche ESR-Messung bei unterschiedlichen Magnetfeldern ließ erwarten, dass voraussichtlich die

Entstehung beziehungsweise die Veränderung dieser Hybridisierung darstellt wird. Weiterhin sollten ESR-Messungen bei der Art der Quantenphasenübergänge in HFs wertvolle Daten ergeben.

Eine Erklärung eines QPT (und eines NFL-Verhaltens) ist das Verschwinden der Quasiteilchen und das Vorkommen einer unendlichen Korrelationslänge im Material. Eine andere Interpretation von QPTs geht davon aus, dass die Quasiteilchen auf beiden Seiten des QCPs existieren und die magnetischen Ordnungen eine Folge von ihnen sind. Anders ausgedrückt beschreiben diese zwei theoretischen Ansätze einen QCP durch 1) ein Spindichtewellen-Szenario beziehungsweise 2) ein lokales (Dipol)-Momente-Szenario oder Kondo-Zusammenbruch. Im ersten Szenario, bekannt als Spindichtewellen-QCP, ist die Spinpolarisation der Fermi-Fläche die Ursache der magnetischen Ordnung. Im zweiten Szenario, bekannt als Kondo-Zusammenbruch-QCP, brechen die hybridisierten (schweren) Elektronen bei QCP zusammen und lassen die magnetischen Quasiteilchen erneut auftreten. Die Entstehung der Kondo-Singulets impliziert intuitiv, dass die f -Elektronen kein ESR-Signal mehr zeigen, weil die abschirmenden Leitungselektronen die sonst leeren Zustände im magnetischen Atom belegen. Aus einer anderen Sichtweise verursachen die typischen Spin-Fluktuationen in den Kondo-Ionen eine zu breite ESR-Linie außerhalb der Detektion. Wenn trotzdem ein HF ein klares und relativ schmales ESR-Signal ergibt, ist ein interessanter physikalischer Mechanismus für dieses Phänomen zu erwarten. In dieser Arbeit wurden die HFs YbRh_2Si_2 und YbNi_4P_2 mit antiferromagnetischen (AFM) beziehungsweise ferromagnetischen (FM) Ordnungen in ihren Phasendiagrammen untersucht.

J. Sichelschmidt et al. [2] hat überraschenderweise ein sehr klares und deutliches ESR-Signal bei ca. 1,5 K im X- und Q-Frequenzband entdeckt. Angesichts der hohen Kondo-Temperatur von YbRh_2Si_2 sollte die ESR-Linienbreite $\frac{k_B T_K}{\mu_B} \approx 37$ T sein. Jedoch wurden ESR-Signale mit schmalen Linienbreiten im Bereich von 10 bis 150 mT mit dem entsprechenden g -Faktor von $\approx 3,47$ bis $\approx 3,60$ beobachtet; Kapitel 3, Abschnitt 3.2.1.

Das scharfe, dysonförmige ESR-Signal wurde als Unterdrückung des Kondo-Effekts in der Nähe vom QCP interpretiert und unterstützte die Idee eines Kondo-Zusammenbruch-QCPs in YbRh_2Si_2 . Andere Untersuchungen haben auch vergleichbare Ergebnisse gezeigt. HF-Verbindungen von Ce zeigen auch detektierbare ESR-Signale.

Die Beobachtung eines ESR-Signals in HFs sogar bei $\approx 0,5$ K und bei höheren Magnetfeldern bis zu 8 T (360 GHz) lässt vermuten, dass ein scharfes ESR nicht nur von den lokalen magnetischen Momenten verursacht werden kann, sondern dies auch eine kollektive Reaktion von den ferromagnetischen Fluktuationen der f -Spins darstellen kann. FM-Fluktuationen, die durch RKKY-Wechselwirkungen erfolgen,

könnten die translatorische Diffusion der quasilokalen f -Elektronen von einem Ort zum nächsten durch die Bereitstellung der ähnlichen lokalen Feldern für die Spins ermöglichen. Dieser Mechanismus für die schmalen ESR-Signale in einem Kondo-Gitter ($T < T_K$) ist als Bewegungsverschmälerung (Motional Narrowing) bekannt.

Experimentelle Forschungen können weitere ergänzende Daten liefern und Klarheit bringen, ob die ESR von Kondo-Gittern durch lokale magnetische Momente oder durch die kollektiven Reaktionen verursacht ist. Ein nützliches Experiment zur Überprüfung der Gültigkeit der FM-Fluktuationen-Idee ist die ESR-Untersuchung eines Kondo-Gitters mit geprüften (langreichweitigen) FM-Korrelationen wie YbNi_4P_2 . Das Material YbNi_4P_2 ist eine quasi-eindimensionale Verbindung aufgrund der Yb-Ionen-Anordnung, deren kristalline Struktur im Bild M-2 [3] dargestellt ist. Diese HF-Verbindung sollte den theoretischen Diskussionen um FM-Fluktuationen unter den f -Spins nutzbringende Daten zu Verfügung stellen, weil sie eine langreichweitige FM-Ordnung neben ihrem QCP und FM-polarisierten Phasen in ihrem magnetischen Gitter hat.

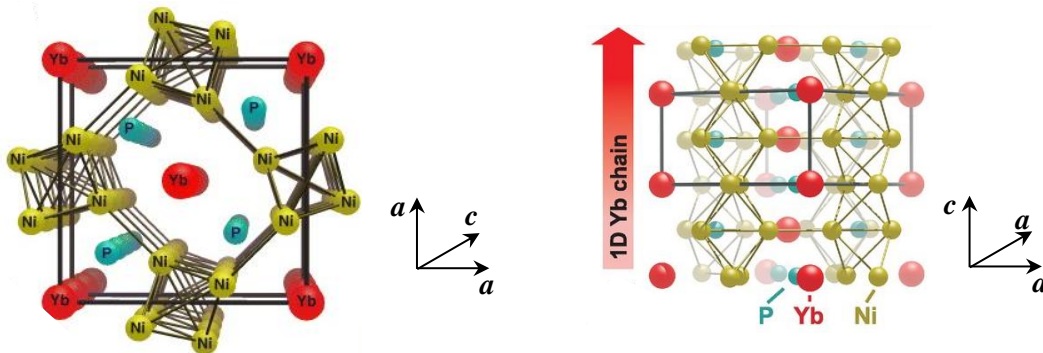


Bild M-2. Die kristalline Struktur von YbNi_4P_2 in verschiedenen Richtungen [3].

Die FM-Ordnung in der geordneten Phase ist senkrecht zur c -Richtung. Die Anisotropie in YbNi_4P_2 ist erheblich, obwohl die Symmetrie um jedes Yb-Ion identisch ist. Das ist infolge der ungleichen kristallinen elektrischen Felder, die die Yb-Ionen in einer Kette im Vergleich zu den Nachbarketten erfahren, da diese Ketten um $\frac{c}{2}$ relativ zueinander verschoben sind. Das führt zu einer geometrischen Frustration zwischen nebeneinander liegenden Yb-Ionen, die Teil verschiedener Ketten sind. Dieser Fakt im Zusammenhang mit den typischen und unterschiedlich starken Elektronen-Korrelationen in dieser Verbindung begünstigt einen Quantenphasenübergang.

Die NFL-Phase in HFs ist eine Folge der starken Korrelationen zwischen den Ladungen der Elektronen. Es sind jedoch nicht immer die Wechselwirkungen zwischen den elektrischen Ladungen, die zu exotischem Verhalten führen, sondern auch die Spins und die starken magnetischen Korrelationen können Phänomene wie Quantenphasenübergänge verursachen.

Ein Quantenspinflüssigkeit (Quantum Spin Liquid, QSL) wird von hoch korrelierten Spins gebildet, deren Frustration einen bestimmten Grundzustand sogar bei 0 K vermeidet. Mit anderen Worten: Quantenfluktuationen in diesen Materialien vermeiden einen bestimmten geordneten Grundzustand. Der Grundzustand ist die Superposition der unterschiedlichen möglichen Zustände. Die interessante Frage ist: Was ist die Reaktion solcher Systeme auf eine Elektronspin-Anregung? In manchen HF-Systemen konnte ein ESR-Signal beobachtet werden, obwohl die magnetischen Momente von den umliegenden Ladungen (Leitungselektronen) abgeschirmt wurden. Wird bei einem frustrierten System ein ESR-Signal beobachtet?

Ein praktisches Beispiel eines QSL-Systems ist κ -(BEDT-TTF) $_2$ Cu $_2$ (CN) $_3$: eine molekulare Schichtstruktur wie im Bild M-3 [4] [5] [6] gezeigt. Die BEDT-TTF (Bis(Ethylenedithio)-Tetrathiafulvalene)-Moleküle können unterschiedlich nebeneinander angeordnet werden. Ihre Molekülorbitale überlappen einander und ermöglichen den Elektronentransfer von einem Molekül zum nächsten.

BEDT-TTF-Moleküle bilden Ladungstransfersalze. In einem Ladungstransfersalz geben j BEDT-TTF-Moleküle ein Elektron ab, um gemeinsam mit einem anderen Molekül, bezeichnet mit X, eine (BEDT-TTF) $_j$ X Verbindung zu bilden. Bei $j = 2$ formieren sich Dimere. X ist ein Anion aufgrund der negativen erhaltenen Ladung von (BEDT-TTF) $_j$.

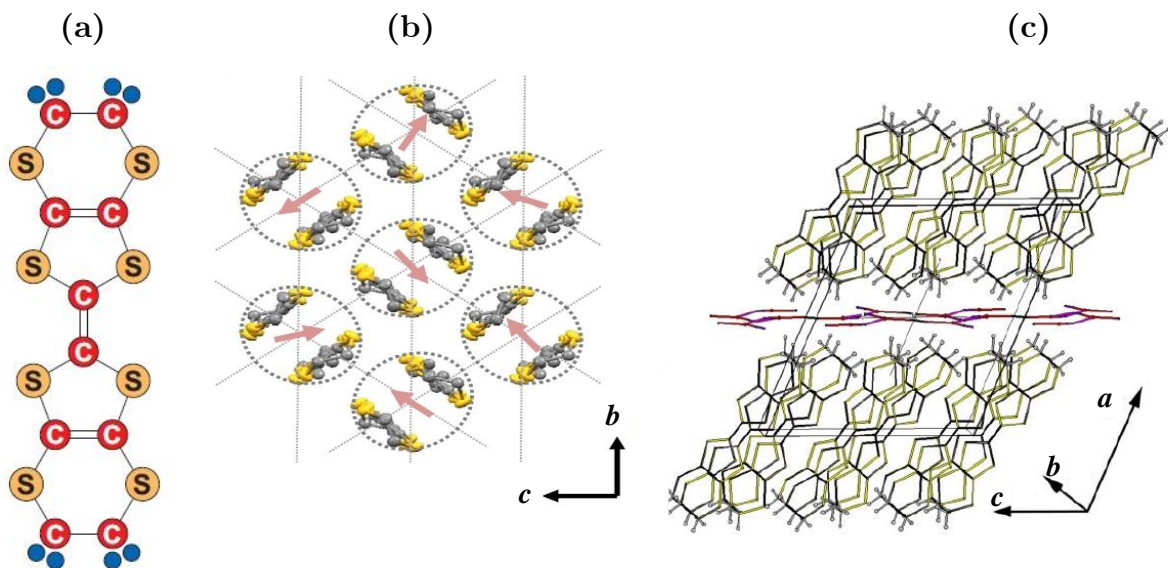


Bild M-3. (a) BEDT-TTF-Molekül-Skizze [4] (b) Draufsicht der BEDT-TTF-Schicht, in der die BEDT-TTF-Dimere (Spinonen) durch gestrichelte Kreise gekennzeichnet sind [5] (c) Die Schichtstruktur von κ -(BEDT-TTF) $_2$ Cu $_2$ (CN) $_3$ [6].

κ -(BEDT-TTF) $_2$ Cu $_2$ (CN) $_3$ ist ein Mott-Isolator mit antiferromagnetischen Spin- $\frac{1}{2}$ BEDT-TTF-Dimere ((BEDT-TTF) $_2^+$) mit einem dreieckigen magnetischen Gitter;

Kapitel 3, Abschnitt 3.3. κ ist das Zeichen für die stehende Anordnung der benachbarten BEDT-TTF-Dimere. κ -(BEDT-TTF)₂Cu₂(CN)₃ ist ein geeigneter Kandidat zur Untersuchung des QSL-Zustands, da aufgrund wenig diffundierter Verunreinigungen in der Probe sauberere Daten erhalten werden. ESR-Messungen von κ -(BEDT-TTF)₂Cu₂(CN)₃ lassen definitiv interessante Daten zum Verständnis der Korrelationen in geometrisch frustrierten Systemen erwarten.

Die in dieser Arbeit vorgestellte Methode eröffnet zahlreiche Möglichkeiten für Mikrowellen-Spektroskopie-Messungen bei Tiefsttemperaturen. Die dargestellten Daten und Ergebnisse ermöglichen neue Sichtweisen zum Verständnis der Ladungs- und Spin-Korrelationen hoch korrelierter Systeme. Darüber hinaus zeigen sie geeignete Wege für zukünftige Experimente in ähnlichen Forschungsfeldern auf.

1. Introduction

In condensed matter science, spectroscopy studies the interaction of radiations and particles with matter and opens insights into the electronic and atomic configurations and their mutual interactions. Materials absorption and emission of energy by stimulation of the appropriate energy states are the basis of spectroscopy and, hence, it has been a key tool in developing fundamental and vast theories in physics like quantum mechanics. However, it is not only in the recent century that the researchers have been looking at the dispersive response of matters, but it began in 1666 by Isaac Newton when he passed light through a prism and triggered the field of spectroscopy. In the early 1800s Fraunhofer systematically studied the solar spectrum and the dark lines of the light spectra which were obtained via his own made device [7]. Based on these observations, other scientists like Herschel, Talbot and Angstrom investigated different emitted spectra from sources such as flames and arcs and found the emitted bright spectral lines were characteristic of the elements in the matters. In the mid-1800s Foucault demonstrated for the first time a laboratory absorption spectrum. Kirchhoff and Bunsen successfully exploited spectroscopy as an efficient tool in chemical analysis. For instance, they discovered the new metals cesium and rubidium by observing new colored lines in the line spectra [8]. Also, Kirchhoff found during his research activities that any material which emits a particular wavelength can absorb the radiation with the same wavelength also. In all these experiments, it was clearly observed that atoms do not emit a continuous range of wavelengths, but discrete. Analyzing these achievements by other people continued and many attempts were done to regulate relationships between the dark/bright lines, although, without any impressive success. However, in 1885, Balmer represented a simple mathematical formula which phenomenologically described the wavelengths of the visible spectral lines of atomic hydrogen [9]:

$$\lambda_n = \frac{3645.6 n^2}{n^2 - 4}, n = 3, 4, 5, 6. \quad (1.1)$$

Rydberg and others developed this further by generalizing it for some other elements like alkali metals, as well as the alkaline earth metals and other elements also. He expressed (1.1) in a more general form and in a frequency base:

$$\nu_n = \frac{R}{(n'+\mu)^2} - \frac{R}{(n+\mu)^2} \quad (1.2)$$

with n and n' integers and μ and μ' fractional constants for a particular series and R as the Rydberg constant. This formula described quantitatively the frequencies of the emerged bright lines in many recorded spectra. However, two questions were not yet answered: Why should these frequencies be always calculable as the difference between two quantities and why is there a universal constant for them? In 1913, Niels Bohr, inspired of quantum ideas of Planck and Einstein, answered these questions by his theory of planetary atom and orbiting of the electrons around the nuclei in discrete circular orbits [10]. He proposed that these orbitals are states of constant energy and the electrons in them can emit/absorb energies only during a transition from the upper/lower state to the other. This energy is identical to the energy difference between the two states. So was the mutual contributions of spectroscopy investigations and quantum mechanics theories in the development, understanding and confirmation of the postulations of each other in the early twentieth century.

The Rutherford-Bohr orbit theory continuously developed by physicists like Sommerfeld who extended the Bohr's model by taking elliptical orbits and relativity effects to account. The theory was providing acknowledged understandings of electrons arrangement in atoms, although, the understanding and justifying the results of several studies had remained unexplained curiosities: some experimental observations ascertained the duplexity issue, so called by Werner Heisenberg, that the number of states was double what was predicted by Bohr-Sommerfeld quantization rules. This issue was already theoretically touched and accounted when in 1917 Albert Einstein showed in his calculations of stimulated emission that his coefficients of emission (A) and absorption (B) of electromagnetic fields (by an atom) were each associated with two states of an atom [11], and, also, when in 1924, Einstein translated and published Satyendra Nath Bose's paper on Planck's quantum radiation law derivation by counting states with identical properties [12]. The other sets of experiments with unexpected results were in 1922 when Stern-Gerlach experiments [13] [14] [15] showed that the number of the particles deflect in a magnetic field either up or down is equal. What they in fact showed was the spatially quantized orientation of angular momentum in atomic scale. These ambiguities were eventually addressed by the discovery of electron's "4th degree of freedom" by Goudsmit and Uhlenbeck.

In 1925 Ralph Kronig and Samuel Goudsmit published a paper on the intensities in the Zeeman effect [16] as a result of their collaboration in Paul Ehrenfest group in Leiden. A short time later George Uhlenbeck joined them in the group. In February of the same year Wolfgang Pauli published his well-known Exclusion Principle; no two electrons can have identical quantum numbers [17]. After Goudsmit explained m_s , the fourth quantum number, to Uhlenbeck, it was Uhlenbeck who viewed it as “the fourth degree of freedom of an electron”. He proposed that the electron has another degree of freedom and that is its rotation around its own axis. Goudsmit worked on the idea considering the electron to be magnetic with the appropriate magnetic moment and this led to the formulation of the complicated Zeeman-effects by him. Thus, electron was considered spinning and so, “Spin” was discovered!

When Goudsmit and Uhlenbeck discussed their idea of spinning electron with Hendrik Lorentz, he strictly rejected it by this fact that “if electron have a spin, the speed of the surface of the electron would be greater than the speed of light. So, it is impossible!”. However, this argumentation could not avoid the spreading of the “Spin” idea since the written paper of “spinning electron” of Goudsmit and Uhlenbeck was already submitted to *Naturwissenschaften*. The paper was later published [18] and thus, the term “Spin” was coined. So, m_s was defined and reintroduced as an intrinsic property of the electron.

Nowadays, after tremendous theoretical and experimental studies we define the electron spin as the intrinsic angular momentum of an electron which is characterized by a spin quantum number s with the value of $\frac{1}{2}$.

The Stern-Gerlach experiments could then be explained considering the new electron properties of “Spin”. The components of spin angular momentum along a given axis, widely named as the z -axis, is $\hbar/2$ or $-\hbar/2$ referred as in turn spin “up”, $|\uparrow\rangle$, and spin “down”, $|\downarrow\rangle$. This quantum adaptation of values is the result of taking only one of $2s + 1$ possible values for the angular momentum. The spin angular momentum operator is defined by $\hat{S} = \frac{1}{2}\hat{\sigma}$ where $\hat{\sigma} = (\hat{\sigma}_x, \hat{\sigma}_y, \hat{\sigma}_z)$ is the vector of Pauli spin matrices. \hat{S} is defined by its component along x , y and z directions which are:

$$\hat{S}_x = \frac{1}{2}\begin{pmatrix} 0 & 1 \\ 1 & 0 \end{pmatrix}, \quad \hat{S}_y = \frac{1}{2}\begin{pmatrix} 0 & -i \\ i & 0 \end{pmatrix}, \quad \hat{S}_z = \frac{1}{2}\begin{pmatrix} 1 & 0 \\ 0 & -1 \end{pmatrix} \quad (1.3)$$

The representation of spin up and down is particularly simple if the spin points along the z -axis where the eigenvalues of \hat{S}_z take the values $m_s = \pm\frac{1}{2}$ and the corresponding eigenstates are:

$$|\uparrow_z\rangle = \begin{pmatrix} 1 \\ 0 \end{pmatrix}, \quad |\downarrow_z\rangle = \begin{pmatrix} 0 \\ 1 \end{pmatrix} \quad (1.4)$$

In other words, the eigenstates correspond to parallel and antiparallel orientation of spin in respect of z -axis. We know the parallel and antiparallel orienting of a spin in another context. That is when the spin is in an external magnetic field. So, for convenience we define the direction of the external magnetic field as the z -axis.

A spin angular momentum is always associated with a magnetic moment. This magnetic moment can have a component equal to $\mu_e = -g\mu_B m_s$ along a particular axis where g is known as the g -factor and μ_B is the Bohr magneton. g -factor expresses the magnitude of the magnetic moment to the angular momentum (\hat{S} or \hat{L}) ratio in respect to Bohr magneton. Setting g -factor ≈ 2 (2.00231930436182 for a free electron [19]), the corresponding magnetic moment along the external magnetic field (z -axis) is equal to $\approx \mp\mu_B$ (\mp stands for the antiparallel orientation of the magnetic moment in respect to the angular momentum). The energy of the electron in magnetic field is $E = g\mu_B m_s B$. Since $m_s = \pm\frac{1}{2}$ two degenerate states of energy are available in the absence of magnetic field and by applying an external magnetic field this degeneracy is lifted as schematically shown in Figure 1.1. This is called Zeeman splitting.

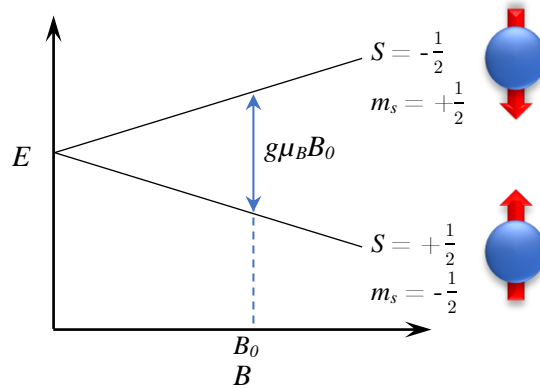


FIG. 1.1. Zeeman splitting of energy for a spin $\frac{1}{2}$ magnetic moment on applying magnetic field

The existence of Zeeman levels and their separation allow a low-high state transition if the required energy of $\Delta E = g\mu_B B$ is appropriately provided to the system. A quantum of radiation can supply the ΔE for the transition through the Bohr frequency statement:

$$\Delta E = \hbar\omega = g\mu_B B \quad (1.5)$$

The magnetic moment of the electron will interact with the magnetic component of the applied radiation. This was the basis of the work of Zavirosky (1944) to detect electron spin resonance (ESR) absorption in solids and founding a new way of spectroscopy.

The light spectroscopy science which dates back to the early 1800s decade could significantly help to raise a new sea of thoughts and rules under the name of quantum mechanics and, mutually, the advances in quantum mechanics could originate

innovative ideas to create new techniques of spectroscopy like ESR experiments. The field of spectroscopy has been extending by the time and at the present it is subdivided into multiple divisions from static (0 to 60 Hz) detecting by simple volt- and ammeters to high energy cosmic rays ($> 10^{25}$ Hz) detecting by extensive shower detectors as briefed in Table 1.1 [20].

1.1. Electron Spin Resonance; an Overview of the Phenomena

ESR is a widely utilized magnetic resonance technique to sense the local environment of an electron. The spin resonance is the transition of the electron spin state from up to down between the Zeeman levels by absorption of the provided energy which is, as already mentioned, a proper radiation. The applied energy is proper when the frequency of the radiation matches the precession frequency, known as Larmor frequency $\omega_L = \gamma B$, of the magnetic moment in the external magnetic field. γ is the gyromagnetic ratio and ω_L rounds about 28 MHz for 1 mT of magnetic field for a free electron. The response of an orbital electron in a lattice to the external perturbations is determined by the crystal fields, collective excitations, as well as spin-orbit coupling and hyperfine interactions, all of which depend fairly critically on the form of the wavefunction of the orbital under study. These parameters can also deviate the electron g -factor from its free electron value and one must use $J = L + S$ as the total angular momentum rather S and L alone and this means $\mu_e = -g\mu_B m_J$. This shows, in the environment of a condensed matter, the energy of an atom's electrons in an external magnetic field cannot be completely described simply by (1.5) but a spin Hamiltonian of the form below [20]:

$$\mathfrak{H} = \mathfrak{H}_{elect} + \mathfrak{H}_{cf} + \mathfrak{H}_{LS} + \mathfrak{H}_{SS} + \mathfrak{H}_{Zee} + \mathfrak{H}_{hfs} + \mathfrak{H}_Q + \mathfrak{H}_N \quad (1.6)$$

$$\mathfrak{H}_{elect} = \text{Electronic energy} \approx 10^4 - 10^5 \text{ cm}^{-1}$$

$$\mathfrak{H}_{cf} = \text{Crystal field energy} \approx 10^3 - 10^4 \text{ cm}^{-1}$$

$$\mathfrak{H}_{LS} = \text{Spin-orbit interaction} \approx 10^2 \text{ cm}^{-1}$$

$$\mathfrak{H}_{SS} = \text{Spin-spin interaction} \approx 0 - 1 \text{ cm}^{-1}$$

$$\mathfrak{H}_{Zee} = \text{Zeeman energy} \approx 0 - 1 \text{ cm}^{-1}$$

$$\mathfrak{H}_{hfs} = \text{Hyperfine structure} \approx 0 - 10^{-1} \text{ cm}^{-1}$$

$$\mathfrak{H}_Q = \text{Quadrupole energy} \approx 0 - 10^{-2} \text{ cm}^{-1}$$

$$\mathfrak{H}_N = \text{Nuclear spin energy} \approx 0 - 10^{-3} \text{ cm}^{-1}$$

Table 1.1. Summary of the various divisions of spectroscopy [20].

Frequency			Energy Units		Typical Radiation		
Branch	Hz	Wavelength	Name	Value in Joule	Phenomenon	Generator	Typical Detector
Static	0 - 60		Joule	1		Battery	Ammeter Voltmeter
Low or radio frequency	$10^3 - 10^5$	300 - 3 km	Calorie kHz	4.186 6.62377×10^{-31}	Dielectric absorption	Mechanical	
Radio frequency	$10^6 - 10^8$	300 - 3 m	Joule	1	NQR, NMR, dielectric absorption	Tuned circuit Crystal	Antenna
Microwaves	$10^9 - 10^{11}$	30 cm - 3 mm	cm^{-1} MHz	1.98574×10^{-23} 6.62377×10^{-28}	Molecular rotations, ESR	Klystron Magnetron Solid state generator	Antenna Crystal Bolometer
Infrared, Terahertz	10^{12} to 3×10^{14}	300 - 1 μm	cm^{-1} kcal/MJoule	1.98574×10^{-23} 4.186×10^3	Molecular vibrations	Heat source	Bolometer PbS cell
Visible, Ultraviolet	4×10^{14} to 3×10^{15}	0.8 - 0.1 μm	Erg eV MHz	1×10^{-7} 1.60207×10^{-19} 6.62377×10^{-28}	Electronic transitions	Incandescent lamp	Photocell
X-Rays	$10^{16} - 10^{19}$	30 - 0.03 nm	eV keV	1.60207×10^{-19} 1.60207×10^{-16}	Electronic transitions	Discharge tube	

γ -Rays	$10^{19} - 10^{22}$	$3 \times 10^{-9} - 3 \times 10^{-12}$ cm	MeV	1.60207×10^{-13}	Inner shell electronic transitions	Heavy element bombardment	Geiger counter Photomultiplier
Low energy, Nuclear	$10^{19} - 10^{23}$	$3 \times 10^{-9} - 3 \times 10^{-13}$ cm			Nuclear energy level transitions	Radioactive nuclei	Scintillation detector
High energy, Nuclear	$10^{23} - 10^{26}$	$3 \times 10^{-13} - 3 \times 10^{-17}$ cm	BeV	1.60207×10^{-10}	Strange particle creation	Accelerator (e.g. synchrotron)	Bubble chamber
			GeV	1.60207×10^{-7}			Spark chamber
High-energy cosmic rays	$> 10^{25}$	$> 3 \times 10^{-16}$ cm			Extraterrestrial	Star, magnetic field in galaxy	Extensive shower detector

The spin Hamiltonian parameters are to modify and get altered by external and intrinsic perturbations or conditions. For an atom, which has zero-field splitting the term \mathfrak{H}_{SS} is 0. \mathfrak{H}_Q and \mathfrak{H}_N are much smaller than the other terms and therefore ignorable. If the study is aimed to consider the electrons, on whose wavefunctions the crystal field effects do not have significant effects, one can ignore \mathfrak{H}_{cf} either. This has another remarkable influence on the data interpretation of an ESR test also, and that is, when crystal fields are not effective on the wavefunction of the studied spin, \mathfrak{H}_{Zee} can yield adequate information about spin-orbit coupling by itself. Thus, of all the terms in the Hamiltonian (1.6), \mathfrak{H}_{Zee} and \mathfrak{H}_{hfs} could be considered as the most dominant terms in calculation of spin dynamics for particular paramagnetic species. These two can be directly extracted from ESR data.

By applying external magnetic fields on a pool of spins the distribution of the number of spins between the Zeeman levels splits into two populations which is described by the Maxwell-Boltzmann statistical law:

$$\frac{n_{\downarrow}}{n_{\uparrow}} = e^{\frac{-\Delta E}{kT}} \quad (1.7)$$

where k is the Boltzmann constant, T is the absolute temperature, $\Delta E = g\mu_B B$ and $\frac{n_{\downarrow}}{n_{\uparrow}}$ is the ratio of the number of down oriented spins ($S = -\frac{1}{2}$ and $m_s = +\frac{1}{2}$) to up oriented spins ($S = +\frac{1}{2}$ and $m_s = -\frac{1}{2}$) with respect to external magnetic field. Figure 1.2 pictures the ratio of $\frac{n_{\downarrow}}{n_{\uparrow}}$ on changing temperature and magnetic field.

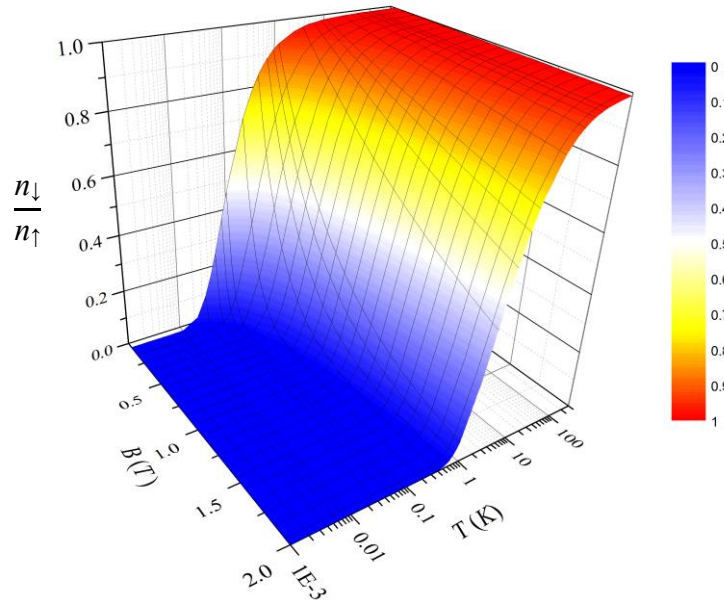


FIG. 1.2. The color map surface for $\frac{n_{\downarrow}}{n_{\uparrow}}$ for a spin complex with g -factor of 2.0023 (free electron) by alteration of temperature, T (K), and magnetic field B (T).

Lowering the temperature and increasing the magnetic field have the same effect in the trend of spin population splitting. When the lower Zeeman level is more populated, the ESR absorption grows and therefore the signal intensity rises. Therefore, for the systems in which no new interactions or phase transitions by lowering T or increasing B happen, usually the ESR is stronger at lower temperatures and higher magnetic fields which corresponds for higher frequencies.

The excited spins at higher energy, subsequently release the excess energy and return to their equilibrium state and realign with the magnetic field. This process is called relaxation and is explained in two various forms under the names of spin-lattice relaxation and spin-spin relaxation with corresponding time scales of T_1 and T_2 respectively. In spin-lattice relaxation the released energy (through relaxation) is transferred to lattice causing phonons. This dissipation of energy (relaxation) of excited spin is characterized by an exponential decay of energy as a function of time as in (1.8) and also (1.9).

$$n(t) = n_0(1 - e^{-\frac{t}{T_1}}) \quad (1.8)$$

$$M_z(t) = M_0(1 - e^{-\frac{t}{T_1}}) \quad (1.9)$$

where $n(t)$ is the initial difference in population of the parallel and antiparallel oriented spins by applying the magnetic field. In fact, $n(t) = n_{\downarrow} - n_{\uparrow}$ (cf. 1.7) after the time t is elapsed. n_0 is $n(t = 0)$ and $M_z(t)$ is the recovered (longitudinal) magnetization in the direction of the applied static magnetic field after the time t is elapsed from the applying the alternating field. M_0 is the initial magnetization; $M_z(t = 0)$. By another way of explanation, T_1 is the time constant the spin system needs to exchange energy with its surroundings (lattice). Regarding the collective nature of the magnetization phenomena, relationship (1.9) is a more appropriate definition for T_1 than (1.8).

Spin-spin relaxation, on the other hand, reinitialize the stimulated spins to their equilibrium state through the interactions among the spins themselves and not between the spins and the lattice [21]. The slight differences in the Larmor frequencies of the spins causes a phase decoherence among them after pushing them away from the equilibrium state by the alternating field. The decomposing of the transverse magnetization, which is the flipped longitudinal magnetization, smears it out the by time (1.10):

$$M_{xy}(t) = M_{xy,0}(e^{-\frac{t}{T_2}}) \quad (1.10)$$

where $M_{xy,0}$ is the transverse magnetization that is the immediate flipped M_z (for a $\frac{\pi}{2}$ pulse).

In spin-lattice relaxation the spin needs the lattice as the reservoir of energy for relaxation, whereas, in spin-spin relaxation the interaction between the spins cause the relaxation. That is a reason that T_2 can be (much) shorter than T_1 , specially at low temperatures [22].

The importance of T_1 and T_2 is signified in the analysis of their effects on the ESR linewidth (ΔB). ΔB is determined by the both of T_1 and T_2 .

$$\Delta B \propto \frac{1}{T_1} + \frac{1}{T_2} \quad (1.11).$$

In solutions T_1 may equal T_2 but as mentioned above also, T_2 is mostly much shorter than T_1 and therefore the linewidth depends mainly on spin-spin relaxations.

(1.11) expresses the shorter the T_1 , the wider the ΔB . This is very intuitive to understand by Heisenberg Uncertainty Principle (1.12) [23] when the lifetime of the excited spin becomes shorter:

$$\Delta E \Delta t \geq \frac{\hbar}{2} \quad (1.12)$$

$$\hbar \delta\omega \delta t \geq \frac{\hbar}{2} \quad (1.13)$$

$$\delta\omega \geq \frac{1}{2T_1} \quad (1.14)$$

where $\Delta E (= \hbar\delta\omega, \omega$ is frequency) is the uncertainty in the energy and Δt is the uncertainty in the lifetime measurement. \hbar is the reduced Planck's constant. T_1 gets longer when the temperature of the spin system decreases. For many systems, an ESR signal is detectable (ΔB is narrow enough to detect) by decreasing the temperature. On the other hand, when T_1 is too long the saturation phenomena happens. This is the equally occupation of the up and down states and will lead to a reduction in the signal intensity.

T_2 increases if the density of the spins increase. This will decrease the spin-spin distances and thus the spin-spin interactions are stronger. The higher the number of the spins results to the wider range of the Larmor frequencies of them and so the linewidth will become wider.

To have a detailed study, an ESR spectrum of a system should be recorded and studied at multiple frequencies, microwave powers, temperatures etc. However, this strongly depends on instrumental challenges and technology level to provide us desirable ranges of the mentioned variables.

1.2. ESR Spectrometers

Most commercially produced ESR spectrometers utilize cavity resonators. A microwave resonant cavity is a both end short cut box (a closed section of a waveguide), with different geometries like cylindrical or rectangular, fabricated from a high conductive metal with dimensions comparable to the wavelength. The most used cavity resonators in ESR experiments show the resonance (≈ 9.5 GHz) in X-band range (8 - 12 GHz). A cavity resonator can show multiple resonances by stimulating it with higher frequencies whose (spatial) wavelength match the volume of the cavity. However, each mode has different electric and magnetic fields distribution than other modes in at least two dimensions of the cavity. This is due to the single conductor construction of cavities and transverse electric (TE) or transverse magnetic (TM) fields (with longitudinal magnetic and electric field components respectively) of the formed resonances [20] [24]. Regarding the usual perpendicular orientation of the external static magnetic field (spin orientations) and the magnetic component of the alternating field (resonance in the cavity), TE₁₀₂ (also called TE₀₁₂) is the most important mode used in ESR experiments. This limits the utilization of ESR cavity spectrometers to just a single frequency.

The resonance frequency of any TE_{*mn*l} or TM_{*mn*l} of a rectangular cavity resonator is given by [24]:

$$f_{mnl} = \frac{c}{2\pi\sqrt{\mu_r\epsilon_r}} \sqrt{\left(\frac{m\pi}{a}\right)^2 + \left(\frac{n\pi}{b}\right)^2 + \left(\frac{l\pi}{d}\right)^2} \quad (1.15)$$

where c is the light vacuum frequency, μ_r and ϵ_r are in turn the relative permeability and permittivity of the filling material of the cavity. m , n , l and a , b , d are shown in Figure 1.3.

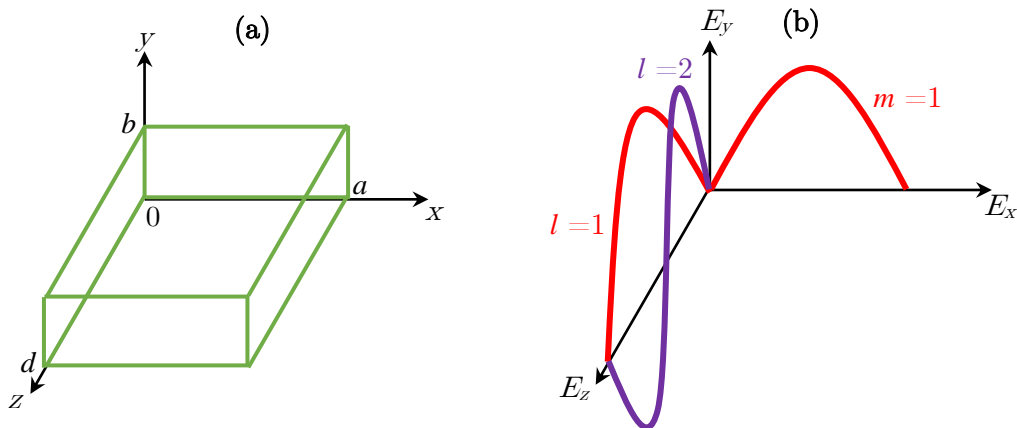


FIG. 1.3. Schematic of a rectangular cavity resonator with the corresponding dimensions (a) and the electric field distributions of TE₁₀₁ and TE₁₀₂ resonance modes (b). The figure is redrawn from [24].

The sizes of the rectangular cavities are in the range of 2 to 5 centimeters. This compared to the size of many physical samples which are sometimes as small as 0.5 mm^3 , is a huge volume. Therefore, the typical filling factors are relatively small. Filling factor must be regarded since the ESR signal intensity is directly proportional to the amount of the absorbed signal by the sample.

Low temperature ESR measurements are necessary for technical goals like stronger signal and lower noise as well as studying interesting physics of materials like the phase transitions at low temperatures. Furthermore, for some spin systems, because of their e.g. very short relaxation times, an ESR line is detectable only at low temperatures (liquid Nitrogen $\approx 77 \text{ K}$ and liquid Helium $\approx 4 \text{ K}$) or even ultra-low temperatures in the range of milli-Kelvin (mK) or lower. Ultra-low temperatures are accessible by dilution refrigerators. The large volume of the cavities, and also, the large size of the waveguides in comparison with typical small embedded space in dilution refrigerators restricts the compatibility of these two with each other.

The mentioned drawbacks of the conventional ESR spectrometers (the single frequency application and the big size) can be resolved by replacing the waveguide systems by coaxial line systems; a transmission line based on two conductors. The usual mode of wave propagation in a coaxial system is transverse electromagnetic (TEM). In a TEM mode the electric fields are drawn radially from the center conductor to the outer conductor, changing the direction along the line depending on the frequency (wavelength) of the propagating signal. The magnetic field lines are concentric circles surrounding the center conductor and perpendicular to the electric field lines at each point of the space. This is schematically shown in Figure 1.4.

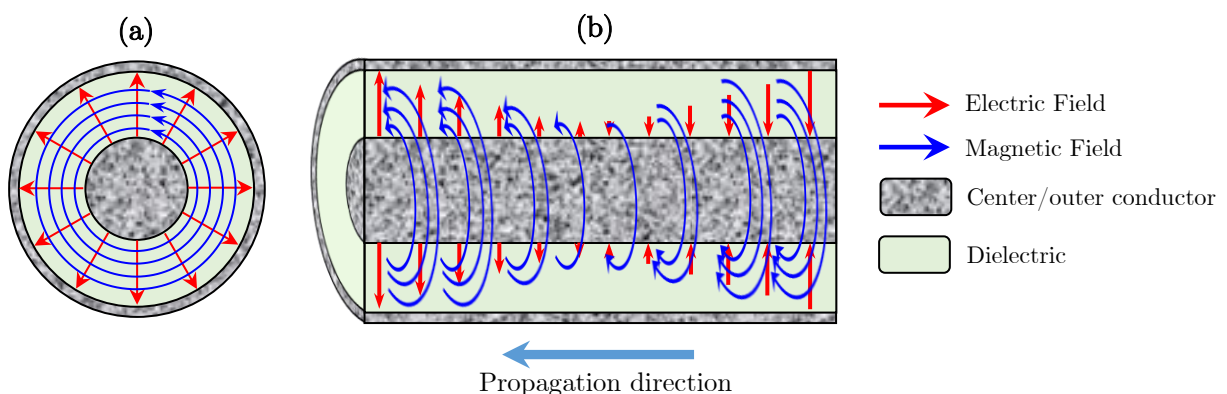


FIG. 1.4. Schematic of the front cross section of a coaxial line (cable) and the field distributions of TEM mode (a) and the side cross section (b).

Thereupon, in case of having a resonator based on a transmission line structure, the TEM mode is hold for every mode and an ESR experiment with such a system could be performed at several frequencies by using a single resonator.

Regarding the size issue, microtechnological manufacturing methods like photolithographic fabrications have made producing two dimensional planar types of transmission line with dimensions practicable down to micrometers. A significantly higher filling factor, compared to cavity resonators, is achievable for small size samples. The whole box containing the transmission line chips and connectors is possible to be placed in a volume of $\approx 1 \text{ cm}^3$. Such a compact and miniaturized system is easily mounted on dilution refrigerators and play a substantial role in mK ESR studies. To lead the alternating signal to the point of chip and sample, coaxial cables are utilized.

In 1974 Johansson et al. [25] introduced a TEM mode stripline resonator with the fundamental of $\approx 3.3 \text{ GHz}$ and used it in ESR applications. Since then many experimental attempts and studies have been successfully exploring and showing the application of micro-size planar transmission line structures for ESR experiments which will be mentioned in the text later.

1.3. ESR Experiments via Coplanar Waveguides

In microwave components and devices, coplanar waveguides (CPW) are one of the most applicable transmission lines which can be produced of the both of superconducting [26] [27] and metallic (non-superconducting) materials [28] [29] [30]. Easily adapting to active or passive components and having conductor strip and ground planes on the same side of the substrate have made CPWs suitable for the classical engineering applications such as sensors [31] and filters [32] as well as for some parts of new modern physics like circuit quantum electrodynamics [33] and quantum information processing [34]. Their way into physics experiments owes to the efficient and orientable coupling of the electric and magnetic energy of the carrying signal to the surrounding medium. For ESR studies, the functionality of planar structures (microstrip, stripline and coplanar) in the both forms of a transmission line and a resonator is already proven [25] [35] [36] [37] [38] [39] [40] [41] [42] [43] [44] [45].

From this point on in this text, the term “transmission line” is designated to the two conductor waveguides through which the signal passes without any purposefully reflection point and formation of standing waves in the way that resonators are designed. The schematic of a coplanar transmission line and resonator are pictured in Figure 1.5. A coplanar resonator is in fact a coplanar transmission line whose center conductor is separated from the rest of the line via two coupling gaps (FIG. 1.5 (c)).

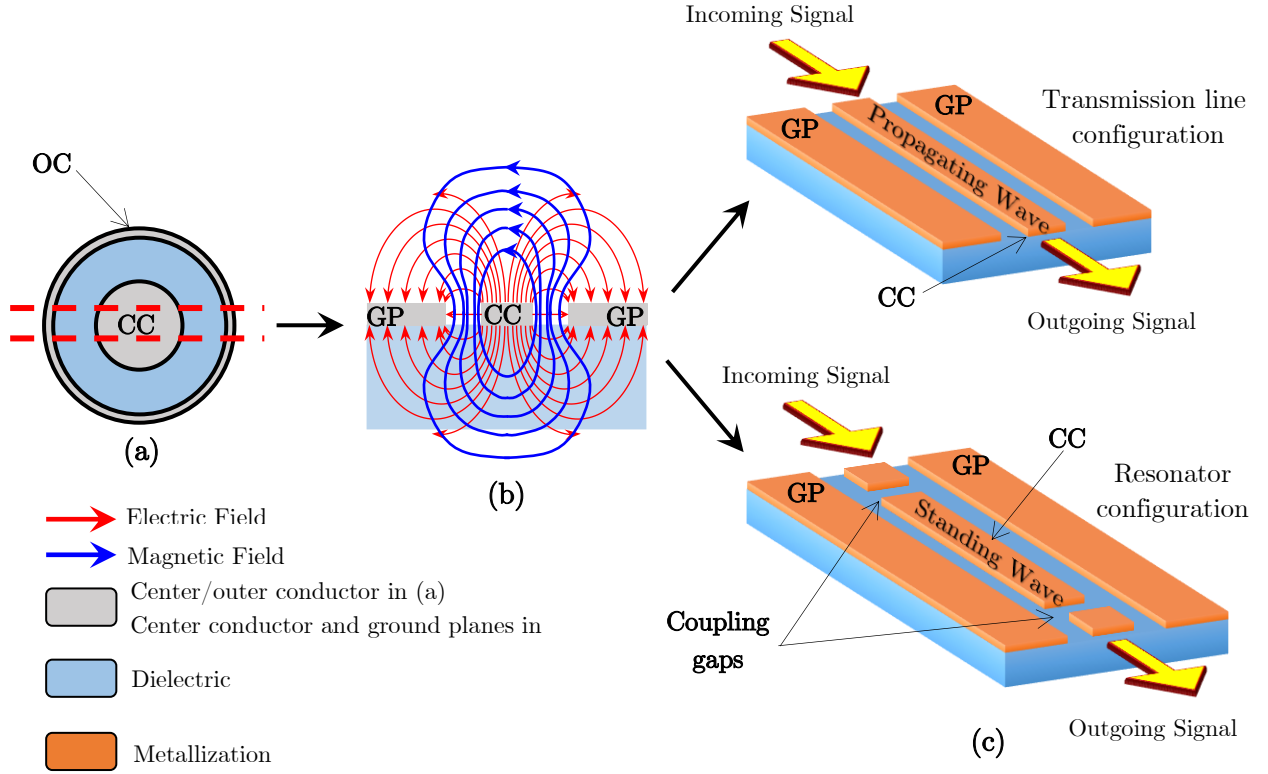


FIG. 1.5. (a) The front cross section of a coaxial cable. (b) A coplanar structure may be explained as a restructured part of a coaxial cable, e.g. the section between the two dashed lines in (a), with extended outer conductors (OC) which are named ground planes (GP) in planar structures terminology. “CC” stands for center conductor. The quasi-TEM field lines of the signal in a coplanar line are also schematically shown in (b). The fields of the coplanar waveguide mode (even mode) are more concentrated near the gaps between the center conductor and the ground planes. In an even mode the electric field lines are directed from the center conductor to the ground planes. The magnetic field lines surround the center conductor. (c) Broad band or selective transmission of signal power are two possible forms of functionality of a coplanar structure by a transmission line and a resonator respectively.

One of the substantial differences between a transmission line and a resonator is the posture and the manner of the signal in the structure whether it is a propagating wave or a standing wave. In the case of a transmission line a propagating wave is passing the line without any intentional reflection of a designed reflection point. In this case the electric and magnetic field of the signal are in phase alternating and propagating forward. In contrast, in a resonator the incoming wave meets a discontinuity in the line (the first coupling gap) and reflects from the point leaving a part of the power induced into the center conductor part. The induced wave propagates along the center conductor until it reaches to the end point of it and reflects backward and the reflection happens at the beginning point of the center conductor again. The (trapped) wave reflects back and forth several (many) times and in the case of the proper wavelength

(this will be elaborated later) a standing wave will form along the center conductor. This standing wave can also pass over the second coupling gap and reaches where the detector is. The electric and magnetic field of the standing wave are in a $\frac{\pi}{2}$ phase shift relative to each other.

The travelling of the quasi-TEM modes in microstrip lines is dispersive. The electric and magnetic fields of the signal are more concentrated in substrate as the frequency increases. This means the higher the frequency, the less portion of the signal above the microstrip in air superstrate. In contrast, a CPW structure keeps 50% of the signal power in either side of the metallization non-depressively i.e. independent of the frequency of the carrying signal. This is an essential feature to have a right estimation of the ESR signal intensity at different frequencies. On the other hand, spectroscopy experiments with strip line structures, in which one of the ground planes is substituted by the sample, are more appropriate for charge dynamics probing rather spin dynamics [44]. This is due to that in such sample-resonator configuration the electric fields of the signal interact much more efficient than the magnetic lines with the sample. Therefore, for an ESR experiment via planar transmission lines or resonators the coplanar configurations are more appropriate choices than microstrips or strip lines. It is worth to mention that microstrip resonators have also been successfully used in the ESR measurements [25] [36] [37] [40] [44] [46].

Depending on the desired application of coplanar waveguides, they may be fabricated from normal high conductive metals like copper or from superconducting materials if the ambient temperature of the experiment is enough low. In ESR experiments exerting magnetic fields are inevitable; ignoring some zero field tests. By approaching the critical magnetic field of the superconducting materials, the functionality of superconducting components is affected, and so will it also be for a coplanar resonator or a transmission line [43] [47] [48]. A precise analysis of the affected background of the ESR spectra which were obtained by Niobium coplanar resonators in the 1. Physikalisches Institut, required more than a year intensive regression analysis. For more information about the analysis and the corresponding data refer to section 4.7 and Appendix I. Furthermore, the repelling of the magnetic field by superconductors can lead to the deviations between the sensed field intensity by the sample and the expected (ordered) amount.

Transmission lines, beside the resonators, have also been utilized for ESR experiments. However, the feasibility of obtaining a more significant signal from a low number spin system makes the use of resonators more demanding than transmission lines. Of course, the great possibility of broadband measurements via transmission lines should not be neglected [35] [43].

In this thesis, a new approach for room, low and ultra-low temperature ESR measurements is studied and developed. The method is based on optimized metallic (normal conducting) coplanar waveguides for ESR experiments. In the next chapter the theory of coplanar structures will be mentioned. Chapter 3 will discuss the materials and systems including one ESR calibrating sample, two heavy fermion compounds and one spin liquid systems, which were studied during this project by the developed resonators at low and ultra-low temperatures. The design and optimization procedures of the resonators and transmission lines are introduced in chapter 4. The primary results of ESR experiments on the ESR calibrating sample of DPPH are offered in chapter 5. Chapters 6 and 7 contain the obtained results of the ESR study of the correlated solid matters and at the end a summary and prospective view (summary and outlook) will be presented.

2. Metallic Coplanar Waveguides; Introduction and Theory

In this chapter an introduction to the coplanar waveguides and their quantitative characteristics will be offered.

2.1. Loss and Attenuation

An electromagnetic wave is formed from alternating electric and magnetic fields each of which transfers corresponding electrical and magnetic energy along the propagation of the wave. While transferring the power, a part of it may get lost because of the lossy medium or may get reflected due to impedance mismatching between two media. Loss is in fact the separation of a part of wave power by the material which will be reradiated out to the ambient such that it is not detectable by our detectors; in other words, it is not correlated any more. The material parameters such as dielectric constants ϵ , conductivity σ and permeability μ , determine the wave propagation quality like dissipation and propagation constants. The following dispersion relation between the wavevector \mathbf{q} and the frequency ω shows that the wave propagation in a medium encounters an attenuation and a wavelength alteration compared to free space [49]:

$$\mathbf{q} = \frac{\omega}{c} \left[\epsilon_1 \mu_1 + i \frac{4\pi \mu_1 \sigma_1}{\omega} \right]^{\frac{1}{2}} \mathbf{n}_q \quad (2.1)$$

where $\mathbf{n}_q = \frac{\mathbf{q}}{|\mathbf{q}|}$ and ϵ_1 and σ_1 and μ_1 are the real parts of permittivity, conductivity and permeability respectively (with cgs units). Loss or attenuation are reductions in the electric and magnetic fields magnitude of the propagating wave and there may be a phase shift with respect to each other. Waveguides which are produced of lossy materials insert loss on the transmitting power. Even in the superconducting waveguides the loss can stem from e.g. dielectric loss and the lossy radiation of the signal. A simple relationship describing the insertion loss of a waveguide based on the incoming and outgoing power is given at the following. In this formula, the calculated insertion loss, IL , contains the reflected power, return loss, also.

$$IL = -20 \log(T) \quad (2.2)$$

where T is the transmission. As mentioned above, (2.2) includes the return loss, RL , also which is defined as:

$$RL = -20 \log(\gamma) \text{ where } \gamma = \frac{Z_L - Z_0}{Z_L + Z_0} \quad (2.3)$$

γ is called reflectivity, Z_L and Z_0 are in turn line and load impedance. Impedance will be explained shortly later.

Another very noticeable impacts of the loss parameters on the wave propagation is the phase shift between the electric and magnetic fields of the wave. In non-conducting mediums, the propagations of the electric and magnetic fields are in phase [49]:

$$\mathbf{H} = \left(\frac{\epsilon_1}{\mu_1}\right)^{\frac{1}{2}} \mathbf{n}_q \times \mathbf{E} \quad (2.4)$$

$$\mathbf{E} = \left(\frac{\mu_1}{\epsilon_1}\right)^{\frac{1}{2}} \mathbf{n}_q \times \mathbf{H} \quad (2.5)$$

Hence, in designing waveguides in which lossy metals are used, the probable phase shift between the electric and magnetic fields should be noticed.

There is one more effect resulting from the causes of loss and that is, the TEM mode of propagation could be affected by loss of the system [49]. For a typical coplanar structure, TEM mode is already changed to a quasi-TEM by the different sub- and superstrates (dielectric and air). One should however be aware of the effect of lossy materials also on the violating of TEM mode formation.

2.2. Quality Factor

In the context of resonators, the most impressionable property of the line by the loss of the system is quality factor, Q . Quality factor is a quantity which shows the amount of stored energy, in the forms of magnetic and electric energies, in comparison with the amount of lost energy in the system. Thus, the higher the loss the lower the quality factor [24]:

$$Q = \frac{\text{Total Power in the system}}{\text{Dissipated Power in the system per cycle}} = \frac{\omega \cdot \text{Average Energy Stored}}{\frac{\text{Energy Loss}}{\text{Second}}} \quad (2.6)$$

At and around resonance, a microwave resonator can be estimated and analyzed by making either a series or a parallel RLC lumped-element equivalent circuit. The components of the circuit are in fact the physical models for the constructing parts of

the resonator like wires, dielectrics etc. A series lumped-element circuit is shown in Figure 2.1.

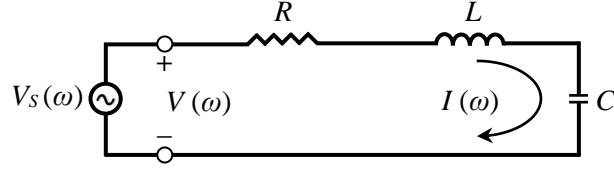


FIG. 2.1. A series RLC circuit. One should note that, for simplicity purposes in, the ω sign is not written after V_s , V , I and P in the following text although they are frequency dependent, i.e. $V_s(\omega)$, $V(\omega)$, $I(\omega)$ and $P(\omega)$.

The dissipated power, P_{loss} , is calculated only by the resistor R since in the equivalent circuit model collect all the existing resistances of the circuits at a single point and represent it as R . P_{in} which is formulated by (2.8) could be expressed as $P_{loss} + P_{stored}$.

$$P_{loss} = \frac{1}{2} |I|^2 R \quad (2.7)$$

$$P_{in} = \frac{1}{2} |I|^2 \left(R + i\omega L - i \frac{1}{\omega C} \right) \quad (2.8)$$

where the term $\left(R + i\omega L - i \frac{1}{\omega C} \right)$ is the input impedance, Z_{in} [24].

(2.7) and (2.8) are the average power values of the time dependent power of:

$$P(t) = V \cos(\omega t) \cdot I \cos(\omega t + \varphi) \quad (2.9)$$

The average stored magnetic and electric energies in L and C are in turn:

$$W_m = \frac{1}{4} |I|^2 L \quad (2.10)$$

$$W_e = \frac{1}{4} |I|^2 \frac{1}{\omega^2 C} \quad (2.11)$$

whose substitution in (2.8) results to:

$$P_{in} = P_{loss} + 2i\omega (W_m - W_e) \quad (2.12)$$

When W_m and W_e are equal, the applied voltage has stimulated a resonance condition in the circuit. This leads Z_{in} to be equal to R at resonance condition ($W_m = W_e$) since:

$$Z_{in} = \frac{2P_{in}}{|I|^2} = \frac{P_{loss} + 2i\omega (W_m - W_e)}{\frac{1}{2} |I|^2} = \frac{P_{loss}}{\frac{1}{2} |I|^2} = R \quad (2.13)$$

Therefore, the impedance of the circuit at the resonance is purely resistive [24]. This implies that at resonance the inductor and capacitor combination acts as a short circuit

and the current flowing in the system is in phase with the source voltage [50]. Thus, at resonance P_{loss} is maximum and is equal to $\frac{1}{2} \frac{V_{S,max}^2}{R}$.

From $W_m = W_e$ the resonance frequency can also be calculated:

$$\omega_0 = \frac{1}{\sqrt{LC}} \quad (2.14)$$

Another way of writing (2.6) by (2.10) and (2.11) at resonance is:

$$Q = \omega \frac{W_m + W_e}{P_{loss}} = \omega \frac{2W_m}{P_{loss}} = \frac{\omega_0 L}{R} \quad (2.15)$$

$$Q = \omega \frac{W_m + W_e}{P_{loss}} = \omega \frac{2W_e}{P_{loss}} = \frac{1}{\omega_0 RC} \quad (2.16)$$

A general definition for the ratio of the output to the input of a circuit is the Transfer Function [51]. The transfer function, $H(s)$ where s is the variable of the circuit e.g. frequency, for an RLC circuit like Figure 1 is defined as [50]:

$$|H(\omega)| \equiv \left| \frac{V_R}{V_S} \right| = \frac{\omega RC}{\sqrt{(1 - \omega^2 LC)^2 + (\omega RC)^2}} \quad (2.17)$$

where V_R is the potential difference across the resistance R . (2.17) is called Frequency Response also. The frequency by which $|H(\omega)|$ is decreased by the factor $\frac{1}{\sqrt{2}}$ from its maximum value is called cutoff frequency. $|H(\omega)|=1$ when $1 - \omega^2 LC = 0$ which is the resonance condition (2.14). The power which is delivered by the circuit at cut off frequency is half of the maximum power since $P_{in} \propto V^2$. Solving (2.17) for $|H(\omega)| = \frac{1}{\sqrt{2}}$ two roots of the equation are obtained as ω_1 and ω_2 :

$$\omega_1 = -\frac{R}{2L} + \sqrt{\left(\frac{R}{2L}\right)^2 + \frac{1}{\omega_0^2}} \quad (2.18)$$

$$\omega_2 = \frac{R}{2L} + \sqrt{\left(\frac{R}{2L}\right)^2 + \frac{1}{\omega_0^2}} \quad (2.19)$$

From (2.15), (2.18) and (2.19) a simple relationship for Q can be calculated as:

$$Q = \frac{\omega_0}{BW} \quad (2.20)$$

where BW is the band width at half maximum power. Figure 2.2 shows schematically a spectrum of a delivered power by a resonator and the corresponding quantities.

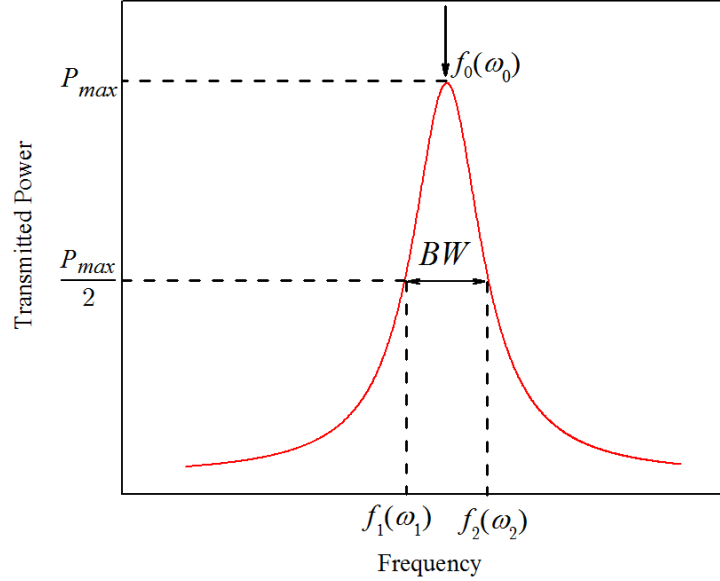


FIG. 2.2. Demonstration of ω_0 and BW of expression (2.20) on a delivered power curve by a resonator.

To measure the transmission properties of a resonator, an external circuit (cabling from and to the signal generator) is inevitable. Hence, the measured Q of a resonator is the loaded Q (Q_L). However, if the coupling gaps size are optimized Q_L is very close to the unloaded or internal Q (Q_{int}) which is the Q of the resonator itself without any perturbation of the external circuit. Q_L , Q_{int} and external Q (Q_{ext}) are related to each other via:

$$\frac{1}{Q_L} = \frac{1}{Q_{int}} + \frac{1}{Q_{ext}} \quad (2.21)$$

As just mentioned if the coupling gaps are so optimized that the resonator is in the under-coupled regime then $Q_{ext} \gg Q_{int}$ is fulfilled and $Q_{int} \approx Q_L$. In a CPW resonator the coupling gaps size determine if the system is in an under-coupled or in an over-coupled ($Q_{ext} \leq Q_{int}$).

2.3. Characteristic Impedance

As already mentioned, in addition to the attenuation of a propagating wave in a medium, a part of the wave is reflected at the interface when the medium is changed. Reflection is because of the allowed proportion of the electric and magnetic field intensities for a propagating wave are different from one medium to the other. This property of the medium is called impedance and has the unit of Ohm (2.3). In a very similar manner, each waveguide has an impedance which is known as its characteristic impedance, Z_0 .

Another to be defined concept is the impedance. Impedance is the quantity which determines the ratio of potential and current, $\frac{V}{I}$, in an AC circuit. Impedance may be an imaginary number since in an AC circuit there should be a phase difference between V and I . Impedance could be defined for a medium (intrinsic impedance of a medium), for a plane wave (wave impedance) and for a waveguide (characteristic impedance) as well. The different mentioned impedances are defined based on one common notion and that is the ratio of the electric field to the magnetic field of the wave in the medium. For a plane wave to propagate in medium or along a waveguide, the wave impedance must be or become equal to the intrinsic impedance and the characteristic impedance respectively. In fact, reflection happens to match the wave impedance with the medium impedance.

Characteristic impedance, as the name implies, is a characteristic parameter of a line. Characteristic impedance of a coplanar line is dependent on its geometrical characteristics and the materials used in its structure. The very first formulation for the characteristic impedance of a planar structure is defined as [52]:

$$Z_0 = \frac{\eta}{4} \frac{K(k)}{K(k')} \quad (2.6)$$

η is the medium impedance which is equal to $\sqrt{\frac{\mu}{\epsilon}}$. $K(k)$ and $K(k')$ are the complete elliptic integral of the first kind and its complement, i.e. $k' = \sqrt{1 - k^2}$. It is proved [52] that it is possible to get simple, useful and general formulas without calculations from elliptic integral theory. Elementary conformal mappings will suffice to extract a straightforward formula for the characteristic impedance of a coplanar line [53] [54] [55] [56]. The following analysis for Z_0 is considering a negligible thickness of the metallization, infinitely large ground planes and infinitely thick substrate.

The capacitance per unit length of a CPW is estimated as the summation of the capacitance (per unit length) for the substrate (dielectric), C_d , and superstrate (air), C_a .

$$C_d = 2\epsilon_0\epsilon_r \frac{K(k)}{K(k')} \quad (2.7)$$

$$C_a = 2\epsilon_0 \frac{K(k)}{K(k')} \quad (2.8)$$

k is the geometrical parameter defined as $\frac{w}{w + 2s}$ where w is the center conductor width and s is the distance between the center conductor and the ground plane (Figure 2.4).

Calculation of the complicated ratio $\frac{K(k)}{K(k')}$ could be avoided by using the simplified, but still comparable in accuracy with other simulation based analysis, formulas of:

$$\frac{K(k)}{K(k')} = \frac{\pi}{\ln\left(2\frac{1+\sqrt{k'}}{1-\sqrt{k'}}\right)} \quad \text{for } 0 \leq k \leq 0.707 \quad (2.9)$$

$$\frac{K(k)}{K(k')} = \frac{\ln\left(2\frac{1+\sqrt{k}}{1-\sqrt{k}}\right)}{\pi} \quad \text{for } 0.707 \leq k \leq 1 \quad (2.10)$$

The total capacitance is $C_{total} = C_d + C_a$ and the effective permittivity is $\epsilon_{eff} \approx \frac{\epsilon_r + 1}{2}$ where ϵ_r is the relative dielectric constant.

The characteristic impedance is then estimated as:

$$Z_0 = \frac{30\pi}{\sqrt{\epsilon_{eff}}} \frac{K(k')}{K(k)} \quad (2.11)$$

For a CPW with $\epsilon_r = 10$, $w = 20$ (or 100) μm and $s = 8$ (or 40) μm , Z_0 is, from (2.11), equal to 48.23 Ω . Having a low loss coefficient, Sapphire is a good candidate to be utilized as substrate [57]. It has an anisotropic relative permittivity changing from 9.5 to 11 at different crystalline directions. Figure 2.3 shows the approximated characteristic impedance of for a CPW with sapphire as substrate for different orientations for different ratios of $\frac{w}{s}$.

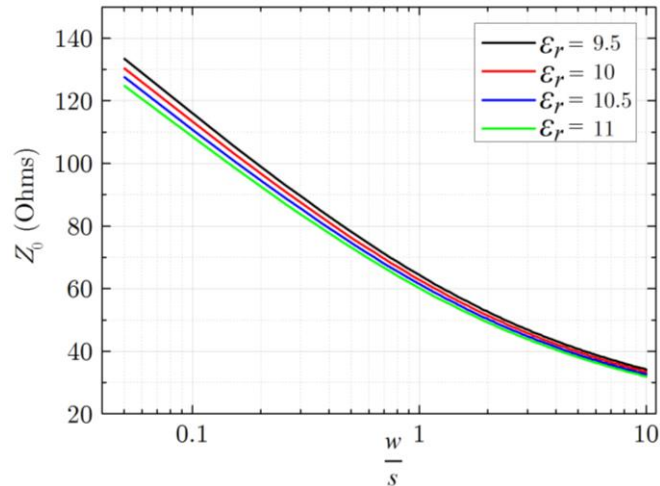


FIG. 2.3. Characteristic impedance of a CPW with a Sapphire substrate with infinite thickness calculated by (2.11) against $\frac{w}{s}$ for different relative permittivity values since Sapphire substrates have anisotropic permittivity.

In practice, however, a substrate cannot have an infinite thickness and the metallization thickness sometimes is not negligible. In addition, the ground planes size is in many practical cases quite comparable with w and is not much larger. The lines are designed for many purposes in a meander shape and the final chip of a CPW is placed in a shielding (box) in many cases. The effects of some determining parameters like metal thickness, ground plane size, absolute values of geometrical dimensions, shielding effects, substrate thickness etc. on Z_0 , ϵ_{eff} and the attenuation of the line will be shown which are experimentally and theoretically studied. Figure 2.4 shows a simplified schematic picture of the main geometrical dimensions, constituents and components of a coplanar waveguide whose influences on the line characteristics will be the topic of this part of the thesis. In chapter 4 some more geometrical parameters for meander structures, which are implemented in the CPW resonators in this thesis, will be introduced.

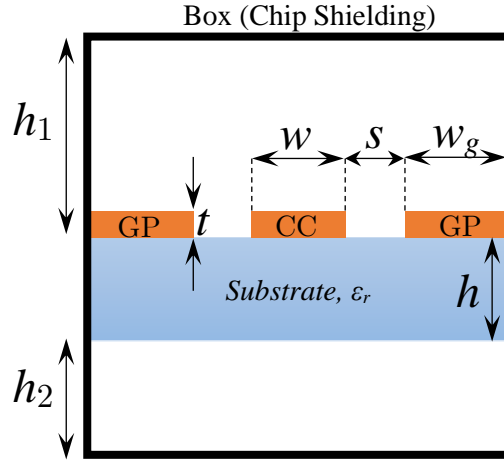


FIG. 2.4. The geometrical dimensions of a coplanar structure. “GP” stands for the ground planes. “CC” represents the center conductor. The ground plane distance is shown by “ s ” and the thickness of metallization and substrate are given by “ t ” and “ h ” respectively. “ w ” is the center conductor width and “ w_g ” the width of the ground planes. “ h_1 ” and “ h_2 ” are the distances between the chip and the shielding.

Furthermore, the absolute value of geometrical dimensions also, like the value of s , apart from fractional values like $\frac{w}{s}$, take determinant roles in the variation of line characteristics. Elaborating this more, according to (2.11) if two CPW structures have an identical value of $\frac{w}{s} = 2.5$ but for one $w = 20 \mu m$, $s = 8 \mu m$ and for the other $w = 100 \mu m$, $s = 40 \mu m$, they must have a similar impedance, however, since the effective dielectric constant changes by changing s value, having the equal impedance or effective permittivity values will not be the case [58] [59]. Such an example is shown in Figure 2.5 taken from Ref. [59].

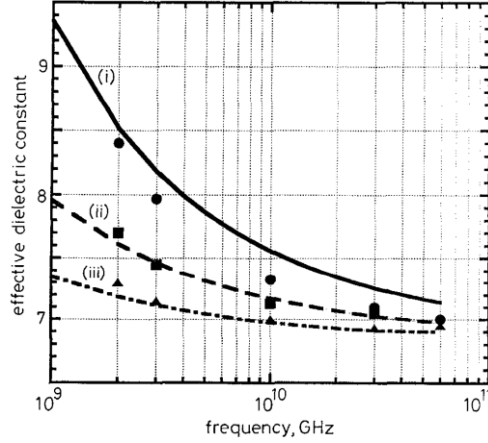


FIG. 2.5. ϵ_{eff} vs. frequency for three different CPWs with various absolute parameters of w and s but the same ratio of $\frac{w}{s}=1.5$. $\sigma = 3.3 \times 10^7$ S/m, $t = 1 \mu\text{m}$, $h = 500 \mu\text{m}$. (i) $s = 6 \mu\text{m}$, $w = 9 \mu\text{m}$ and (ii) $s = 12 \mu\text{m}$, $w = 18 \mu\text{m}$ and (iii) $s = 24 \mu\text{m}$, $w = 36 \mu\text{m}$ [59].

Beside the aforementioned points, the dispersive line characteristics should not be neglected, although, one of the biggest advantages of CPWs is very rigorous constancy of the line properties at different frequencies.

As one notes, in practical uses, there are several non-negligible factors which affect the loss, characteristic impedance, effective dielectric constant and dispersive behavior of a CPW. These have been studied by the time and tried to be formulated by many publications including books and papers. In these studies models and procedures are proposed considering the presence of upper shielding, finite-extent lateral ground planes, different thicknesses for metallization and dielectric and so forth. At the following a brief review of the effective factors on the line characteristics is represented.

2.4. The Effect of Geometrical Parameters

The line characteristics like characteristic impedance, loss, effective permittivity and their dispersion behavior are under the influence of the geometrical dimensions. Here the parameters of w and s of Figure 2.4 are discussed. The rest of the dimensions will be discussed in the further parts. The following analysis are based on various theoretical (modeling) and experimental studies. The deviations of the investigated characteristics by different models and approaches of each other are in many cases around 5% [60] [61] [62]. Furthermore, the discussions shown here are all about an even mode of a CPW which is the field configuration shown in Figure 1.5 b.

The center conductor width, w , is a very decisive parameter of a CPW structure. Usually, as shown above, to obtain a particular value of characteristic impedance w

and s change with each other so that the ratio $\frac{w}{s}$ remains constant. However, by alteration of w , even by having constant ratio of $\frac{w}{s}$ line characteristics change.

A significant or monotonic change of ϵ_{eff} by changing w is not observed. The effect is strong and inverse proportional for thin substrates ($h < 100 \mu\text{m}$) and weaker and direct proportional for thick substrates ($h > 100 \mu\text{m}$) [63] [64]. ϵ_{eff} is more dispersive for a wider w [65].

By keeping s unchanged the attenuation will increase by increasing w . This is because of the higher concentration of the fields in the slot between the center conductor and the ground planes which leads to a higher concentration of current on the edges of the conductors (center conductor and ground planes) [58]. Also, one should note that decreasing w further so that $\frac{w}{s} < 0.2$ will cause an upgoing in loss trend [63]. These are explicitly shown in Figure 2.6 [58]. In contrast, the attenuation will be lower by increasing w and saving the ratio $\frac{w}{s}$. The dispersion of attenuation is also lower if w is larger [58].

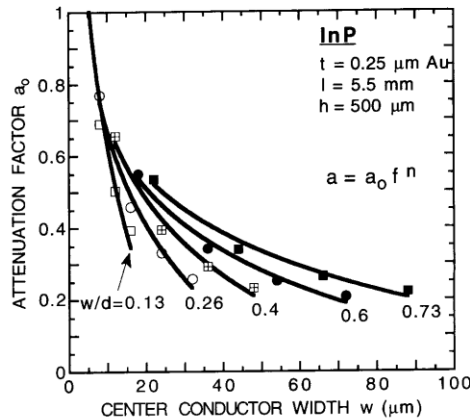


FIG. 2.6. Attenuation factor vs. w for different $\frac{w}{d = w + 2s}$. The substrate is made of InP and “l” stands for the length of the CPW [58].

Widening the center conductor width, and keeping all the other parameters constant, decreases the characteristic impedance [53] [64] [66].

In the case of having s as the only changing parameter, the studies show that by increasing s the effective permittivity decreases [65] [62]. This decrease is, however, dispersive (increasing by frequency). It is less than 1% for a ratio of $\frac{s}{h} = 0.3$ (h constant) and around 5% for $\frac{s}{h} = 0.9$ up to 40 GHz [62]. At higher frequencies, the concentration of the field is more in the substrate and thus ϵ_{eff} increases. Thus, to have a lower

sensitivity of ϵ_{eff} on frequency the lower s values are recommended. It is briefed in Figure 2.7 for the both modes of even and odd. The odd mode curves are dimmed since they are not in the context of our discussion.

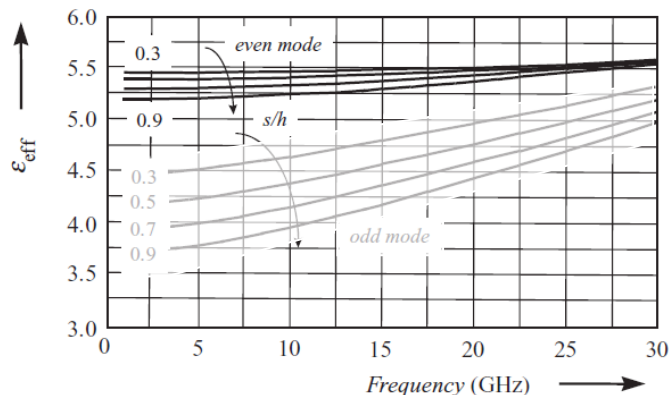


FIG. 2.7. ϵ_{eff} vs. frequency for a CPW and s as the parameter. $\frac{s}{h}$ values = 0.3, 0.5, 0.7, and 0.9. $\epsilon_r=10$, $h = 635 \mu m$ [62].

The attenuation of the line, on the other hand, increases by decreasing s [58]. This has two reasons whose first is that to keep a given characteristic impedance (while keeping the same constructing materials) the center conductor width must decrease either and this will increase loss. The second reason is because of the very high concentration of the fields in the slot which leads to a concentration of current on the edges of the conductors (center conductor and ground planes). Therefore, the lower the s , the higher the loss.

The variation of the characteristic impedance has a direct relationship with s . Intuitively, one can interpret the higher Z_0 for higher s (keeping w constant) so that the wider slot makes the way of the fields reaching from center conductor/ground planes to ground planes/center conductor longer. This is, however, concludable by following the expression (2.9) to (2.11) also.

A summary of the effects of the line parameters on the line characteristics is offered in Table 2.1 at the end of this chapter.

2.5. The Effect of Ground Planes Size

In practical implementations of coplanar lines for e.g. monolithic microwave integrated circuits (MMICs) applications the size of the ground planes must be limited or comparable with some other distances like w and s . Small size of ground planes lead to improper grounding like different electrical potentials between the ground planes. This may excite parasitic modes and odd modes. Parasitic modes are discussed shortly in 2.7.

Ground plane size may alone change the characteristic parameters of the line. Critically finite ground planes width leads to a slight increase of the line impedance in comparison with infinite ground planes. According to Ref. [67] the ratio $\frac{w_g}{w+2s}$ must not be less than 0.5 to keep the ground plane width effect away from the characteristic impedance of the line. This is independently approved by [64] to a very large extent for the both finite and infinite thickness of the substrate; Figure 2.8 (a) and (b). The ratio $\frac{b}{c}$ in Ref. [64] can be converted to (2.12) which is based on the parameters in this text.

$$\frac{b}{c} = \frac{1}{1 + 2\frac{w_g}{w+2s}} \quad (2.12)$$

Figure 2.8 shows that if $\frac{b}{c} < \sim 0.5$ the characteristic impedance lies on an almost straight line and does not change by changing c (w_g). Having $\frac{b}{c} = 0.5$ leads to $\frac{w_g}{w+2s} = 0.5$ which is already stated by Ref. [67] also.

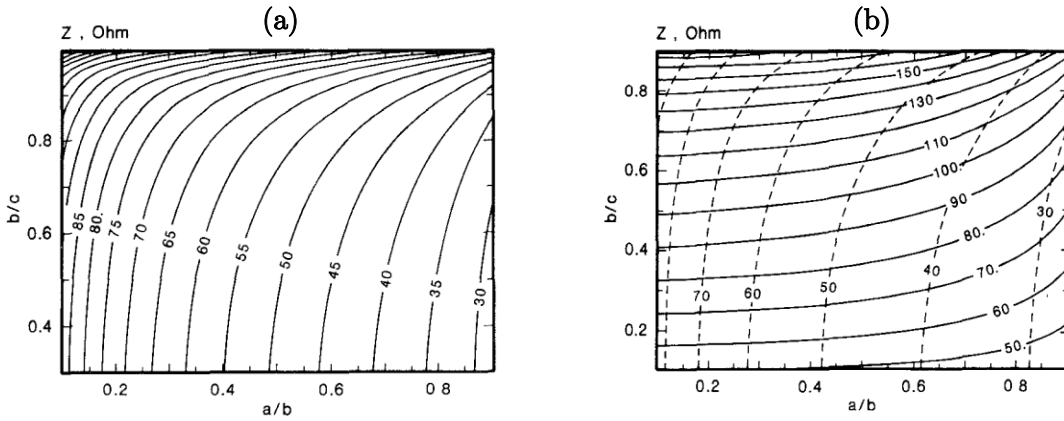


FIG. 2.8. Constant impedance curves for coplanar waveguides with finite ground planes for as a function of shape ratio $\frac{a}{b} = \frac{w}{w+2s}$ and the inverse of a ground plane width $\frac{b}{c}$ for (a) finite GaAs substrate thickness ($h = \frac{w}{2} + s$) ($\epsilon_r = 13$), (b) infinite substrate thickness (dashed lines) [64].

Characteristic impedance of a finite ground plane line is more dispersive compared to infinite ground plane ones [68].

Effective permittivity is reported to increase by decreasing the ground planes size [69] [70]. The increase is about 5% when the ground planes become 15 times narrower shown in Figure 2.9 [69]. In Ref. [62] the dependence of ϵ_{eff} on w_g is mentioned to be negligible.

Although it is shown that reducing the width of the ground planes leads to a significant reduction in radiation loss [71] at very high frequencies of above 100 GHz, the conductor loss will be lower with wider ground planes [62] at 1 GHz. On the other hand, there is

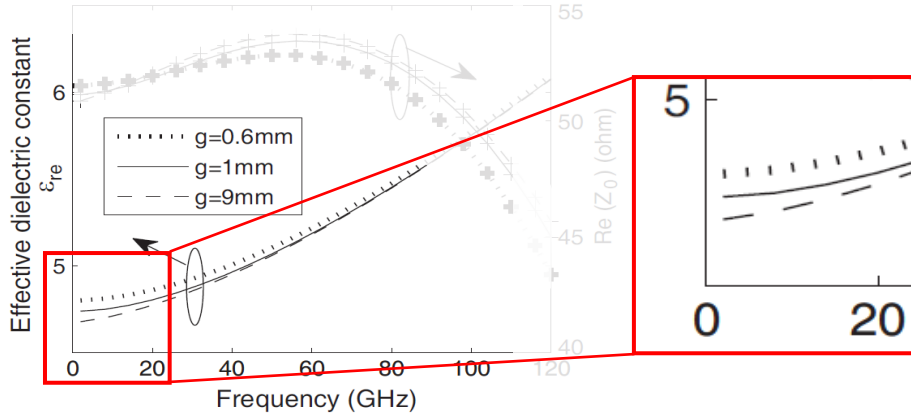


FIG. 2.9. The increase of ϵ_{eff} by decreased w_g [69]. The parts of the diagram which are not in the scope of the discussion are dimmed. The dispersion of ϵ_{eff} was discussed previously.

no strong presentation of total line attenuation dependence on the width of the ground planes from 1 to 120 GHz according to Figure 4 in Ref. [69].

2.6. The Effect of Metallization Thickness

Both effective permittivity and characteristic impedance decrease when the thickness of metallization increase [53] [72] [73] [74] [75] [76]. The metallization thickness t may have some significant effects in variation of the line parameters only if it is in the order of the other geometrical dimensions of the line. Figure 2.10 (a) and (b) show that $\frac{t}{s}$ is to be above 5% if the change in Z_0 is going to be 5% or more for a CPW with $\epsilon_r = 10.5$.

Formula (2.11) is in fact proposed for $t = 0$. When t is increased, the capacitance of the line increases and the inductance decreases which leads to a decrease in Z_0 . From [73]:

$$Z_0 = \sqrt{\frac{R + i\omega L}{G + i\omega C}} = \sqrt{\frac{L}{C}} = \frac{1}{v_0 \sqrt{CC_0}} \quad (2.13)$$

$$\epsilon_{eff} = \frac{C}{C_0} \quad (2.14)$$

where R , G , L , C are in turn resistance, conductance, inductance, capacitance of the line with dielectric substrate and C_0 is the capacitance of the line without dielectric substrate. v_0 is the wave speed in vacuum. Theoretically, the ohmic losses of a CPW are not effective on the (quasi-TEM) propagating mode of the signal. This means R and G can set to zero in (2.13) as in a lossless line. By increasing the thickness, C_0 and

C both grow, however, since C_0 increases more than C , ϵ_{eff} decreases [73]. Figure 2.11 is an example of the obtained results from the analysis of the effect of metallization thickness on Z_0 , ϵ_{eff} and attenuation of the line [74] [76].

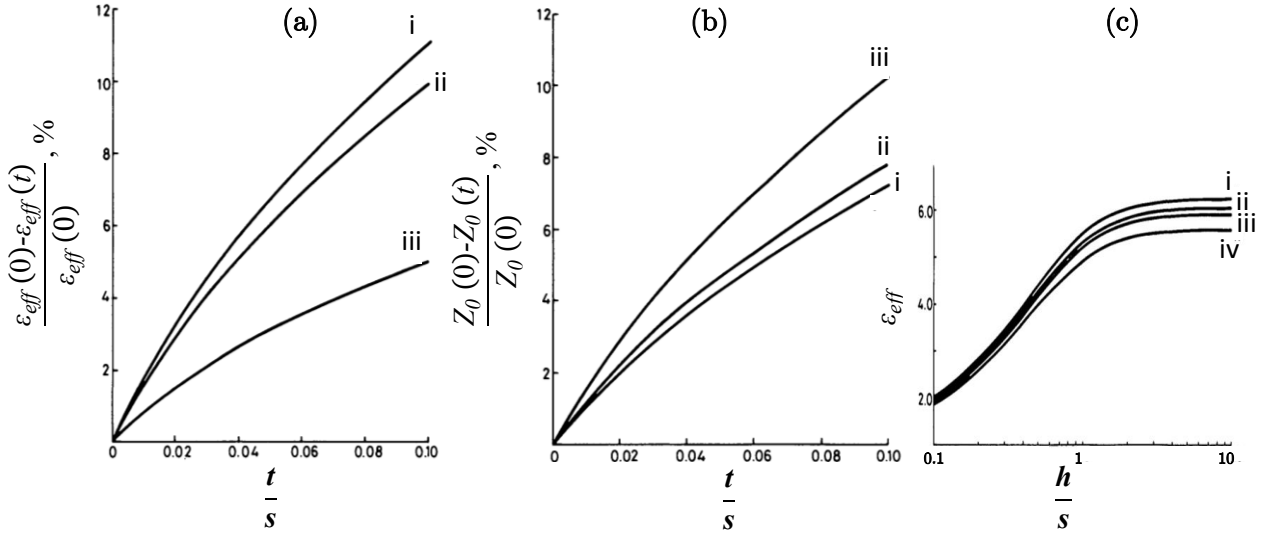


FIG. 2.10. Relative change of Z_0 (a), and ϵ_{eff} (b) against the variation of $\frac{t}{s}$ for CPWs with $\frac{w}{2s} = 0.25$, $\frac{s}{h} = 1$ (i) $\epsilon_r = 20$ (ii) $\epsilon_r = 10.5$ and (iii) $\epsilon_r = 2.6$. $\epsilon_{eff}(0)$ and $Z_0(0)$ belong to $t = 0$ which is an ideal case. (c) shows that the higher the ratio $\frac{s}{h}$, the higher the effect of thickness on ϵ_{eff} . (i), (ii), (iii) and (iv) correspond to $\frac{t}{s}$ ratios of 0, 0.02, 0.04 and 0.10 respectively [73].

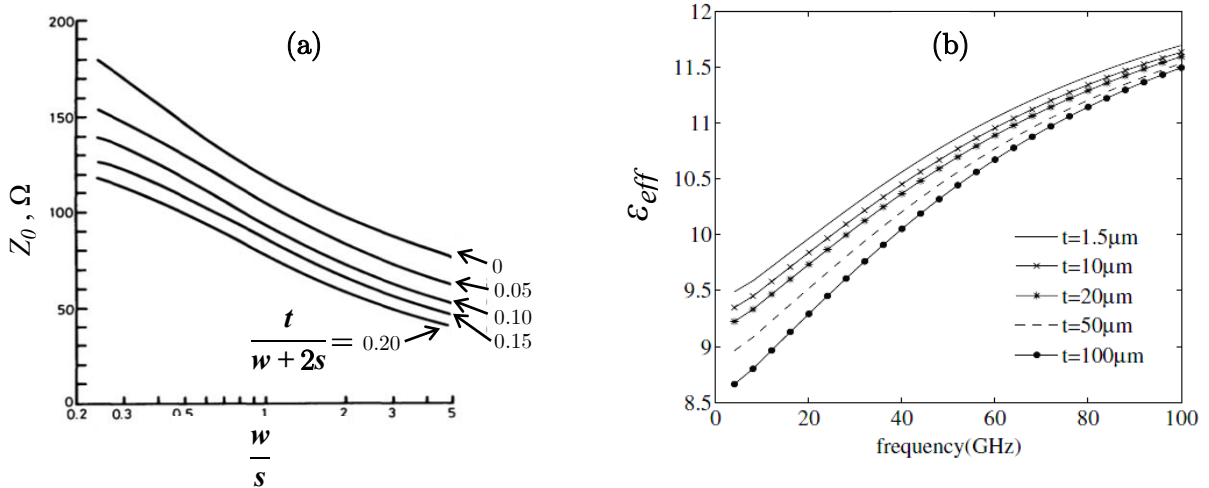


FIG. 2.11. (a) Z_0 against $\frac{w}{s}$ with t as the parameter. The impedance becomes smaller on increasing t at a constant $\frac{w}{s}$ [74], and, (b) ϵ_{eff} vs. frequency with t as the parameter. The increase of t leads to a decrease in ϵ_{eff} [76].

Thickness of the metal film also has a significant effect on the attenuation of the line. Conductor loss decreases by increased t [72] [76] [77]. As t increases, the attenuation

values decrease strongly until the thickness is almost 3 times of the skin depth, δ . Further increasing of t does usually not have a significant effect on the attenuation.

The skin depth is calculated by [72]:

$$\delta = \sqrt{\frac{\rho}{\pi f \mu_0 \mu_r}} \quad (2.15)$$

As $t > 3\delta$, the current doesn't exist in the inner regions at deeper than 3δ of the conductor, making the loss almost independent of the conductor thickness. Figure 2.12 from [76] [77] show the change of attenuation as a function of t and frequency. The other effect beside the thickness which is also related to the metallization is the surface roughness of the conductor which becomes more pronounced as frequency increases. At higher and higher frequencies δ and surface roughness of the metallization become comparable in depth. The current will then be concentrated through the uneven surface of the metal film and the increase of the attenuation become steeper by increasing the frequency.

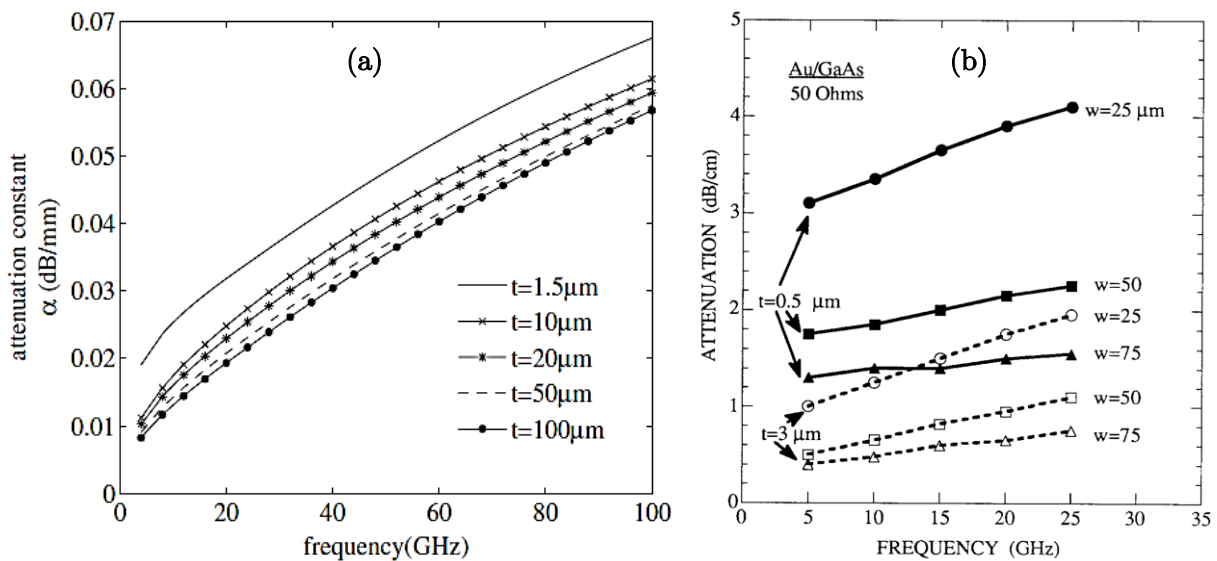


FIG. 2.12. The effect of metallization thickness on attenuation. Panel (a) from [76] and panel (b) from [77].

2.7. The Effect of Shielding; Box Effects

The practical implementations of CPWs in monolithic MMICs, typically makes it necessary to enclose the chip with a metallic shielding. This usually leads to an additional parasitic mode with a zero cutoff frequency whose fields distributions are similar to an even mode of CPWs. The schematic fields lines are shown in Figure 2.13 [62]. The spatial extension of the parasitic mode is most intense among the three

considered modes (even mode, odd mode and parasitic mode), and it propagates mostly in the air space above the conductors and below the substrate [62].

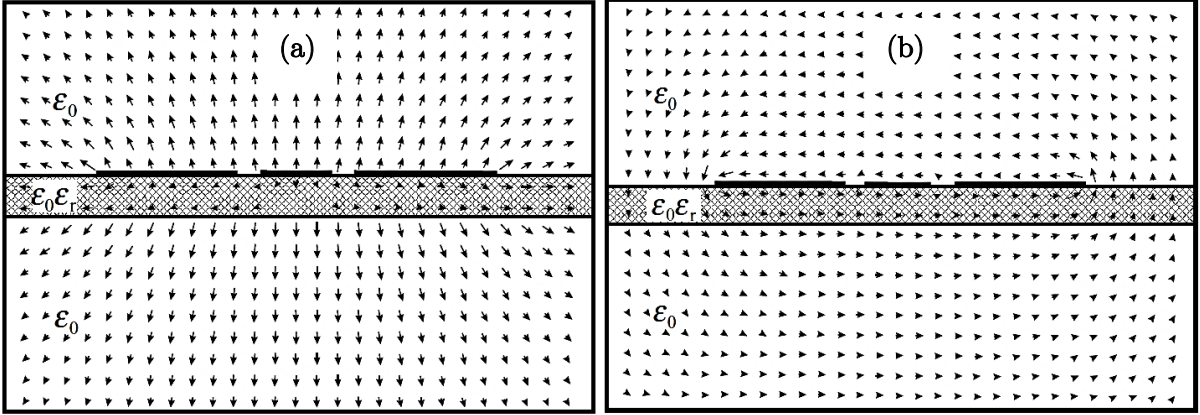


FIG. 2.13. The field distribution of the parasitic even mode on a coplanar waveguide with a single center strip. (a) The electric field, (b) the magnetic field [62].

The change of characteristic impedance by variation of the shielding dimensions (mainly h_1 and h_2 in Figure 2.4) is, according to the studies, sensible when it is comparable with the chip dimensions. For example, in [64] when all parameters are kept constant except h_1 , further increasing of h_1 when $\frac{h_1}{w/2+s} \geq 4$ do not have any notable effect on Z_0 and ϵ_{eff} as shown clearly in Figure 2.14 (a) and (b). A similar analysis is shown by [78] in which the substrate is stretched down to touch the lower shielding. According to this analysis, if the ratio $\frac{h}{w}$ is bigger than 8 (Figure 2.14 (c)), Z_0 is governed by $\frac{w}{w+2s}$ or in other words the ratio $\frac{h}{w}$ does not have a significant role in changing Z_0 . Figure 2.14 (d) also shows ϵ_{eff} curve is much more stable for the structures with $\frac{h}{w}$ of bigger than 8.

2.8. The Effect of Constituents' Materials and Substrate Thickness

Metallization and substrate are where the materials in the structure of a CPW can be changed. The more lossy the material in either of the metallization or substrate, the higher the loss of the line [72]. Metals are different in conductivity. Conductivity, beside its main role in the loss, changes the skin depth (formula (2.15)) which leads to an alteration in dispersion behavior. Using a metal with higher loss in the structure of a CPW has the similar effect of metallization thickness on ϵ_{eff} [76]. Figure 2.15 shows the effect of conductivity of the metal on ϵ_{eff} and attenuation of a CPW.

Z_0 and ϵ_{eff} are under the influence of the substrate thickness h quite significantly. That is, however, quite understandable since these parameters are determined by the amount

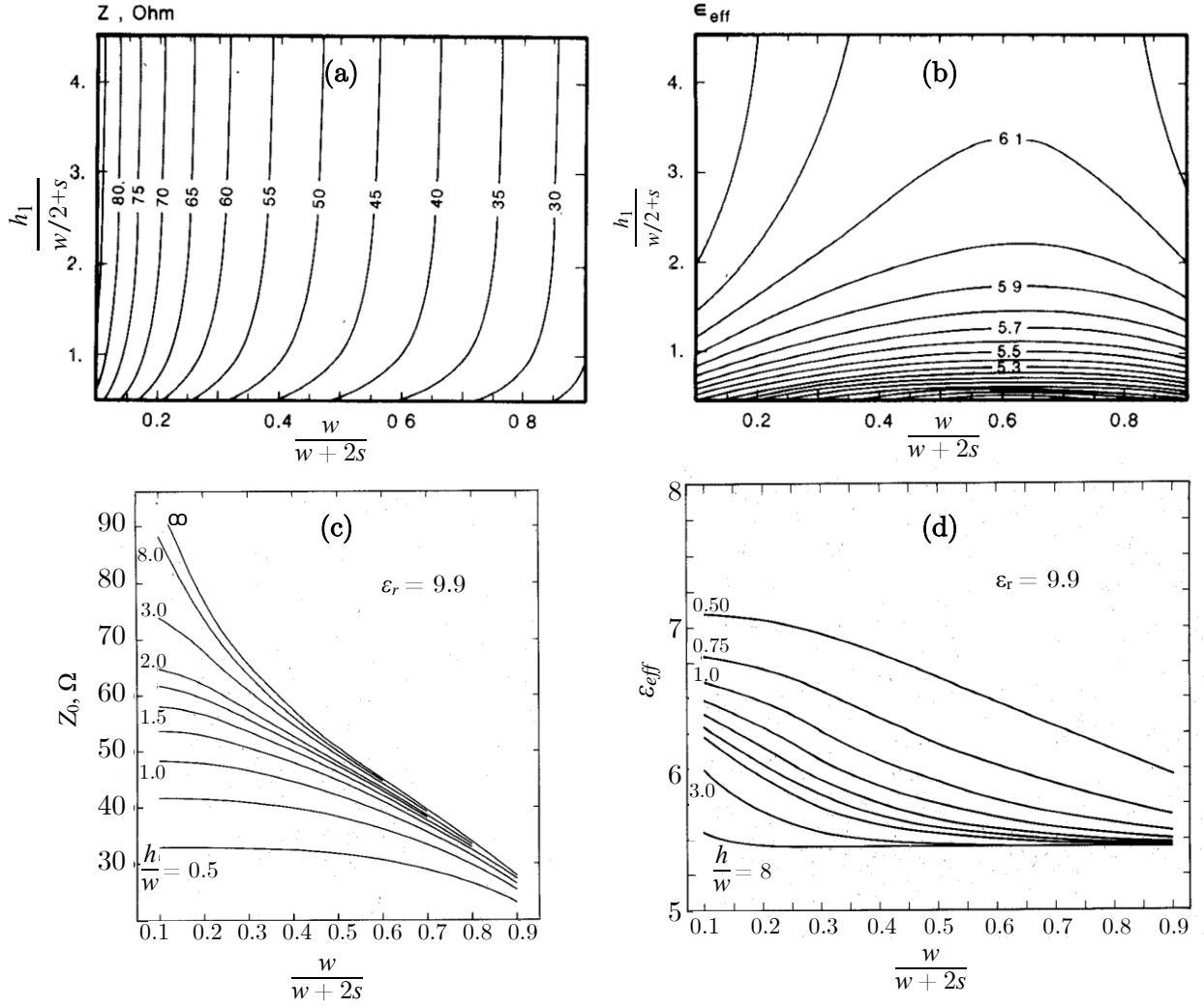


FIG. 2.14. Constant impedance curves (a) and constant ϵ_{eff} curves (b), for coplanar waveguides with upper shielding as a function of shape ratio $\frac{w}{w+2s}$ and the cover height $\frac{h_1}{w/2+s}$ for finite GaAs substrate thickness ($h = \frac{w}{2} + s$) ($\epsilon_r = 13$) [64]. (c) and (d) are the constant $\frac{h}{w}$ curves for coplanar waveguides with lower shielding as a function of Z_0 and ϵ_{eff} and shape ratio $\frac{w}{w+2s}$ [78]. All the information on the diagrams (c) and (d) including the numbers and axis labels are rewritten. Form (a) to (d) the parameters of the axis are reparametrized and rewritten to be compatible with the introduced parameters in this thesis.

and distribution of signal fields in air (superstrate) and dielectric (substrate). When the higher proportion of the signal is concentrated in the dielectric, the effective permittivity is expected to have a higher value.

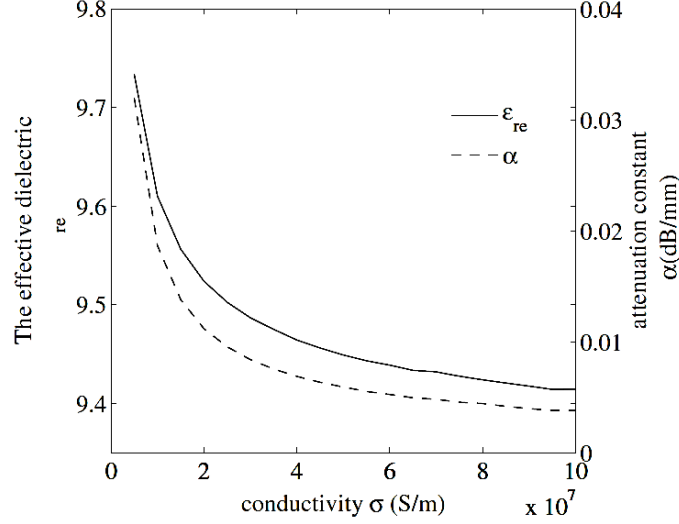


FIG. 2.15. The effective dielectric constants ϵ_{eff} and attenuation constant against the conductor conductivity σ at the frequency 1 GHz, $t = 3 \mu\text{m}$ [76].

In Ref. [64] and [73] the effect of h on Z_0 and ϵ_{eff} are presented as shown in Figure 2.16. From Ref. [64] one concludes that for the substrate thickness which make the ratio $\frac{h}{w/2+s}$ bigger than 4, the both of Z_0 and ϵ_{eff} do not change anymore by increasing h . This expresses in fact a minimum substrate thickness of $4(\frac{w}{2} + s)$ for a CPW. The minimum substrate criterion is stated by [73] as $h_{min} \approx 5.1s$. This is fairly compatible with $h_{min} \geq 4(\frac{w}{2} + s)$ concluded from [64].

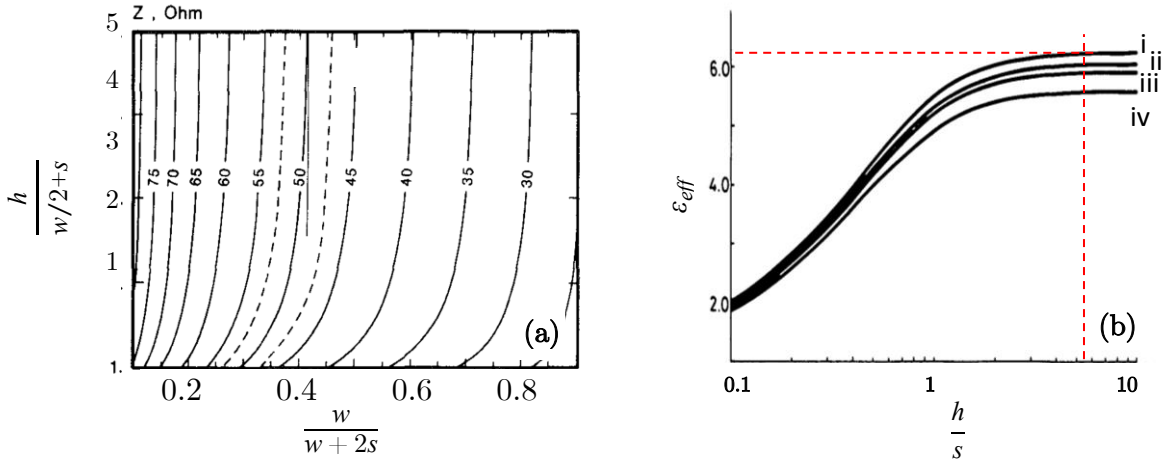


FIG. 2.16. Constant impedance curves (a) for coplanar waveguides as a function of shape ratio $\frac{w}{w+2s}$ and the cover height $\frac{h}{w/2+s}$ for GaAs substrate ($\epsilon_r = 13$) [64]. (b) shows the increase of ϵ_{eff} by increasing h . ϵ_{eff} stays almost constant when $\frac{h}{s}$ ratio is around 5.1. (i), (ii), (iii) and (iv) correspond to of $\frac{t}{s}$ ratios of 0, 0.02, 0.04 and 0.10 respectively [73]. All the information on the diagrams including the numbers and axis labels are rewritten. For both (a) and (b) the parameters of the axis are reparametrized and rewritten to be compatible with the introduced parameters in this thesis.

2.9. Coupling of the Lines

When two CPWs are placed in the adjacent of each other they can under particular circumstances couple to each other. The coupling between neighboring CPWs is sometimes unwanted and is the result of improper design. The distance between the lines must be therefore accurately considered to avoid unwanted couplings and parasitic modes. The reason of coupling is rooted in the leakage of power away from the waveguide in the form of a surface wave which can cause unwanted crosstalk between neighboring portions of the circuit [64] [79] [80] [81]. Line-to-line coupling or crosstalk of two CPWs does not have to essentially happen for two separate line, but rather through a single CPW which has e.g. a meander line structure.

The crosstalk, T , between two CPWs is obtained by the given expression by Ref. [80] as:

$$T = 10 \log \left| \frac{V_{12}}{V_1} \right|^2 = 10 \log \left(\frac{(2\pi f \Delta C l Z_0)^2}{1 + (2\pi f \Delta C l Z_0)^2} \right) \quad (2.16)$$

where V_1 is the amplitude of the signal with frequency f at the input of the first assumptive CPW which would generate a crosstalk voltage of V_{12} on the neighboring CPW. ΔC is the capacitance between the two CPWs whose lengths are l and have a separation of $2c$. Figure 2.17 shows an approximate evaluation of line-to-line coupling by Ref. [64] and [80]. In order to line-to-line coupling to be less than 40 dB, Ref. [64] states that the distance between the middle points of the center conductors of the two adjacent CPWs, designated by D , must follow the relationship $\frac{D}{w/2+s} \geq 7$ as shown in Figure 2.17 (a). This is confirmed to a high extent by [80] in which two neighbor coplanar lines are analyzed towards crosstalk avoiding. According to Ref. [80], the ratio $\frac{D}{w/2+s}$ must be equal and bigger than ~ 8.33 to keep the line-to-line coupling less than 40 dB. As one sees, quite close results to $\frac{D}{w/2+s} \geq 7$ of Ref. [64] are obtained although the structure dimensions in Ref. [80] are two orders of magnitude bigger than the ones in Ref. [64]; Figure 2.17 (b). Of course, it is also mentioned in [80] itself that the acquired data are extensible to structures with 100 times smaller dimensions and correspondingly 100 times higher frequencies.

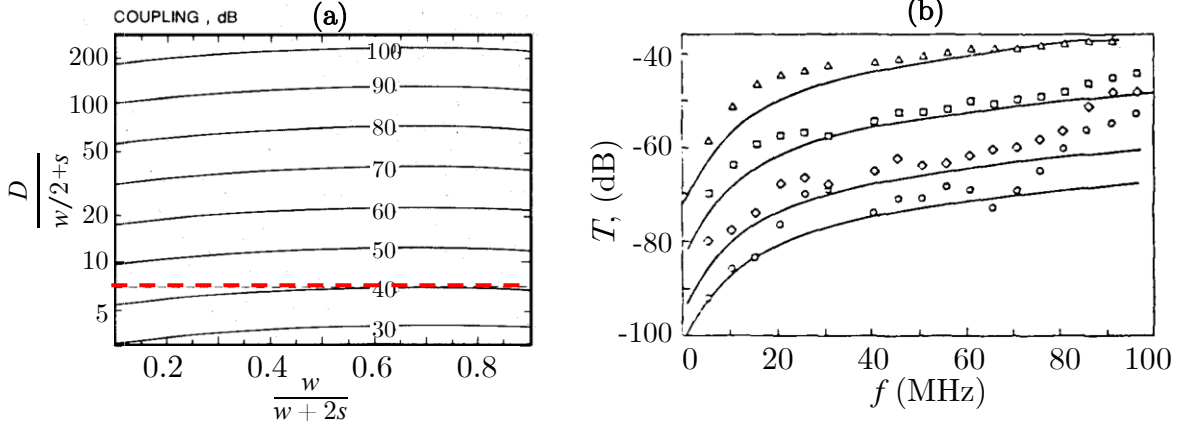


FIG. 2.17. (a) Constant coupling curves for parallel coplanar lines on infinitely thick GaAs substrate ($\epsilon_r = 13$) as a function of the shape ratio $\frac{w}{w+2s}$ and the normalized distance $\frac{D}{w/2+s}$ (logarithmic scale) [64]. (b) Crosstalk measured between two 59 cm CPWs ($w = 6 \text{ mm}$ and $s = 3 \text{ mm}$) vs. operating frequency from 5 MHz to 100 MHz. Here Δ , \square , \diamond and \circ are experimental data points for separation $D = 5 \text{ cm}$, 10 cm , 20 cm , and 30 cm , respectively. The corresponding theoretical predictions are shown as solid lines. If lateral dimensions are scaled down by a common factor of 100, the crosstalk will be the same for operating frequency 100 times as large (0.5 GHz to 10 GHz) [80]. All the information on the diagrams including the numbers and axis labels are rewritten. For (a) the parameters of the axis are reparametrized and rewritten to be compatible with the introduced parameters in this thesis.

2.10. Briefing Table

Table 2.1. A summary of the line parameters effects on the line characteristics. “Direct” and “Inverse” mean in turn the direct and inverse relationship between the line parameters and the line characteristics.

	Effective Permittivity, ϵ_{eff}	Loss and Attenuation Coefficient, α	Characteristic Impedance, Z_0
Center Conductor Width, w	Direct	Inverse (if $\frac{w}{s}$ is constant) Direct (if $\frac{w}{s}$ increasing)	Inverse
Slot, s	Inverse	Inverse	Direct
Ground Plane Width, W_g	Inverse	Inverse	Inverse
Metallization Thickness, t	Inverse	Inverse	Inverse
Shielding, h_I	Direct	Inverse	Direct
Substrate Thickness, h	Direct	Direct	Direct
Metallization Conductivity, σ	Inverse	Inverse	---

3. Studied Systems and Materials

Electron spin resonance is one of the most useful techniques to observe magnetic resonance of materials with unpaired electrons. In this work three different systems of materials are investigated including a simple paramagnetic system, 2,2-diphenyl-1-picrylhydrazyl abbreviated as DPPH, two Kondo lattice systems of heavy fermion (HF) compounds YbRh_2Si_2 and YbNi_4P_2 and one spin-liquid system $\kappa\text{-(BEDT-TTF)}_2\text{Cu}_2(\text{CN})_3$. Generally, all heavy fermion materials and spin liquids (and some other categories like high T_c superconductors) belong to strongly correlated Fermi systems.

ESR measurements on powdered DPPH were performed in order to prove and calibrate the ESR performance of the developed metallic resonators at liquid helium temperatures, otherwise, the spin dynamic properties of DPPH itself was not in the scope of this work. In contrast, interesting physics at low and ultra-low temperatures could be investigated by performing ESR measurements on HF and spin-liquid systems.

3.1. 2,2-diphenyl-1-picrylhydrazyl; DPPH

Having a stable chemical structure and a very narrow ESR line, the free radical DPPH in powder form is a widespread ESR calibration compound [82] [83]. It is one of the first and mostly used standard samples for estimation of the g -factors of spin species as well as for measuring the concentration of the unpaired spins of a system in ESR experiments [84] [85]. DPPH is a free radical whose g -factor is reported very often by many studies to be 2.0036 ± 0.0001 and has a single sharp Lorentzian ESR line [82] [83] [84] [85] [86] [87]. It has a stable paramagnetic state down to 400 mK. At lower temperatures the paramagnetic DPPH changes to an antiferromagnetic (AFM) [86] [88]. A schematic picture of one DPPH molecule is shown in Figure 3.1.

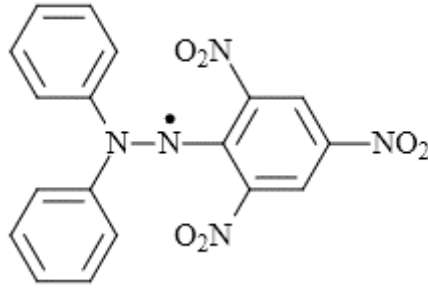


FIG. 3.1. The free radical of a DPPH molecule is shown as a black dot above the N atom [89].

The synthesis of DPPH is one of the crucial steps for the purity of the product. Remaining some amount of the solvents in the final product causes deviations in the corresponding magnitudes of the magnetic properties [87] [90] [91]. In addition, DPPH molecules in solvents show pair formation at temperatures lower than 150 K which influences the number of the free spins in the sample [90].

The standard ESR samples are usually in a black powder form, although, single crystalline DPPH are also available. The g -factor for a single crystalline DPPH is anisotropic [87]. The spectra of polycrystalline samples of the DPPH-doped in DPPH_2 exhibit a slight asymmetry which is explained by a small anisotropy of the g -tensor [92].

The ESR spectrum of DPPH is already recorded through using planar resonators. In Ref. [25] they used a stripline resonator for ESR applications and obtained the room temperature ESR spectrum of a DPPH sample dissolved in acetone. They observed the hyperfine spectrum of the sample. In Ref. [38] [39] a powder sample of DPPH was used and the ESR spectrum was recorded at 300 K by an “ Ω ” and an “R” shape planar resonator and the sensitivity of the system is discussed quantitatively in details. The authors of Ref. [38] and [39] measured the ESR spectrum of DPPH down to 10 K by their planar resonators [46].

In this work, the ESR spectra of a powder DPPH sample was obtained down to 1.6 K. The measurements were performed by placing the sample directly on the surface of the resonators. Moreover, some further measurements were performed with the focus of finding the influence of the signal intensity at different places along the center conductor of the resonator on the ESR signals. In these measurements which were performed in the frame work of two “Blockpraktikum”s, the used sample was DPPH powder which was placed on a moving holder above the resonator surface.

In [93] some sorts of ESR measurements were performed on DPPH down to mK temperatures by using dilution refrigerators and superconducting coplanar resonators. The g -factor and the linewidth change were clearly observed at around 400 mK.

3.2. Heavy Fermion Metals

Strongly correlated systems are a classification of solids which, in contrast to weakly correlated materials, cannot be described by some of the already promoted analytical methods like e.g. band theory of solids. The very first reason for this, is the strong interactions of their (elementary) particles, like electrons, with each other so that they cannot be described as the non-interacting entities. In particular cases, even the constructed fields to describe strongly correlated materials like Landau theory of Fermi liquid is insufficient to explain some other strongly correlated systems like e.g. non-Fermi-liquid properties of heavy fermion compounds (HFs). At the following a brief description of HFs and some other related concepts are offered.

The existing theories for weakly correlated materials provide credible description and analysis for the systems in which the kinetic energy of the delocalized electrons is much higher than their Coulomb interaction energy [94]. To study the materials which cannot be classified in weakly correlated materials, some new analysis and fields were founded and developed among them “quasiparticles” could most effectively open the ways to theoretically study and investigate the correlated materials.

The idea of effective mass of a particle was born by introducing the quasiparticle concept which was a new method and a new way of analysis in understanding of many-body systems and (strongly) correlated materials. Landau was of the first people who worked on the idea of quasiparticles and showed its efficacy [95]. The quasiparticles are intuitive substituting entities for particles like electrons in a material if the correlation among them is nonnegligible. The quasiparticles interact with each other via an effective interaction V_{eff} [94]. Accordingly, in the correlated system which is now defined by quasielectrons (quasiparticles of electrons) interact weakly and have still the same charge and spin of the normal electrons, however, the collective behavior of the matter like electronic specific heat, $C_{elec.}$, is defined by the mass of these quasiparticles which is defined as a modified mass of the normal electrons; effective mass M^* .

$$C_{elec.} \propto M^* T \quad (3.1)$$

The systems of fermionic quasiparticles are called Fermi-liquid (FL). In the quasiparticle based analysis of the systems the effective interaction V_{eff} has a tuning role which causes phase transitions at particular values [96]. In other words, an external perturbation which alternate V_{eff} can cause a phase transition in a system. V_{eff} was at that time the parameter by which one could predict all possible phase transitions. However, observing a deviation of $C_{elec.}$ of ^3He at temperatures around 100 mK from the linear expression of (3.1) [97], appearing superfluidity at 2.6 mK [98] [99] and the growth of spin susceptibility at low temperatures [100] were not explainable by the developed

calculations and analysis based on V_{eff} . The implication of these observation was the dependence of the effective mass on temperature which is quite in a contradiction to the theory of Fermi-liquid. This means the weakly correlated quasiparticle theory (Fermi-Liquid Theory) was not enough equipped to explain the new observed exotic phenomena.

A big number of the unpredictable phenomena by cooling the materials exist in strongly correlated materials. Of them, HFs have received a remarkable amount of attention for their very reach phase diagrams at low and ultra-low temperatures. HFs are intermetallic compounds containing metals with open $4f$ and $5f$ orbitals. The electrons in these orbitals have a very narrow band and thus experience strong Coulomb repulsions. This causes the interaction of their spins, charge, and generally all of their internal degrees of freedom, leading to exotic behaviors when the system temperature is so down that the total energy of the system is low compared to the electrons energies. These interactions are then very sensitive to small variations of an external perturbation like temperature, pressure or magnetic field [94].

In HFs, mobile electrons at low temperatures behave as if their masses were hundred times the mass of an electron in a silicon or a simple metal. This is due to the strong electron-electron correlations. HF systems exhibit a great variety of interesting phenomena like anomalies in electric and thermal conductivity, quantum phase transition between magnetically ordered state and superconductivity, emergence and dissociation of local magnetic moment, etc. These are not explainable by Landau Fermi-liquid (LFL) theory. This inability is sometimes so significant that HFs have often, in their phase diagram, very vast regions under the name of non-Fermi-liquid (NFL) phase. The exponents of the power-law behavior of the physical quantities in an NFL state of a strongly correlated Fermi system is quite different than FLs. This will be shown later in this chapter.

It is generally accepted that the fundamental physics that gives rise to the high- T_c superconductivity and non-Fermi-liquid behavior with a recovery of the Landau Fermi-liquid behavior (under the application of magnetic fields observed in HF metals and high- T_c compounds (cuprate superconductors)) is controlled by quantum phase transitions. This has made quantum phase transitions currently a subject of intensive investigations. Such a phase transition at $T = 0$ K (in contrast to the classical phase transitions in which thermal fluctuations play the main role) is driven by an external parameter like a magnetic field, pressure, doping etc. and is called a quantum phase transition (QPT). The point at which the phase transition happens is called a quantum critical point (QCP). A typical QCP is shown in Figure 3.2. The phase diagram represented in this figure belongs to YbRh_2Si_2 which is one of the most studied HFs.

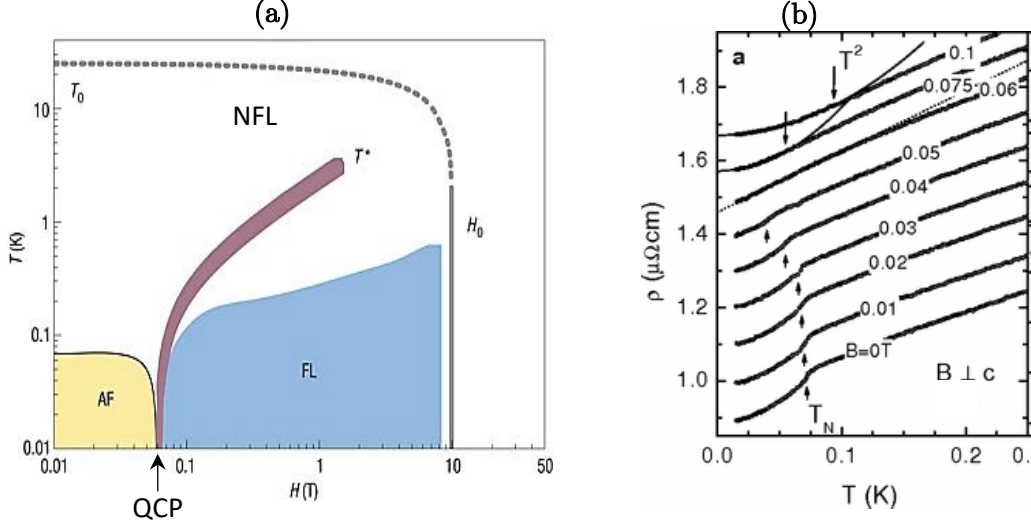


FIG 3.2. (a) The temperature versus magnetic field phase diagram of YbRh_2Si_2 on logarithmic scale [1]. Magnetic field applied perpendicular to the c -axis (see FIG. 3.5 (a)). AF stands for antiferromagnetic, LFL is the Landau Fermi-liquid and NFL is the abbreviation for non-Fermi-liquid. The gray dashed line represents the region of HF behavior confined to the range of $T < T_0$ and $H < H_0$. (b) Low temperature electrical resistivity of YbRh_2Si_2 from $H = 0$ to 0.1 T (perpendicular to the c -axis) [101]. The T^2 behavior in LFL regime is pointed out in the last two curves of 0.075 and 0.1 T. T_N stands for Neel temperature of AFM transition. The linear T behavior in NFL is significant, particularly in the case of $H = 0.06$ T which is almost ending to QCP at $T \rightarrow 0$.

To investigate quantum critical phenomenon, the HF systems are high potential candidates since they can be tuned continuously from a magnetically ordered phase to a paramagnetic metallic state by a control parameter. In other words, the strength of the $4f/5f$ and conduction electron hybridization, can be tuned by introducing of magnetic field, external pressure or chemical substitution.

One explanation for a QPT and NFL behavior is vanishing the quasiparticles and appearing a correlation length in the material which is infinitely large. Such a QPT is called ordinary or conventional QPT (CQPT). In this case, the physics is determined by thermal (classical) and quantum fluctuations of the critical state, while quasiparticle excitations are destroyed by these fluctuations. This has, however, some difficulties in explaining the formation of NFL phase at comparably high temperatures in some materials like YbRh_2Si_2 even at 10 K (crossover ≈ 25 K, Figure 3.2 (a)). At such a high temperature, the very large correlation length is not able to form since the thermal fluctuations are too high to let such a large correlation happen. In addition, the formation of Landau FL by application of magnetic field and observation of universal behavior like Kadowski-Woods ratio and Wiedemann-Franz law cannot be explained

by destruction of quasiparticles. The generic Kadowski-Woods ratio observation is shown in Figure 3.3.

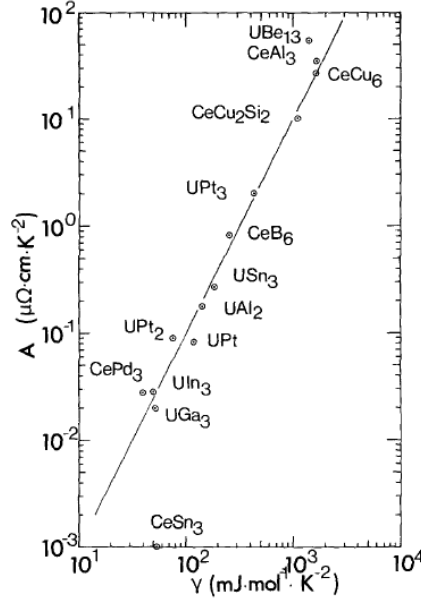


FIG. 3.3. The heavy fermion materials fit the universal Kadowski-Woods ratio of $\frac{A}{\gamma^2} = 1 \times 10^{-5} \mu\Omega\text{cm}/\left(\frac{\text{mJ}}{\text{mol K}}\right)^2$ where A is the coefficient of the quadratic term in resistivity-temperature relationship of $\rho(T) = AT^2 + \dots$ (T^2 is the electron-electron interaction term in addition to which, residual resistivity phononic and Kondo terms are to be considered). γ (Sommerfeld coefficient) is the coefficient of the linear term of the specific heat-temperature relationship of $C(T) = \gamma T + \dots$ (T is the electronic specific heat term and the phononic term is to be added to it). At sufficiently low temperatures the phononic terms of $\rho(T)$ and $C(T)$ are ignorable [102].

In contrast to CQPT (the absence of quasiparticles), the physics of a Fermi system near fermion condensation quantum phase transition (FCQPT) is controlled by the system of quasiparticles analogous to the Landau quasiparticles [103]. These two theoretical discussions describe the heavy electron QCP by: 1) a spin density wave scenario (CQPT) [1] [104] [105] and, 2) a localized moment scenario or Kondo breakdown (FCQPT) [1] [106]. In the former, known as spin-density-wave (SDW) QCP, the spin polarization of the Fermi surface is the origin of magnetism. In the latter, known as Kondo breakdown QCP, heavy electrons disintegrate at the QCP and form very well-defined quasiparticles.

The sharpest difference between the quasiparticles in an FCQPT NFL state and an LFL state quasiparticles is the dependence of M^* (of NFL quasiparticles) to external parameters like magnetic field, doping, pressure, frequency etc. [103]. In an LFL, M^* is determined only by particle density and their interaction. In fact, what makes HF's alluring to study is, their depart from the finite and independent M^* of a FL to, as for

in an NFL phase, $M^* \rightarrow \infty$ at QCP at $T = 0$ K. This point is clearly illustrated in Figure 3.4 in the case of the HF metal YbRh_2Si_2 . To understand the procedure of extracting the curves in Figure 3.4 (b), the direct explanation of the authors in reference [94] is quoted at the following:

“To show that the behavior of C/T reported in Fig. 3.4 (a) [in this thesis] is of generic character, we recollect that in the QCP vicinity it is helpful to use “internal” scales to measure the effective mass $M^ \propto C/T$ and temperature T . As it is seen from Fig. [3.4 (a) in this thesis], a maximum structure in $C/T \propto M_L^*$ at temperature T_M appears under the application of magnetic field B and T_M shifts to higher T as B is increased. The value of the Sommerfeld coefficient $C/T = \gamma_0$ is saturated towards lower temperatures decreasing at elevated magnetic field. To obtain the normalized effective mass M_N^* , we use M_M^* (maximal value of the effective mass) and T_M as above “internal” scales: The maximum value of C/T has been used to normalize C/T , and T was normalized by T_M . In Fig. 3.4 (b) [in this thesis] the obtained $M_N^* = M^*/M_M^*$ as a function of normalized temperature $T_N = T/T_M$ is shown by symbols. Note that we have excluded the experimental data for magnetic field $B = 0.06$ T. In that case, as will be shown, $T_M \rightarrow 0$ and the corresponding T_M and M_M^* are unavailable.”*

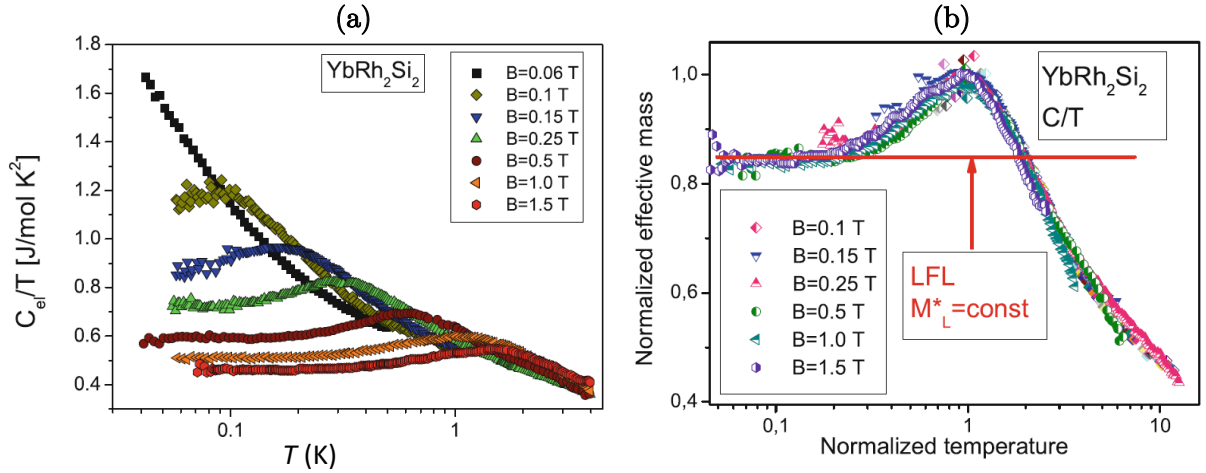


FIG. 3.4. (a) The electronic specific heat coefficient of YbRh_2Si_2 , $\gamma = C_{el}/T$, versus temperature T as a function of magnetic field B [107] (legend). Note: This picture is taken from reference [94]. (b) The normalized effective mass M_N^* (see the text) versus normalized temperature T_N . M_N^* is extracted from the data of (a) (specific heat $\frac{C}{T}$ on YbRh_2Si_2). The red solid line shows the constant effective mass M_L^* inherent in normal Landau Fermi [94].

One of the unexpected behavior of some HFs in the NFL regime is an increase in resistivity by lowering the temperature. This was later explained in the framework of a Kondo lattice. The experimental observation which motivated the theorist to study and define the Kondo effect was a minimum in the resistivity vs temperature curves of

(impure) gold at around 8 K [108] although for a pure simple metal like gold a monotonic decrease (down to residual resistivity regime [109]) in resistivity is expected on cooling. Later experiments also proved the minimum feature and showed that the magnetic impurities are responsible for the emergence of this minimum. This was theoretically studied and explained by Jun Kondo [110]. He expressed the minimum as a logarithmic contribution of temperature in the resistivity-temperature expression of the resistivity:

$$\rho(T) = \rho_0 + AT^2 + BT^5 + JC \log(T) \quad (3.2)$$

where ρ_0 is the residual resistivity, A and B are the coefficients of the electronic and phononic terms. The logarithmic term is the Kondo contribution with the coefficient of C . J is negative when the Kondo term is dominant [110]. Kondo explained the effect as an additional scattering mechanism of conduction electrons caused by the spin of the magnetic impurities. The idea is based on the formation of a new state (Kondo resonance) at the Fermi level which makes the tunneling of the magnetic impurity possible for a short time [111]. Then, an electron from the conduction band can fall into the temporarily empty state of the impurity with an opposite spin of the impurity and form an antiferromagnetically singlet [112]. According to Kondo's model the resistivity will be strictly increasing even at lower temperatures, however, it is not the case in the experimental data. This was explained by the theorists in a theory framework of "Renormalization Group" which prove that the magnetic impurity spin is totally screened by conduction electrons and the scattering ceases [113]. If in a system there is a systematic distribution of the magnetic atoms, which contain a lattice of unpaired f electrons as it is in HFs, we face a Kondo lattice and the scattering of the conduction electrons become coherent.

The formation of Kondo singlets, intuitively implies that the unpaired but hybridized f electron(s) (with conduction electrons) must not be able to show any ESR signal since the screening conduction electrons occupy the otherwise empty states on the magnetic atom. Also, the typical spin fluctuation rate of the Kondo ions, causes a large ESR linewidth beyond of its detection. But if an HF system like YbRh_2Si_2 is showing a very significant and relatively narrow ESR signal [2], a very interesting physics is expected which is to get investigated and understood. In addition, ESR can be utilized to probe the evolution of the Kondo state [114].

3.2.1. YbRh₂Si₂

YbRh₂Si₂ with the tetragonal crystalline lattice is one of the few clean and stoichiometric synthesized heavy fermion compounds which has been intensively studied since the QCP in this compound is easily accessible by applying magnetic field and at ambient pressure as shown in Figure 3.2. Several phase transitions with unique properties can be tuned by magnetic field and temperature. The QCP is located between an AFM ordered phase region and a LFL region. “Melting” this AFM phase by applying magnetic field is explained to be likely due to the increasing $4f$ -conduction electrons hybridization; in other words, it is a Kondo breakdown phase transition which is already introduced as the unconventional quantum criticality or FCQPT [115]. Dominancy of the so-called RKKY interaction (between the local f states via the sea of conduction electrons) over Kondo interaction, favors the magnetically ordered ground state. YbRh₂Si₂ is the intermetallic compound where the delicate balance between Kondo and RKKY interactions are explored. As Figure 3.2 shows, the Neel temperature of the AFM phase is 70 mK and a very vast area of the phase diagram contains a NFL state up to 25 K (10 K) at 0 T (10 T) [1] [101] [116]. The Yb³⁺ moments, with $J = \frac{7}{2}$ multiple state which is split into four Kramer’s doublets under the influence of crystalline electric fields [117] [118], form an easy-plane square lattice perpendicular to the crystallographic c -direction (Figure 3.5 (a)). This means a small amount of 60 mT magnetic field applied parallel to the ab -plane (perpendicular to c) suppresses the AFM phase at QCP (Figure 3.2 (a)). Applying magnetic field parallel to c -direction, the AFM state resist up to 660 mT [119].

The borders between the adjacent phases in Figure 3.5 (b) are not very sharp and well defined as were schematically shown in Figure 3.2.

As pointed in the inset of Figure 3.5 (c) the Kadowski-Woods ratio for YbRh₂Si₂ equals roughly the reported values of other HF systems (cf. Figure 3.3 or reference [102]). This is in striking variance to the SDW scenario [101]. Actually, the breakdown of the Kondo singlets happens below a critical Hall field ($B_H(T)$) and not only at QCP [120]. The line (or more precise to say, the range) T^* in the $B - T$ phase diagram is one of the Lifshitz transition region where the topology of the Fermi surface changes from a big (high fields) to a small Fermi surface (low fields) [118]. This has been investigated by Hall measurements also [120] [121].

Breaking down of a Kondo singlet can be the result of applying very high magnetic fields to a HF system too. In this case, the magnetic field must be so high that its effect equals increasing the temperature beyond the formation of Kondo lattice.

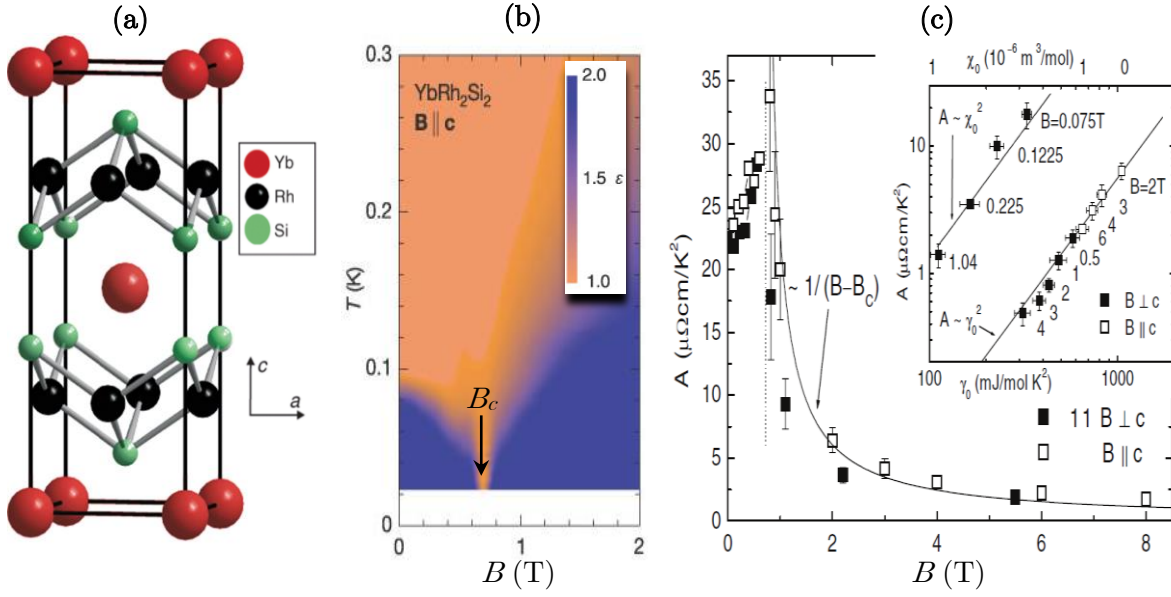


FIG. 3.5. (a) The unit cell of YbRh_2Si_2 [122]. (b) The temperature – field phase diagram of YbRh_2Si_2 which represent the evolution of ϵ defined as $\Delta\rho(T)=[\rho(T)-\rho_0]\propto T^\epsilon$ [119]. The NFL behavior, $\epsilon=1$ (orange), appears at the lowest temperatures right at the QCP where $B=B_c\approx 660$ mT (almost 11 times bigger than easy plane $B_c\approx 60$ mT; cf. Figure 3.2 (a)), and in a largely extended area at higher temperatures [119]. (c) Coefficient $A=\frac{\Delta\rho}{T^2}$ (3.2) vs field B . Data for B perpendicular to c -direction (in-plane) have been multiplied by 11. Dashed line marks B_{c0} , and solid line represents $(B-B_c)^{-1}$. Inset shows double-log plot of A vs χ_0 and A vs γ_0 for different magnetic fields. Solid lines represent $A/\gamma_0^2=5.8\times 10^{-6}\mu\Omega\text{cm}(\text{Kmol}/\text{mJ})^2$ and $A/\chi_0^2=1.25\times 10^{12}\mu\Omega\text{cmK}^{-2}/(\text{m}^3/\text{mol})^2$ [101].

YbRh_2Si_2 has a Kondo temperature of around 80 K [123] as the “higher” Kondo temperature and 25 K as the “coherent” Kondo Temperature below which Kondo-lattice coherence sets in and hybridized HF bands start to form [117] [118]. A high magnetic field of around 10 T along the easy plane of magnetization suppress forming any HF state even at 0 K.

In Ref. [118], the influences of applying a magnetic field to a HF system are categorized to:

- 1) Similar to increasing the temperature. In this case, the single-ion Kondo effect is weakened and even totally suppressed.
- 2) Zeeman splitting(s) which cause Lifshitz transitions. In this case, the Fermi surface topology may change because a band may get spin-split beyond the Fermi energy.
- 3) Metamagnetic transition. Many heavy fermion compounds face to such a transition at a characteristic magnetic field at the easy direction of magnetization.

There is, however, one more effect which is the main subject of this thesis and that is the probable Zeeman splitting of the existing magnetic moments in the structural lattice of HF system which makes electron spin resonance (already introduced, ESR) possible. However, such transitions are not expected to be observed since, as already discussed, the magnetic moments are believed to be screened via the Kondo interaction.

In case of any ESR possibility, the typical spin-fluctuation rate of the Kondo ions causes a large ESR linewidth beyond detection (relationships (1.11) to (1.14)). This was, however, surprisingly violated by appearing very sharp and significant ESR signal [2] at temperatures well below the coherent Kondo temperature, T_K , of YbRh_2Si_2 (≈ 25 K) down to 1.5 K at the X- and Q-band range of microwave frequency. Regarding high Kondo temperature of this compound, the ESR linewidth should be $\frac{k_B T_K}{\mu_B} \approx 37$ T which, however, was found to be in the range of 10 to 150 mT and the corresponding g -factor of ≈ 3.47 to ≈ 3.60 as shown in Figure 3.6.

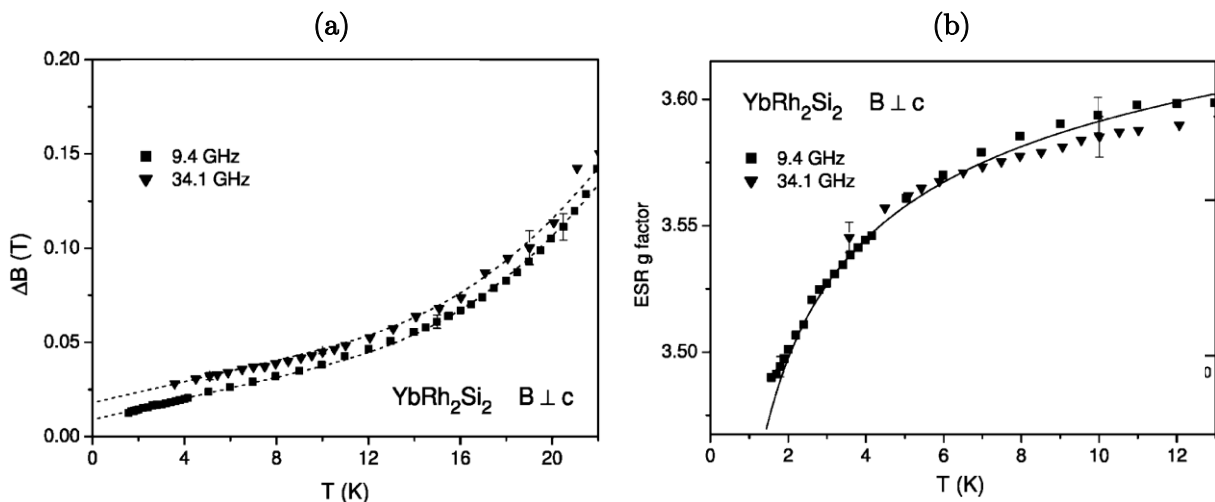


FIG. 3.6. (a) The ESR linewidth and (b) the g -factor for YbRh_2Si_2 reported in [2].

The observation of the ESR signal was interpreted as to be due to the quantum phase transition which leads to the suppression of the Kondo effect near the QCP. In other words, these data were explained as an experimental proof which reinforces the idea of the unconventional QCP in YbRh_2Si_2 as stated by the authors of the paper also:

“In YbRh_2Si_2 the electron spin resonance (ESR) reported in this Letter proves the existence of localized moments down to the lowest accessible temperature of 1.5 K, i.e., substantially below the Kondo temperature $T_K \approx 25$ K, and therefore seems to favor the localized moment scenario in that system.”

Since then, many other experiments have shown the same results with partly different conditions like temperature or frequency range [44] [114] [124] [125]. The obtained ESR lineshape was Dysonian and further experiments on YbRh_2Si_2 like angular dependence

of the g -factor [126] ($g_{\perp} = 3.56$, $g_{\parallel} = 0.17$ at $T = 5$ K when the sample is rotated out-of-plane). These two are indeed in accordance with the ESR of Yb^{3+} ions since the tetragonal symmetry of the electric crystal field. These attempts are not restricted only to YbRh_2Si_2 but other HF/Kondo lattice systems also [125] [127] [128] [129] [130] [131] [132] [133]. The ESR is then not exclusively related to the Yb ions since a Ce compound also have the ESR capability.

It should however be mentioned that, the Dysonian ESR line shape could be because of the heavy states of conduction electrons [134] [135] as well as due to the resonating localized spins [136] [137] [138], and therefore, the line shape alone cannot be a proof that the signal belongs to the f -electrons in the case of a heavy fermion. In a similar way, the g value(s) and its anisotropy do not reject the collective response theory. It could be so interpreted that the behavior of the heavy fermions, which arise from the hybridization of the f -electrons and the conduction states, are dominated by the f -electrons close to the Fermi level and, so, the g -tensor is mainly defined by the crystalline field scheme of the f -states [139].

Although, the obtained ESR of YbRh_2Si_2 was introduced (or speculated) as a proof for the unconventional QCP, the observation of ESR signal at even down to ≈ 0.5 K [140] and up to very high magnetic fields of 8 T (360 GHz) [114] motivated the experimentalist and theoreticians to study the phenomenon more in details and deeper. These studies showed that the sharp observed ESR lines can happen not solely by the local magnetic moments, but it could be a collective response stemming from the ferromagnetic (FM) fluctuations of f -spins.

Theoretical [141] [139] [142] and to some extent experimental works [114] [143] exist which have explored this and have concluded that the observability of ESR signal in a heavy fermion Kondo lattice in the NFL state is due to the formation of a collective spin mode of quasi-localized f -electrons and wide-band conduction electrons in conjunction with FM fluctuations [141] [139]. The importance of the FM fluctuations, which are resulted by RKKY interaction, is to facilitate the translational diffusion of quasilocalized f -electrons from one site to the next by providing the similar local fields for the spin. This is feasible if the RKKY interactions are FM. The existence of FM fluctuations is the common property of the compounds which show a narrow ESR line [144]. This proposed mechanism for ESR signal in a Kondo lattice ($T < T_K$) is called motional narrowing [142]. The narrowing of the ESR line from tens of Tesla to tens of milli-Tesla is incorporated with the ratio of $\frac{m}{m^*}$; the ratio of electron normal mass to the heavy electron mass.

There could still be one more proposition for this observed signal and that is the conduction electron ESR. This, however, seems unlikely since the spin-orbit coupling severely shortens the electron spin lifetime [114] [145].

The experimental works could yield more complementary data and shed light on this discussion whether the ESR of the Kondo lattices are local or collective. One helpful experiment is partially substituting the Kondo ions (rare earth ions e.g. Yb^{3+}) by the nonmagnetic elements with the similar properties like for instance La or Lu [146]. From the local theory one expects the resonance do not significantly change with (a slight) change in concentration since the dilution increases the average distance among the magnetic ions. However, broadening the linewidth because of the inhomogeneous alloying makes such experiments not very applicable. This is attributed to the break of the coherence of heavy fermion state and enhancing the spin lattice relaxation [139].

Another useful experiment could be testing the Kondo lattices which have very significant and proven (long range) FM correlations. This is in fact the motivation of exploring YbNi_4P_2 which is a ferromagnetic HF metal. This will be explained more in explaining this material.

In this thesis, the ESR measurements on YbRh_2Si_2 were performed at temperatures of between 40 mK to 800 mK and some measurements at 1.7 K to 2 K.

In an ESR experiment the electric field of the radio wave signal is also touching the sample and in case of any loss of the electric field by the under-study sample, the signal may be affected. This point should be in attention on analyzing the relevant data. Now if the transport properties of the sample are altering under the application of the magnetic field or in other words, if the sample possess any magnetoresistivity properties, it is to pay attention to it and not neglect it.

The magnetoresistivity (MR) properties of YbRh_2Si_2 is, to some extent, comprehensively discussed in reference [118]. Figure 3.7 shows the magnetoresistivity analysis of YbRh_2Si_2 up to 15 T. The MR is defined as $\text{MR} = \frac{\rho_{xx}(B) - \rho_{xx}(B=0)}{\rho_{xx}(B=0)}$. ρ_{xx} is the resistivity of the sample. Both the current (j) and magnetic field (B) are applied in easy plane (perpendicular to c -direction) and the resistivity is measured in the same direction of the current. The Hall measurements are also reported in the same reference.

The positive MR at lowest temperatures is attributed to the coherent state. The step-like transition at lowest temperatures in Figure 3.7 (b) (shown by the upward arrow) is reported to be due to the Fermi surface reconstruction related to the unconventional QCP. With increasing the temperature, at lower fields, the resistivity increases which is attributed to progressive inelastic scattering of conduction electrons. In contrast, at

higher temperatures the MR is negative through the whole of the field range due to the magnetic-field suppression of the spin-flip scattering [118].

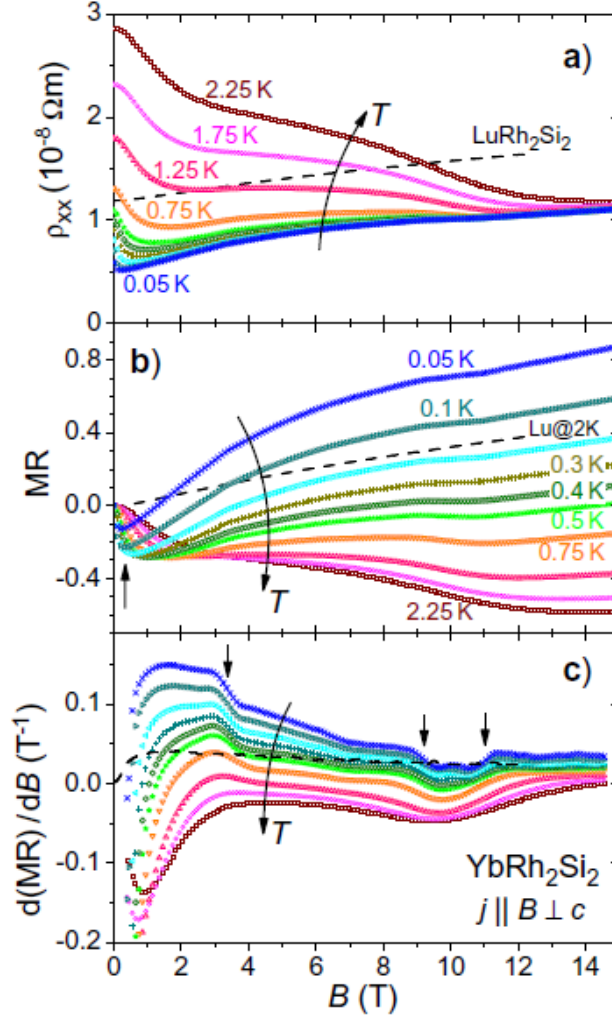


FIG. 3.7. (a) Resistivity ρ_{xx} as a function of external magnetic field, (b) magnetoresistivity MR and (c) field derivative of the MR as functions of magnetic field. All panels have the same temperatures, $0.05 \text{ K} \leq T \leq 2.25 \text{ K}$, and the same color code [118].

3.2.2. YbNi₄P₂

YbNi₄P₂ is a HF compound with a Kondo temperature of about 8 K and has an FM long range order under 150 mK at zero magnetic field [3] with tetragonal crystal lattice. The crystalline structure and parameters of YbNi₄P₂ have made this compound to be introduced as a quasi-one-dimensional heavy fermion metal [3]. The crystalline structure is shown in Figure 3.8 (a) and (b). The structure contains isolated edge-connected Ni tetrahedra chains along c -direction and these neighboring chains are linked by Ni–Ni bonds between the corners of the tetrahedra. Between the channels of the Ni tetrahedral chains the Yb atoms are located along c -direction also. The central Yb chains are shifted by $\frac{c}{2}$ along c -direction (Figure 3.8 (a) and (b)).

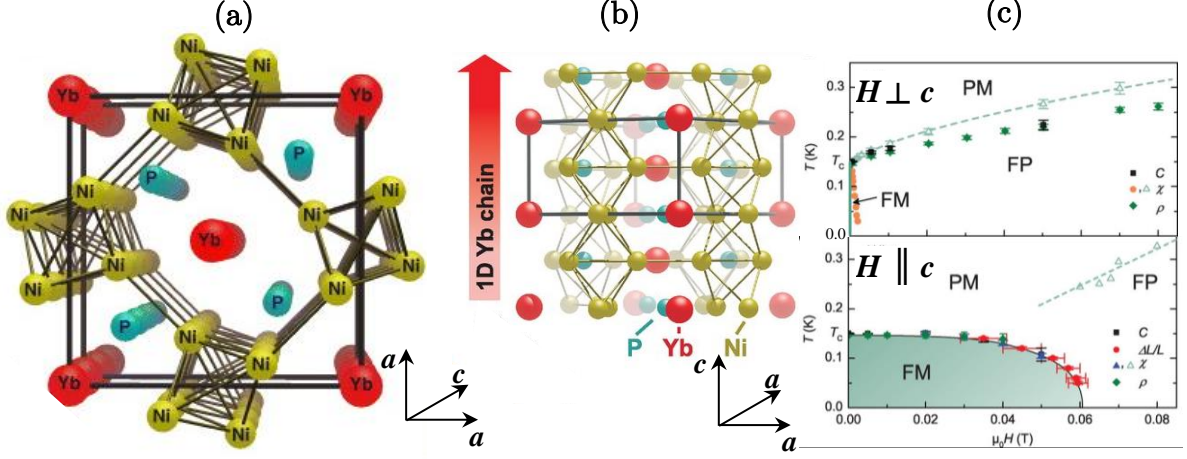


FIG. 3.8. (a) The tetragonal crystal structure in which the Yb chains are along c -axis and located in the channels between chains of edge-connected Ni tetrahedra [3]. In (b) the same structure of (a) is shown after 90° rotation. The shift between the 1D Yb chains along c -direction is pictured [147]. The coordination axes have two directions labeled “ a ” and one direction labeled “ c ” to emphasize at the *isotropic* properties at “ aa ” plane. (c) The H - T phase diagrams for different magnetic field application directions [147] in the vicinity of the QCP.

The ferromagnetic to paramagnetic QCP makes this compound distinguished among the other HF compounds since they are mainly antiferromagnetically ordered right before QCP. A QCP is a second order transition while theoretical and experimental studies in the recent years have shown that FM ground states transitions are typically first order transitions, which suppress QC fluctuations [148] [149]. Low temperature measurements on this compound has revealed the existence of the FM phase in a very strong anisotropy [147] [150] [151].

From the magnetization data one concludes that the FM ordering in this compound is perpendicular to c -direction [147]. The strong suppression of FM phase in the case of the perpendicular magnetic field in c -direction (Figure 3.8 (c)) could also be interpreted as a hint toward the spin alignment direction. This interpretation could be considered for YbRh₂Si₂ as well, although, the ordered phase in this compound is antiferromagnetic.

Theoretical studies show that in a ferromagnetic f -electron Kondo-lattice system, the Kondo screening may become completely suppressed inside the ferromagnetically ordered phase [149]. It is still, however, not proven whether the ferromagnetic QCP is a Kondo-destroying (unconventional) type QCP.

Since in this thesis the results of the ESR measurements at different crystallographic directions of the YbNi₄P₂ samples are reported, it is worth to mention some properties of this compound regarding anisotropy. The anisotropy of YbNi₄P₂ properties is significantly strong, although the symmetry on each Yb ion site is identical. This is due

to the dissimilar crystalline electric fields that Yb ions experience in one chain in respect to the neighboring chain since the chains have the mentioned shift of $\frac{c}{2}$ relative to each other [152]. This leads to a frustration between Yb ions next to each other which are in adjacent chains. This together with strong electron-electron correlations enhances the quantum fluctuations strength [147]. Figure 3.9 (a) to (c) (modified from reference [147]) show the static susceptibility and electrical resistivity of single crystalline YbNi₄P₂ sample at the parallel and perpendicular directions regarding *c*-direction.

By looking at the dependence of the resistivity on the external applied magnetic field, one finds a significant magnetoresistance in this compound also, as depicted in Figure 3.9 (b) and (c).

As already mentioned in the discussion about the ESR observability in some Kondo lattices, a Kondo system could reveal ESR signals when a ferromagnetic correlation exists among the Kondo ions. This doesn't need to essentially be a long-range ferromagnetic order but short-range correlations also suffice. If the correlations among the spins are antiferromagnetic (and not essentially a long-range AFM order) the ESR linewidth is expected to be in the order of Kondo temperature which means for a system with $T_K = 20$ K the ESR linewidth will be over 35 T. However, the FM correlations (motional narrowing) can reduce the linewidth proportional to the effective mass of the fermions. The higher the effective mass means the narrower the Kondo states and thus the narrower the linewidth. The anisotropy in *g*-factor of Kondo lattices like YbRh₂Si₂ which is already mentioned in the previous section, could also be explained by the FM correlation among *f*-spins sites. According to this explanation, the observed *g*-factor anisotropy is not necessarily resulting from the Kondo ions but from the alignment of the short-range FM correlation in- or out of plane [139].

YbNi₄P₂ is, as a Kondo lattice HF, an interesting compound for ESR investigations. Studying this system may shed light to some extent on the theoretical discussion which explains the observed ESR in Kondo lattice HFs as the result of a collective response of the system based on FM fluctuations among the *f*-spins. This compound has a proven long-range FM order and ferromagnetic polarized region (shown by FP in Figure 3.8 (c)), and, therefore, it is a very suitable candidate to check ESR observability.

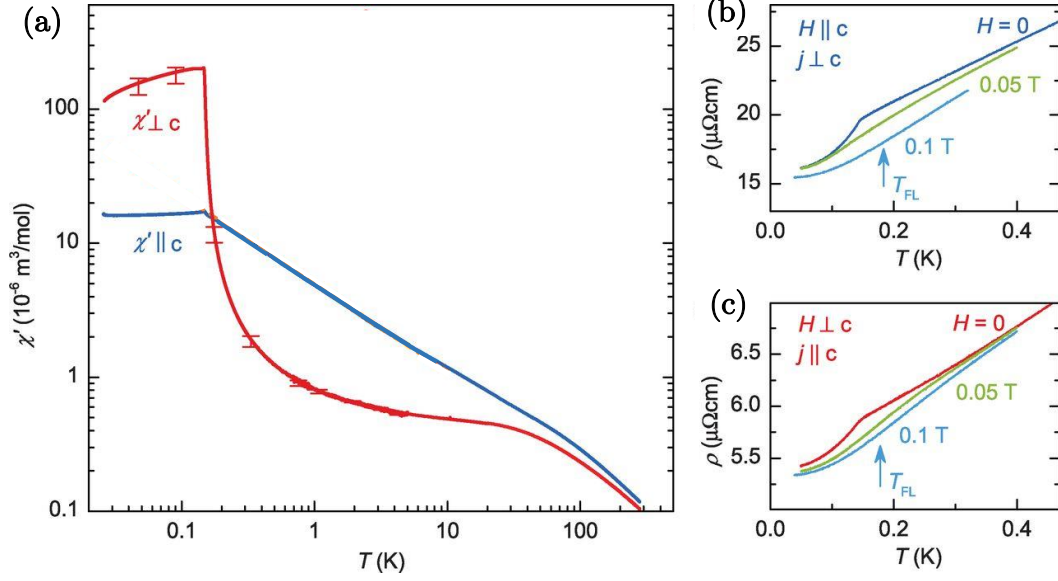


FIG. 3.9. Temperature dependence of the magnetic susceptibility and electrical resistivity of the YbNi_4P_2 single crystal sample. (a) The magnetic susceptibility (χ') as a function of temperature for parallel and perpendicular applications of magnetic field respect to c axis. (b) and (c) are the resistivity plots by changing temperatures for different magnetic field strengths. The curved part of the resistivity curves for $H = 0$ T is the FM phase signature which is shown in Figure 3.8 (c). Below Curie temperature, T_C , the resistivity follows a T^n power law, with $n_{\perp} = 2.9$ and $n_{\parallel} = 2.5$, probably because of charge scattering from FM magnons. “ j ” denotes the applied electrical current in the resistance measurements. At $H = 0.1$ T, the both resistivity curves in (b) and (c) follow a temperature dependence close to T^2 below T_{FL} (arrows). This figure is taken from reference [147] and is slightly modified in comparison with the original.

3.3. Spin Liquid System; κ -(BEDT-TTF) $_2\text{Cu}_2(\text{CN})_3$

What causes the exotic (Non-) fermi liquid state (behavior) is actually the strong correlation among the charges of the charge carriers; electrons. However, when strongly correlated, not only the charge but the spins of the charge may also lead to exotic behaviors. A spin liquid system is a direct result of highly correlated spins in which a well-defined ground state has difficulties to form. In this case, the ground state is the simultaneous existence of many ground states (superposition). The interesting question is now what could be the response of such a system to an electron spin resonance excitation? In some HF Kondo systems, a significant ESR signal could be observed although the magnetic moments were screened by the surrounding charges (conduction electrons). Could through a (similar) mechanism an ESR signal be obtained in a frustrated system in which the magnetic moments are strongly affected of each other? To answer the question, an ESR investigation is worth to be performed on a spin liquid system.

The term (quantum) spin liquid, QSL, is applied for a state of matter in which the quantum (and not classical) fluctuations avoid a well-defined ordered state. The spins (magnetic units) are disorderly arranged because of the frustration in their favorable states as the result of the simultaneous presence of the competing exchange interactions. The spins are highly correlated, but a definite ground state is not able to form because of strong fluctuations down to even 0 K [153]. The fluctuations of the spins in a spin liquid show remarkable collective phenomena such as fractional particle excitations [154]. The simplest (2D) example of frustration image was proposed by Anderson [155] for the first time as a prototypical triangular lattice with AFM ordering (Figure 3.10 (a) and (b)). A 3D model of spin order frustration is also imagined with the name of pyrochlore lattice shown in Figure 3.10 (c) [154].

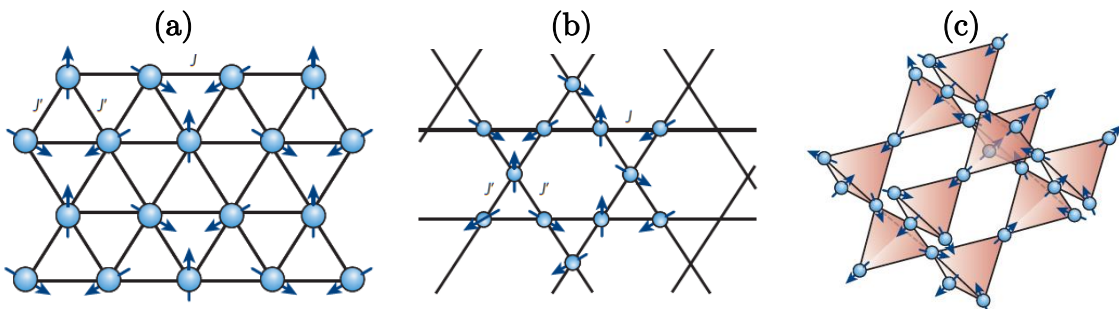


FIG. 3.10. (a) The triangular Anderson lattice of a spin order frustrated system. Considering just one triangular set of spins, two spins can orient antiferromagnetically but the third one is frustrated since it is impossible to be antiferromagnetic with the other two at the same time. Therefore, the system fluctuates and a well-defined magnetic order is suppressed. (b) The Kagome lattice. Since the rotational symmetries in a real lattice may not be perfect, different exchange interactions (j and j') are possible to happen at the same time in different directions [154]. (c) The 3D system of order frustration [154].

Frustration does not exclusively happen in spin liquids. At QCPs, systems exhibit characteristic scale invariance and consequently, thermodynamic and dynamic quantities obey a universal scaling relation [153] [4] (for more details please refer to the references Nr. 5 to 7 of [4]). Ref. [4] expresses a subtle point which is taken from Ref. [156] as the following: The LFL state as the result of Kondo-breakdown quantum critical transition in HF systems, is a spin liquid phase of the localized f -electrons. The universality of QPTs, indifference of happening in a HF system or QSL system, is fascinating when an exotic system like high- T_c superconductors could be studied and get more understood by considering it as either an NFL or QSL phase.

Frustration in a spin liquid state causes the lattice ground state to be a superposition of various states. The theory of the superpositioning of the ground state was proposed by Anderson as the resonating valence bond state (RVB); routed from valence bond state. The differences between the RVB and valence bond solid is the presence of long

range entanglement and nonbroken symmetry (no spontaneous symmetry breaking) in RVB [155]; Figure 3.11 (a) to (c). It is worth to mention, depending on the circumstances, the spins may order (instead of fluctuating and total frustration), however, the order moment is in a less obvious manner [154], or in other words, the quantum fluctuations significantly reduce the size of the ordered moment [157]. Frustration in the spin liquid systems results to a kind of gap which is named “spin gap”. Spin gap is the minimum amount of thermal energy which the system need to be capable of showing non-zero susceptibility values; Figure 3.11 (d).

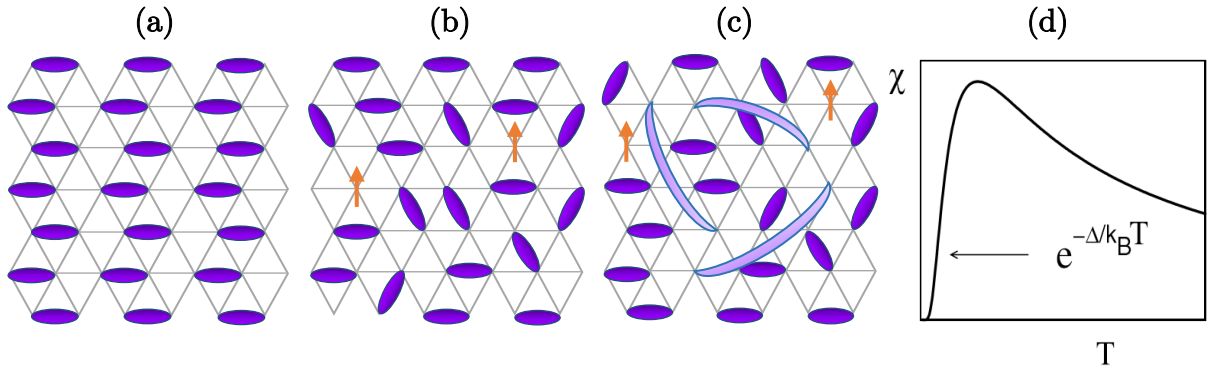


FIG. 3.11. (a) A schematic of valence bond solid which has a specific spinon configuration. The violet ellipsoids ($\uparrow\downarrow$) show the spinons containing of neighboring spin pairs. A more precise definition of the spinons is in fact: $\frac{1}{\sqrt{2}} (\uparrow\downarrow + \downarrow\uparrow)$. In (b) the violet ellipsoids and in (c) light violet elongated arcs show schematically the short- and long-spinons of a time snapshot for the RVB. Spinons are magnetic excitations contained of correlated paired spins. The single orange arrows in (b) and (c) show the exotic excitations with fractional spin number of $\frac{1}{2}$ (the normal spinons have the spin number of zero) which exist in the spin lattice of QSLs. (d) The spin gap representation in the susceptibility vs. temperature curve of a spin liquid system [158].

A prime example of a spin liquid system which showed one of the first experimental existence of a QSL state is the layered molecular system κ -(BEDT-TTF)₂Cu₂(CN)₃ [159] [160] which is schematically depicted in Figure 3.12. Before presenting more detailed information about the physics of κ -(BEDT-TTF)₂Cu₂(CN)₃, it is worth elaborating the compound and logical purposes behind developing this family of materials to some extent.

The BEDT-TTF molecules are flat, so they can be placed beside each other in a variety of arrangement and are surrounded by large molecular orbitals. These orbitals overlap and make the transfer of electrons from one molecule to the other possible. Synthesis of these band structure-forming molecules in an ordered arrangement is usually done in a process of making a charge-transfer salt. In a charge-transfer salt, a number j of BEDT-TTF molecules jointly donate one electron to another type of molecule, labeled X, to form a (BEDT-TTF)_jX compound. In case of $j = 2$, dimers form. X is an anion

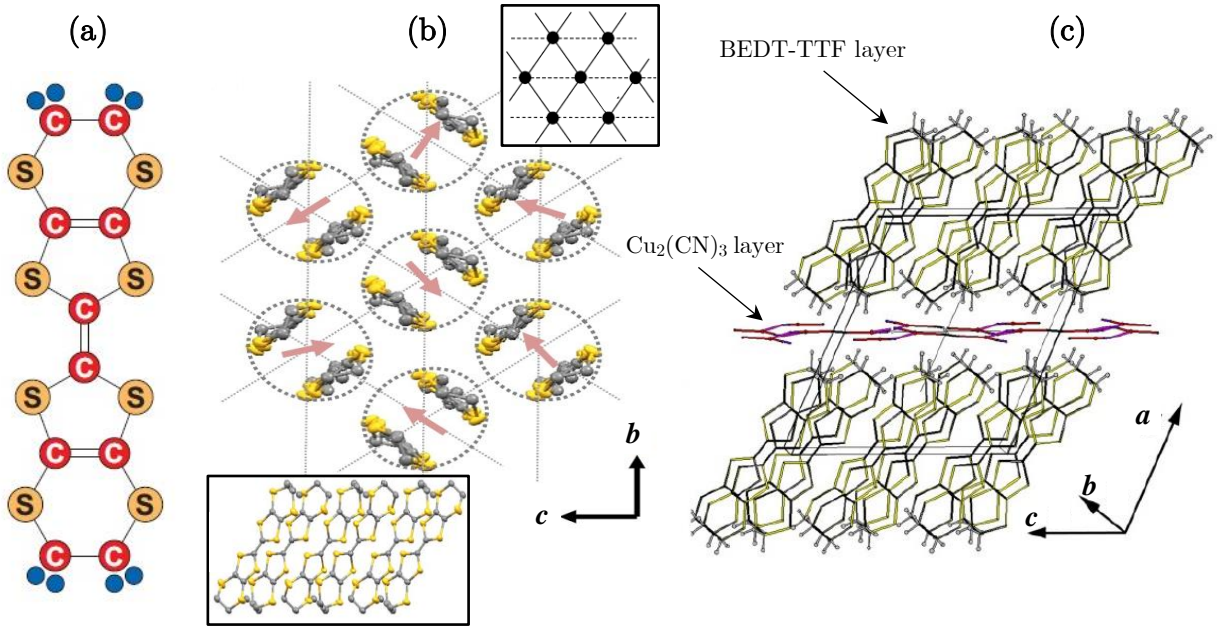


FIG. 3.12. (a) BEDT-TTF molecule sketch [5]. The molecular formula is $C_{10}H_8S_8$ [161]. The red, orange and blue circles represent carbon, sulfur and hydrogen atoms. (b) The lower inset shows the BEDT-TTF molecules along each other to form a BEDT-TTF layer [4]. The middle picture is the top view of the BEDT-TTF layer in which the BEDT-TTF dimers (spinons) are signified by the dashed circles [4]. Each spinon has a spin $\frac{1}{2}$ which is shown by the pink arrows. The molecules have the κ arrangement. Each spinon acts like one spin in a triangular lattice which could be considered like the black points in the upper inset [159]. (c) The layered structure of κ -(BEDT-TTF) $_2$ Cu $_2$ (CN) $_3$. The BEDT-TTF layers are sandwiched between Cu $_2$ (CN) $_3$ layers [6]. (BEDT-TTF) $_2^+$ dimers yield one electron to the Cu $_2$ (CN) $_3$ layer. bc layer is named as the conductive layer since the out of plane conductivity is two orders of magnitude lower than the in-plane conductivity [5].

because of its gained negative charge. The transfer of charge among the molecular groups (dimers for example), bind the charge-transfer salt together. Consequently, the j BEDT-TTF molecules share a hole also. Therefore, the bands formed by the overlap of the BEDT-TTF molecular orbitals will be partially filled resulting the salt to be metallic. They are considered as two-dimensional systems since the BEDT-TTF molecules are able to transfer electrons (by hopping) among them through one layer and not perpendicular between two separated layers. The size of the unit cell can be changed (tuned) by changing the size of the anions. The bigger the anion hexagonals, the further apart the BEDT-TTF molecules, the smaller the charge transfer, the narrower the resulting band and the larger the effective mass. Thus, different anions can be employed to optimize a particular physical property [162]. Beside the emerging interesting physics of BEDT-TTF molecule the aspect of band structure engineering of

these organic molecules is of the motivations of developing them. In continue a brief of the interesting new physics of κ -(BEDT-TTF)₂Cu₂(CN)₃ will be introduced.

κ -(BEDT-TTF)₂Cu₂(CN)₃ is a Mott insulator in whose structure the spin $\frac{1}{2}$ BEDT-TTF dimers ((BEDT-TTF)₂⁺) form a triangular (FIG. 3.10 (a)) magnetic lattice [159] [163] [164]. κ is a sign to show the arrangement of adjacent BEDT-TTF (bis(ethylenedithio)-tetrathiafulvalene) dimers. The dimers (spinons) interact with each other antiferromagnetically by an exchange coupling of j as shown in Figure 3.10. Among many other similar compounds κ -(BEDT-TTF)₂Cu₂(CN)₃ is a very suitable candidate for studying the QSL state, because of much less possible diffusing impurities (during the sample growth) than the other analogous compounds [4] [165] and the possible presence of the quantum criticality [4].

While the coupling constant $j/k_B \approx 250$ K is a large value, no magnetic long-range order happens even at a very low temperature, $T \approx 30$ mK [4] [165]. The Cu₂(CN)₃ is the layer structure between the BEDT-TTF molecules or in other words the BEDT-TTF molecules grow on (between) the Cu₂(CN)₃ layers as pictured in Figure 3.12 (c).

To investigate the magnetic states or probable orderings, low temperature ESR [166], NMR [159] and μ SR [160] studies have been performed on κ -(BEDT-TTF)₂Cu₂(CN)₃. In reference [160] a broad range and detailed phase diagram obtained from μ SR investigations is represented (Figure 3.13).

The phase borders in Figure 3.13 are separating the areas which had different corresponding coefficients (of the μ SR experiments). They show that applying a small magnetic field causes a quantum phase transition between the spin-liquid phase and an AFM phase which has a strongly suppressed moment. The spin liquid phase in this molecular compound is analyzed as Bose-Einstein condensation of the spin excitations with an extremely small spin gap. The interesting physics is in understanding this spin gap since gap behavior is intrinsic to models with bosonic spins [160]. However, as stated in [160] (with referring to [167] [168]) in a lattice with a spinon Fermi surface, the fermionic spins may go under a pairing transition below a specific characteristic temperature, T_{ch} , and this leads to produce bosons and thus gap behavior. The pairing conversion of fermions to bosons is not essentially universal (all the fermionic spins) but may be partial which in other words means the coexistence of fermionic and bosonic spin excitations [160] [167] [168]. Some traces of the mentioned T_{ch} have already been observed in some properties of κ -(BEDT-TTF)₂Cu₂(CN)₃ by showing characteristic features. T_{ch} could be around 6 K since a double Lorentzian shape ESR line [166], a drop in the magnetic susceptibility [159], a peak in the specific heat [169] and dramatic changes in other properties [170] are observed about this

temperature. In reference [160] the authors have interpreted these observations as the formation of bosonic spin pairs from a fraction of the fermionic spins.

As shown in Figure 3.13, further increasing of the magnetic field induces another phase transition (at H_1) to a new AFM phase which has a different moment of the first one. It is explained as the “deconfinement of the spin excitations” [160].

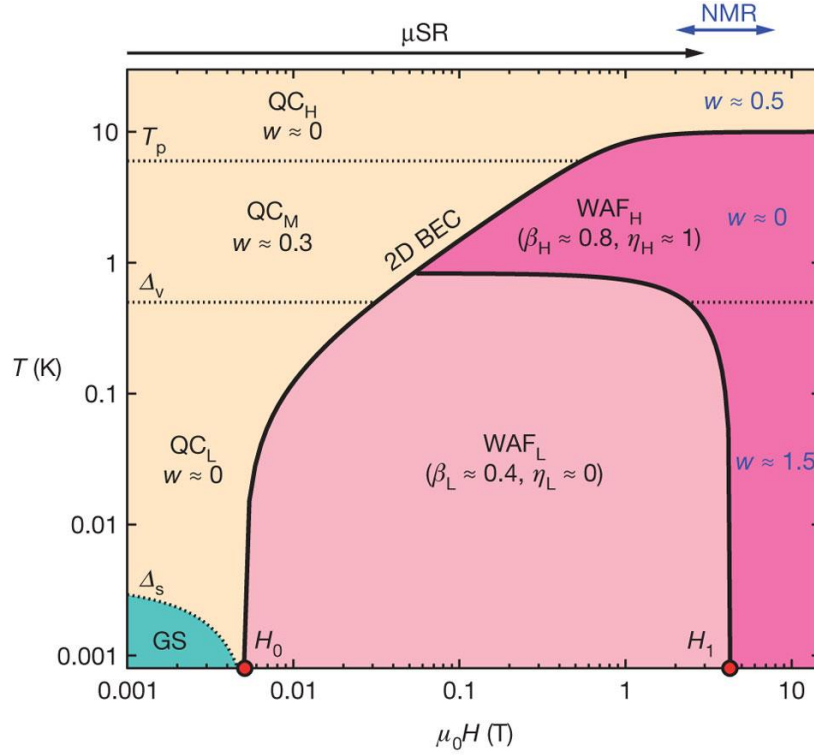


FIG. 3.13. The $H - T$ phase diagram of κ -(BEDT-TTF) $_2$ Cu $_2$ (CN) $_3$ obtained from the μ SR experiments [160] and completed by NMR data [159] whose respective field ranges are indicated on the upper horizontal axes. “GS” stands for “gapped spin” in spin liquid phase. “QC” is the abbreviation for quantum critical. L, M and H subscripts stand show low, intermediate and high temperatures as well as fields accordingly. Weak antiferromagnetic is abbreviated to “WAF”. The QCPs are signified by red circles at H_0 and H_1 on the H axis.

Since an ESR measurement studies the collective response of the electrons (in contrast to μ SR experiments which are local spin probes), it could be a very use- and powerful method in investigating and revealing the fractionalized coexisting states as suggested to be the case in κ -(BEDT-TTF) $_2$ Cu $_2$ (CN) $_3$.

Another fact which should not be neglected by analyzing any kind of gained data from such a molecular material is the lattice purity and single crystal growth process precision. For instance, in [166] the extra ESR signals of Cu $^{2+}$ impurities were reported. The impurities can perturb the coupling between the BEDT-TTF layers and anion layers. This may also be the cause of the data variation from sample to sample.

4. Metallic Coplanar Waveguides; Developments and Measurements

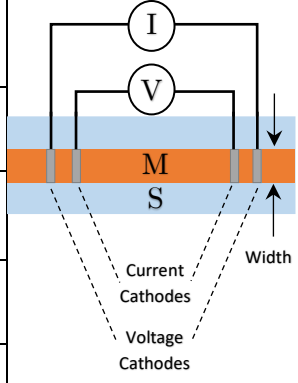
In this section, the development of the metallic coplanar resonators which includes design, fabrication, measurement and further developments (according to the obtained results of the primary experiments) are illustrated and explained.

The first step in the fabrication of the resonators was the material selection since one of the main purposes is to obtain resonators with quality factors as high as possible and this means the material used in the structure of the resonator must have the electric conduction loss as low as possible. Therefore, two metals which are of the metals with lowest electrical resistivity, ρ , were selected; Copper and Gold. The important point is, however, these metals are utilized in the form of thin films and the materials properties must be checked at cryogenic temperatures accordingly. The resistivity of the metals in the both forms of bulk and thin films could be modified (to decrease or increase) by the very well-known process of annealing [171] [172].

4.1. Material Selection

To find the film with the lowest possible ρ , 15 samples of each metal (copper and gold) were thermally evaporated. The samples were a narrow strip of the corresponding metal with the thickness of 500 nm, thermally evaporated on sapphire substrates. Each sample was annealed for a given time and temperature and in a furnace with Argon flow chamber in order to avoid probable oxidations. The resistivity was afterwards obtained from the resistance measured with the 4-point method. Table 4.1 represents the samples specifications, annealing process data and measurement data. As already mentioned, since the resonators are designed for working at low temperatures, the temperature dependence of the resistance of the samples was not fully recorded except for a limited number of the samples.

Table 4.1. The sample, annealing process and 4-Point measurement data.

Material	Sample Specification	Annealing Temperature (°C), Duration (min)	Resistivity at 5 K ($\mu\Omega$) & Reduction after Annealing (%)	4-Point Measurement I (mA) , V (mV)
Copper and Gold	Thickness: 500 nm Width: 0.32 mm NOTE: The length between the two current electrodes and the two voltage electrodes were different at each sample. It was considered during resistivity calculations. <i>see last column for the illustration</i>	0 , 0	Cu: 0.16 Au:2.56	Applied Current: - 1 mA to +1 mA with the increment of 0.1 mA Measured Potential Difference: Depending on the resistance between 0.1 to 0.5 mV  "M" stands for metal "S" stands for substrate (sapphire)
		200 , 120	Cu: 0.17 & - 6 Au: Anomalous	
		200 , 180	Cu: 0.13 & 19 Au: 1.61 & 37	
		300 , 60	Cu: 0.20 & - 25 Au: 2.03 & 21	
		300 , 120	Cu: 0.16 & 0 Au: 1.98 & 23	
		300 , 180	Cu: 0.31 & - 94 Au: 1.81 & 29	
		300 , 240	Cu: 0.17 & - 6 Au: 1.34 & 48	
		400 , 60	Cu: 0.15 & 6 Au: 0.98 & 62	
		400 , 120	Cu: 0.16 & 0 Au: 0.85 & 67	
		400 , 180	Cu: 0.18 & - 13 Au: 1.5 & 41	
		400 , 240	Cu: 0.18 & - 13 Au: 0.86 & 66	
		500 , 60	Cu: 0.27 & - 69 Au: 0.49 & 81	
		500 , 120	Cu: 0.28 & - 75 Au: 0.35 & 86	
		500 , 180	Cu: 0.25 & - 56 Au: 0.17 & 93	
		500 , 240	Cu: 0.37 & - 131 Au: 0.24 & 91	

The used cryostat was a Janis[®] flow cryostat on which an extra wiring was applied to get the proper circuit for the 4-point measurements (for two samples simultaneously). The current-voltage ($I-V$) curves at each temperature was recorded using a Keithley[®] 2400 source-meter. The results are shown as plotted data also in diagrams of Figure 4.1.

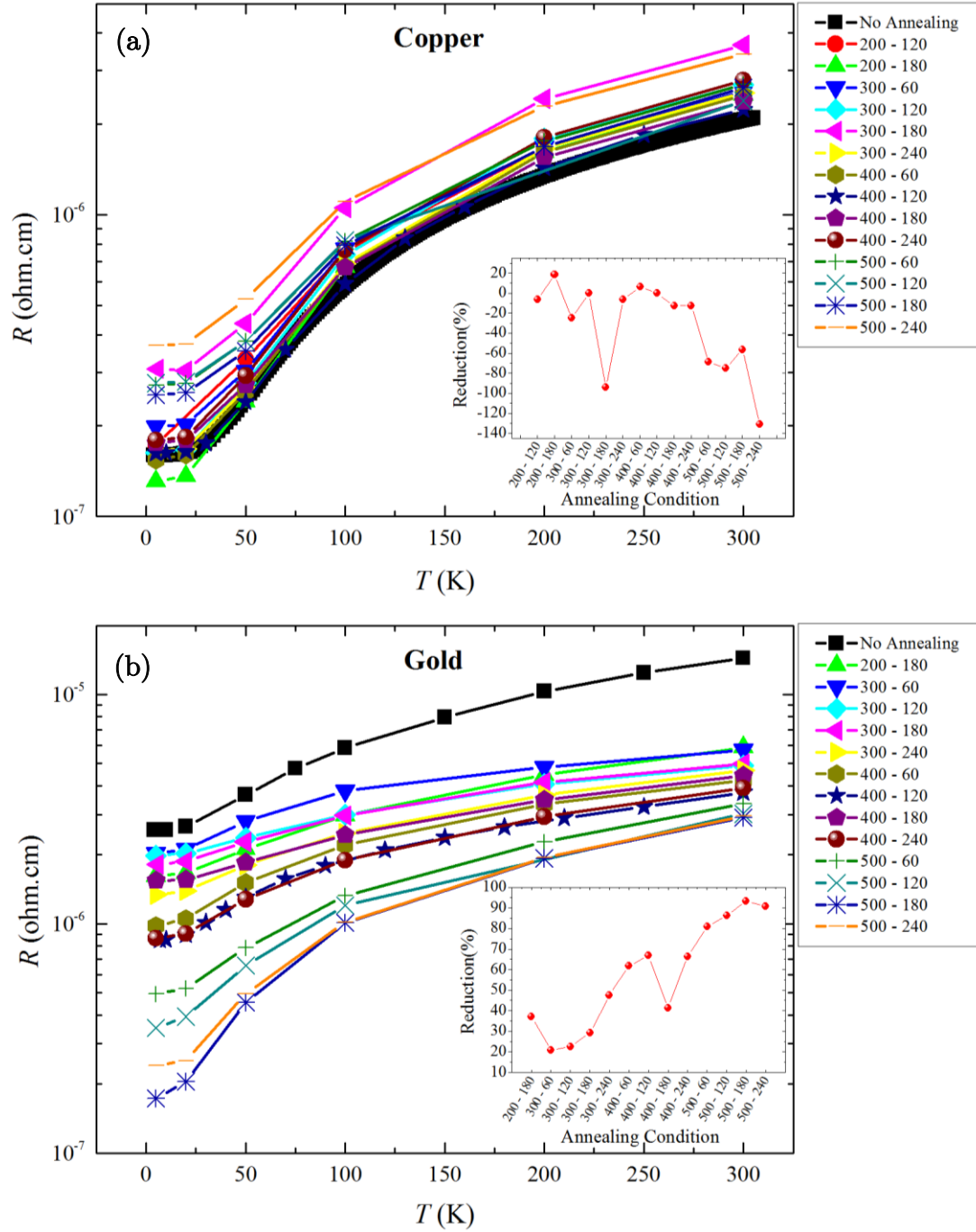


FIG. 4.1. The effect of annealing processes on the resistivity of the thin films of (a) Copper and (b) Gold. The data of the annealing at 200 °C and 120 min for the gold films are not shown because of the anomalous data. The inset of the both figures show the percentage of the reduction of the resistivity relative to the film without any annealing process.

As the results (in Table 4.1 and Figure 4.1) show the copper film without any heat treatment of annealing has the lowest ρ and any try to reduce ρ could not usefully change it. This is mentioned in some literatures for copper thin films [173]. The annealing was very effective in the reduction of the resistivity of the golden films, however, the lowest obtained resistivity for the gold films was even slightly higher than

the copper film without any heat treatment. Therefore, the selected material for the resonators was copper without any annealing process.

In addition to the DC measurements, some sorts of AC measurements were also performed to investigate the high frequency loss when the metallic material of the chip (coplanar transmission line, see Figure 1.5, chapter 1) is changed. The results will be shown and discussed later.

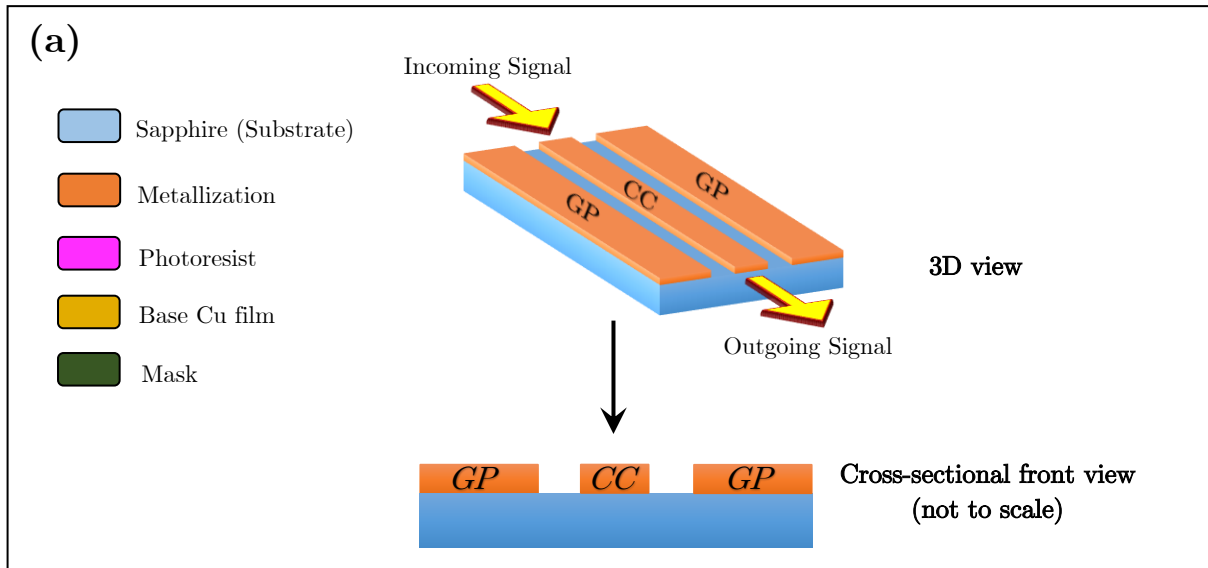
Different thin film deposition processes yield different film resistivity (sheet resistance) since the amount of voidage, the grain size of the film and the surface roughness (important when the skin depth is comparable with roughness) are varying from one process to the other. For example, the sputtered films have lower amount of the voidage compared to the thermally evaporated films (and thus have higher conductivity) or the electroplated films have higher surface roughness in comparison with sputtered or thermally evaporated films. Moreover, each growth technique has some limitations, for example, the sputtered thin films can usually not get more than a few micrometers because the high internal stress of the film will cause a dramatic failure like cracking or complete peeling of the film. In contrast, electrochemically grown films are able to become thick to several tens of micrometers without finding any problem. Hence, the resonators were made by two processes of top-down and bottom-up which are explained in the following.

4.2. Fabrication and Packaging

In a top-down process the main step of the formation and appearance of the structure is based on etching. In this work 1 μm sputtered metallic film on a sapphire substrate was processed photolithographically and then etched down to the sapphire substrate to form the final structure. The corresponding process flow is illustrated in Figure 4.2 (b).

In a bottom-up process the main step of the formation of the structure is based on the growth (deposition) of the final structure. In this work after the photolithography process on a 50 nm thin film, the structure of the resonator (or the transmission lines) was grown by an electroplating process. The corresponding process flow is illustrated in Figure 4.2 (c).

The sapphire thickness was 430 μm in all the fabricated resonator or transmission lines in this work. At cleaning of the sapphire substrate, it is very important not use any tissues and just using chemicals. The substrates were always hold by a tweezer and rinsed at first by Acetone, and right after that, immediately laid in an Isopropanol bath. After taking the substrate from the Isopropanol bath out and drying it by high



(b) Top - Down Process



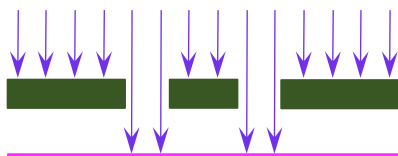
Substrate preparation: The sapphire substrate was precisely cleaned by Isopropanol, Acetone and acid sulfuric.



Film deposition: 1 μm Cu film was sputtered on sapphire. 5 nm Cr buffer layer film was deposited under Cu film.



Photoresist application: A positive photoresist was applied by spin coating and afterwards a baking step was done.



Mask alignment and UV-Exposure: The photoresist was illuminated through a mask with the corresponding designs.

(c) Bottom - Up Process



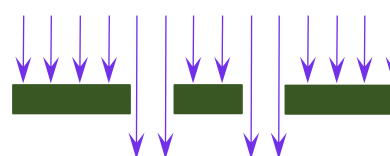
Substrate preparation: The sapphire substrate was precisely cleaned by Isopropanol, Acetone and acid sulfuric.



Base film deposition: 50 nm Cu film was evaporated on sapphire. 5 nm Cr buffer layer film was deposited under Cu film.



Photoresist application: A negative photoresist was applied by spin coating and afterwards a baking step was done.



Mask alignment and UV-Exposure: The photoresist was illuminated through a mask with the corresponding designs.

Continue on the next page:

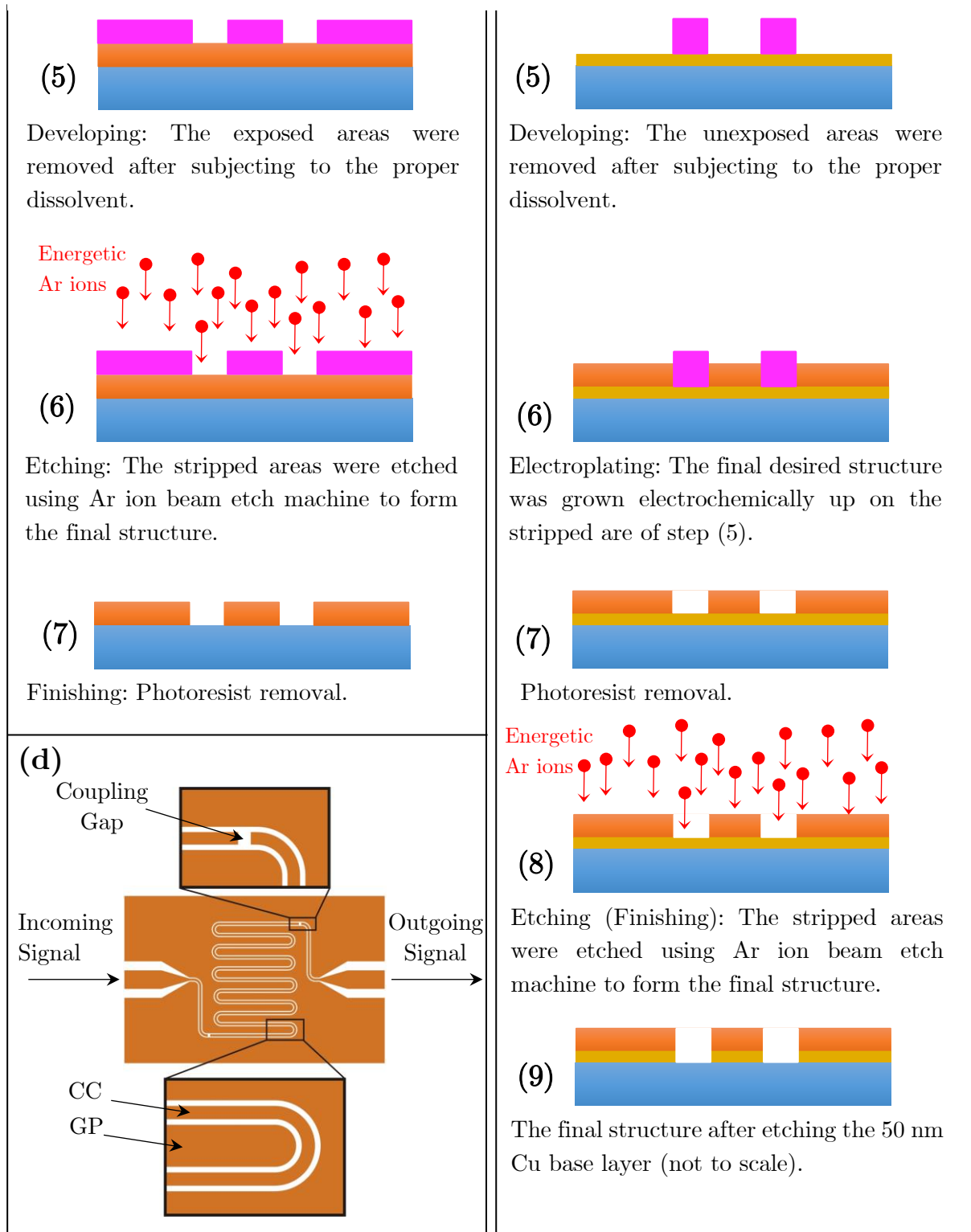


FIG. 4.2. (a) is showing schematically the 3D and cross section view of a coplanar structure (a transmission line in this case, see Figure 1.5). Almost all the real structures were meander shaped which is shown briefly in (d) and will be shown with details later. (b) and (c) show the fabrication steps (process flow) of in turn the top-down and bottom-up methods of the coplanar structure shown in (a). The structure shown in the fabrication steps is the cross-sectional view as illustrated in (a) also. The essential details of the steps are brought in the text.

pressure nitrogen (provided in clean rooms), the substrates were laid in a sulfuric acid (99%) bath and subjected to ultrasonic cleaning for 5 minutes. Thereafter, the substrate was brought out from the acid bath and placed in a deionized distilled water to clean the acid off. Thereupon, the substrate was again rinsed by Isopropanol and dried by nitrogen. Beforehand, the oxygen plasma cleaning was used to be utilized for cleaning the substrate, however, because of sitting very fine particles (contaminations) on the substrate during the presence of the substrate in the setup chamber, the oxygen plasma cleaning was not used any longer. The mentioned particles were generated from the setup, probably because of a poor chamber maintenance.

The substrates were finally fully inspected by optical microscopy to verify if they are totally clean. It was very essential to have the whole of the substrate clean to obtain all the chips undamaged and defect free from it. This is important to have the chips, which are to be compared with each other, from one single process of fabrication.

Notable points in top-down process:

The sputtered films were produced in the Nanolab (clean room) of the technical faculty of the university of Kiel. Gold and copper films on the sapphire substrate (which were sent to Kiel) with 5 nm chromium buffer layer were received.

The positive type photoresist with the trade name of AZ[®] 4562 of MichroChemicals GmbH was used in top-down process. The photoresist was spin coated on the Cu film and subsequently baked with the following recipe:

1. Applying the photoresist on the Cu film. One should note that the photoresist should be at room temperature when using it to have the appropriate viscosity and a proper distribution on the film on spin coating. They are usually kept in the refrigerators (cool places) to avoid too fast decline.
2. Ramping up during 5 seconds from 0 to 3500 rpm.
3. Spinning 25 seconds at 5000 rpm.
4. Baking 5 minutes at 90° C.

After baking step of the photoresist, the UV exposure part is to begin. One should make sure that the mask is clean and there is no obstacle to hinder the light reaching the photoresist. The mask could be rinsed by Isopropanol right after once rinsing with Acetone. The time for the exposure was always 45 seconds in contact mode of the mask aligner machine.

After exposure, the photoresist must get developed. The used developer was AZ[®] 726 MIF. For a one piece of assembly (assembly = substrate + film + photoresist + ...) of

a 2-inch substrate (or four pieces of assembly each of which $\frac{1}{4}$ of a complete 2-inch substrate), 200 ml developer divided in two beakers (each beaker 100 ml) is required.

The assembly should be placed and moved (agitation) in the first bath of the developer for 30 seconds and in the second bath for 15 seconds. Two baths are required to have a much better developing result compared to one bath. Right after the developing, the chip should be laid in a water bath to stop developing process. The chip should then get dried carefully by nitrogen gun. The developed chips should be inspected under microscope and in the case of observing no deviation or serious discrepancy in the photolithography process the next step can start. The thickness of the photoresist was always measured by Dektak[®] 150 profilometer. The thickness was usually in the range of 5 to 6 μm .

The Ar ion beam etching process removes all the parts which are not covered by the photoresist and therefore the final structure can form. After etching, the photoresist is to be removed by Acetone and afterwards rinsed by Isopropanol.

The chips in the assembly were gone under a wire-cutting process to get single chips ready to be placed in the box which will be explained later.

Notable points in bottom-up process:

The 50 nm base film was evaporated right after 5 nm Cr evaporation deposition. The evaporation process was electron beam type. It was done in the electron beam evaporation machine which has six crucibles for different materials.

The negative type photoresist with the trade name of AZ[®] 125 nXT of MichroChemicals GmbH was used in bottom-up process. The photoresist was spin coated on the Cu film and subsequently baked with the following recipe:

1. Applying the photoresist on the Cu film. AZ[®] 125 nXT-10A has a very high viscosity of 5000 cSt at room temperature and thus it is very essential to pay attention that the photoresist be at room temperature when using to have a proper distribution on the film on spin coating.
2. Ramping up during 5 seconds from 0 to 3500 rpm.
3. Spinning 55 seconds at 5500 rpm.
4. Baking 30 minutes at 90° C.

60 seconds UV exposure was found to yield very suitable mask to photoresist dimension transfer.

The used developer was AZ[®] 726 MIF. For a one piece of assembly (assembly = substrate + film + photoresist + ...) of a 2-inch substrate (or four pieces of assembly

each of which $\frac{1}{4}$ of a complete 2-inch substrate), 300 ml developer divided in two bechers (each becher 150 ml) is required. The assembly should be placed and moved (agitation) in the first bath of the developer for 45 seconds and in the second bath for 15 seconds. In the case of AZ[®] 125 nXT using two baths is very essential to have a much better developing result (compared to one bath) and to avoid any residual photoresist sitting back on the film. Right after the developing, the chip should be laid in a water bath to stop developing process. The chip should then get dried carefully by nitrogen gun. The developed chips should be inspected under microscope very carefully since the thickness of this photoresist reaches up to 25 μm (measured by Dektak[®] 150 profilometer) and this causes deviations in the transferred structure. Reaching to high photoresist thicknesses is necessary to make sure that the electroplated structure has the minimum vertical slope.

The electrolyte using in the electroplating level was a commercial alkali copper electrolyte bought from Conrad Electronics. After electroplating the photoresist washed away by Acetone. In addition, 10 minutes ultra-sonic cleaning (having the assembly in an Acetone bath) was performed. The assembly must be rinsed by Isopropanol after bringing it out from the Acetone bath.

The Ar ion beam etching process removed then the base film where it is not covered by the photoresist and therefore the final structure form. The assembly were gone under a wire-cutting process. All the fabrication steps, except electroplating, were done in the MSL (Microstructure Lab.) of the faculty of physics of the university of Stuttgart. The electroplating process was done in the Chemistry Lab. of the 3rd Institute of Physics.

One example of the finished structures on the sapphire wafer is shown in Figure 4.3. In this figure, the structures are already cut and got separated of each other.

When the assembly is cut to single chips, placing them in the box and connecting the connectors is necessary to be usable in a circuit. As shown in Figure 4.3 (c) the box was made of brass and the SMA type microwave connectors were attached to it by the screws. The inner conductor of the connector was glued on to the chip (resonator or center conductor) by the conductive epoxy EPO-TEK[®] H20E produced by John P. Kummer GmbH. It is a two-component conductive adhesive whose components are to get mixed with 1:1 weight ratio. After application of EPO-TEK[®] H20E on the desired surface a curing process of two hours at 90° C was performed to harden the glue. The curing process may be done at other time and temperature recipes as the company provides. The reason of replacing the common silver paint by EPO-TEK[®] H20E glue was the breaking down and detaching of the silver paint from the copper surface which led to disconnection of the chip and the connector at low temperatures. This was clearly observed in the microscopy inspections and its effect was very significant in the signal

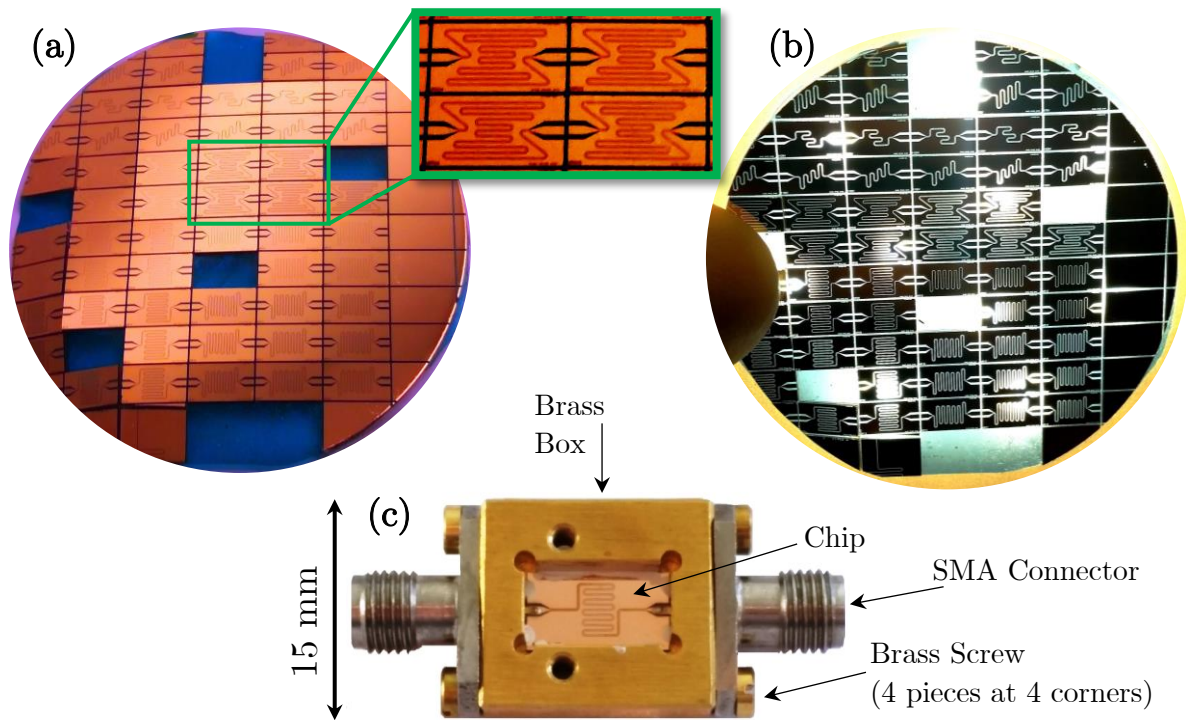


FIG. 4.3. A completely processed wafer with the rectangular copper chips on it. The wafer in this picture has already gone under the cutting process. The black lines between the rectangular chips are the cutting lines. In (a) one can see the blue (plastic) foil at the places where the chips have already been taken out. The blue foil is always used during the cut to hold the wafer fixed. The zoomed part of the wafer shows four chips with the meander line next to each other. (b) shows the same wafer at (a) in front of the light. The light can transmit through the empty distance between the center conductor and ground planes as well as the cut paths. The meander line structure of the center conductors is clearly observable. (c) A chip placed in the brass box and connected to the SMA connectors.

transmission data of many tested transmission lines and resonators where at low temperatures the transmission became order(s) of magnitude lower than room temperature. The significantly higher strength of EPO-TEK[®] H20E removed the disconnection problem permanently. It should be noted that the linking of the edge ground planes of the chip to the box, for the grounding purpose, was still done by silver paint.

4.3. Designs and Geometrical Structures

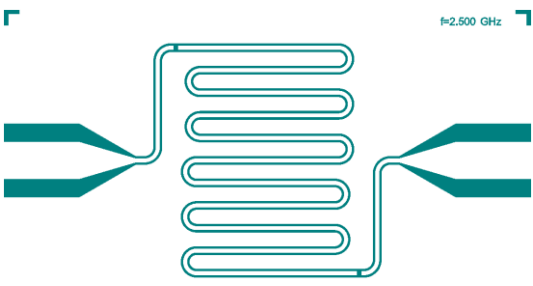
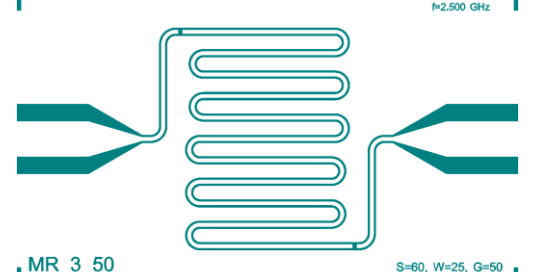
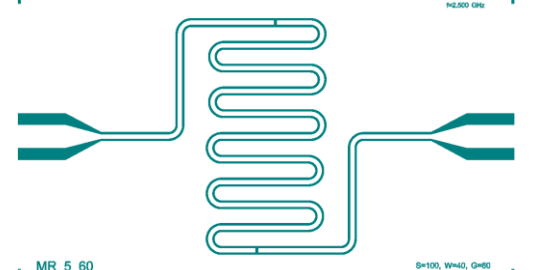
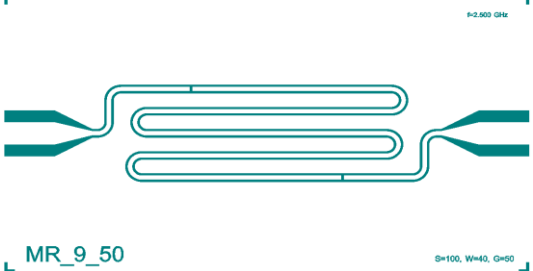
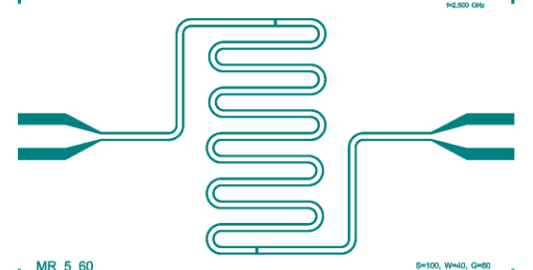
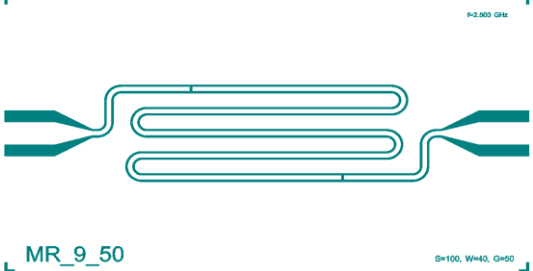
The coplanar structures of this work were meandered (except one case which will be discussed later). More than 90 various resonators and 3 different transmission lines were designed for various purposes. The number of fabricated and measured chips is higher than 300 since in the phase of development some resonators were fabricated several times. All the designs are listed in Table 4.2 with some essential detailed data.

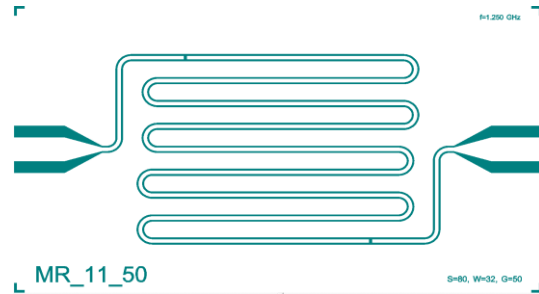
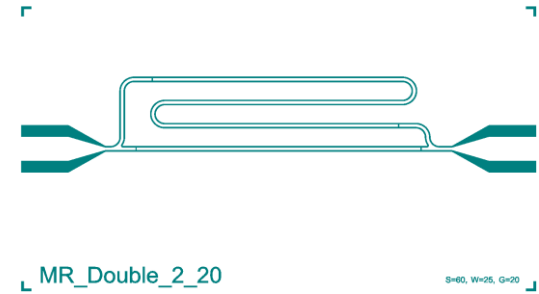
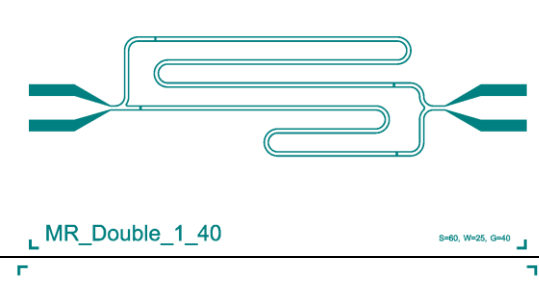
Table 4.2. Showing all the designed (and fabricated) CPW structures in this work. The red-letter designs didn't show normal results or were not measured because of different reasons, for instance, recognized as not to be needed after assessment of the similar structures or fabrication short comings. "CC" stands for Center Conductor.

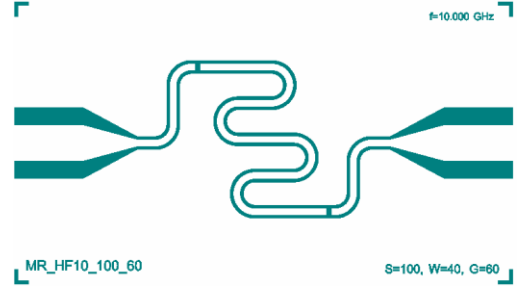
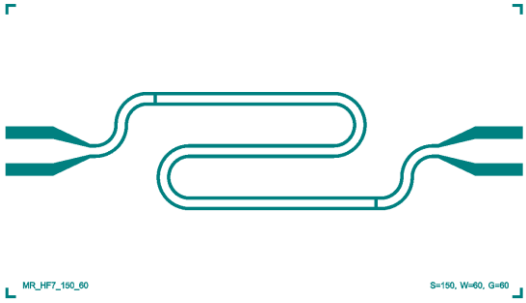
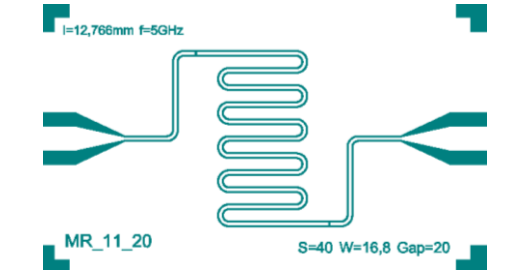
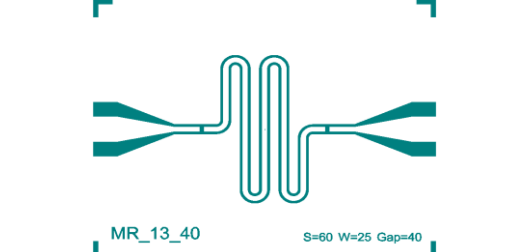
A specimen structure to show the geometrical parameters of the CPWs of this work:

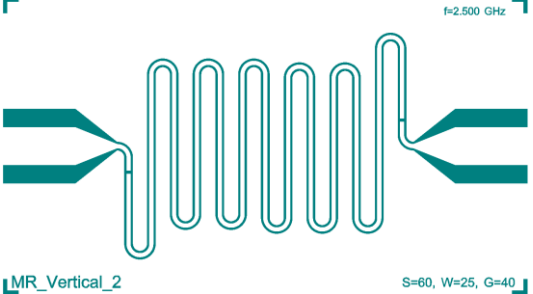
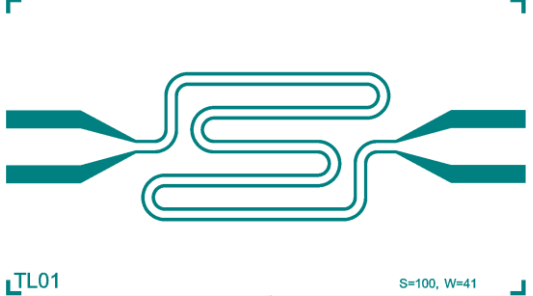
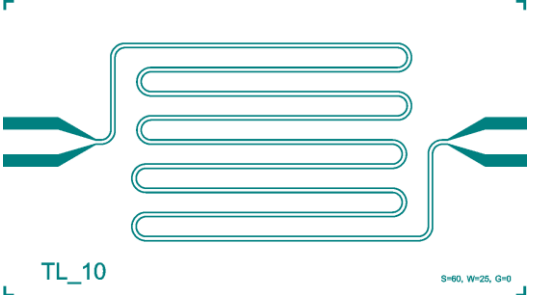
w: Center conductor width
G: Coupling gap
S: Distance between center Conductor and ground plane
D: Distance between the center conductor parts in a meander line

Structure Nr. & Design Purpose	Structure	Remark	Fundamental & CC Length (GHz) & (mm)	w & S (μm)	D & $\frac{D}{w+2s}$	G (μm)	Chip Size (mm×mm)
Nr. 1) One of the first designed and tested resonators in develop- phase		The fundamental was not appeared. Significant box and parasitic modes.	1.5 & 42.5	20 & 8	264 & 7.33	3 10 20	3.8×6.8
				60 & 25	190 & 1.76		

<p>Nr. 2) One of the first designed and tested resonators in develop- phase</p>		<p>In contrast to the structure Nr 1, this design showed all the modes, although, the modes were not equi-distanced.</p>	<p>2.5 & 25.5</p>	<p>20 & 8</p>	<p>264 & 7.33</p>	<p>3 10 20</p>	<p>3.8×6.8</p>		
<p>Nr. 3) Designed to pursue the systematic approach to higher quality factors</p>		<p>The modes were not equi-distanced. Max. Q value: ≈ 300</p>		<p>2.5 & 25.5</p>	<p>20 & 8</p>			<p>264 & 7.33</p>	<p>10 20 30 40 50</p>
<p>Nr. 4) Designed to pursue the systematic approach to higher quality factors</p>		<p>The modes were not equi-distanced. Max. Q value: ≈ 470</p>	<p>80 & 32</p>		<p>240 & 1.67</p>	<p>≈ 1.67 ≈ 1.67</p>	<p>6×10.5</p>		
<p>Nr. 5) To check the effect of the curves number in meander line on the resonator performance</p>		<p>The modes were not equi-distanced. Max. Q value: ≈ 300</p>	<p>2.5 & 25.5</p>		<p>40 & 16</p>			<p>400 & 5.55</p>	
<p>Nr. 3) Designed to pursue the systematic approach to higher quality factors</p>		<p>The modes were not equi-distanced. Max. Q value: ≈ 300</p>		<p>60 & 25</p>	<p>370 & 3.36</p>				
<p>Nr. 4) Designed to pursue the systematic approach to higher quality factors</p>		<p>The modes were not equi-distanced. Max. Q value: ≈ 470</p>		<p>80 & 32</p>	<p>330 & 2.29</p>				
<p>Nr. 5) To check the effect of the curves number in meander line on the resonator performance</p>		<p>The modes were not equi-distanced. Max. Q value: ≈ 300</p>		<p>100 & 40</p>	<p>300 & 1.07</p>				

Nr. 6) Low fundamental achievement	 <p>MR_11_50</p>	The fundamental of 1.25 GHz was successfully reached.	1.25 & 51	20 & 8	440 & 12.22	10 20 30 40 50	6×10.5
				40 & 16	400 & 5.55		
				60 & 25	370 & 3.36		
				80 & 32	330 & 2.29		
Nr. 7) Broad range coverage	 <p>MR_Double_2_20</p>	No desired response was observed	10 & 5.6 3.5 & 16	60 & 25	370 & 3.36	20 40	6×10.5
Nr. 8) Broad range coverage	 <p>MR_Double_1_40</p>	No desired response was observed	3.5 & 16 5 & 12.25	60 & 25	370 & 3.36	20 40	6×10.5
Nr. 9) Higher quality factor achievement	 <p>MR_150_60_60</p>	Max. Q value: ≈ 300 The expected Q value was not achieved, probably because of too close center conductor to the box walls.	2 & 28	150 & 60	770 & 2.85	60	6×10.5

<p>Nr. 10) High fundamental for high quality factors at high frequencies</p>		<p>The modes observed up to ≈ 22 GHz.</p>	<p>10 & 5.6</p>	<p>100 & 40</p>	<p>320 & 1.77</p>	<p>40 60</p>	<p>3.8×6.8</p>
<p>Nr. 11) High fundamental for high quality factors at high frequencies</p>		<p>The modes observed up to ≈ 22 GHz.</p>	<p>5 & 12.25</p>	<p>150 & 60</p>	<p>770 & 2.85</p>	<p>40 60</p>	<p>6×10.5</p>
<p>Nr. 12) Small chip size for performance check</p>		<p>No significant point in functionality was observed compared to the bigger structure.</p>	<p>5 & 12.25</p>	<p>40 & 16</p>	<p>130 & 1.8</p>	<p>20</p>	<p>3×3.6</p>
<p>Nr. 13) Vertical structure for non ESR tests</p>			<p>8 & 7</p>	<p>60 & 25</p>	<p>95 & 0.86</p>	<p>40</p>	<p>3×3.6</p>

<p>Nr. 14) Vertical structure for non ESR tests</p>			<p>2.5 & 22.5</p>	<p>60 & 25</p>	<p>190 & 1.76</p>	<p>40</p>	<p>3.8×6.8</p>
<p>Nr. 15) Resonance position check</p>		<p>The second mode was exactly the double of the first mode. Thus, the inequi-distanced modes in the former structures was mainly because of the meandered structure.</p>	<p>9.7 & 6.5</p>	<p>60 & 25 100 & 40 200 & 80 300&120</p>		<p>20 40 60 100</p>	<p>6×10.5</p>
<p>Nr. 16) Broad band measurements</p>			<p>Broad Band</p>	<p>60 & 25 100 & 40</p>	<p>290 & 2.64 270 & 1.5</p>		<p>3.8×6.8</p>
<p>Nr. 17) Broad band measurements</p>			<p>Broad Band</p>	<p>60 & 25</p>	<p>370 & 3.36</p>		<p>6×10.5</p>

4.4. Microwave Measurements at Cryogenic Temperatures

Some general points and specific recommendations are offered at the following in using different setups for all types of the tests of this work including chip characterization and ESR measurements.

The microwave (MW) measurements were performed to characterize the performance of the resonators and transmission lines as well as for the ESR tests. In the former, there was no sample of any material present and the magnetic and electric field of the chip were not perturbed by any external parameter and in the latter the sample of interest was placed on or hanged above the chip. In addition, in contrast to the ESR measurements, there was mostly no external magnetic field involved except one sort of measurements which was aimed to observe the resonator response in the presence of magnetic field whose results will be subsequently reported.

The MW tests were carried out using either network analyzers or the combination of a power source and a power meter. The frequency range in the MW tests ranged from a few hundred MHz to 20 GHz and rarely further up to 30 GHz. The hardware functions as well as data acquisition were constantly and automatically controlled by LabVIEW® virtual instruments.

Various cryogenic setups (cryostats) were utilized depending on the measurement parameters such as the capability of the cryostat for doing the desired experiment (e.g. 4-point DC measurement, resonator characterization or ESR measurement (magnet required)), the lowest required temperature, the duration of the experiment and the rate of the cooling down. Table 4.3 briefs the type and the characteristic of the all used cryostats in this work.

Table 4.3. The list of the used cryostats and their specifications and limitations. “Resn.” and “TL” stand for resonator and transmission line respectively.

	Magnet	Lowest Temperature (K)	Used Applications	Coolant Mechanism	Recommended Test Duration
Flow Cryostat	No	≈ 2.5 (without sample)	4-point DC meas.	Conduction	He can limit
		≈ 4 (with sample)	Resn./TL meas.		
Bath Cryostat	No	≈ 1.3	Resn./TL meas.	Contact gas	≈ 8 h
VTI	Yes	≈ 1.55	ESR	Contact gas	≈ 12 to 14 h
Dilution Refrigerator	Yes	≈ 0.020 at Mixing Chamber	ESR	Conduction	Unlimited

The flow cryostat performance is based on the flowing of the liquid helium in the provided chamber inside the setup. A bypass pump evacuates the chamber constantly to reduce the temperature of the liquid helium to the values lower than 4.2 K. The cooled chamber conductively cools the samples down which are mounted on its beneath in a vacuum shell. The low temperature is stable and usable as long as the liquid helium is continuously provided to it. The flow cryostat is very quick, about 20 minutes, to reach to its lowest temperature from the room temperature. The cooling down process is already explained in some manuals existing in the lab. Here it is worth to add a recommendation as the following to get a stable low temperature: on starting the cooling down process, the valve on the He transport tube (tube valve) is to open 3 complete rounds ($3 \times 360^\circ$). As soon as reaching the temperatures about 20 K during the cooling down, the tube valve is to get closed to have just 1 round open. When the temperature is low around 8 K, it is recommended to close the tube valve to keep maximum one fourth of the round open to have a stable temperature around 4 or 5 K. Keeping the valve more open leads to temperature fluctuations of ± 1 K.

The bath cryostat, as the its name implies, contains a reservoir which is isolated from the laboratory ambient via several isolating and liquid nitrogen shells. The liquid He bath embeds the sample chamber (cylinder) in which the sample is placed and gets cooled down by contacting a cold He gas around it. After pumping the isolation shells out and sealing them, the liquid nitrogen is to get transported to its corresponding shell. The sample chamber must get evacuated also and its pressure is to get adjusted by He gas. The liquid nitrogen cools the sample chamber down to 160 K after couple of hours and at this point the liquid helium could get transported and cooling down to liquid helium temperatures continues.

The VTI sample cooling principle is similar to the bath cryostat; pumping out the high energy He atoms away. However, in a bath cryostat the He bath is directly connected to the pump and in a VTI only the sample cylinder to which a small amount of He is guided through a valve from the reservoir. The main difference is, however, that the VTI is equipped with a superconducting magnet which makes e.g. the ESR experiments possible. According to the gained experience, it is recommended to wait for about one hour after filling the VTI liquid helium reservoir to 100% before starting the experiment. The system has a slight instability and noise at around 1.8 K. By adjusting the bypass needle valve to the minimum (but stable) amount a quite clean experiment at all the temperatures in the range of from 1.6 to 10 K is performable. It is recommended, to finish one complete set of the measurements by one single run. To reach this goal, couple of very efficient and LabVIEW[®] programs (VIs) were developed and used. The algorithm of the LabVIEW[®] VIs were so designed that a sweep of magnetic field for an ESR measurement was done only at the required magnetic field

ranges. In addition, the selected field range could get adjusted so that the resolution of the measurement for the ESR signal range was very fine and at the off-signal range rough and big. So, the ESR experiments were done with much higher quality (because of 0.1 mT resolution at the ESR signal range) and a factor of almost eight faster than the former measurements with the old LabVIEW® VIs.

The dilution refrigerating mechanism for cooling down is based on the endothermic reaction of ^3He diffusion from the concentrated phase of $^3\text{He}/^4\text{He}$ (concentrated of ^3He) to the dilute phase. The dilution refrigerator is utilized for the studies at mK temperature range. Its preparation and cooling down is a two-day process but as long as liquid He bath gets filled, it works with a very satisfactory reproducibility and precision. It is equipped with a superconducting magnet. There is no contact gas involved in the cooling the sample down.

4.5. Transmission Lines Measurements

Transmission lines (TLs) with various designs were fabricated with two purposes: 1) Characterization of the coplanar structures like material dependent MW loss or the metallization thickness effect on the loss, etc. 2) Wide (full) band ESR measurements since resonators range of functionality is limited to discrete resonance frequencies [35]. Measuring the TLs were very helpful in characterization of the other parameters of the whole circuit and not only the intrinsic properties of the coplanar structure. For example, the detaching of the silver paint from the metallization surface was noted during the TL measurements for the first time (Figure 4.4 (a)).

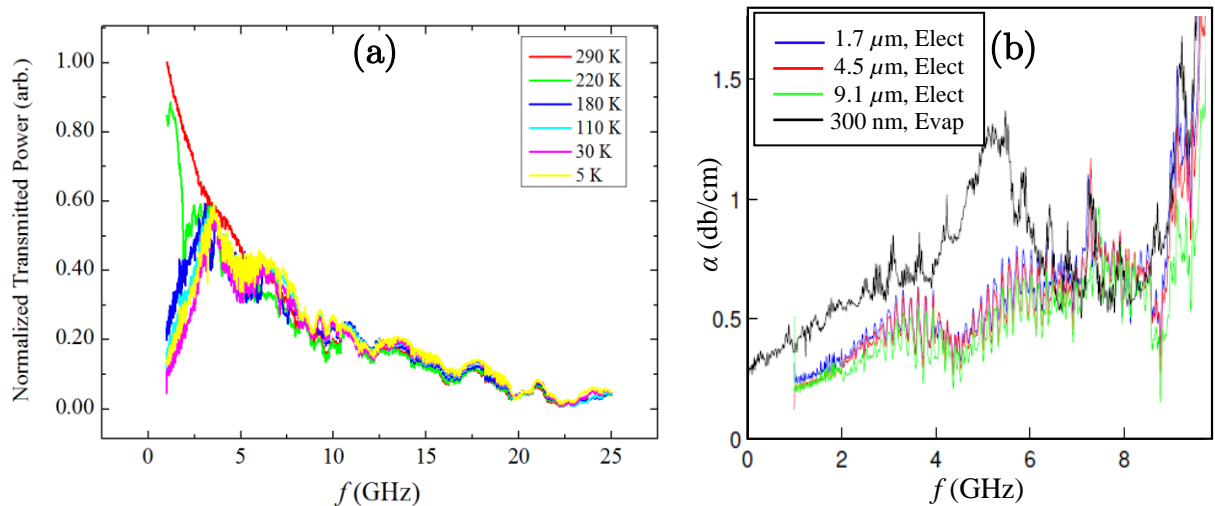


FIG. 4.4. (a) shows the discontinuing of the signal transmission on lowering the temperature. (b) The loss at 5 K in the thick electroplated Cu TLs (thickness in the legend) is significantly lower than the thin evaporated TL. The picture is taken from the final presentation of the corresponding Blockpraktikum. "Elect" and "Evap" stand for electroplating and evaporation.

The first series of the measured TLs (the structures of number 16 in Table 4.2) were thermally evaporated with 300 nm film thickness. The measurement data were recorded at low temperatures of 5 K. DC measurement of the line was done too to study the conformity of the provided theories and the experimentally obtained data.

The calibration measurements at the desired temperatures were done by connecting (shortcutting) the coaxial cables of the measurement line by a connector of the proper type. Then the obtained data (Transmission vs. Frequency) from the measurements of the TL was modified by the calibration data to observe the pure response of the TL.

The second series of the TLs (the same structures of the first series) were electroplated thick structures with the thickness of up to 10 μm . The lowest temperature of these measurements was 5 K and the experiment was performed by the Flow cryostat. As shown in Figure 4.4 (b) the loss is reduced which should be attributed to the higher thicknesses and lower resistance of the electroplated films.

The structure number 17 which was a long transmission line compared to the structures of 16, was another TL structure which was fabricated and measured. This TL has the advantage of providing a relatively large area of the parallel direct lines which provide correspondingly a large area far from the curves of the meandered structure and this makes this TL suitable for the physical measurements in which the MW fields strictly in one direction are required.

It should be noted that the first and second series TL measurements were performed as “Blockpraktikums”.

4.6. Resonator Measurements

The first series of the fabricated and measured resonators were the structures of number 1 and 2 in Table 4.2. These resonators were fabricated by electroplating and very rarely by evaporation process and the aim of the experiments was just to gain the first view and the idea of how the performance of the resonators are and just to check if such CPW structures can work if they are made of normal metals (and not superconductors). These resonators were designed to achieve the fundamental frequencies of 1.5 and 2.5 GHz respectively. Each structure had, as already brought in Table 4.2, the center conductor with two various widths of 20 and 60 μm and the coupling gap sizes of 3, 10 and 20 μm to find the initial optimal geometrical parameters.

The resonators with the structure 1 never showed the fundamental of 1.5 GHz or more exact to say, they never showed the first mode. There were huge parasitic modes (box modes) after 12 GHz in these resonators. One of the probable reason for this may be

the very near round parts of the center conductor line to the walls of the brass box. In these areas, the ground plane is very small which could perturb the functionality of the resonator. Figure 4.5 (a) shows examples of the recorded spectra of the mentioned resonators.

It is necessary to mention two points here:

The first is the procedure of the resonator measuring in the characterization (and not ESR) tests. It started with a wide range measurement and recording the spectrum from about 1 to 26 GHz and in some rare cases to 30 GHz. This was always a rough measurement with the resolution of 5 to 10 MHz. After observing the peaks (modes, resonances), as shown as a sample in Figure 4.5 (a), in the spectrum and making sure that they are not noises or box modes, the resonances were measured precisely with a fine resolution of 0.5 to 1 MHz and the quality factor (Q) was calculated for each mode separately as described and illustrated in section 2.2 and Figure 2.2. One example of a measured mode with a better resolution is shown in Figure 4.5 (b) and (c). One effective way to recognize a box mode and distinguish it of a resonator mode is measuring the suspected peak at very fine resolutions. A box mode shows always a very noisy spectrum at fine resolutions. Furthermore, it has been experienced that the Q of a box mode usually does not significantly exceed 30.

The second is that the very first working resonator was obtained after many failed tries including the both of fabrication and measurement of the resonators. Of these problems, film instability and peeling off, rough surface roughness of the electroplated films, rough surface roughness after chemical etching, undesired standing waves in the coaxial cables because of bad connector joint and silver paint detach are the ones worth to mention. After removing the problems, very reliable, reproducible and stable measurements could get performed and the data which will be (and have been) presented in this work are obtained of the stabilized and optimized measurements.

In comparison with the resonators of structure 1, the resonators with structure 2, showed the modes more ordered and closer to expectation. This may be due to the absence of the sharp curvatures existing in type 1 which leads to the very small ground planes in the corresponding area as mentioned above. For this reason, all the further designed resonators were similar to structure 2 as seen in Table 4.2.

The first significant observation in the primary obtained results was the higher quality factors of the resonators with 60 μm center conductor in comparison with the ones with 20 μm ; independent of the structure 1 or 2. This difference was even up to 100% so that $Q_{20\ \mu\text{m}} \approx 120$ and $Q_{60\ \mu\text{m}} \approx 240$ (at 5 K). This will be elaborated later with more details.

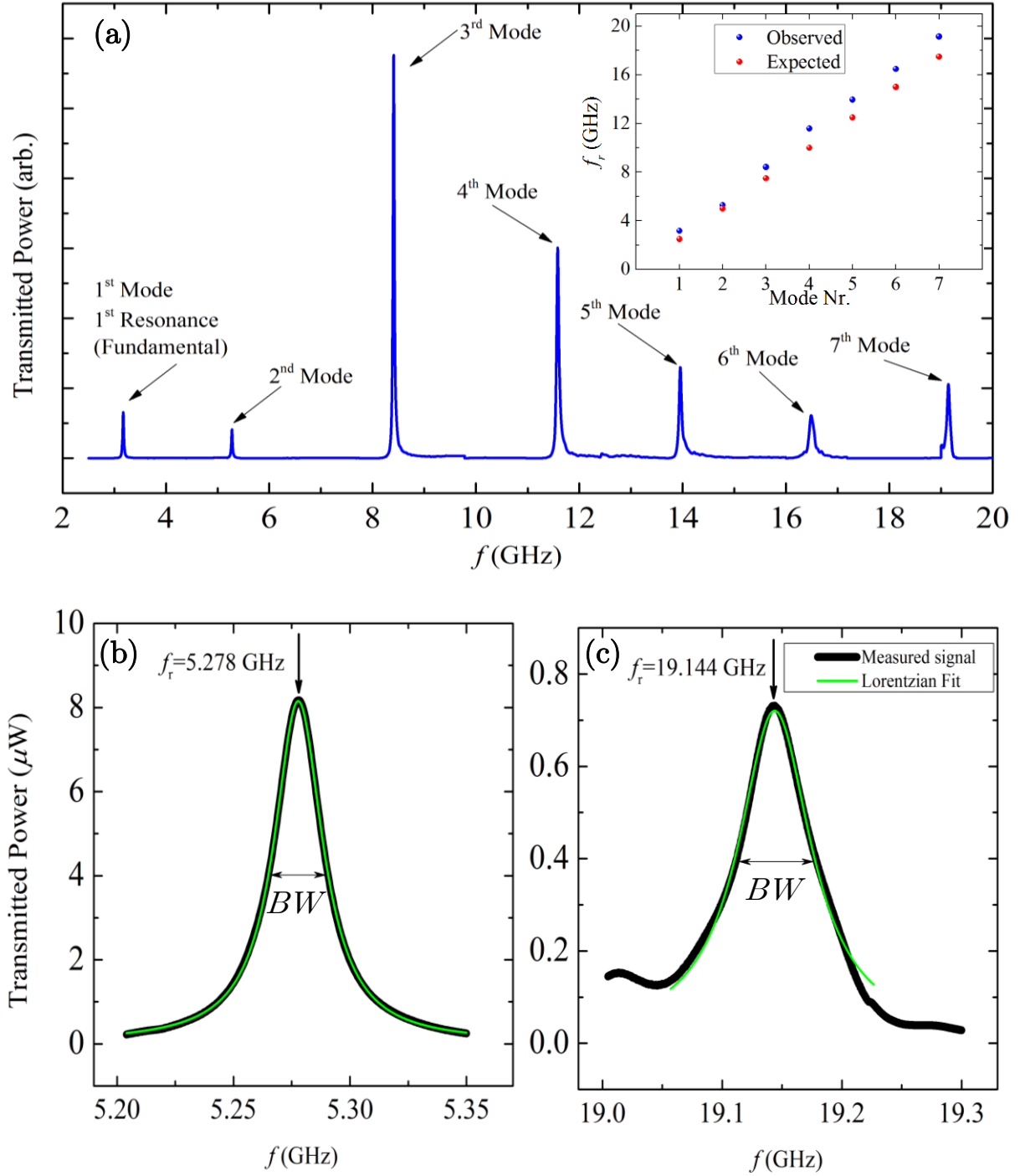


FIG. 4.5. (a) A typical broad band spectrum of the CPW resonators in this work. Inset shows the position of the observed modes and the expected ones. The inset shows the violated accordance between the expected and observed resonance frequencies for each mode. (b) and (c) are the two instances for the obtained resonances and their Lorentzian fits. The shown spectra belong to one of the fabricated resonators with structure 2 in Table 4.2 with $w = 60 \mu\text{m}$ and $G = 20 \mu\text{m}$.

The other notable point, as illustrated in the inset of Figure 4.5 (a), is the positions of the resonances on the frequency axis which are expected to be equally distanced since

the n^{th} mode is supposed to be observed at $n \times$ fundamental. For example, if the fundamental of the resonator is 2.5 GHz the second and third modes are to be at 5 and 7.5 GHz and so on. This is, however, violated for all the measured resonators, one example of which is shown in Figure 4.5 (a) and its inset. The reason is probably stemming from the meandered structure of the resonators which causes a frequency dependent effective permittivity for the chip. This was observed by simulations also. Experimental observations proved the idea either. A straight-line resonator (structure 15 in Table 4.2) was designed and fabricated and subsequently measured. The second mode was observed almost right at the twice (≈ 1.99 times) of the fundamental of the resonator which is shown in Figure 4.6.

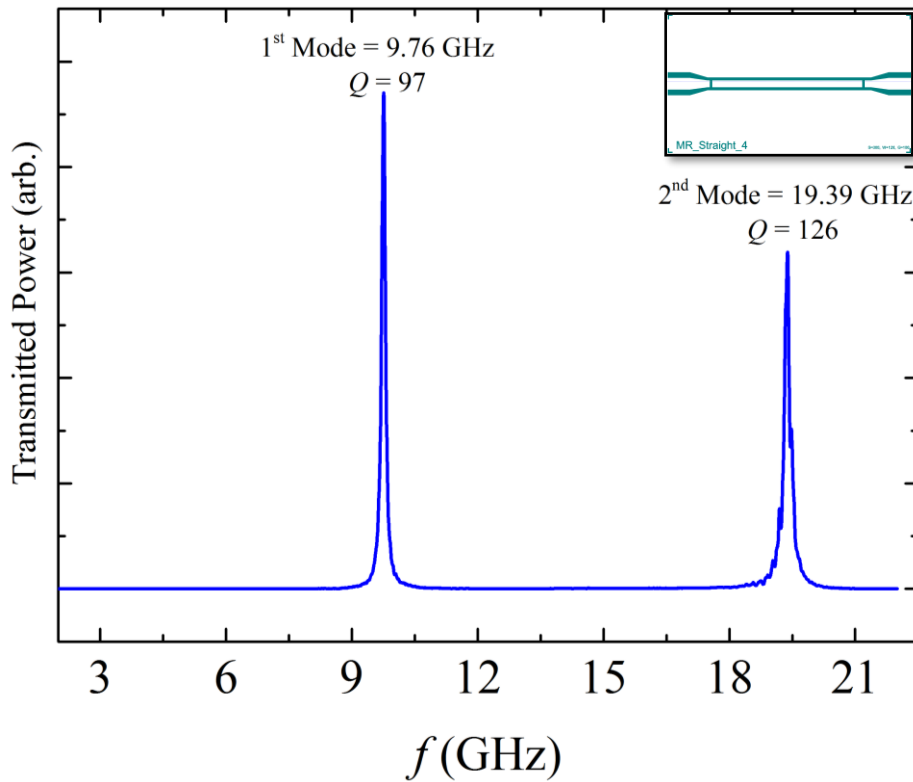


FIG. 4.6. The conformance of the mode coefficient and resonance frequency. The first mode appears at 9.76 GHz and the second at 19.39 which makes a ratio of 1.99. The inset shows the straight-line structure of the measured resonator.

It must be pointed out here that, during the time of the fabrication and measurement of the resonators, to make sure that the observed data and anomalies are pure functional responses of the resonators and not some artefacts of the fabrication or measurement, the fabrication processes and steps (like as mentioned earlier substrate cleaning, film growth and other related actions) were improved and optimized continuously. It definitely helped achieve better functionalities like lower noise etc., however, the main anomaly features (like the inequidistanced resonances) stayed all the time almost the same. At some cases, one resonator was measured several times at

different setups like flow cryostat and the VTI to check any ambient effect on its performance. The performance and obtained results were quite similar, although, the calculated quality factor was at some cases slightly different which was maximum 5%. After establishing robust and reproducible production and measurement procedures, the further structures, with the aim of gaining higher quality factors and having more desired geometries, were designed, fabricated and tested which are represented at the following.

4.6.1. High Q Achievement

As noted already, the resonators with the wider center conductors showed higher quality factors. It is due to the lower resistance which the flowing alternating current experiences in the center conductor (also shown in section 2.4 Figure 2.6). Center conductor geometry has the strongest effect on the quality factor of the resonators since its small width dominates the loss behavior of the all other loss-making factors. Therefore, as the main action to improve the quality factor, resonators with the center conductor width from 20 μm up to 100 μm were designed; structures 3 and 4 in Table 4.2. Each structure was designed with coupling gaps of 10, 20, 30, 40 and 50 μm as noted in Table 4.2. The distance between the center conductor and the ground planes were so chosen that the characteristic impedance of the line equals to 50 Ω . Table 4.4 briefs the geometrical parameters of the resonators under discussion here.

Table 4.4. A brief of the geometrical parameters values of the structures 3 and 4 of Table 4.2.

w (μm)	s (μm)	G (μm)	D (μm)	$\frac{D}{w+2s}$	Chip Size (mm^2)
20	8	10:50	264	≈ 7.33	3.8 \times 6.8
40	16	10:50	226	≈ 3.14	3.8 \times 6.8
60	24	10:50	190	≈ 1.76	3.8 \times 6.8
80	32	10:50	240	≈ 1.67	6 \times 10.5
100	40	10:50	300	≈ 1.67	6 \times 10.5

Beside optimizing the geometrical parameters, another successful action which was taken to account to achieve high quality factor values was utilizing sputtered films which will be mentioned and analyzed later on its turn.

The measurements were all carried out at flow cryostat down to 5 K. The temperature dependence of Q was also monitored by performing the measurements at different temperatures on heating up from the base temperature. Two Cernox[®] thin film resistance cryogenic temperature sensors of type AA were mounted above and below the resonator showing the temperature during the measurements. So one can make sure that the temperature of the resonator is in the desired range. The MW signal was

generated by the power source Agilent® E8257D and measured at the other side by the power meter Agilent® E4418B. The temperature controlling and measurement was performed by LakeShore® 340.

The $\frac{D}{w+2s}$ ratio is bigger than 1 for all the sets which is enough to neglect the ground plane width effect on the characteristic impedance [67].

In the following the remarkable points and observations in the obtained data will be presented and discussed.

The resonance frequency of a CPW resonator depends on ϵ_{eff} and on the geometrical factors. Of course, it is explained in section 2 that ϵ_{eff} itself is impressible by geometrical factors. In the geometrical parameters, the simplest way to manipulate the resonance frequencies is the length of the center conductor, so that in many references the relationship $L = n\frac{\lambda}{2}$, (where L is the center conductor length, n is the resonance mode number ($n = 1, 2, 3, \dots$) and λ is the wavelength of the fundamental frequency) is introduced as a standard formula for estimating resonance wavelengths and subsequently resonance frequencies. Although L in all the measured resonators in this part was identical and equal to 25.5 mm (expecting a fundamental of 2.5 GHz), the measured first modes were various from one series to the other. The observed fundamentals slightly shift up by increasing $w + 2s$. The resonators of $w = 20 \mu\text{m}$ and $s = 8 \mu\text{m}$ showed the first mode at ≈ 2.60 GHz whereas the ones of $w = 60 \mu\text{m}$ and $s = 24 \mu\text{m}$ showed the fundamental at ≈ 3.15 GHz. This is due to the decrease of ϵ_{eff} by increasing $w + 2s$ as is already mentioned in section 2.4 [64] [67] [72]. Then, one expects the fundamentals for both $w = 80$ and $100 \mu\text{m}$ to happen at higher than 3.15 GHz, however, they happened at around 3 GHz. The thickness in these cases is about 100 nm lower (compared to those with $w = 20$ to $60 \mu\text{m}$) which causes ϵ_{eff} to increase and thus the fundamental mode is below 3.15 GHz (chapter 2, section 2.6).

A typical temperature dependence of the resonance frequency is plotted in Figure 4.7. The rightward shift of the resonance frequency on cooling has several reasons from which the following three reasons are the notable ones:

- 1) thermal contraction,
- 2) ϵ_{eff} of the chip decreases in absolute value as the conductivity of the metallic conductor increases (section 2.8, Figure 2.5), and,
- 3) the relative permittivity of sapphire substrate decreases with lowering the temperature [57].

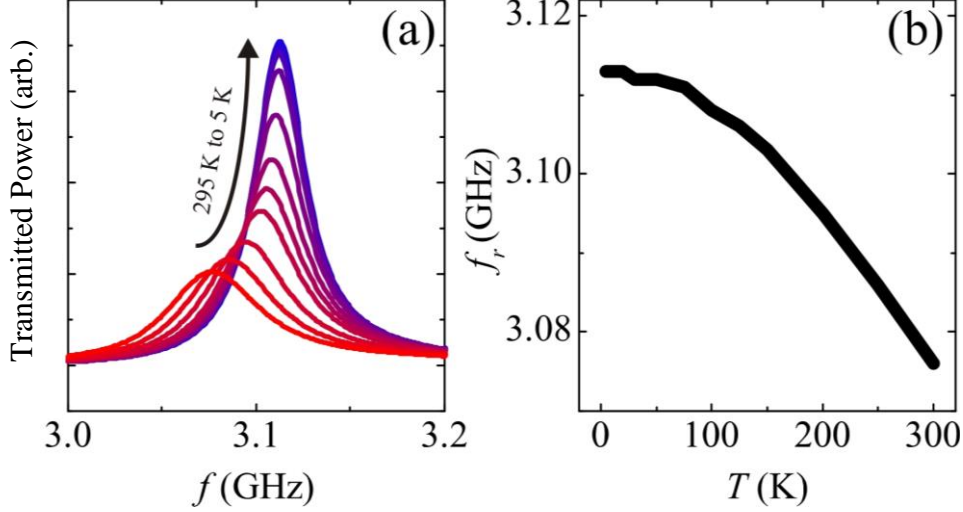


FIG. 4.7. (a) The shift of the resonance peaks by changing the temperature. The higher intensity of the peaks at lower temperature is due to the lower loss because of the lower resistance at lower temperatures. (b) the resonance frequency change with the temperature.

The most important and interesting quantity in the resonators' performance is the quality factor, Q . The Q response of the measured resonators of this section are presented and discussed below.

The introduced Q values are loaded quality factors Q_L (see formula 2.21 in section 2.2) which is approximately equal the internal quality factors of our resonators. The equivalence of Q_L and Q_{int} was experimentally proven by measuring a resonator by different cryostats which have (very) different cabling and temperature distribution in the cables when they are cooled down. In addition, the calculations also show that the Q_{ext} is much higher than the measured Q_L . The calculation is as the following: Considering the coupling capacitance of the resonators which in the extremal case amounts to ≈ 10 fF ($G = 10 \mu\text{m}$ for $w = 100 \mu\text{m}$) [174], one expects the Q_{ext} well above 20000 for all studied resonances, which is much higher than the measured Q_L , and therefore the effect of Q_{ext} (with respect to Q_{int}) in obtaining the Q_L is negligible.

The enhanced Q value at lower temperatures is mainly due to the lower loss which is in turn a result of the higher conductivity of the metal. In Figure 4.7 (a) the resonance peaks are shown to get narrower and higher at lower temperatures. As one can see in Figure 4.8 (a), at around 77 K (liquid nitrogen) the maximum Q (second mode in this case) is more than 2.5 times the room temperature value, and it can reach almost a factor of four upon further cooling to 5 K. This increase of the quality factor comes to a halt around 20 K because the residual-resistance regime is reached. In the residual-resistance regime (observable in Figure 4.1 also), the resistivity of the copper film is governed by defects and does not decrease on further lowering the temperature [109]. In Figures 4.8 (a) and (b) the Q development on cooling down for the first three modes

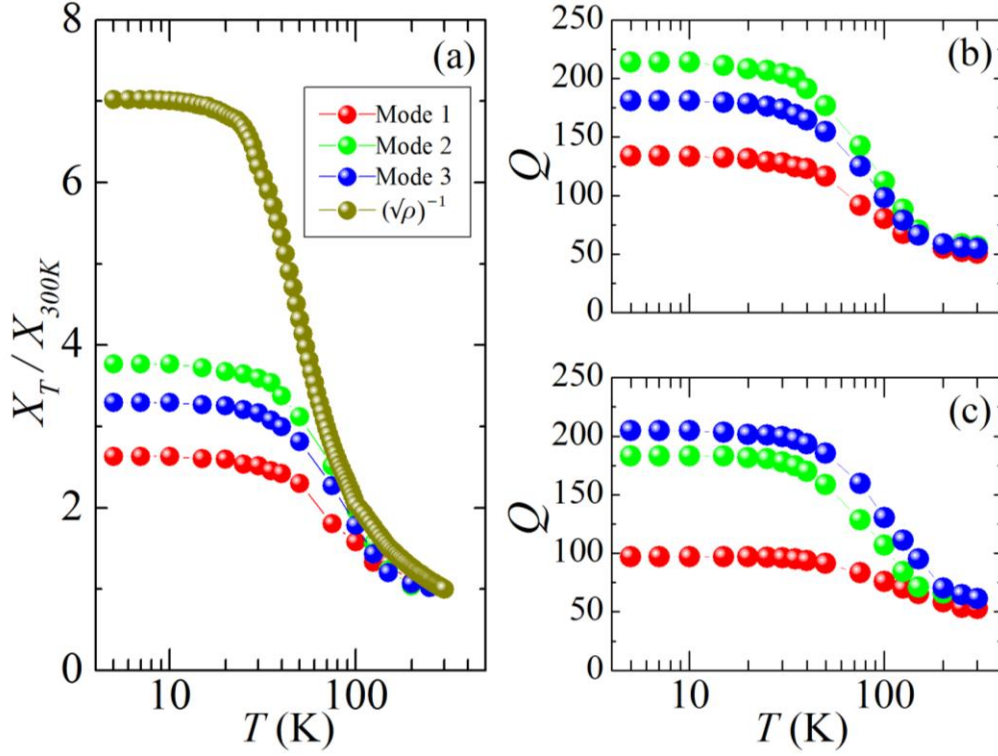


FIG. 4.8. Temperature dependence of the quality factor for different resonator modes and structures. (a) shows the relative change of Q and $(\sqrt{\rho})^{-1}$ (ρ is the DC resistivity; for explanation of $(\sqrt{\rho})^{-1}$ see the text below) for the electroplated structure with $w = 40 \mu\text{m}$ and $G = 40 \mu\text{m}$. X is the both of Q and $(\sqrt{\rho})^{-1}$ depending on the intended curve. (b) and (c) contain the temperature behavior of the first three modes of the electroplated resonator of (a) and the resonator with $w = 60 \mu\text{m}$ and $G = 40 \mu\text{m}$ respectively. The residual-resistance regime in all the three figures is observable as the flat parts of the curves for the temperatures of under 20 K.

of two measured resonators are presented. Although the mentioned 2.5 and 4 times improvement of Q is not observed for all the modes, all the measured resonances showed a trend of improving in Q by lowering the temperature.

The temperature dependence of Q is showing a divergence for different modes by decreasing the temperature as shown in Figure 4.8 (b) and (c) (the data are, however, collected on heating up). The increase of the quality factor on decreasing the temperature is intuitively expectable since the quality factor and conductivity/attenuation have a direct/indirect relationship which is shown quantitatively also below [175] [176]. However, the different orders of magnitudes in improvement of the Q values for different modes, shows the existence of some frequency dependent parameters other than the conductivity or loss which are playing a very important and even dominating role in the final Q value. This matter is clearly seen in Figure 4.8 (a) also by comparing the $(\sqrt{\rho})^{-1}$ and Q trend with temperature. To make this point clearer the following

discussion is offered. The attenuation of a coplanar waveguide, α , is estimated as below [176]:

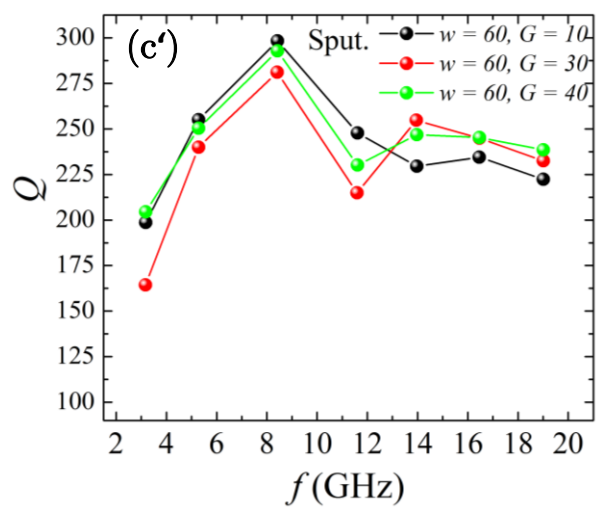
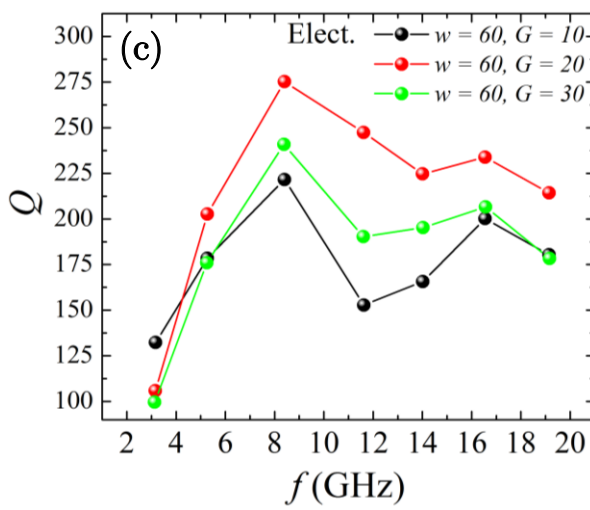
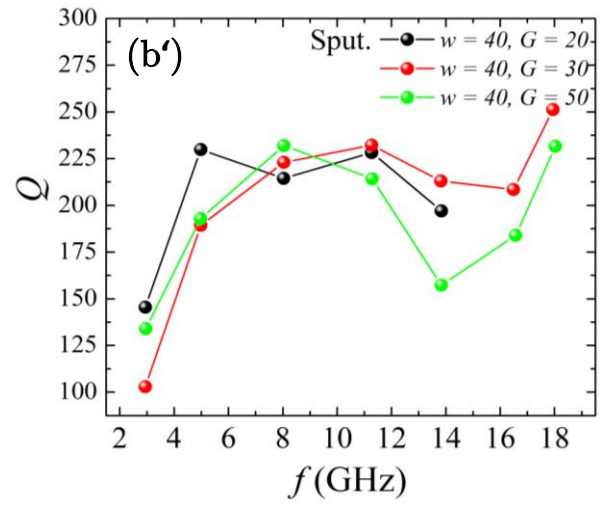
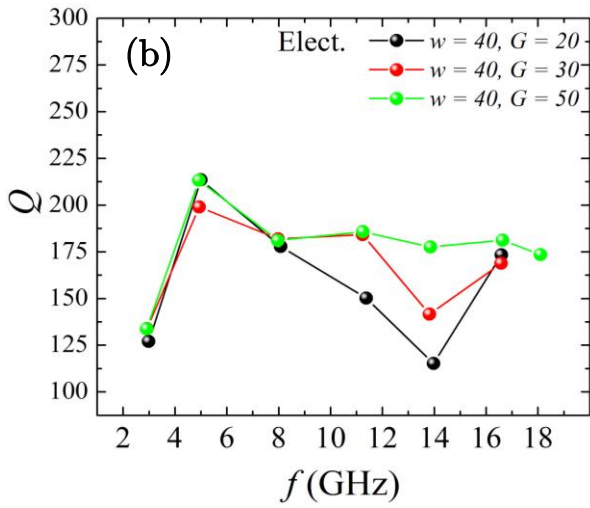
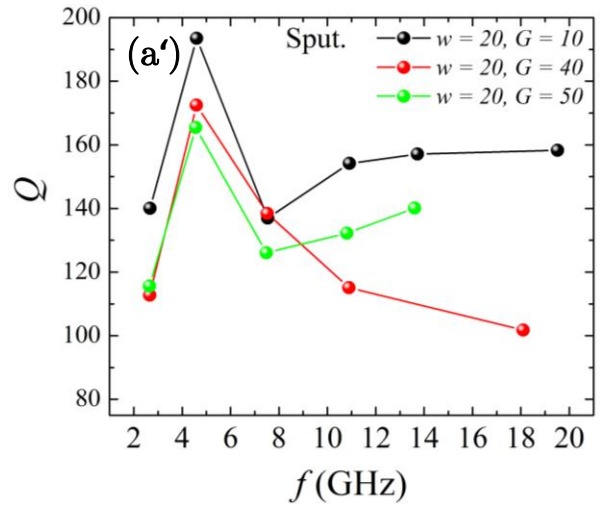
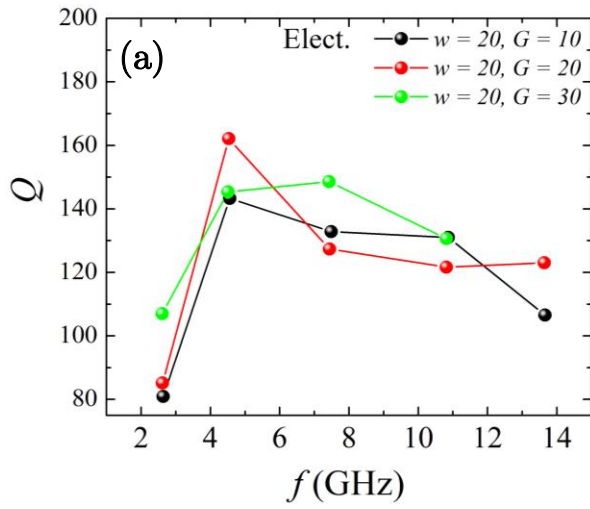
$$\alpha = \alpha_c + \alpha_d + \alpha_i \quad (4.1)$$

$$\alpha_c = GD R_s \sqrt{\epsilon_{r,eff}} \quad (4.2)$$

$$R_s = (\mu_0 \pi f \rho)^{1/2} \quad (4.3)$$

where α is the total attenuation of a CPW, α_c is the metallic resistive losses, α_d represents dielectric losses and α_i is the radiation losses. GD is a geometrical design constant and ρ is the DC resistivity. Since the attenuation in a metallic CPW is highly dominated by metallic resistive losses, $\alpha \approx \alpha_c$. Regarding relationship (4.3), (2.13) and (2.15)/(2.16) (chapter 2, section 2.2), one concludes that $Q \propto (\sqrt{\rho})^{-1}$ since $R \propto \rho$. This means, at a given frequency, if $(\sqrt{\rho})^{-1}$ becomes twice bigger, Q must also increase twice, while as shown in Figure 4.8 (a), $(\sqrt{\rho})^{-1}$ is increased 7 times from room temperature to 5 K and the Q value has increased at most only 4 times.

(4.13) explicitly expresses that microwave losses in metals grow with frequency, and hence, at higher frequencies a lower Q value is expected. According to the skin effect phenomenon, the higher the frequency, the thinner the skin depth and consequently the higher the loss. Hence, one expects a higher quality factor for lower frequencies. Figure 4.9 is showing Q vs. frequency (modes) for the measured resonators at 5 K (The plots containing the full data are shown in Appendix II). The higher Q values for the 2nd or 3rd mode (Table 4.5), depending on the center conductor width, is significant. In Figure 4.9 the data of three resonators (in each series) which showed the highest quality factors are shown. It was just mentioned above that, one expects a higher quality factor for lower frequencies, however, here, for example for the resonators of $w = 60 \mu\text{m}$, independent of the G values and fabrication method, the highest Q values (in the first three modes) belong to the 3rd mode (≈ 8.4 GHz); as shown in Figure 4.9 (c) and (c'). Such behavior is found in all the five sets of resonators. In the recorded data either mode 2 (≈ 5 GHz) for $w \leq 40 \mu\text{m}$ or mode 3 (≈ 8 GHz) for $w \geq 60 \mu\text{m}$, have the highest Q values in the first three modes. Since for the narrower center conductors the highest Q happens at second modes and for wider ones at third mode, one may conclude that one of the line parameters whose value is geometrical dependent as well as frequency dependent is playing a more dominant role as the skin effect and electrical loss. Such a parameter could be the characteristic impedance. Similar observations have been reported previously on aluminum CPW resonators of much larger dimensions and at room temperature [177].



Continue on the next page

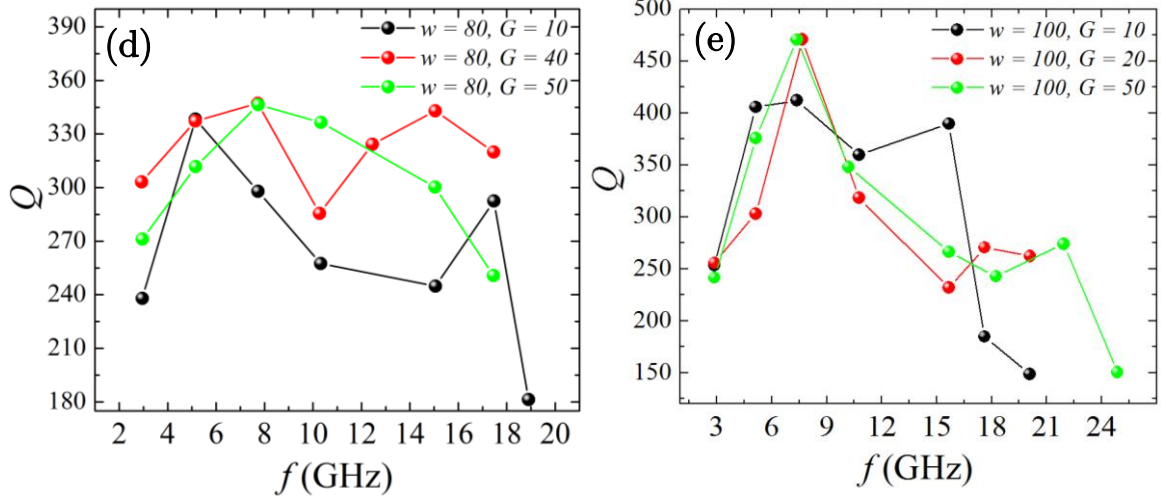


FIG. 4.9. The diagrams with three highest quality factors for each design. “Elect.” and “Sput.” stand for electroplating and sputtering respectively. (a) and (a’) are the data of $w = 20 \mu\text{m}$, (b) and (b’) are the data of $w = 40 \mu\text{m}$, (c) and (c’) are the data of $w = 60 \mu\text{m}$, (d) is the data of $w = 80 \mu\text{m}$ and (e) is the data of $w = 100 \mu\text{m}$. No resonator was fabricated by sputtering for the designs of $w = 80 \mu\text{m}$ and $w = 100 \mu\text{m}$.

Table 4.5 contains the highest Q values for each series of the measured resonators. The table with the fully listed obtained data can be found in Appendix II.

Table 4.5. The higher Q values for the second and third modes of the resonators. For the full data list refer to Appendix II.

w (μm)	Corresponding Mode, G and Q
20	Electroplated: 2, $20 \mu\text{m}$, 162 Sputtered: 2, $10 \mu\text{m}$, 194
40	Electroplated: 2, $20 \mu\text{m}$ and $50 \mu\text{m}$, 213 Sputtered: 2, $20 \mu\text{m}$, 230
60	Electroplated: 3, $20 \mu\text{m}$, 275 Sputtered: 3, $10 \mu\text{m}$, 298
80	Electroplated: 3, $40 \mu\text{m}$ and $50 \mu\text{m}$, 347
100	Electroplated: 3, $20 \mu\text{m}$ and $50 \mu\text{m}$, 471

Figure 4.10 displays the quality factor values for 2nd and 3rd modes for all the resonators studied in this part. The values of between ≈ 300 ($w = 60 \mu\text{m}$ and $G = 10$ and $30 \mu\text{m}$) and 470 ($w = 100 \mu\text{m}$ and $G = 20$ and $40 \mu\text{m}$) are, to best of our knowledge, the highest observed Q values for a metallic CPW resonator whose center conductor widths are narrow in the range of $60 - 100 \mu\text{m}$. At room temperature $Q = 120$ was reached for a resonator with $w = 100 \mu\text{m}$ and $G = 20$ and $50 \mu\text{m}$.

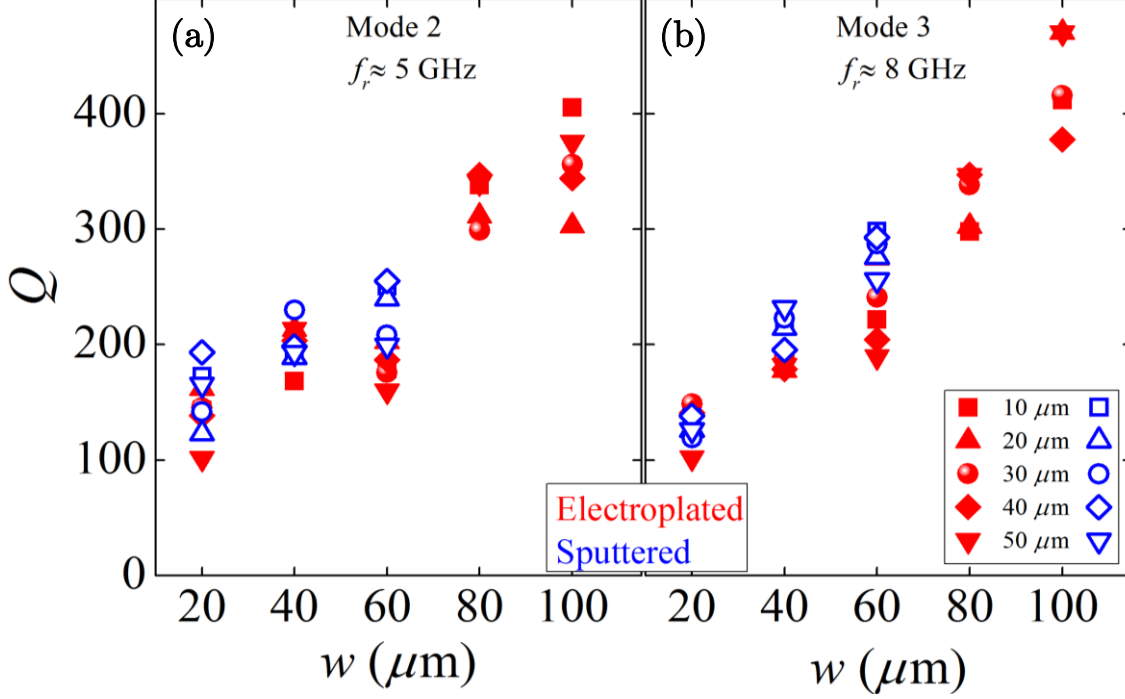


FIG. 4.10. The enhancement of Q by widening the center conductor. (a) shows mode 2, and (b) mode 3. The data belong to $T = 5$ K. The different symbols refer to different G values for the both of electroplated and sputtered resonators.

As far as the geometrical design parameters of the resonator are concerned, the center conductor width clearly is the most relevant in obtaining high Q values. A pronounced dependence of Q on G or $\frac{D}{w + 2s}$ was not observed.

One significant point in the obtained results of the Q measurements is the higher Q of the sputtered resonators compared to the electroplated resonators. This point becomes more interesting when one compares the electric conductivity (DC) of the sputtered and the electroplated films and their residual resistance ratios (RRR). Despite the higher (DC) resistivity and lower RRR of the sputtered films, $\rho_{5K} = 0.0510 \mu\Omega\cdot\text{cm}$ and $\text{RRR} \approx 29$, they have higher Q values. The data for the electroplated copper films are $\rho_{5K} = 0.0415 \mu\Omega\cdot\text{cm}$ and $\text{RRR} \approx 50$. The higher Q values of the sputtered resonators may can be explained by the 13 nm surface roughness of the sputtered films compared to the 60 nm surface roughness of the electroplated films as measured by atomic force microscopy (AFM) shown in Figure 4.11. The surface roughness can play such a decisive role since the roughness of the electroplated films is around 30% of their skin depth ($\delta_{5K,2.5 \text{ GHz}} \approx 227 \text{ nm}$), whereas, for the sputtered films it is about 6.5% ($\delta_{5K,2.5 \text{ GHz}} \approx 205 \text{ nm}$).

Another reason for the better Q values of the sputtered resonators could be realized by SEM inspection of the line edge. The sharper and straighter line edges in the sputtered resonators are displayed in the SEM images of Figure 4.12.

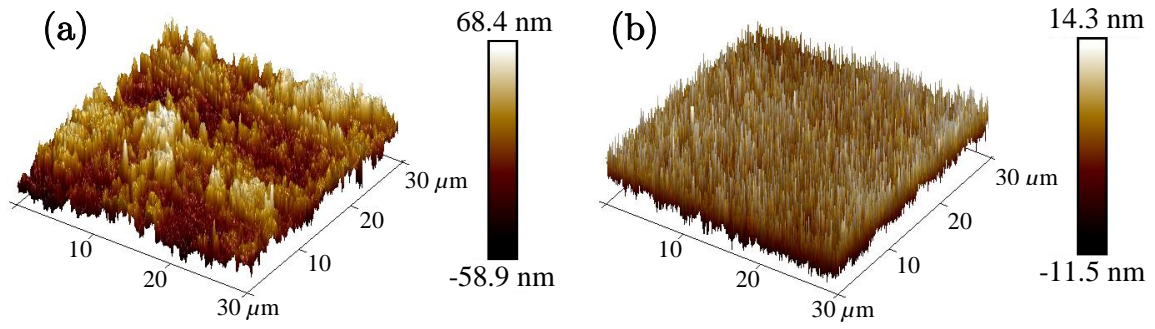


FIG. 4.11. (a) The AFM picture of an electroplated film utilized in electroplated resonators, and, (b) the one for a sputtered.

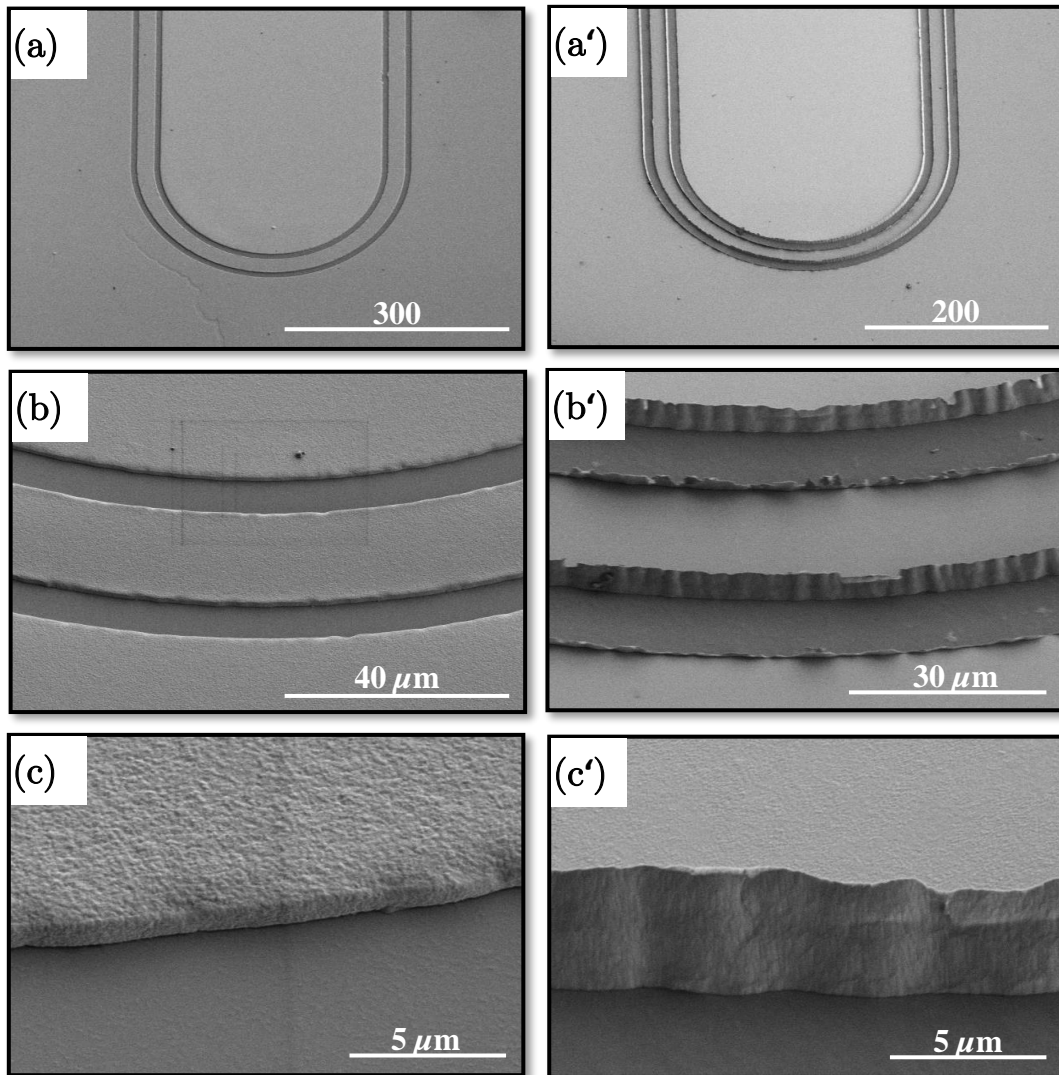


FIG. 4.12. The SEM images of a typical CPW resonator in this work. (a), (b) and (c) are taken of an electroplated resonator and (a'), (b') and (c') of a sputtered one. The magnifications in (a)/(a'), (b)/(b') and (c)/(c') are 180/200, 1300/1800 and 8000/8000 respectively. The meandered line structure of the center conductor is observable in (a) and (a'). The redeposited material along the center conductor and ground planes edges are obvious in (b'). The images are taken at different angles relative to the surface of the resonator.

The better edge definition of the sputtered structures can reduce field leakage and leading to a higher quality factor [178]. However, the redeposited thin raised walls (nonremovable by ultrasonic vibration) during the ion milling process on the edges of the sputtered lines [179] makes it difficult to discuss the edge definition role in the achieved higher Q .

To perform an ESR experiment, the presence of magnetic field is an inherent part of the measurement system, of course not for the zero-field splitting studies. Therefore, the functionality of the produced CPWs is to be tested at the presence of an external magnetic field and without any perturbation by any sample. The influence of an external static magnetic field on the resonators' function at 5 K is given in Figure 4.13. The magnetic field was applied in-plane to the resonator (parallel to the meander lines (the inset in Figure 4.13)). Even at fields as high as 7 T, the reduction in Q is less than 3.5% for all the modes, in contrast to the massive suppression of Q in magnetic fields found in superconducting resonators (section 4.7 and Appendix I) [47] [48] [180] [181].

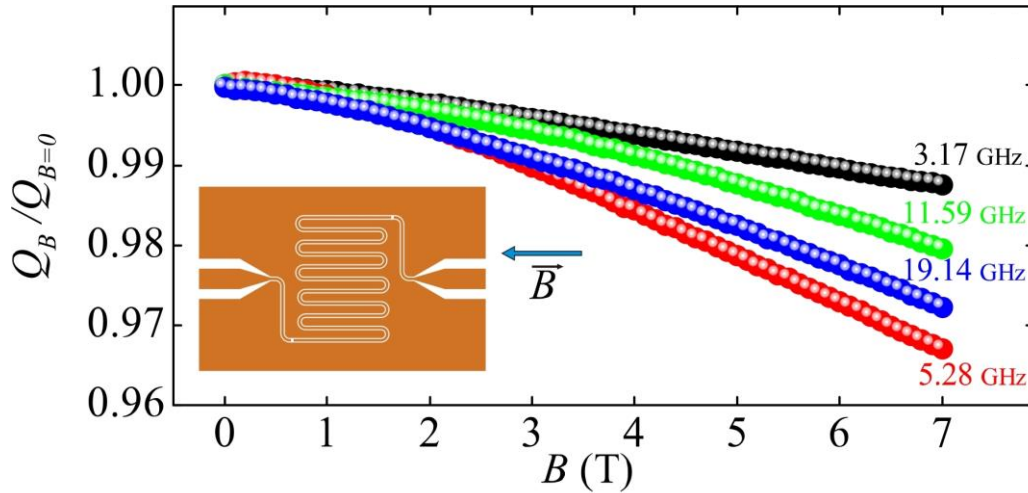


FIG. 4.13. Normalized Q values decay at external magnetic field for various frequencies. Q_B is the measured quality factor at each non-zero magnetic field (0 to 7 T) and $Q_{B=0}$ is the quality factor at zero magnetic field. The data are taken at $T = 5$ K and belong to the resonator with $w = 60$ and $G = 20 \mu\text{m}$.

The loss of quality factor in magnetic field for these resonators can be explained by the magnetoresistance of copper on increasing the field [182].

At the end of this section it should be noted that beside widening the center conductor to gain high quality factors, another accomplishing activity was designing the structures with a lower number of the curves in the meander line. These structures which are listed in Table 4.2, design number 5, had also different coupling gap sizes. The obtained results, however, didn't show a significant difference or improvement in Q value in comparison with the shown data above.

4.6.2. Low Fundamental Achievement

Considering only the geometrical parameters to change (and not the elemental materials like substrate etc.), the very first idea to achieve lower resonance frequencies is to elongate the center conductor. This, however, causes higher loss. To compensate the higher loss due to the longer center conductor, its width must get designed wider, but, this will lead to rightward shift of the resonance frequencies as discussed in the previous section. This means, if the only aim is achieving lower frequencies, and a high quality factor is not the first priority, the desired resonator must have a center conductor as narrow as, and, as long as possible.

The lowest observed frequency as the fundamental of the designed resonators of the previous section was ≈ 2.6 GHz for the resonators with $20 \mu\text{m}$ center conductor width and the length of $L = 25.5$ mm. With the aim of obtaining a fundamental lower than 2 GHz, the structure number 6 in Table 4.2 was designed and the resonators were accordingly fabricated. The center conductor of $20 \mu\text{m}$ and $L = 51$ mm could lower the first mode of the resonator to happen at 1.57 GHz. The obtained quality factors at different modes of this resonator are listed in Table 4.6. This, compared to the already observed Q values of ≈ 470 , does not look a high value, but it should be noted that the goal of designing this resonator was achieving lower frequencies which was reached successfully.

Table 4.6. The obtained data of the “low-fundamental” resonator (structure Nr. 6 in Table 4.2)

	Mode 1	Mode 2	Mode 3	Mode 4	Mode 5
Resonance Frequency	1.57	2.57	4.61	6.34	8:22
Quality Factor	78	71	58	53	73

4.6.3. Straight Line Resonators

The results of the straight-line resonators are already shown in section 4.6 where the unequally distanced occurrence of the resonances was discussed. Measuring the straight-line resonators, experimentally proofed that the meandered structure is the reason for the unordered occurrence of the resonances. The result is already presented in Figure 4.6.

4.6.4. Double Resonators

The idea of designing the double resonators was to have a chip which shows a high number of the resonances with not a large distance between them. Such

a condition can be fulfilled with having a resonator with a low fundamental like for example the resonator of section 4.6.2. However, the problem with such a resonator is the low quality factor and not covering the frequencies above the 7th or 8th mode.

The goal of having a high range coverage (a high number of resonances with high quality factors) could be achieved by having two resonators with significantly different resonances next to each other in one chip. The designed structures are shown in Table 4.2 as 7th and 8th structures. The thought result of this idea would look like the drawn schematic diagram in Figure 4.14 (a). Despite of the accurate fabrication, the double resonators did not yield the desired functionality and results. One possible reason for that could be the two simultaneous transmitted standing wave signals (resonances) of the adjacent resonators interfere each other and due to the phase differences, a noise-like spectrum such as Figure 4.14 (b) forms.

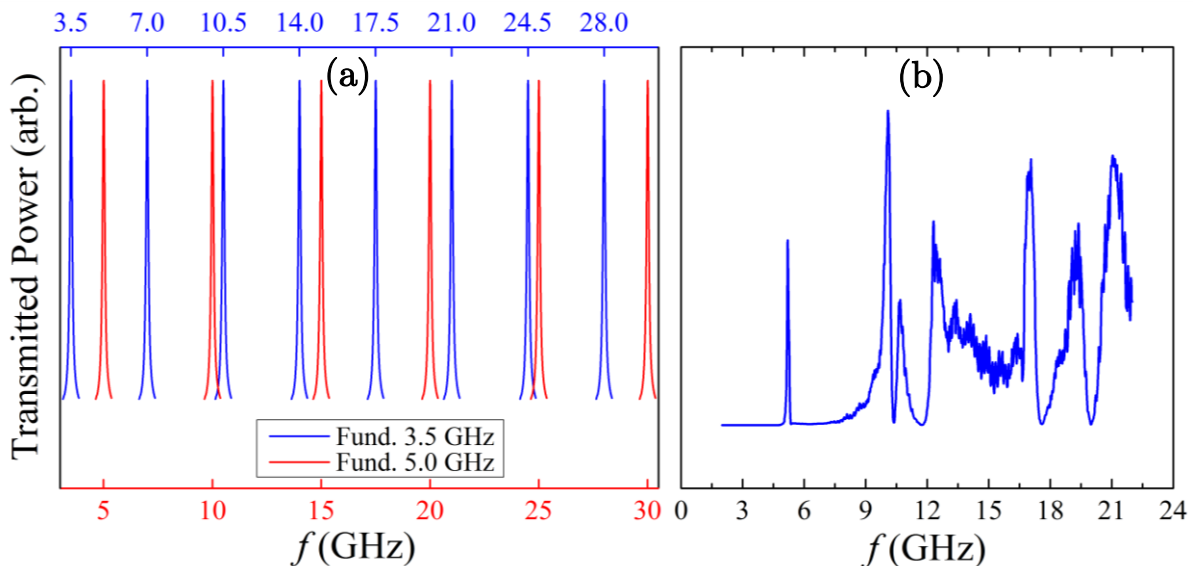


FIG. 4.14. (a) The schematic diagram of the thought result which would be expected from a double resonator like the one of structure number 8 with two resonators adjacent of each other with the fundamentals of 3.5 GHz (the blue resonances) and 5 GHz (the red resonances). (b) shows the typical experimental results obtained of a double resonator.

4.6.5. Golden Resonators

Just to investigate any probable and unexpected outcomes, some sort of the resonators of structure 3 (Table 4.2) were fabricated by using 1 μm sputtered gold film. The obtained data were qualitatively quite similar to copper resonators. However, the quality factors were remarkably lower than the copper resonators.

4.7. Numerical Analysis of the Quality Factor Loss Background for Superconducting CPW Resonators

It was mentioned in the previous chapters and sections that the superconducting resonators functionality, mainly the quality factor, is affected by applying external magnetic field. This definitely affects any kind of obtained signal also if the experiment is performed in external magnetic field. This means to gain the pure signal (e.g. ESR) from the sample under experiment, one must analyze and modify the recorded data. At the following one related example is shown. The gained data of extensive ESR measurements which were carried out by using niobium superconducting CPW resonators, were to numerically analyze in order to correct the deformed ESR signals due to the Q loss background. Here a brief introduction of the procedure of this analysis is presented. More details can be found in Appendix I.

In these measurements, superconducting coplanar resonators were used above which a YbRh_2Si_2 sample was mounted. At a particular magnetic field, electromagnetic signal with a given range of the frequency was sent to the resonators. If signal energy is suitable to perform spin resonance between the splitting spin states (Zeeman Effect), the signal is absorbed by the sample (Figure 1.1 in chapter 1). The signal absorption by the sample is demonstrated by a significant decrease of the quality factor by sweeping the magnetic field through on- and off-resonance values; Figure 4.15.

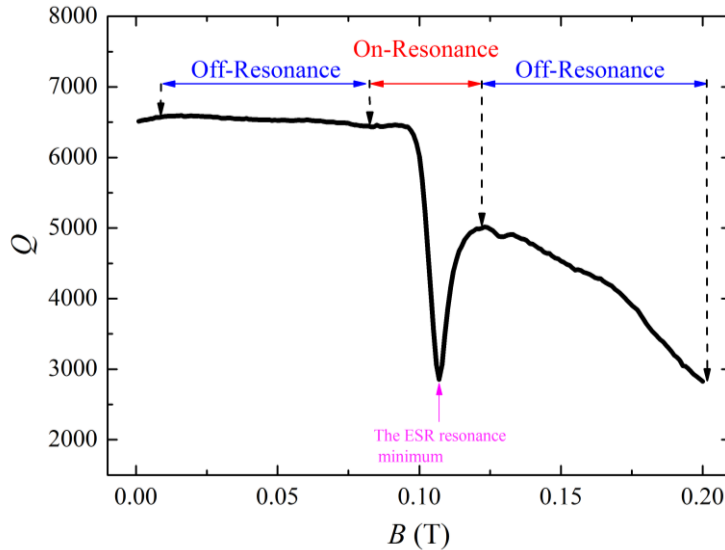


FIG. 4.15. One typical Q vs. B (Magnetic field in Tesla unit) plot obtained by using a superconducting CPW resonator. The deep minimum is caused by the ESR resonance field. The On-resonance (the area of the ESR effect) and the Off-resonance areas are shown.

For each mode the ESR range was determined and deleted from the data set. The remnant points were then fitted, and so, the cut piece of data (the ESR points) was numerically interpolated by a constructed formula (Appendix I). Then the curve

containing the ESR signal was subtracted from the corresponding fitting (interpolating) curve to obtain the ESR signal without the background effect. This is shown as an example in Figure 4.16.

Finding an appropriate formula which describes all the features of the obtained curves was a critical part of the job. Another challenge was to set the varying parameters of the formula so that the regression is harmonic from one curve to the other at different temperatures. That was an extensive amount of work for the obtained data with very short off-resonance parts.

The accurate performing the process takes time several months of time. Metallic resonators do not need such an analysis and the (final) signal is directly and without any further processing observable.

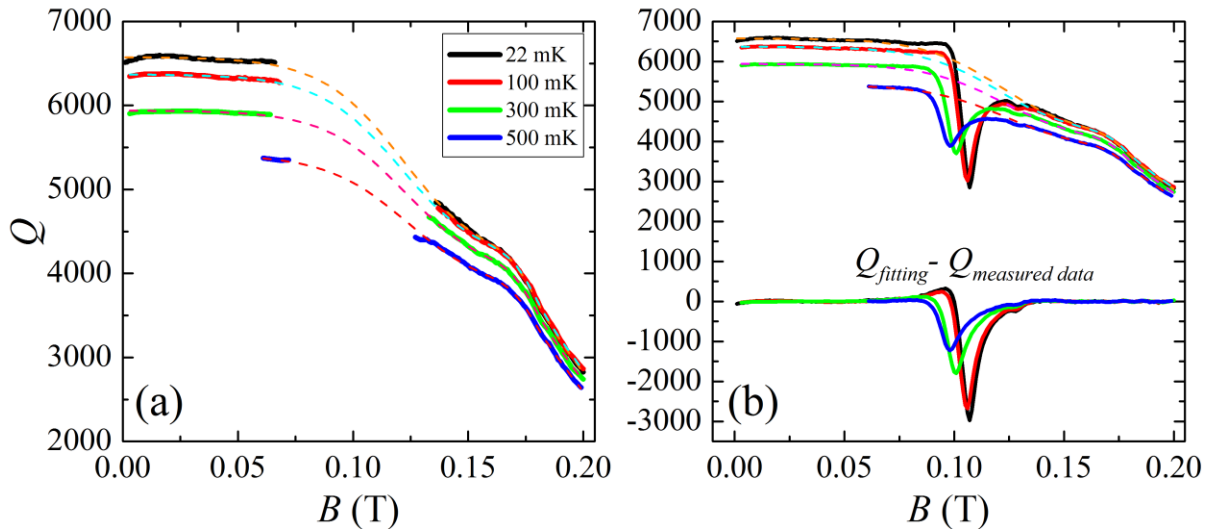


FIG. 4.16. (a) The data points belonging to the ESR section of the curves are omitted from the measured data and the remnant points are fitted. The dashed line curves are the fitting data and solid line curves are the experimental data. The curves belong to mode 3 of the used resonator. (b) The upper curves show the measured data (solid lines) and their corresponding fitting curves (dashed lines). The lower curves are measured data subtracted from the fitted data; $Q_{measured\ data} - Q_{fitting}$. The temperatures are the mixing chamber temperature of the dilution refrigerator. The legend of (a) is valid for (b) also.

5. Primary ESR Measurements

As it is already explained in section 3.1 in chapter 3, showing a very strong and significant ESR signal has made DPPH a very typical and standard sample in ESR studies. In this work also, the sample which used to test the ESR functionality of the produced metallic resonators was DPPH powder. Various measurements with different aims were performed whose conditions and results are presented in the following.

Most of the DPPH ESR measurements were done at 5 K and since the magnetic field is necessary, the utilized was cryostat was (always) the VTI. In general, all the ESR measurements of this work were carried out as the following:

1. Cooling down the sample, which is properly placed on the resonator, at zero magnetic field.
2. If that were required to measure the ESR at several frequencies (modes of the resonator) and several temperatures, one of the two following procedures were chosen. The first: at each temperature all the modes were measured and then the next temperature was reached and the measurement was repeated. The second: only one mode was measured at each temperature and after reaching the last desired temperature, the sample was cooled down again to start measuring the second mode and so forth. All the presented ESR results in this work were obtained by the first method except the data of the spin liquid sample which will be explained on its own turn.
3. At each magnetic field point the range of the frequency for the mode was recorded, then, the magnetic field was increased to the next point and again the mode was measured and so on.
4. The Q value of every single frequency spectrum (each mode) was calculated and plotted versus the magnetic field.

The result, for a nonmetallic sample, would be a diagram like what is schematically shown in Figure 5.1 (a).

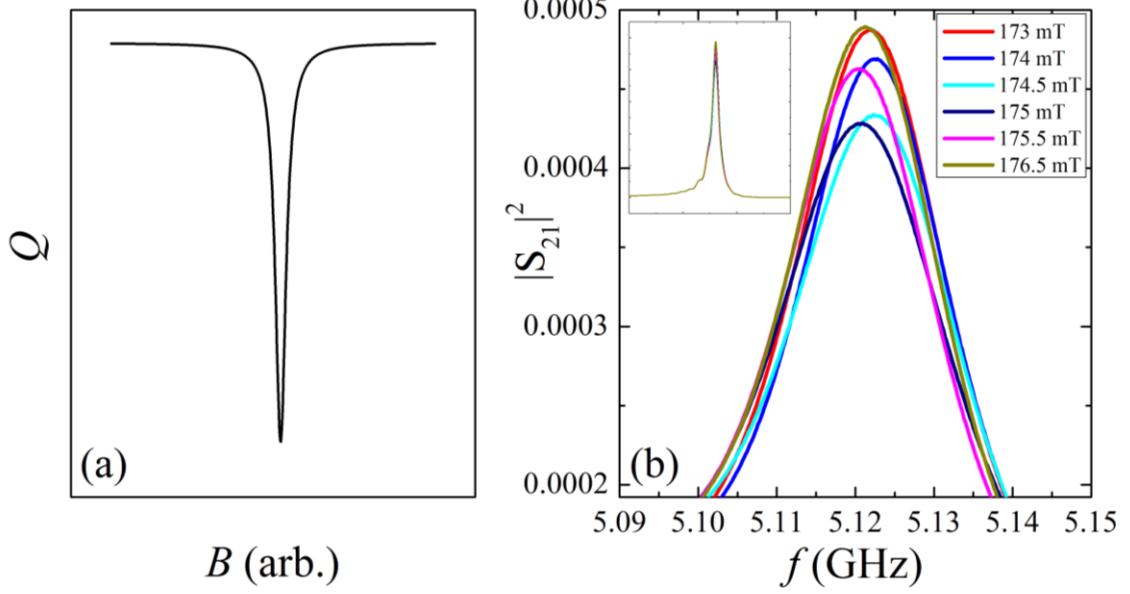


FIG. 5.1. (a) Q vs. B diagram which shows an ESR signal. The picture is schematic for a non-metallic sample. (b) The (zoomed-in) resonator resonance peaks in on- and off-ESR-Resonance areas. 173 mT and 176.5 mT curves belong to the off- and the rest belong to the on-resonance of a real case of DPPH ESR measurement. The inset shows the zoomed-out picture of the resonance peaks. The MW setup used in this measurement was a Network Analyzer and S_{21} is the S-parameter (scattering parameter).

In Figure 5.1 (b), the measured resonance peaks are shown at the points in the ESR signal area and the points far from resonance where the signal is not perturbed by any kind of ESR absorption. One sees that the signal intensity is reduced at ESR area and the Q value is thus smaller. Plotting the calculated Q values together versus the external applied magnetic field makes the ESR signal lines observable as schematically plotted in Figure 5.1 (a).

Several series DPPH ESR measurements, as calibrating or introductory tests, were carried out using developed metallic CPW resonators from which a part is represented in Figure 5.2. The sample was a small ($\approx 200 \times 100 \mu\text{m}^2$) mass of powder DPPH which was placed on the middle of the resonator meander line and fixed by a small amount of vacuum grease.

It was in Figure 1.2 (section 1.1, chapter 1) where the ratio $\frac{n_{\downarrow}}{n_{\uparrow}}$ was shown to be lower at higher magnetic fields and/or at lower temperatures. The lower $\frac{n_{\downarrow}}{n_{\uparrow}}$ means the higher the number of the up spins ($S = +\frac{1}{2}$, $m_s = -\frac{1}{2}$, anti-parallel in respect to the external

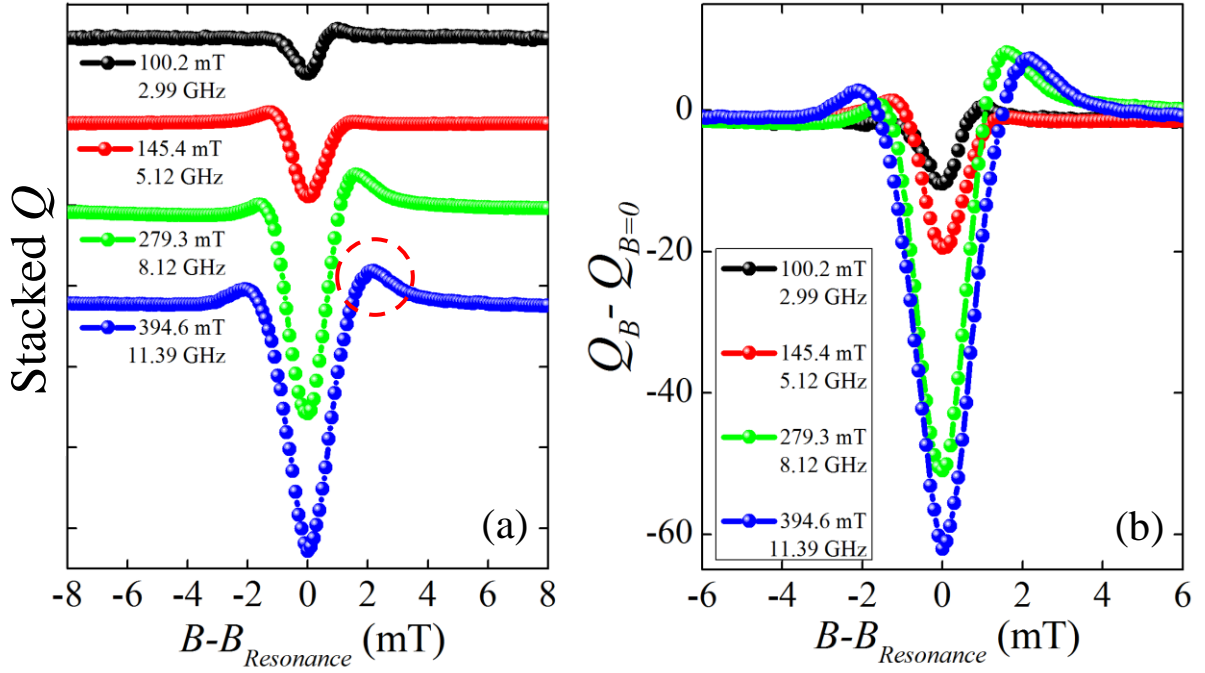


FIG. 5.2. The ESR signal (Q vs. B) of DPPH obtained by utilizing a metallic CPW resonator ($w = 60 \mu\text{m}$ and $G = 20 \mu\text{m}$) at 5 K. In (a) the vertically shifted Q vs. B curves for four different resonances are displayed. All the curves are horizontally also shifted since the magnetic field values are subtracted by the ESR resonance field ($B - B_{\text{Resonance}}$). The ESR resonance frequency (which equals the resonator resonance frequency) is shown with the ESR resonance field value next to each curve. The red dashed circle points a measurement artefact which will be explained later in text (Figure 5.3). In (b) the same curves of (a) are stacked upon each other to indicate the signal intensities difference among the data. The originally obtained Q values are subtracted by the Q value at $B = 0$ mT (the first data point).

magnetic field, see Figure 1.1). This will lead to more absorption of the signal and thus stronger ESR signals; more precisely to speak, it leads to the larger surface area of the ESR signal curve. This implements that at higher frequencies and correspondingly at higher magnetic field, the ESR signal must have higher intensity. This fact is observable and confirmed in the obtained data of Figure 5.2 (b).

The extra bumps right before and after of the ESR signals, one of which is for instance shown in Figure 5.2 (a) with the red dashed circle on the blue curve, are due to the narrower ESR linewidth than the resonator mode frequency range. This was found during a fine data analysis and is illustrated in Figure 5.3. The left or right parts of the Lorentzian shape resonance can provide ESR at in turn lower and higher magnetic fields than the currently applied magnetic field. This makes the BW of the resonator resonance (see FIG. 2.2, section 2.2, chapter 2) narrower, whereas the peak height stays constant and thus the Q value becomes bigger. What are seen as the two bumps (peaks) on the left and right side of the ESR trough, are these escalated quality factors. A similar feature is seen in Ref. [183] where they did ESR with metallic microstrip CPWs.

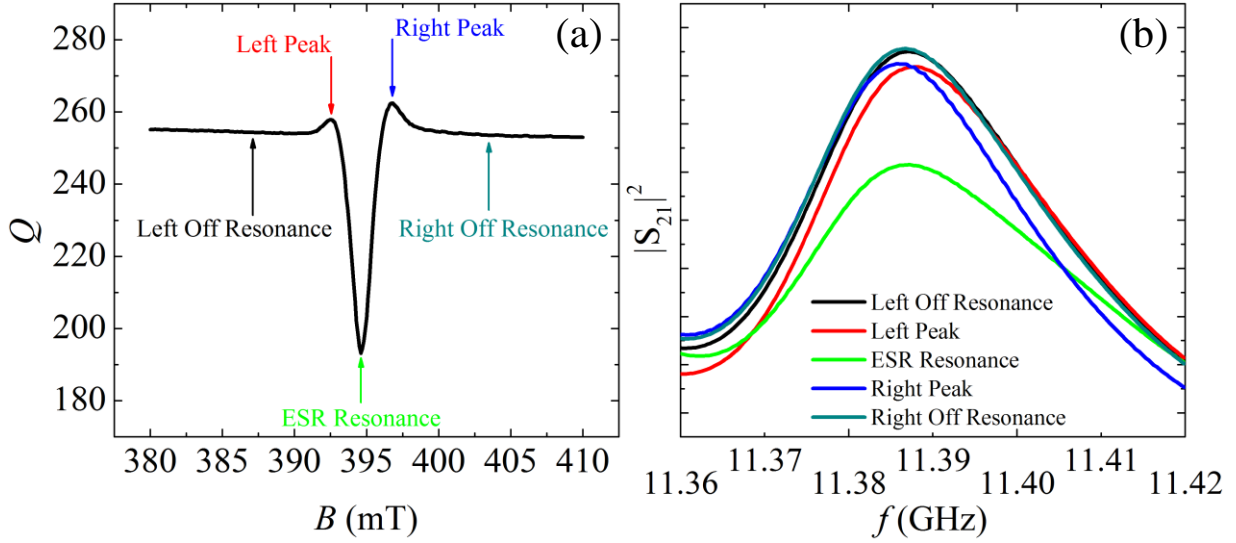


FIG. 5.3. (a) The ESR signal (Q vs. B) of DPPH at 394.6 mT and 11.388 GHz (≈ 11.39 GHz). The corresponding resonance curves of the points pointed by the arrows in (a) are given in (b).

The g -factor of standard DPPH samples is very well-known to be 2.0036 as already mentioned in section 3.1 of chapter 3. The obtained value for the DPPH g -factor from the data of Figure 5.1 is 2.0457, shown in Figure 5.4 (a), which has a deviation of 2.1% from 2.0036.

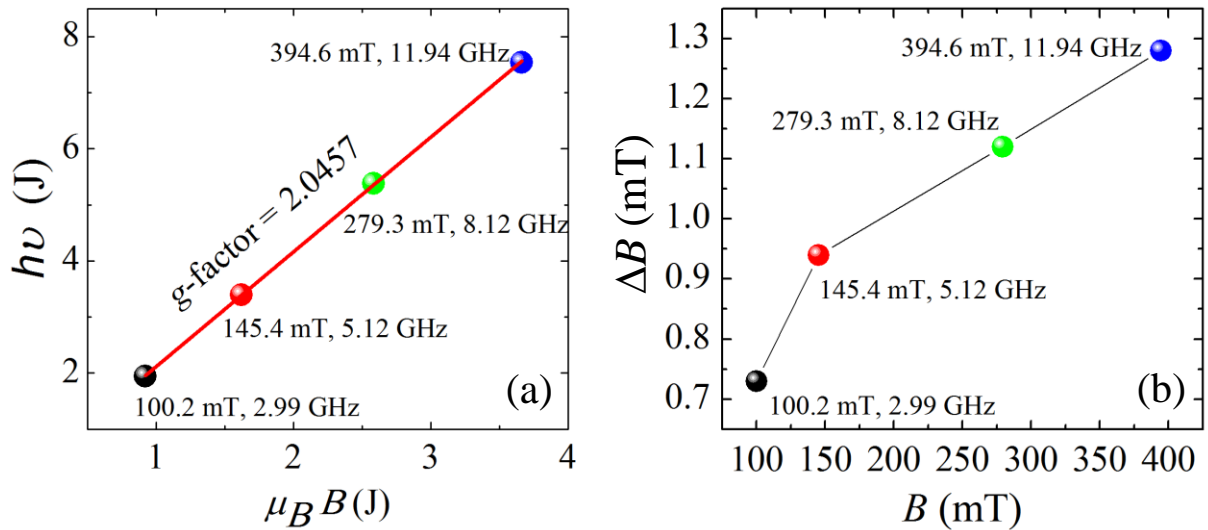


FIG. 5.4. (a) represents the modulated frequency ($h\nu$) against the modulated field ($\mu_0 B$) to obtain the g -factor along with $\Delta E = h\nu = g\mu_B B$. The g -factor is the slope of the red line which is the linear fit of the resonance data points. (b) shows the ESR linewidth values (ΔB) vs. magnetic field. ΔB is obtained from Lorentzian fits of the curves in (a).

2 to 5% deviation is relatively high for a g -factor value. In some fields like atomic physics the attempts are focused to improve the accuracy in the calculation of the g -factors of the particles or samples in their investigations to the tenth number after the point.

Among the all probable causes for the 2% mismatching, the instrumentation causes like e.g. magnet calibration etc. is in our case more probable. This conclusion is made since in Ref. [93], DPPH g -factor at 4.7 K is obtained to be ≈ 2.0825 (3.9% mismatch) and there a superconducting CPW resonator is used. This deviation is attributed to the modulation of the external magnetic field at the surface of the superconducting material because of the Meissner effect. In the case of a metallic resonator there is no Meissner effect, however, a slight field modification at the sample place because of the neighboring metallic parts of the setup is imaginable.

Another reason for this deviation could be the partial chemical changes in sample because of keeping conditions in laboratory.

In Ref. [184] the laboratorial effects are fairly discussed and deviations in e.g. the estimation of molar amount of DPPH based on ESR absorption are mentioned to be easily influenced by environmental and instrumental conditions, so that, having 2-5% deviation has counted as a high accuracy:

“It is worthwhile to mention that usually for a given laboratory and instrument the total error in carefully performed experiment on the quantitative EPR measurements due to the instrumentation, sample and spectrum processing factors may be reduced to 2-5%.” Quoted from Ref. [184].

The increase of ESR linewidth with the magnetic field (frequency), as represented in Figure 5.4 (b), can be explained by the same discussion in section 1.1 of chapter 1 (and relationship 1.1). T_2 increases if the density of the up spins increase. At stronger magnetic fields this happens. This will decrease the spin-spin distances and thus the spin-spin interactions are stronger. The higher the number of the spins results to the wider range of the Larmor frequencies and so the linewidth will become wider.

Several other sets of DPPH ESR experiments, like for example two “Blockpraktikum”s, were carried out to increase our knowledge about using metallic CPW resonators in ESR measurements, however, the data are not represented here.

6. Heavy Fermion Metals; YbRh_2Si_2 and YbNi_4P_2

Observing electron spin resonance in heavy fermion (HF) materials (in the heavy fermion state) has been one of the most surprising observed phenomenon in condensed matter physics. Some theoretical considerations were already pointed out in section 3.2 of chapter 3.

Several YbRh_2Si_2 ESR studies are offered in various publications and literatures so far and although they are precise and innovative, they have always been having some drawbacks like not to be able to reach very low temperatures of under 500 mK or if the temperature was enough low to look at the Landau Fermi Liquid (LFL) phase, the utilized tool was a superconducting CPW resonator [185] which applies severe background effects, as discussed in the previous chapter. Here, the mK ESR data of YbRh_2Si_2 will be offered which are obtained by the beneficial developed modules; metallic CPW resonators.

ESR measurements were performed on two various samples of YbNi_4P_2 as well. There is no published work on the ESR investigation of this material thus far, and to best of our knowledge, no observed ESR signal. The ESR investigations and the obtained results in this work can help orient the further works which will be focused on this compound for studying its spin dynamics.

The measurements were carried out from ≈ 40 mK up to 800 mK and at 1.7 K are represented. In the case of YbRh_2Si_2 , a sort of additional measurements was carried out in order to investigate explicitly the magnetoresistance of this metal and exploring the possibility if such measurements using metallic CPWs are meaningful at all.

6.1. YbRh₂Si₂

6.1.1. ESR of YbRh₂Si₂

To measure the ESR of a metallic sample, one cannot place the sample directly on the resonator (as for DPPH) since the shortcut between the center conductor and the ground planes stops the function of the resonator. Thus, the sample is to hang above the resonator surface without touching the surface. A detailed schematic picture of the system is shown in Figure 6.1. Furthermore, the metallic sample cannot get placed too close to the metallic (not superconducting!) resonator surface since the electric fields of the MW signal make a strong interaction with the sample and this affects the correct function and desired field distribution of the resonator (see Figure 1.5 (b), section 1.3, chapter 1) and causes parasitic modes (see Figure 2.3, section 2.7, chapter 2).

Based on the above information, YbRh₂Si₂ sample was attached (by silver paint) on the tip of a screw. The screw was already passed through a brass lid of the resonator. The distance between the sample and the surface of the resonator was set to be eight times than the distance between the center conductor and the ground planes which means in the case of using a resonator with $w = 25 \mu\text{m}$ the sample was hanged $200 \mu\text{m}$ above the sample. The used sample in this section (grown by Cornelius Krellner group in Frankfurt) was a broken part of a bigger (single crystalline) sample shown in Figure 6.1 (c). The (biggest) dimensions of the measured piece were almost $3 \times 4 \text{ mm}^2$.

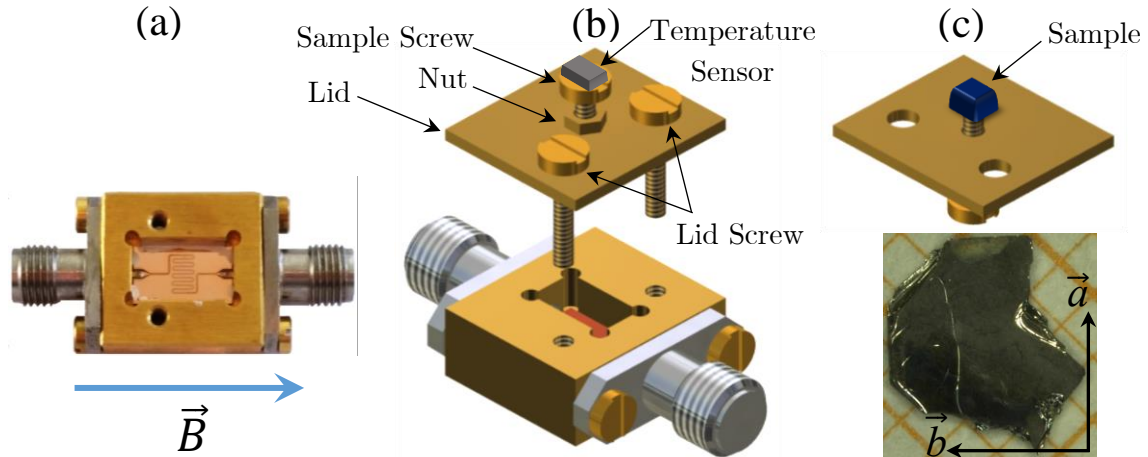


FIG. 6.1. (a) a typical assembly of a CPW resonator developed and used in this work (already shown in FIG. 4.3 in chapter 4). (b) shows schematically the lid through which the sample screw has passed. A fastening nut (“Nut”) tightens the sample screw, on whose other tip the sample is pasted by silver paint as schematically shown in (c). The lid gets screwed to the box by the lid screws. All the components containing the lid, the nut, the sample and the lid screws were made of brass. A smaller part of the sample shown in (c) was used.

The ESR measurements were carried out by two different cryostats; the VTI and the dilution refrigerator. The VTI was used for the primary tests at 1.7 to 1.9 K. The probed ESR points lay in the areas which are shown by the dimmed rectangular windows in the phase diagram of YbRh_2Si_2 in Figure 6.2. The similar measurements with superconducting CPW resonators were already done before [185], however, it was essential to investigate this material with metallic CPW resonators also in order to compare data and note if there has been any artefact in the either of the obtained data.

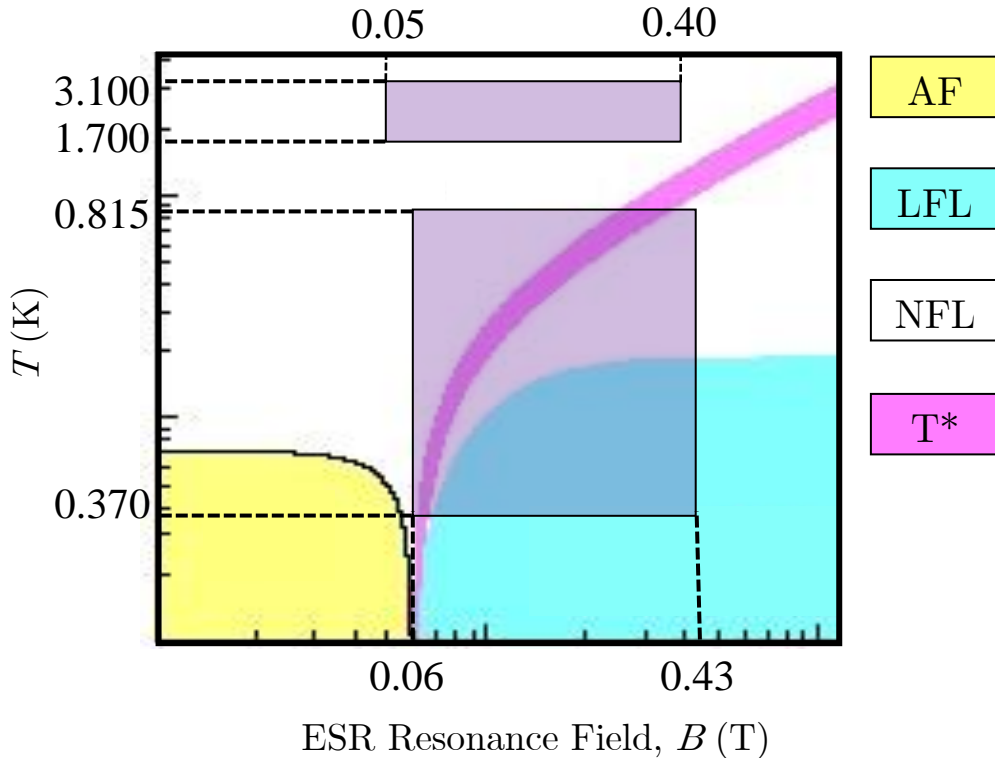


FIG. 6.2. The areas of YbRh_2Si_2 phase diagram which were probed by ESR in this work, are shown by the transparent dimmed rectangles. The phase diagram is a cut piece of the original one in [117]. The VTI measurements (upper rectangle) were performed from 1.7 K to 4 K from 50 mT to 404 mT, however, except couple of exceptional cases, the data of above 1.9 K were very noisy. The milli-Kelvin temperature measurement ranged from 37 mK to 815 mK (sample temperature) and 60 mT to 430 mT.

The purpose of the VTI measurements of YbRh_2Si_2 was only to check if any ESR signal is detectable. After finding the ESR signatures in the VTI measurements (Figure 6.3), the mK tests to probe the low temperature phases were performed from 37 to 815 mK. The external applied magnetic field was in-plane which is perpendicular to c -direction of the sample (see Figure 3.5 in section 3.2.1, chapter 3). To observe the strongest possible signal the static external magnetic field is to be perpendicular to the alternating magnetic field of the MW signal in the resonator. this requires the external magnetic

field to be parallel with the straight-line parts of the meandered center conductor (Figure 6.1 (a)).

Figure 6.3 contains a selected part of the obtained ESR lines of YbRh_2Si_2 for 1.7 K to 1.9 K ranges and couple of 3 and 4 K data points obtained by using different metallic CPWs at different conditions e.g. the sample-resonator distance. The goal of utilizing different resonators was to check the reproducibility of the data. Because of the instability of the used cryostat at long-time measurements, at each series of measurements a remarkable amount of the obtained results appeared too anomalous or noisy and for this reason, the offered data in Figure 6.3 are sometimes not continuous. Anyhow, the aim of the experiments was successfully achieved and the ESR signals were appeared and recorded.

One very important point to consider is that the resonance frequencies of the resonator find a shift (sometimes up to 400 MHz) by hanging such that large metallic sample above the resonator surface.

The Dysonian lineshape of the lines was expected as the sample is metallic. This will be explained with more details later.

Although the VTI measurements of YbRh_2Si_2 had only a checkout aspect, one can do some corresponding analysis like g -factor calculation as offered in Figure 6.4 (a). Linewidth calculation was not possible with a satisfying accuracy since the resolution of the obtained data was not enough fine (in the ESR trough) to yield a precise fitting for obtaining the accurate ESR linewidth.

The shown data in Figure 6.4 (a) are the average values of the g -factors obtained at each resonance field. The average value is calculated of the ESR curves for various temperatures shown in each diagram of Figure 6.3. For each resonance field (each diagram) there were 3 or 4 ESR curves for the temperature range of 1.7 K to 1.9 K. Each curve yields a g -factor as shown in the inset of Figure 6.4 (a). The 100 mK temperature differences among the ESR curves (in each diagram) does not lead to any systematic and observable change in the g -factor values.

The average value and the single values are in a high accordance with the data introduced in other literatures like Ref. [2] as shown in Figure 6.4 (b). The obtained values for g -factor of YbRh_2Si_2 strongly implies that the ESR signal belongs to the Yb $4f$ moments [186]. In Ref. [186] the ESR of the Yb ions in a very dilute mixture of Yb in an Au matrix is observed. The Kondo temperature of this mixture is around 10 μK and the obtained ESR signal is at the temperatures far above the Kondo temperature where no screening of the magnetic moments is expected.

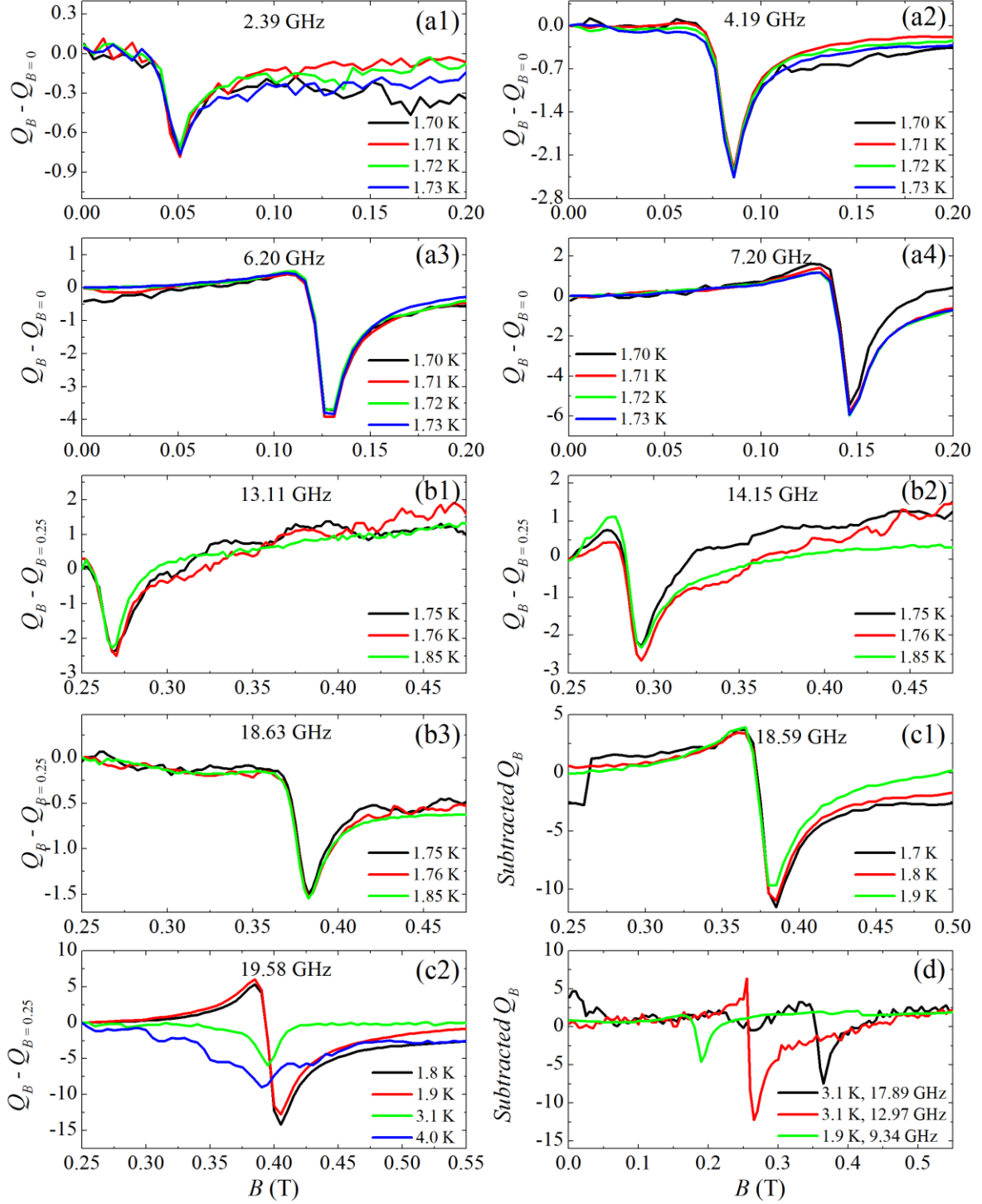


FIG. 6.3. The recorded ESR signal of YbRh_2Si_2 at 1.7 K and some higher temperatures as the checkout measurements for observability of the ESR signal. Form (a1) to (a4) are obtained by a resonator with $w = 40 \mu\text{m}$ and $G = 30 \mu\text{m}$ with the distance of $200 \mu\text{m}$ between the sample and the resonator. (b1) to (b3) are obtained by a sputtered resonator with $w = 60 \mu\text{m}$ and $G = 30 \mu\text{m}$ with the distance of $400 \mu\text{m}$ between the sample and the resonator, and, (c1) and (c2) with the same resonator of (b) but with distance of $200 \mu\text{m}$ between the resonator and the sample. (d) shows some other pieces of data which were obtained in other measurements, e.g. with a resonator with the structure 5 of Table 4.2.

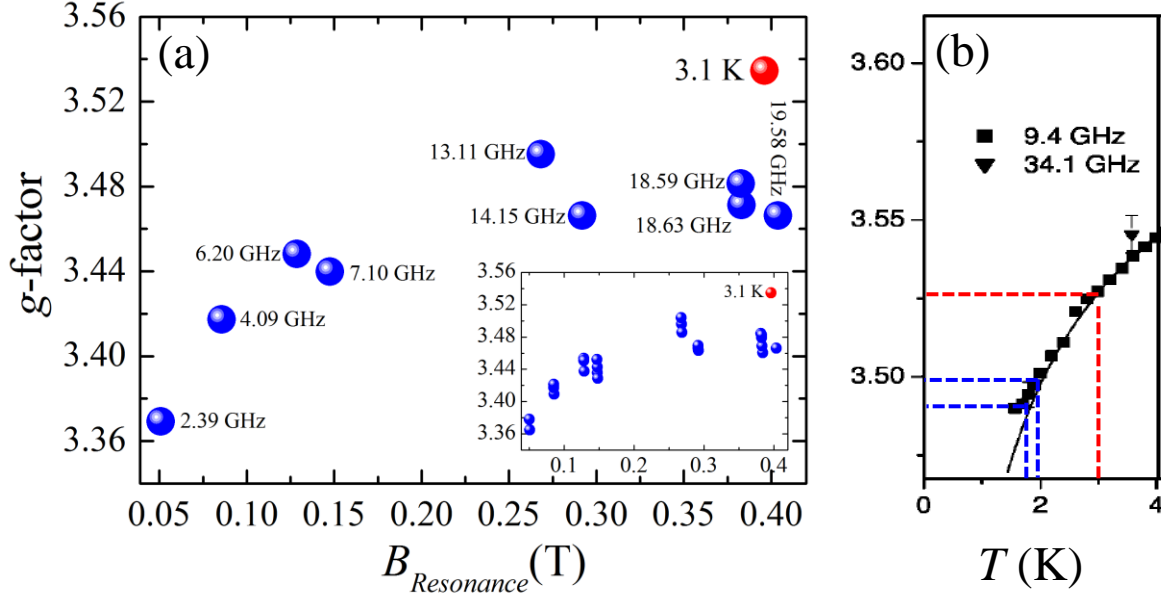


FIG. 6.4. The g -factor values of the single crystalline YbRh_2Si_2 at 1.7 K (a) obtained from the experimental data in this work and shown as averaged g -factor vs. magnetic field. The single data points (without averaging) are shown as the inset. The 100 mK temperature differences among the ESR curves does not lead to any systematic and observable change in the g -factor values. (b) the g -factor values vs. temperatures at for 9.4 GHz and 34.1 GHz (one data point) reported in Ref. [2]. The range between the blue dashed lines and the point shown by the red dashed line are the comparable with the data represented in (a).

After the VTI measurements of YbRh_2Si_2 (1.7 K and higher) the milli-Kelvin measurements were carried out by using the dilution refrigerator. In these measurements, all the existing modes were measured at each single temperature and then the temperature was ramped up to the next step.

Two points are to consider for the measurements at temperatures lower than 100 mK: 1) the rate of the external magnetic field sweep, and, 2) the input power of the MW signal. If any of these two parameters is set improperly, it leads to an increase of the sample temperature. The rate of the magnetic field was always set to ramp up (or down) at 0.1 mT/second and 1 mT/second for the temperatures of lower and higher than 100 mK respectively. The input power was always optimized and typically found to be maximum -15 dBm for all the dilution refrigerator measurements (of this work). This is comparable with -5 dBm for the measurements done with the VTI.

Figure 6.5 shows the ESR lines of YbRh_2Si_2 at mK ranges obtained by using metallic CPWs. As once mentioned above briefly, the Dysonian lineshape of the lines was expected as the sample is metallic.

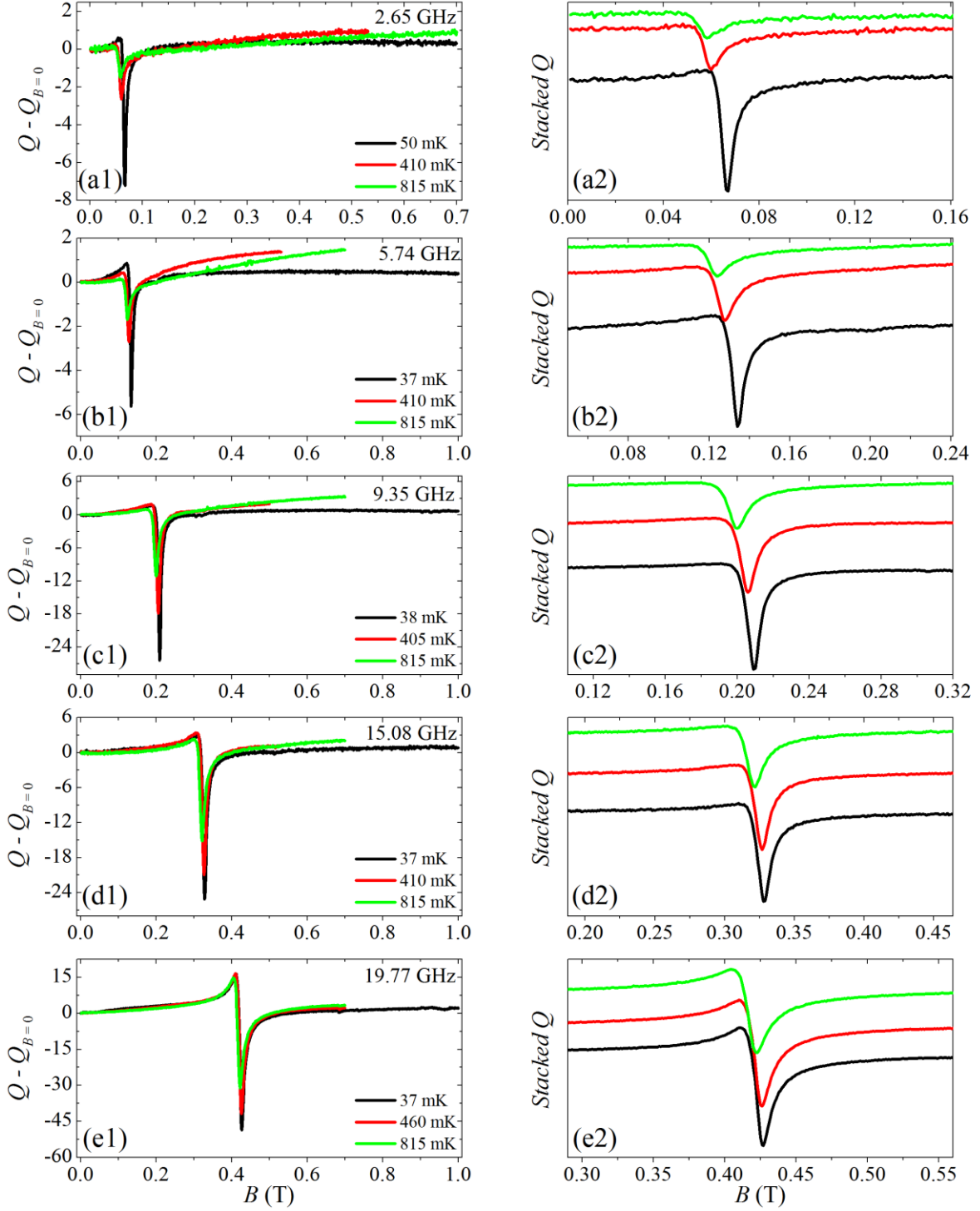


FIG. 6.5. The used resonator had a $w = 60 \mu\text{m}$ and $G = 30 \mu\text{m}$. The upraising of the off-resonance parts of the ESR lines at higher temperatures ($\approx 400 \text{ mK}$ and $\approx 800 \text{ mK}$) was explored with more details and much wider field range which will be explained later.

The linewidth is calculated by using the Dysonian fitting formulae as below [187]:

$$Q = -a \left[\frac{\Delta B + \alpha(B - B_0)}{4(B - B_0)^2 + \Delta B^2} + \frac{\Delta B + \alpha(B + B_0)}{4(B + B_0)^2 + \Delta B^2} \right] + C \quad (6.1)$$

where Q is the quality factor (vertical axis) in each form of subtracted or original data, ΔB is the ESR linewidth, B_0 is the resonance field, B is the magnetic field (horizontal axis) and “ α ” is the dispersion-to-absorption ratio. The minus sign after the equal sign is due to the plotting of Q vs. B and not absorbed power vs. B . “ a ” and “ C ” are the fitting constants.

The ESR lineshape of highly conductive materials is Dysonian [134] [135]. This stems from the existence of the free (conductive) electrons in these materials in which the (Microwave) penetration depth is shorter than the sample size [188]. Microwave on a metallic conductor are absorbed within the skin depth of the sample. When the sample dimensions are bigger than the skin depth and the electron has enough mobility to diffuse (spin diffusion) in and out of the skin depth on the time scale of the ESR, a Dysonian lineshape occurs [134] [135] [189].

The (Dysonian) ESR lineshape depends on four time-scales. The spin-lattice relaxation, T_1 , the spin-spin relaxation, T_2 , the time which electron needs to diffuse through the skin depth, T_D , and the time which electron needs to traverse the sample T_T . In the case of a metallic sample where the thickness is large compared to skin depth, the Dysonian line shape parameters are determined by the ratio of $\frac{T_D}{T_2}$ [20] [134] [135] [190]. According to Ref. [134] whose analysis are used by Ref. [20] (chapter 12 of the book) as well as Ref. [190] (chapter 9 of the book) also, it is possible to make statements on for example the skin effect type (normal or anomalous) or the presence and participating of paramagnetic impurities in ESR in a metallic sample. This is possible by analyzing the line shape asymmetry ratios which yield information about the ratio of $\frac{T_D}{T_2}$. This discussion (with details) is however out of the scope of this text, but, a few calculations and qualitative analysis were done as offered in Appendix III.

Determining the actual temperature at which the sample during the measurements in the dilution refrigerator is, needs a numerical calculation and is not directly readable from the setup and sensors. The reason for this is that, the actual sample temperature was determined by reading out the measured resistance of the RuO temperature sensor by an AVS 47 resistance bridge and converting it via a corresponding formula. The sensor was always mounted on the sample screw which is already shown (schematically) in Figure 6.1 (b). It must be noted that, the sample temperature was determined only by the recorded data during the time period of the ESR range. This means, if the ESR resonance field range was from 75 mT to 125 mT, only the sensor data of this 50 mT range was taken to account, although, the measurement was performed e.g. from 0 mT to 500 mT.

Figure 6.6 illustrates the $T - B$ phase diagram of YbRh_2Si_2 and the measured points in this work on it, shown by the red spheres.

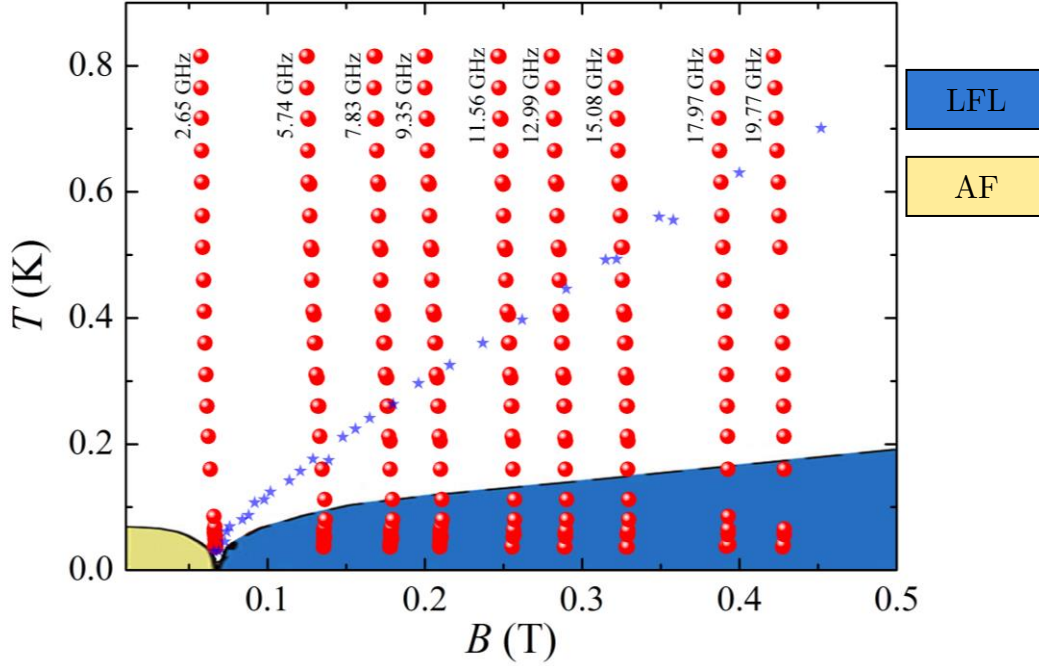
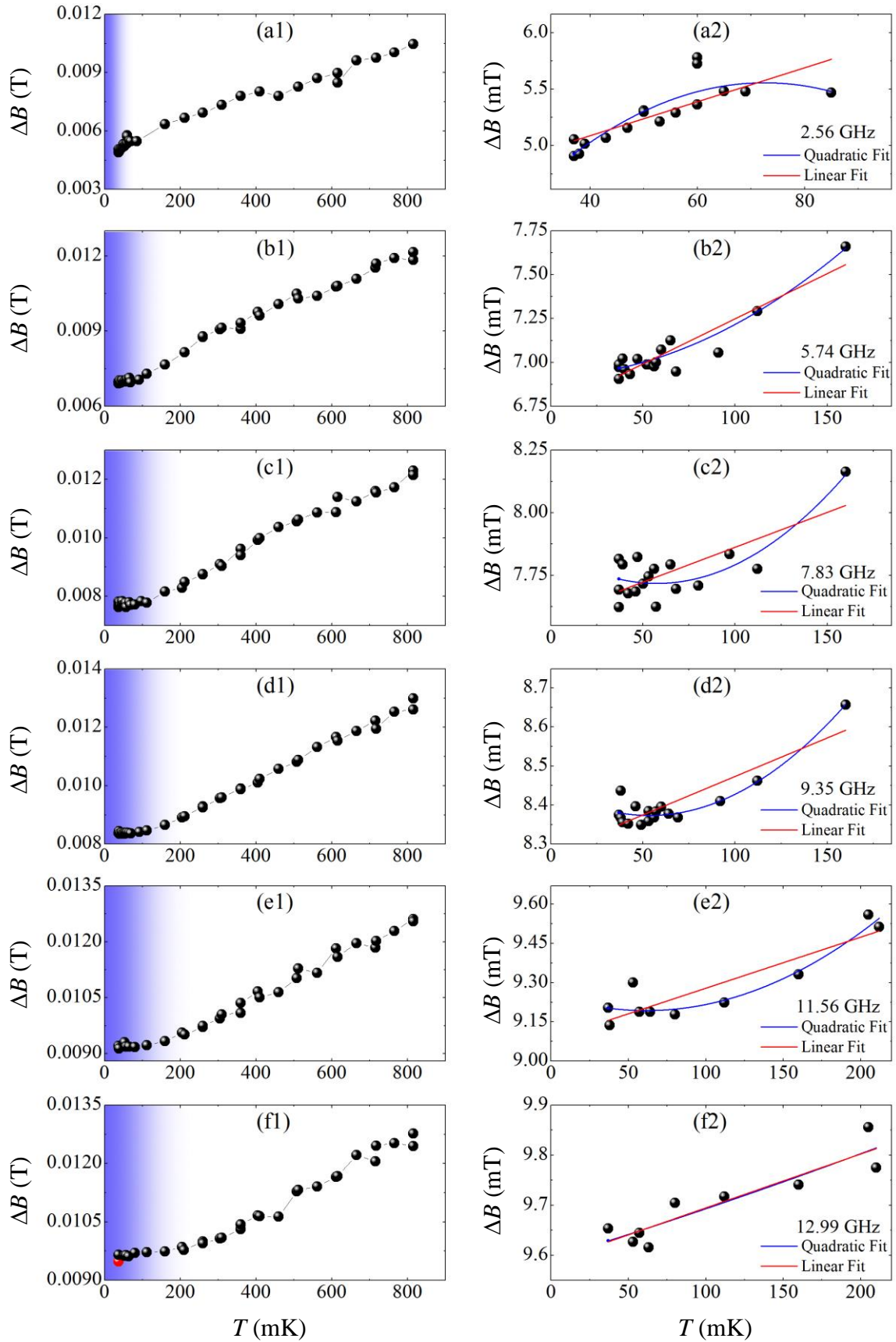


FIG. 6.6. The linear scale (and not logarithmic) phase diagram of YbRh_2Si_2 retrieved from [191]. The red circles are the measured data points of the phase diagram in this work. The resonance frequency at which the data are recorded are noted next to each series. The star marks show the T^* line of the diagram which are retrieved from [192]. It should be noted that the T^* is in fact a wide range (area) and not a very well defined border between two regions of the phase diagram.

The ESR linewidth, ΔB , and its dependence on temperature or magnetic field can yield worthwhile information. Whether the change in ΔB value is of the phononic contribution (spin-lattice relaxation) or pure quasiparticle scattering effects, could be differentiated to some extent since in the case of sufficient different g -factors between the conduction and f -electrons, the linewidth shows T^2 as well as H^2 dependence [141]. In Figure 6.7 the ESR linewidth of the measured sample and its dependence on temperature is illustrated. The blue part in each diagram shows the LFL regime of the phase diagram. The data in the LFL are zoomed in and drawn in a separate diagram next to the full temperature range diagram. They are fitted linearly and quadratically at the same time. For some data series, one clearly observes the T^2 following of the data compared to the linear, however, the other series are not capable to show a (appropriate) dominant T^2 trend like (a2), (f2) and (i2). This is partly because of low number of data points too. This lays mainly on the noise level and the high sensitivity of ΔB value on the artefactual parameters in the measurements.



Continue on the next page

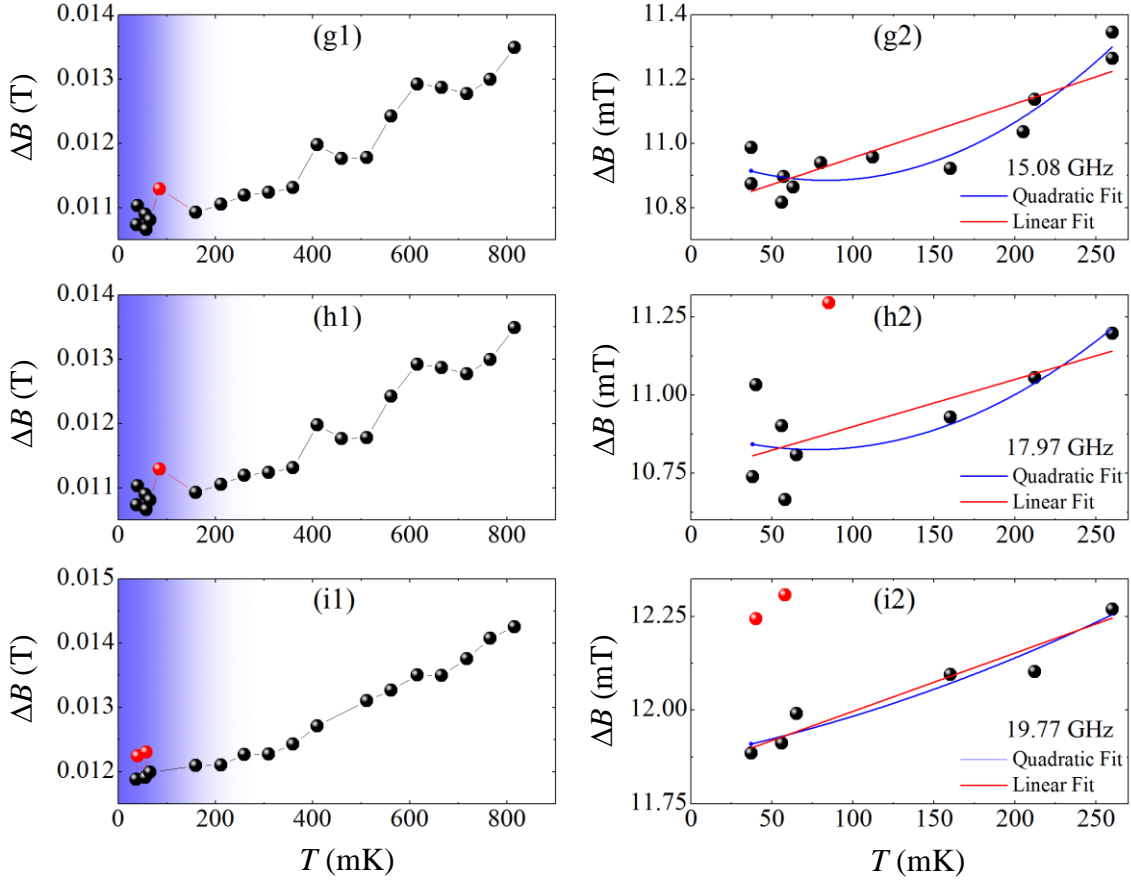


FIG. 6.7. The ESR linewidth of the measured YbRh_2Si_2 vs. the sample temperature. The left-hand side diagrams contain the full range temperature and right-side ones the data in LFL regime (blue region of the left diagrams). Two linear (red color line) and quadratic (blue color curves) fittings are shown together. The corresponding frequency for each diagram pair is written in the left side diagrams. The single red colored data points are the obtained data from the measurements but not included in the fittings since their value look anomalous.

The ESR linewidth could be shown as the curves at constant temperatures versus the external magnetic field also. This illustration is offered in Figure 6.8 as two different diagrams; the upper one contains the curves only for five various temperatures for a better illustration of the data alteration by temperature and the lower one as a colored map to have an over view for all temperatures.

In each diagram of Figure 6.8 there is one very interesting point. The low temperature curves in FIG. 6.8 (a), show almost a strict increase in ΔB as one expects and accepts as the typical result and manner of change of ΔB vs. B . This is because of the number of the aligned spins are higher at higher magnetic fields and hence, the Larmor frequency in the system has a larger variety which directly results to a wider ESR linewidth. No strong signature of state transition through the T^* line (range) can be observed in ΔB vs. B data.

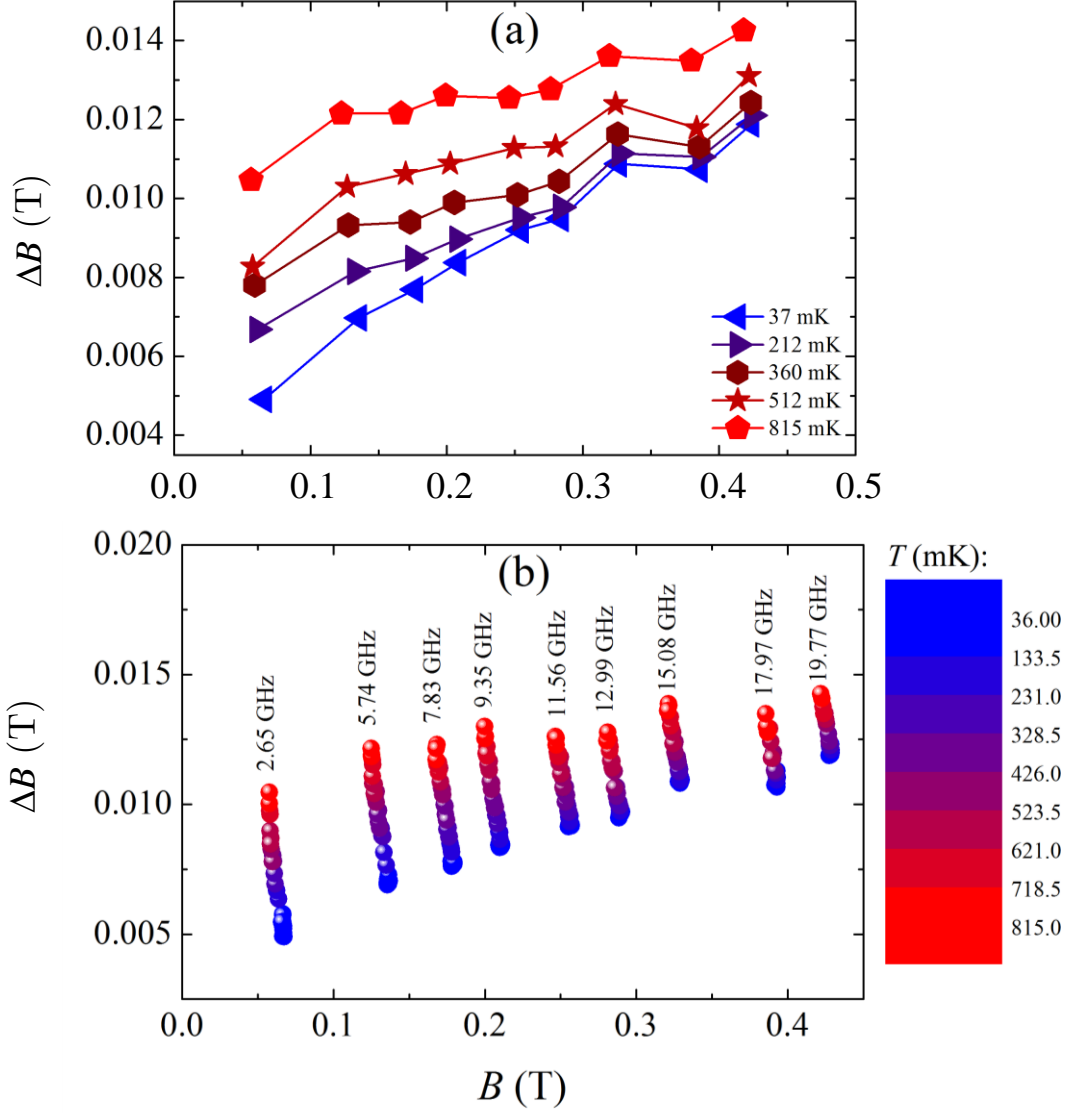


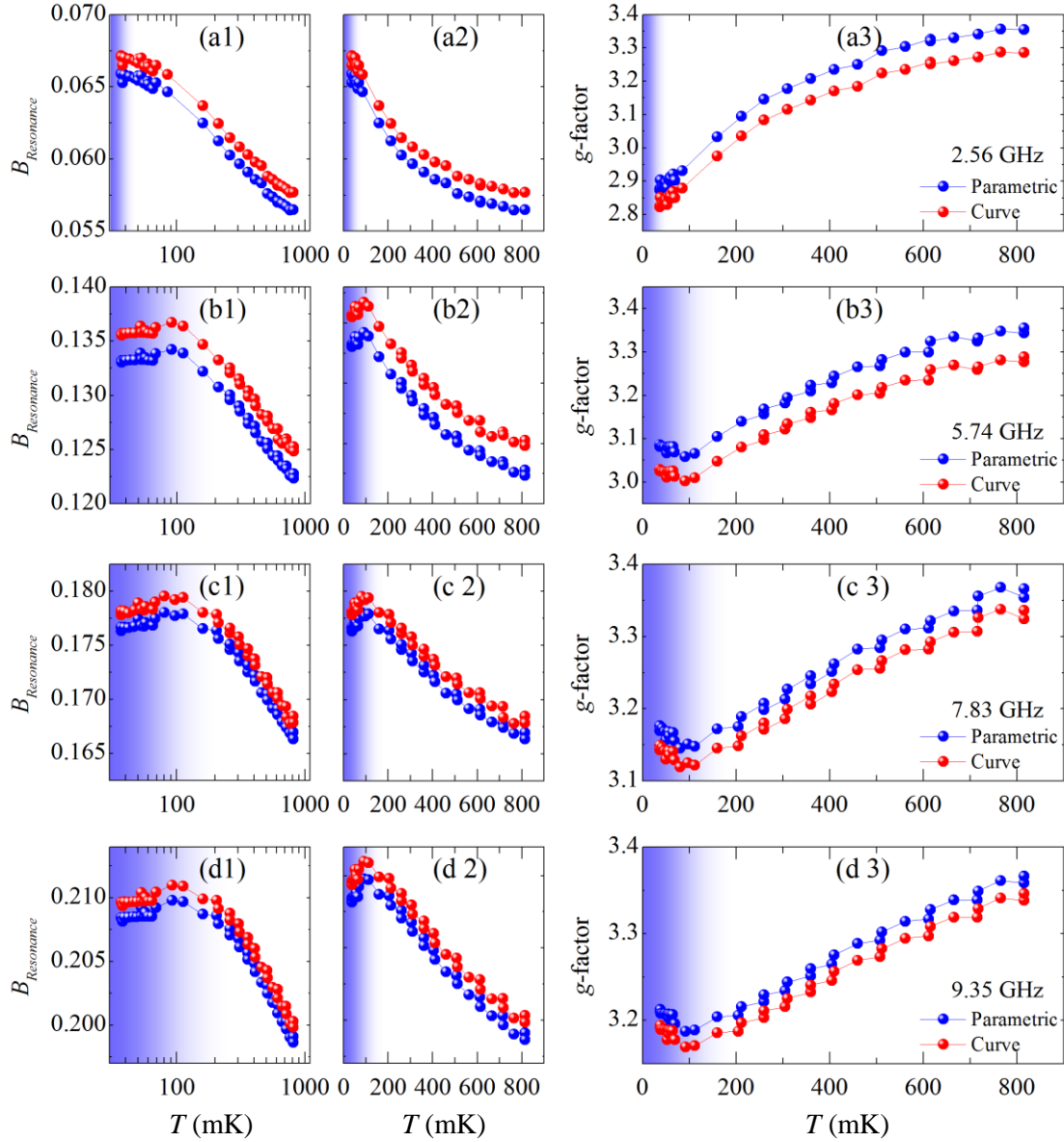
FIG. 6.8. The plotted linewidth values versus the external magnetic field. (a) a few curves at fixed temperatures and (b) for all temperatures with a color map.

One of the former interpretations of the T^* is that, it is a border (although not a sharp and well-defined border) between the small and large Fermi surface from left to right respectively. This was deduced by some sudden changes in transport properties by crossing T^* [120], however, revealing no change in Fermi surface on cooling down to 1 K at zero field by ARPES [193], questions the validity of this statement. The ΔB trend shown in Figure 6.8 shows no significant change on meeting T^* neither.

The second remarkable point which is observable more clearly in Figure 6.8 (b) is the reduction of the ΔB change range for a given frequency through the temperature range (≈ 40 mK to ≈ 800 mK) on increasing the external magnetic field. This point is, however, not far from the mind, since the both of temperature and the magnetic field are energy scales applied to the system and by increasing one sort of the energy the effect of the other one become less sensible for the system.

The change of g -factor on temperature and magnetic field in various phases of the material can yield helpful information about the interaction kinds in the system. The calculated g -factor of the measured YbRh_2Si_2 sample is shown in Figure 6.9.

The ESR resonance fields (named as B_0 or $B_{\text{Resonance}}$) are determined by two different ways. Once taken as the B_0 of the Dysonian fit formula 6.1 and once chosen as the minimum point of the ESR curve (Q vs. B). These two values have always a shift of between 1 to 5 mT. The data chosen directly from the ESR curve (and not Dysonian fit) in the case of VTI measurements of YbRh_2Si_2 (FIG. 6.4) had a better compatibility with the data already shown in the other literatures [2].



Continue on the next page

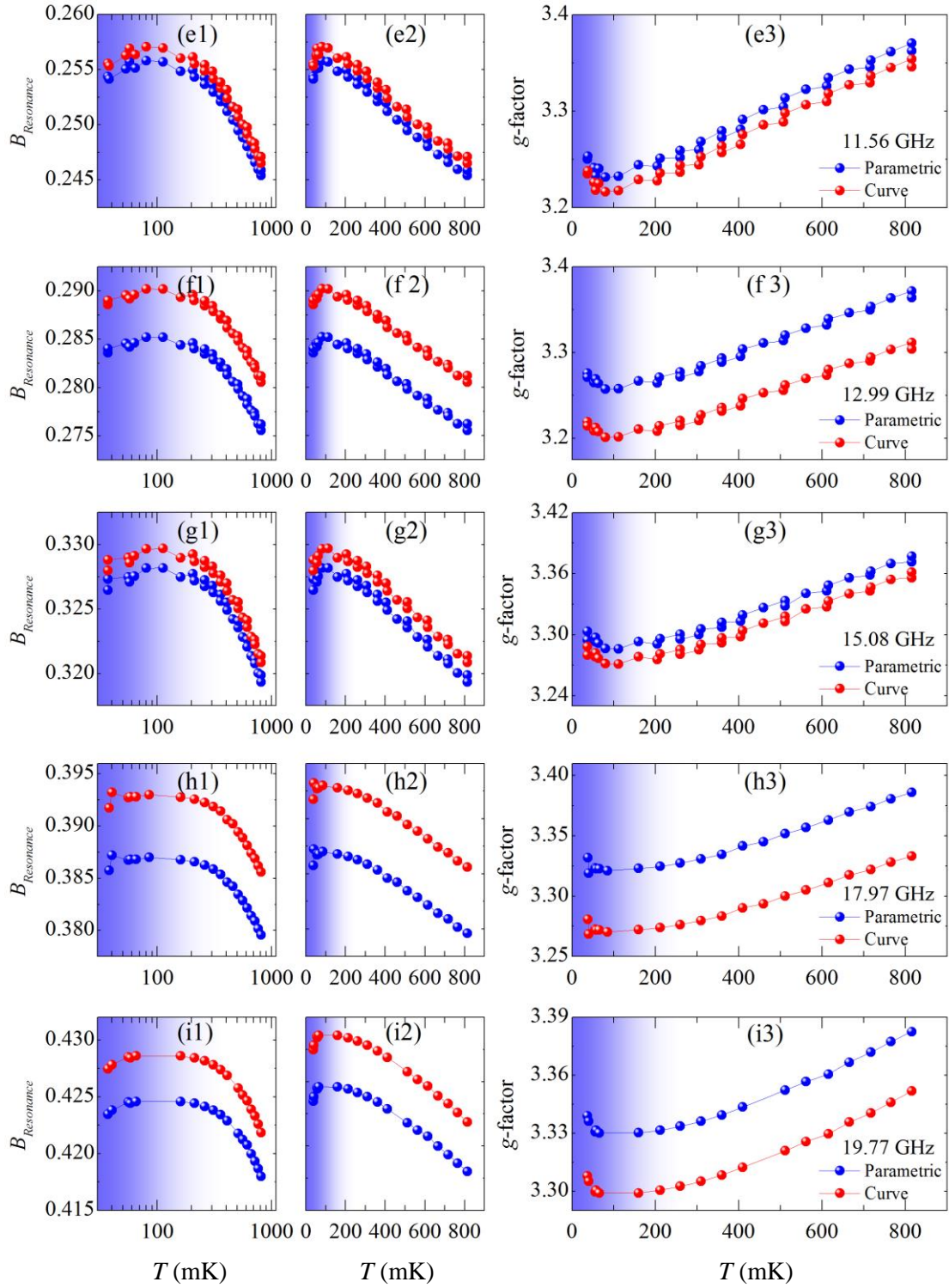


FIG. 6.9. The resonance field vs. temperature curves in left hand side diagrams and their corresponding g -factor vs. temperature curves on the right side. In $B_{Resonance}$ diagrams, the blue data points are determined by the Dysonian fit and the red curve data points are determined by considering the minimum point of the ESR curve as the resonance field. The blue regions show the LFL regime. In $B_{Resonance}$ diagrams, the left one has a logarithmic scale and the right one a linear scale for the temperature axis.

In Ref. [194] the linear dependence of $B_{Resonance}$ (g -factor) on $\log(T)$ is mentioned for high temperatures of 4 K to 10 K. In the presented data of Figure 6.9 the linear dependence of $B_{Resonance}$ is observable for the temperatures higher than the cross over temperature mentioned in FIG. 3.4 of section 3. The cross over temperature shown in Figure 3.4 was the range of the temperature between the pure LFL state, where the effective mass stays constant, and heavy fermion state, where the effective mass changes. The obtained data in the cross over range here are, however, obviously out of linearity.

Another remarkable point is that, the previous mK ESR measurements of YbRh_2Si_2 which were performed by superconducting CPW resonators [185] showed no change of the g -factor in the LFL regime, however, the present measurements, as clearly observable in Figure 6.9, show that the g -factor increases in the LFL region. The increase of the g -factor with further cooling down in LFL could probably be justifiable with this that, the resultant magnetic field on one spin point become intensified by decreasing the temperature further in the LFL state.

Evaluating the g -factor behavior versus magnetic field (Figure 6.10) is in accordance with Ref. [185] as showed the g -factor change at higher temperatures is not as large as lower temperatures. The smaller ratio of $\frac{\Delta g}{\Delta T}$ at higher magnetic fields agrees with the theory [194]. Similar to the change of ΔB vs. the magnetic field (Figure 6.8 (b)), one sees obviously the interacting effects of temperature and magnetic field as two various energy scales on the system. The increase of the g -factor by increasing the magnetic field (at a constant temperature) could be understood by increasing the resultant magnetic field on each spin site since the number of the aligned spins in the field direction is higher. The change of g -factor by temperature is attributed to the Zeeman energy scales change.

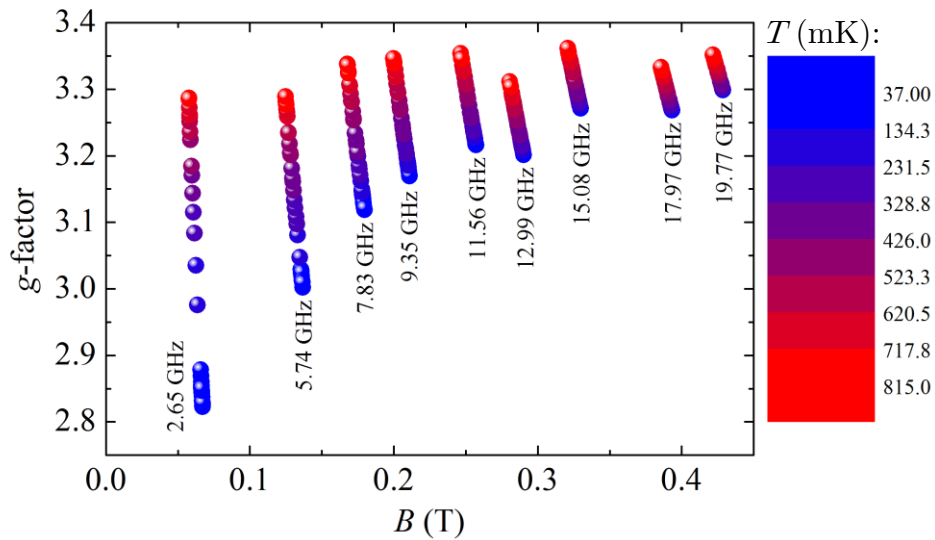


FIG 6.10. The plotted g -factor values versus the external magnetic field for all measured temperatures with a color map.

6.1.2. Non-ESR Measurements on YbRh_2Si_2

It was mentioned above in the caption of Figure 6.5 that in some of the higher temperature obtained data, the off-resonance part of the ESR line (the range of the magnetic field after the ESR signal) has an uprising trend in contrast to the data of lower temperatures. This could not be considered as a pure resonator artefact as shown in Figure 6.11 (b) and (d) since there is almost no difference between the Q vs. B curves of a bare resonator (without any sample above it) from 100 mK to 800 mK. Thus, the observed effect was explored and observed further at much higher magnetic fields. The most probable reason for this uprising is the magnetoresistance of YbRh_2Si_2 as explained in section 3.2.1 and shown in Figure 3.6 in section 3.2.1 of chapter 3.

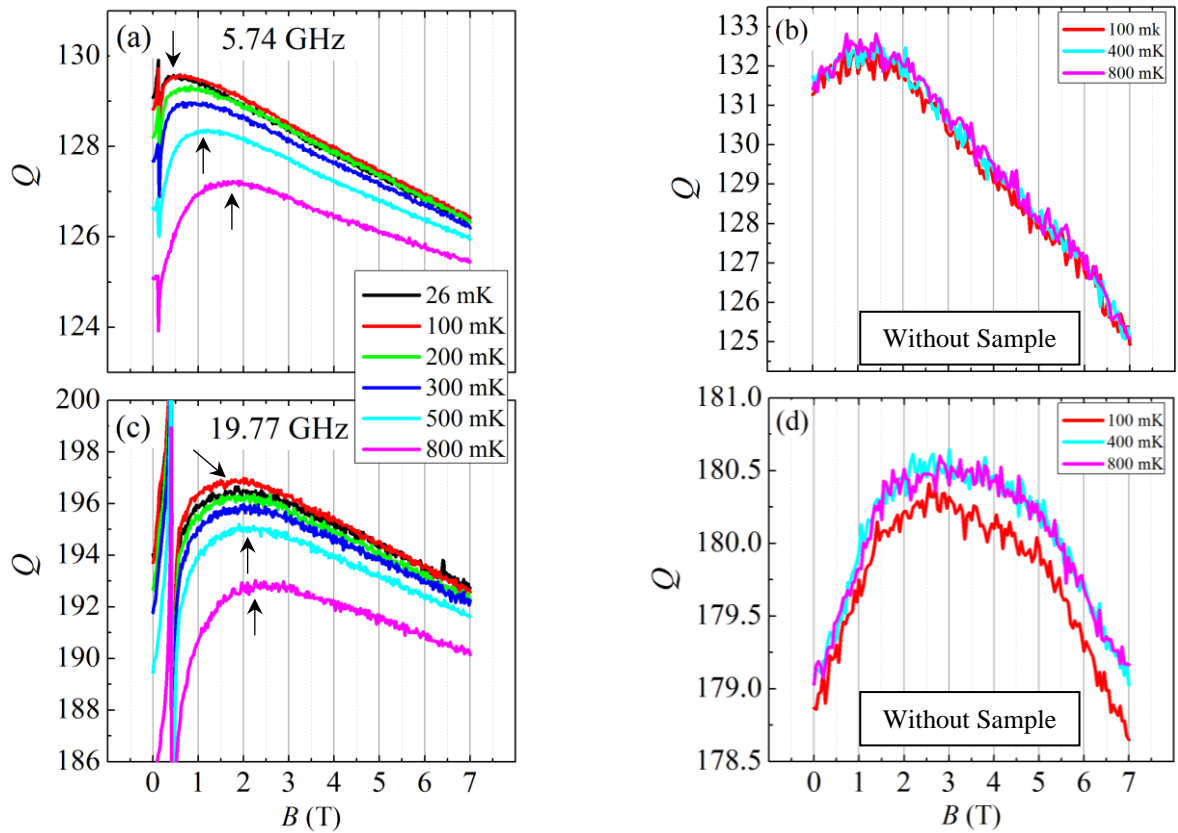


FIG 6.11. High field investigation of YbRh_2Si_2 . (a) and (b) show the Q vs. B for the experiments with and without sample at 5.74 GHz respectively for different (Mixing Chamber) Temperatures. (c) and (d) show similar data at 19.77 GHz.

Figure 6.11 (a) and (c) shows Q vs. B curves of the resonator with the YbRh_2Si_2 sample hanging above it. This is the same system which was used for the ESR measurements. The lower position of the high temperature curves (the lower quality factor values) in diagrams is due to the higher loss of the sample at higher temperatures. This shows the strongly dominated quality factor by the sample. The Q value of the metallic resonators in this work do not face to a change under ≈ 20 K as already mentioned.

The presence of the maximum in the off-resonance part of the ESR line, $Q_{off-max}$, which are indicated by the black arrows on some curves in Figure 6.11 (a) and (c), is a sign of the lower loss of the sample as well as the resonator characteristics at that point. In other words, one affecting parameter in observing the extremum yielding behavior of Q vs. B data, is the behavior of the resonator itself. This is clearly proven by the shown lines in Figure 6.11 (b) and (d). The other parameter is the magnetoresistance behavior of YbRh_2Si_2 since there is a minimum in the resistance data of this material; Figure 3.6 (section 3.2.1, chapter 3).

The change in the position of $Q_{off-max}$ (the magnetic field at which $Q_{off-max}$ occurs) by temperature could only be attributed to the mentioned magnetoresistance. The Q vs. B data of a bare resonator (Figure 6.11 (b) and (d)) does not show any shift in the maximum point in the whole temperature range. If the dominant loss for the non-ESR ranges of the lines is assumed to be the electrical (and not magnetic) loss of the sample, the results which are plotted in Figure 6.11 (a) and (c) are in a fair agreement with the electrical loss measurements of Figure 3.7 in which the DC resistivity of YbRh_2Si_2 shows a minimum between low fields up to around 2 T from 50 to 750 mK. By increasing the temperature, the minimum point in ρ (Figure 3.6 (a)) shifts toward higher fields which is what exactly happening to $Q_{off-max}$ at each given frequency; Figure 6.12 (a).

It should be noted that, the positions of the maximum points (on B axis), which are shown in Figure 6.12 (a) in the off-resonance region, were found by fitting a range of the line (in which the maximum is visually seen) with a quadratic function. Figure 6.12 (b) and (c) show some examples of the fitting to find the maximum point position for the data of 6.11 (a) and (c) at three temperatures.

One more interesting point in $Q_{off-max}$ position is its rightward shift in the lines for higher frequencies at a constant temperature as seen in Figure 6.12 (a). One can interpret this as a frequency dependent AC magnetoresistance of YbRh_2Si_2 .

Drude relaxation at MW frequencies in heavy fermion metals has already been investigated [195]. Unfortunately, no tracing and exploring of Drude model in the presented data in this section is possible since the Q values differ from one resonance to the other and this makes the analysis of the effect of frequency on the AC conductivity of the sample almost impossible. As a thought experiment, if we had a resonator with an identical quality factor for its resonances, by placing the sample above it and measuring the change in Q values, one could confirm if the sample is following Drude model. This experiment could be done at different magnetic fields also. The MW signal fields distributions in resonator at different resonances and interacting with sample would not be neglected in such an experiment.

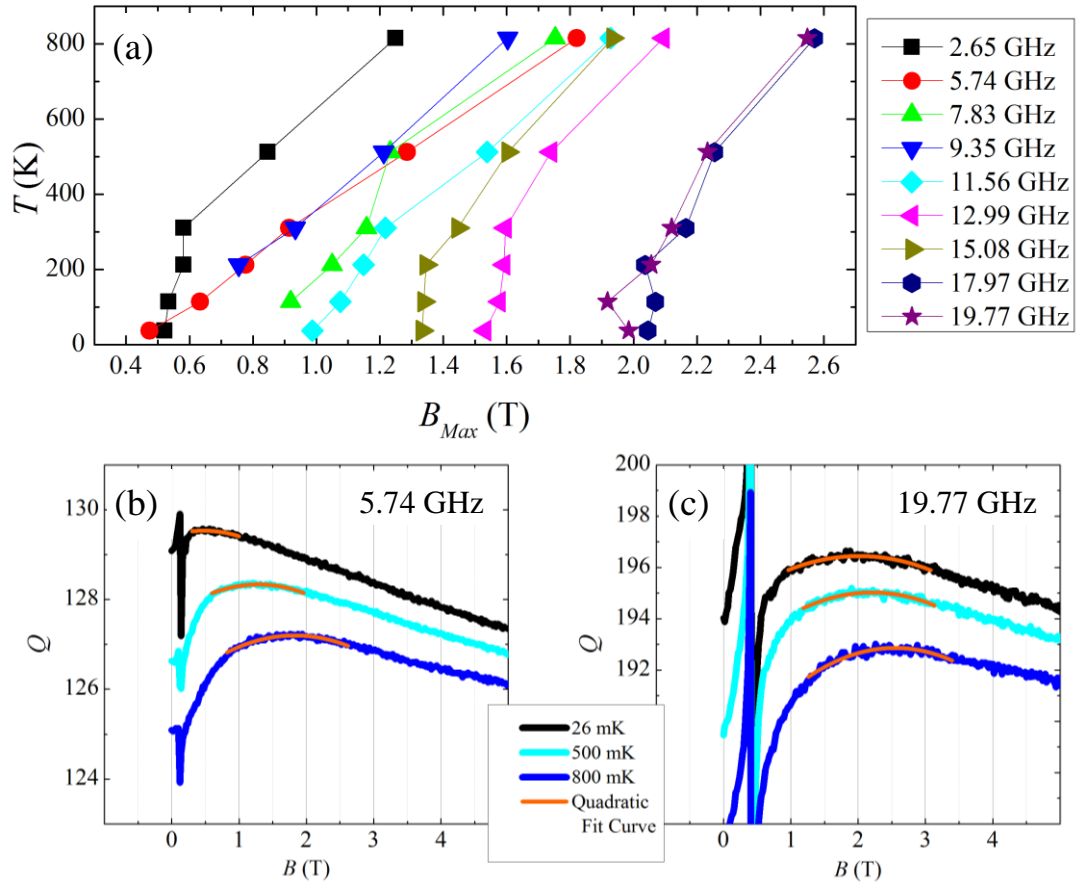


FIG. 6.12. (a) $Q_{off-max}$ positions at different (Mixing Chamber) temperatures and resonances. (b) and (c) contain examples of the quadratic fitting (orange curves) to find $Q_{off-max}$ positions.

6.2. ESR of YbNi_4P_2

YbNi_4P_2 was measured two times with two different samples. The both samples were provided by Cornelius Krellner group. They had different sizes and different sample growth methods [196]. The first sample was a single crystalline needle-shape sample (named as “needle sample” in this work) grown in [001] crystallographic direction and the second sample was a planar large one (named as “plane sample” in this work) which in fact could get cut in any arbitrary direction from the mother sample. Figure 6.13 shows the described samples.

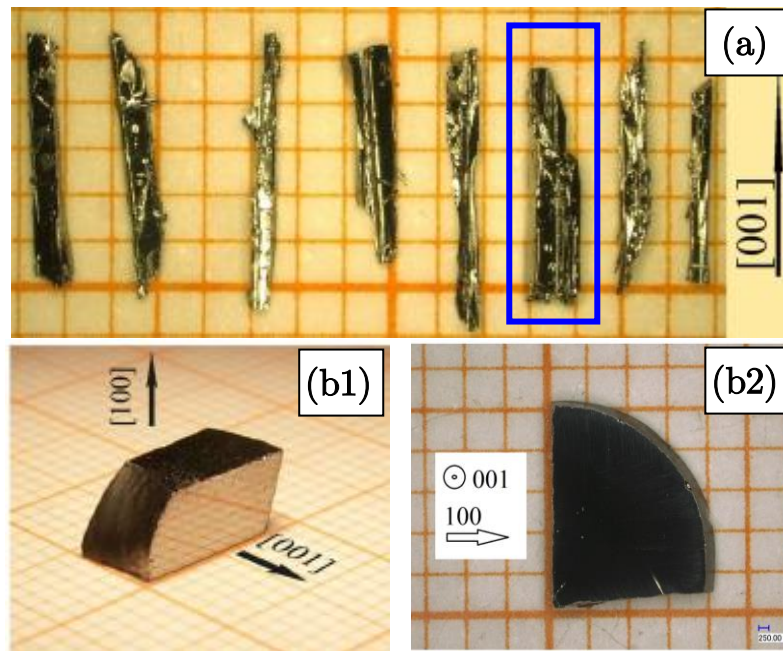


FIG. 6.13. (a) shows single crystalline YbNi_4P_2 samples grown by Bridgman growth [196]. The sample which is pointed by the blue rectangle, was measured in this work. The sample mass is 2.22 mg and Ni impurity level is lower than 20 ppm. (b1) The single crystal ingot grown by Czochralski method from which the sample in (b2) was cut and measured in this work. The sample mass is 94 mg and Ni impurity level is max. 0.045%.

The ESR measurements of YbNi_4P_2 , for the needle sample, were performed at first from 1.7 K to 1.9 K at the VTI and subsequently at mK range by the dilution refrigerator. The needle sample was measured in [001] direction which means the external magnetic field was applied in this direction (parallel with the biggest length of the sample). Plane sample was measured only at mK range. The measurement direction was [100]. That means, for the both samples, the direction of measurement was perpendicular to c -direction (see Figure 3.8 in section 3.2.2, chapter 3).

At VTI temperatures, the needle sample did not show any ESR signature. Several attempts using different resonators, different distance between the sample and the resonator surface and even placing the sample on the resonator with a thin piece of

Mylar foil in between were done to make sure that unobservability of any ESR signal is not because of the improper setting ups and adjustments.

In the milli-Kelvin range measurements, however, an ESR-like signal was obtained, although, it was not significant and sharp signal. The weakness of the gained ESR signatures were not because of the weak coupling of the sample(s) with the resonator signal. It was proven experimentally by placing the sample closer to the resonator surface in various experiments and, furthermore, the shown data in Figure 6.14 suggest the quite satisfying coupling of the sample with the MW signal.

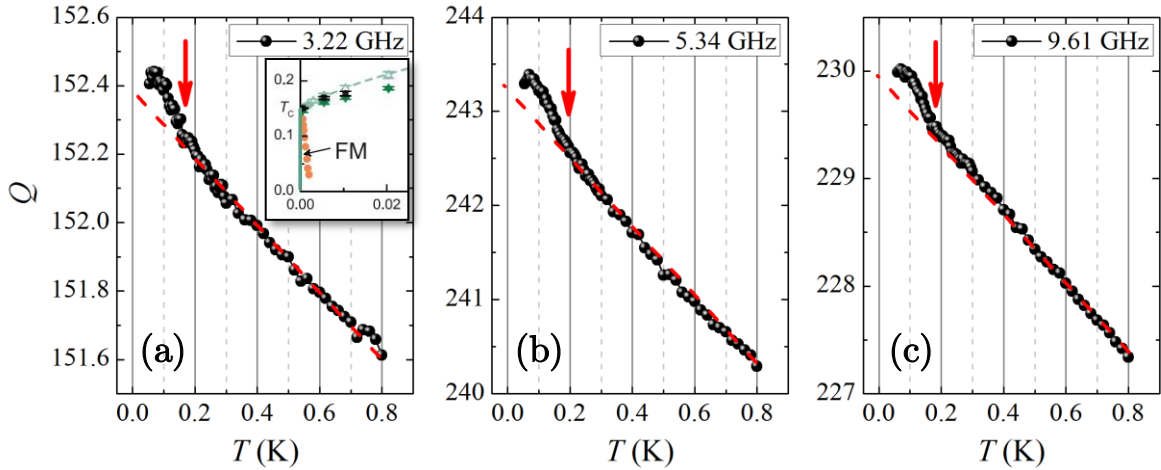


FIG. 6.14. Quality factor versus temperature (Q vs. T) at zero magnetic field for different frequencies of (a) 3.22 GHz, (b) 5.34 GHz and (c) 9.61 GHz for the needle sample, hanging above the resonator surface. The inset of (a) shows a part of the $B-T$ phase diagram of YbNi_4P_2 (see Figure 3.8 (c) in section 3.2.2, chapter 3). The red dashed linear trendlines showing the linear part of the data.

The decrease of the quality factor by increasing the temperature in all the diagrams of Figure 6.14 is in fact the sample effect since the electrical loss of the sample is higher at higher temperature as shown already in Figure 3.9 (b) and (c) (section 3.2.2, chapter 3) for H (or B) = 0 and higher magnetic fields. The higher electrical loss of the sample leads Q to become lower since the carrying signal contain electric fields also which is interacting with the sample.

Another significant feature in these data is the low temperature part of the curves which is deviating from the linear trend of the rest. The beginning point of these features are indicated by the red arrows which match well to the Curie temperature, T_c , of the ferromagnetic (FM) phase of YbNi_4P_2 at $B = 0$ T as seen in Figure 3.9. Hence, this low temperature Q behavior, could be attributed to T^2 alteration of the DC resistivity (Figure 3.9 (b) and (c)) of YbNi_4P_2 in FM phase. This causes the Q to change with a trend following the T^2 trend of the FM DC resistivity. The signature of phase

transitions which are observed in DC transport properties can sometimes be seen in MW spectroscopies also. Ref. [197] discusses signatures of phase transitions in the MW response of YbRh_2Si_2 . In general, phase transitions or alterations which affect DC transport properties of a material, could be sensed in MW probing also to some extent, as for example was shown in section 6.1.2 as well where the non-ESR measurements on YbRh_2Si_2 were discussed.

Some of the obtained Q vs. B curves from ESR measurements of the needle sample are offered in Figure 6.15. All the shown data are taken at lowest possible temperature at dilution refrigerator (≈ 40 mK).

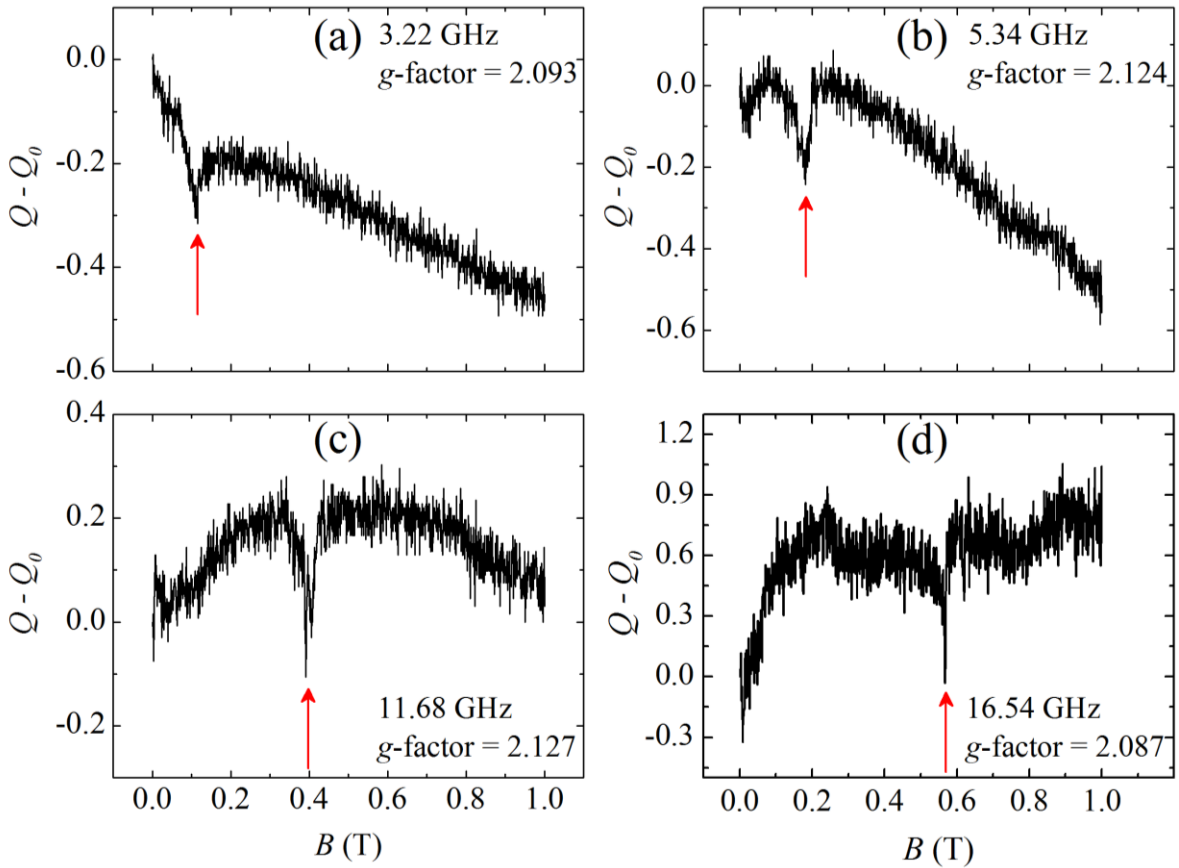


FIG 6.15. The plotted Q ($Q(B)-Q(0)$) versus B for the needle sample of YbNi_4P_2 at ≈ 40 mK. The ESR signature, pointed by the red arrows, is very weak with a g -factor of around 2 which is significantly different than the known g -factor value for Yb^{3+} (≈ 3). The used CPW resonator for these data had a $w = 60 \mu\text{m}$ and $G = 30 \mu\text{m}$.

This very weak ESR signature cannot be attributed to Yb^{3+} ions if considering the calculated g -factor value of around 2 since it does not match the already observed values of around 3 for Yb^{3+} ions. One probability for the origin of this ESR signal are the conduction electrons and another possibility are impurities.

The strong Dysonian ESR signal like YbRh_2Si_2 was not observed from YbNi_4P_2 needle sample in these measurements. One may think that YbNi_4P_2 does not show such an ESR signal inherently, i.e. in other words a type of magnetic moment or phenomenon which is causing the ESR signal in YbRh_2Si_2 does not exist in YbNi_4P_2 , however, the attempts were not stopped at this stage since not obtaining an ESR signal can be simply due to not capturing an ESR signal. In other words, not observing the expected ESR in this case could have some roots in the sample properties and size, instrumentation and laboratorial conditions. To make stronger and more reliable conclusions, the ESR investigations were continued some time later with another single crystalline YbNi_4P_2 sample which was very different than the needle sample in aspect of size and growth method. The new sample was the plane sample as already introduced and shown in Figure 6.13.

As just mentioned above, the ESR study of YbNi_4P_2 was continued by receiving the plane sample and measuring it in $[100]$ direction. Because of the large size sample, the used resonator was selected of the big size resonators with $w = 100 \mu\text{m}$ and $G = 10 \mu\text{m}$. One sort of temperature dependent measurements at $B = 0$ like the ones of Figure 6.14 were carried out to find out if the sample is “seen” by the resonator. Very similar results were obtained as shown below in Figure 6.16. The change in the Q alteration trend at lower temperatures can be attributed to the phase transition to the FM and the T^2 behavior of YbNi_4P_2 DC resistivity in the FM phase; cf. Figure 3.9 (b) and (c).

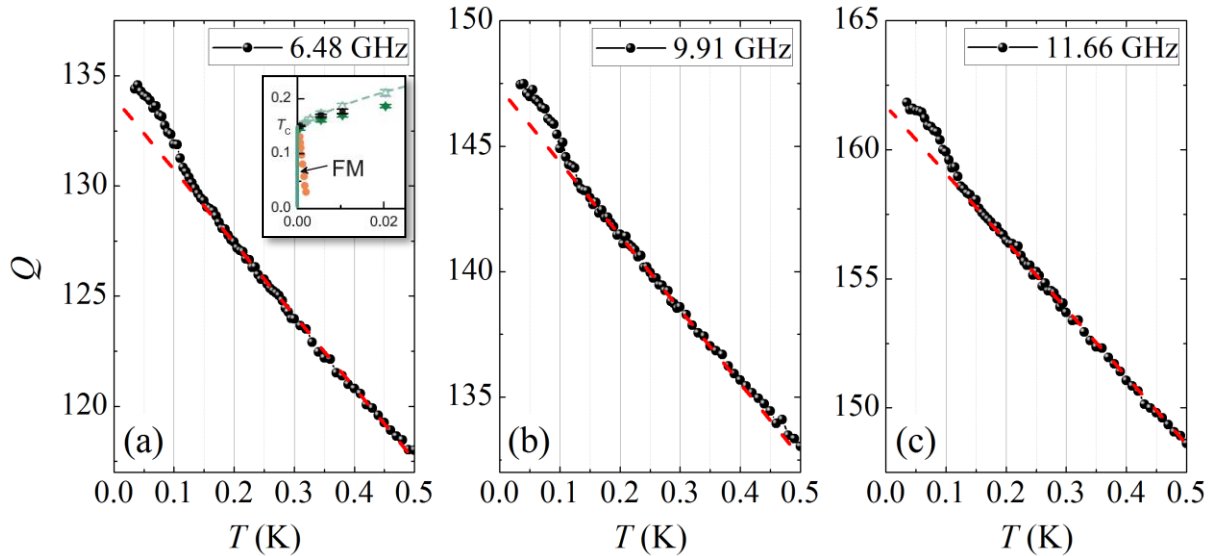


FIG. 6.16. Quality factor versus temperature (Q vs. T) at zero magnetic field for different frequencies of (a) 6.48 GHz, (b) 9.91 GHz and (c) 11.66 GHz for the plane sample, hanging above the resonator surface. The inset of (a) shows a part of the $B-T$ phase diagram of YbNi_4P_2 (see Figure 3.8 (c) in section 3.2.2, chapter 3). The red dashed linear trendlines showing the linear part of the data.

The Q vs. B plots are offered in Figure 6.17. The ESR signatures are shown by the red dashed lines. Each pair of the panels belongs to a given resonance frequency and the right one of which contains the ESR lines for the lowest three temperatures stacked (vertically shifted) upon each other.

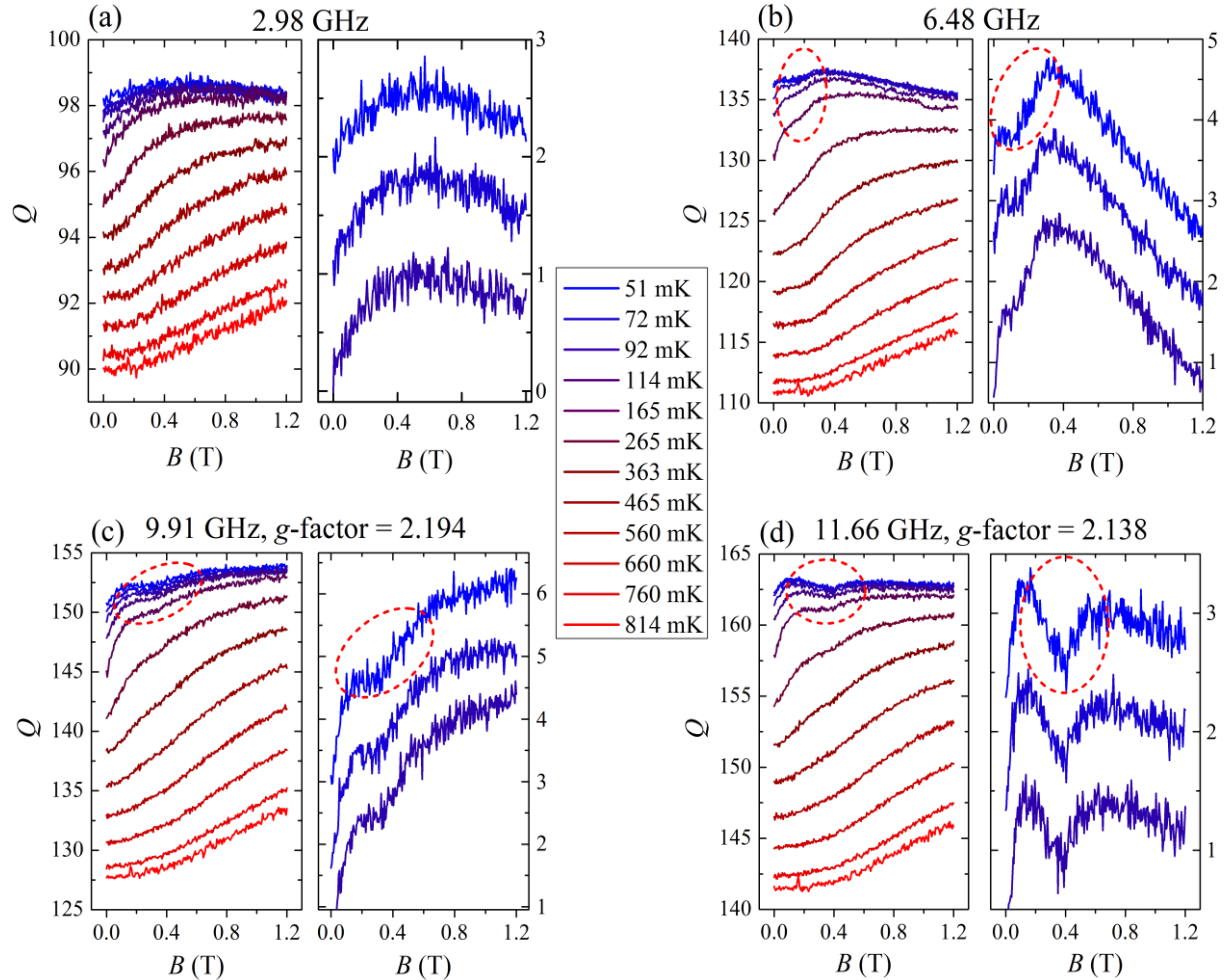


FIG 6.17. Q vs. B curves obtained by the ESR measurements on the plane sample of YbNi_4P_2 . In each pair of the diagrams from (a) to (d) the left side panels contain all the measured temperatures and the right-hand side ones show the curves of the three lowest temperatures slightly shifted vertically (stacked) upon each other for a closer look. The used CPW resonator had a $w = 100 \mu\text{m}$ and $G = 10 \mu\text{m}$.

Before discussing the ESR signals of the lines, it is worth to analyze some of the features, trends and behavior of the lines on changing the temperature as well as the magnetic field. In the left-hand side panels, one notes that by increasing the temperature the lines lay under each other. Since no systematic and significant change in the Q value of the metallic resonators of this work is expected and has been observed (see Figure 6.11 (b) and (d)) in this temperature range, this methodical ordering of the lines under each other is a proof for the dominated response of the system by the sample which had been hanging above the resonator surface.

Another remarkable feature of these lines is the increasing of Q on increasing B . This is more intensified at higher temperatures. This trend could be attributed to the magnetoresistance of YbNi_4P_2 as seen in Figure 3.9 (c) (and (b)) where the resistivity curves of higher magnetic fields are under the ones of the lower magnetic field. This means YbNi_4P_2 has a negative magnetoresistance which is shown for $B \parallel c$ -direction in Ref. [198]. The lower resistivity at higher magnetic fields will accordingly lead to higher Q values.

By analyzing these ESR signatures, one finds that the g -factor value, the intensity of the ESR signals and the range on which the signal is stretched are in good agreement with the results obtained of the needle sample. These g -factors are far different from the well-known g value of Yb^{3+} ions. As discussed already in the case of the needle sample, one probability for the origin of this ESR signal are the conduction electrons and another possibility are impurities.

By considering the obtained data from the both needle and the plane samples, it is possible to make a statement that the ESR is not observable in YbNi_4P_2 or does not happen as for YbRh_2Si_2 . Maybe the 1D characteristics of the Yb ion chains in the crystalline structure of YbNi_4P_2 is an obstacle for motional narrowing. In other words, “moving” of the single $4f$ -spins from one lattice point to the other in ab -plane is not possible since the 1D Yb chains are along c -direction while the FM ordering (fluctuations) is perpendicular to c -direction.

7. Spin-Liquid System

κ -(BEDT-TTF)₂Cu₂(CN)₃

Several series of ESR measurements were carried out at low temperatures on the spin-liquid samples of κ -(BEDT-TTF)₂Cu₂(CN)₃ utilizing the metallic CPW resonators. The frustrated spin states in this (and similar) compound, makes it interesting for investigations which are focused on spin interactions in matter.

The used samples in this work were produced by two different groups R. Hübner in 1. Physikalisches Institut, University of Stuttgart and K. Kanoda's group in University of Tokyo. The former was a larger sample and the latter was a smaller one which will be named as "primary" sample and "secondary" sample respectively in this text. Unless otherwise stated, all the shown data here belong to the primary sample which was intensively used in this ESR study. The primary sample (placed on the CPW resonator) is shown in Figure 7.1 (a) and highlighted by the red line border.

The measurements were performed at the VTI and the dilution refrigerator. The results of the latter will not be mentioned since the temperature coupling of the sample and the heat sinks of the setup were not proven to be proper and secondly the quality and intensity of the obtained data were too poor.

The temperature range for the VTI measurements was from 1.55 K to 9 K. The highest achievable frequency was around 16 GHz since the sample has higher conductivity at higher frequencies [199]. Between the resonator surface and the sample, a 20 μ m Mylar foil was placed. The sample was fixed by vacuum grease only at one side of it on the Mylar foil and the Mylar foil was also fixed with vacuum grease on the resonator. It is worth to mention that several attempts were done to find an optimum configuration of sample positioning on the resonator to have higher frequencies since by placing the sample directly on the resonator surface no frequency above \approx 11 GHz was obtainable.

Figure 7.1 shows the measured area and points on the phase diagram of κ -(BEDT-TTF)₂Cu₂(CN)₃. The phase diagram is taken from Ref. [160].

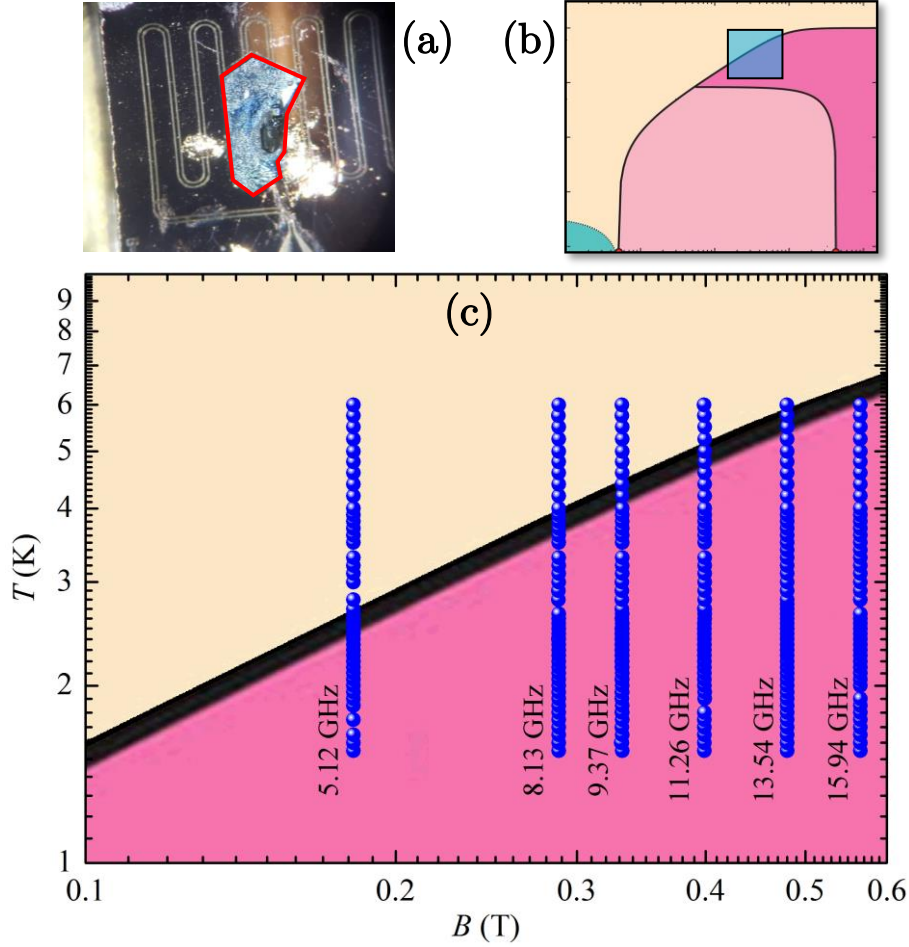


FIG. 7.1. (a) shows the primary sample placed on the resonator. The border of the sample is highlighted by the red line. The used sputtered resonator had a $w = 60 \mu\text{m}$ and a $G = 40 \mu\text{m}$. (b) The $H-T$ phase diagram of $\kappa\text{-(BEDT-TTF)}_2\text{Cu}_2(\text{CN})_3$ [160] on which the measured points in this work are confined in the transparent blue rectangle. (c) is the zoomed in part of the phase diagram with the measured points at various frequencies (fields). Both axes are scaled logarithmically.

The procedures of the measurements were like the previous cases for other materials. However, the data were sometimes collected for all temperatures at a single mode and the next mode was measured afterward and so forth. Since the stability of the VTI during the long-time scales (longer than ≈ 8 hours) is a matter of concern, to have a consistent data for a range of temperature, it was preferable to measure one single mode completely for all desired temperatures in one run. The experiment is then repeated for the next mode in a new cooling run.

All the measurements of the primary sample were performed in-plane (bc -plane, shown in Figure 3.12 (c), chapter 3) in c -direction which means the magnetic field was applied parallel to c -direction.

In Figure 7.2 some examples of the ESR lines (Q vs. B) are given. The lines are stacked above each other. In the figure a limited number of the obtained lines are shown. The experiments were done with 0.05 K steps from the base temperature up to 3 K, then 0.10 K up to 4 K and bigger steps at higher temperatures.

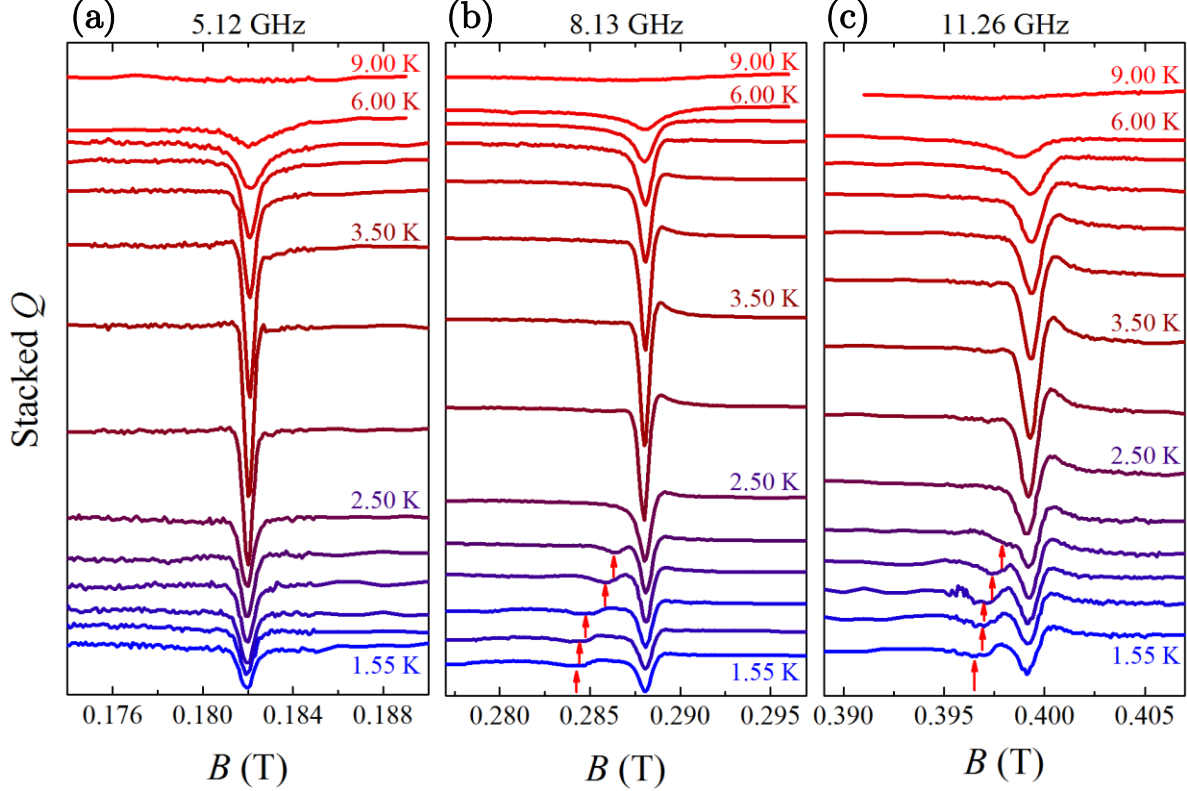


FIG. 7.2. The typical obtained ESR lines examples from κ -(BEDT-TTF) $_2$ Cu $_2$ (CN) $_3$ by a metallic CPW resonator. The lines are stacked (shifted vertically). The red arrows in (b) and (c) show an emergent new absorption which will be discussed and elaborated later.

In several transport and thermodynamic properties studies of this compound, anomalies have been observed around 6 K [4] [159] [164] [166] [169] [200]. However, since the obtained data for above 6 K in this work were not enough intense for further analysis, no comment or comparison can be made about the famous 6 K anomaly. The ESR signals above 6 K were noisy and very poor to be recognized. This does not solely caused by the physics of the material but the sensitivity of the signal detection in this system also.

The first very interesting observation in our data is the change of the intensity of the signal by approaching 3.3 K. Depending on the resonance frequency (resonator mode), the signal intensity is the highest between 3.2 K to 3.5 K, with no difference for upward or downward ramping of the temperature. This is shown for the ESR lines obtained at 8.13 GHz in Figure 7.3.

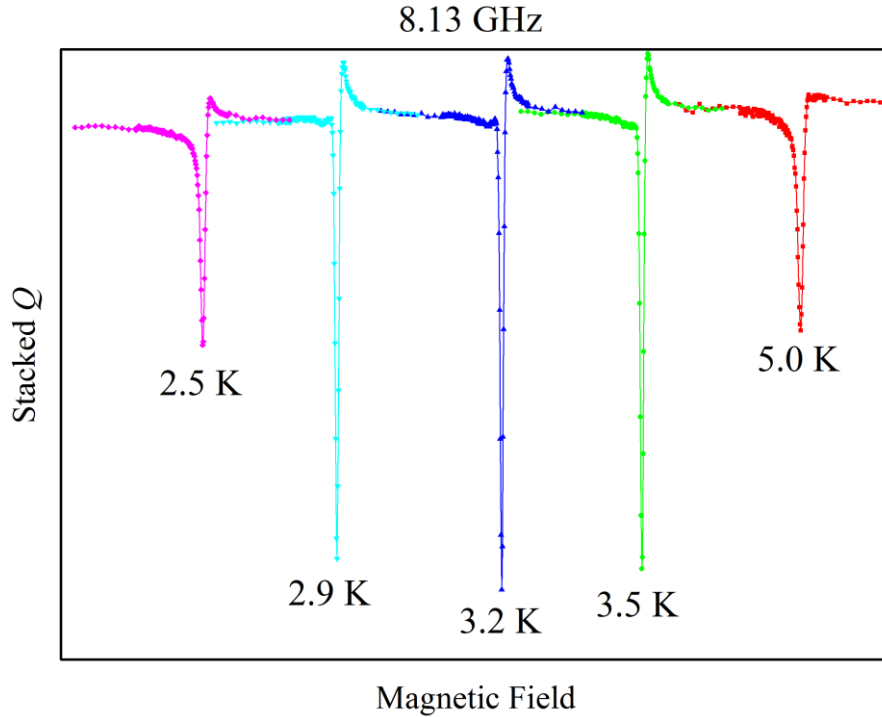


FIG 7.3. Q vs. B curves (ESR lines) of measurements on κ -(BEDT-TTF) $_2$ Cu $_2$ (CN) $_3$ for different temperatures. The intensity of the curve at 3.2 K is significantly bigger than the others. The applied magnetic field resolution is different at and near the ESR signal from the ranges far from it. This is mentioned and discussed in the text. The curves are shifted vertically and horizontally to be comparable in intensity

A detailed analysis of the signal intensity, susceptibility χ , will be offered later when other features of the ESR lines were mentioned. This change in the intensity of the signal could be interpreted as entering a new phase.

The other feature which attracted our attention was the emergence of a new ESR feature. By lowering the temperature, at around 2.4 K the new ESR signature emerges which is shown briefly in Figure 7.2 (b) and (c) by red arrows. Figure 7.4 shows this with more details. It must be noted that this new ESR feature was observed for all resonance frequencies except 5.12 GHz. At this frequency no emergent ESR signal was seen down to 1.55 K which was the lowest achievable temperature by the VTI. Although not shown in Figure 7.4, the emergent ESR was observed at the frequencies of 9.37 GHz and 15.94 GHz also. However, the signal (for the new ESR line) was not analyzable because of the excessive level of noise in these two frequencies.

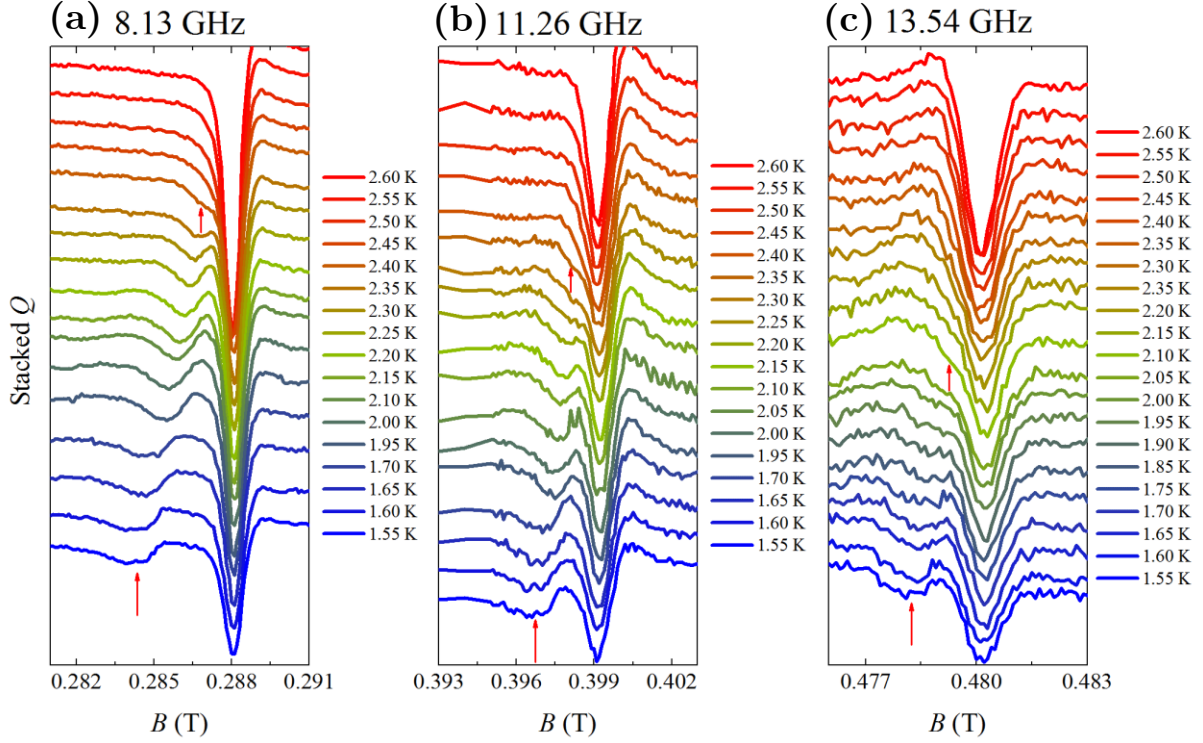


FIG. 7.4. The evolution of the ESR lines with temperature. The new ESR absorption occurs on the left-hand side of the main ESR signal and moves leftward by decreasing the temperature in all the three panels of (a) 8.13 GHz, (b) 11.26 GHz and (c) 13.54 GHz. The upper red arrows show the (almost) first temperature at which the new signature becomes observable and the lower arrows show the emergent signature at the lowest achievable temperature in these experiments which was 1.55 K.

The occurrence of the new ESR signal with lower resonance field and subsequent moving toward lower fields is anisotropic which was tested and will be shown later.

As mentioned above, the highest signal intensity belongs to 3.2 K to 3.5 K. In some other publications also, an anomaly between 3 K to 4 K is observed [164] [169] [201], however, it is not explained or even not mentioned. Figure 7.5 shows the susceptibility calculated of the ESR lines by fitting them with a Lorentzian formula.

Since ESR takes place at a given frequency, the ESR signal intensity is directly proportional to the imaginary part of the magnetic susceptibility (at the same frequency of the ESR) of the material. The occurrence of the maximum susceptibility in the range of 3.2 K to 3.4 K matches very well the data given as the imaginary susceptibility of κ -(BEDT-TTF)₂Cu₂(CN)₃ in Ref. [201] which is shown here as Figure 7.6 (a). It must be noted that the data of Figure 7.6 (a) are taken at different magnetic fields although the frequency stays constant at 16.5 GHz, whereas, in our ESR data when the external magnetic field changes to higher values the frequency must also change accordingly to fulfill the conditions for ESR. Thus, one cannot expect the same effect which field increasing has on χ'' trend at a single frequency to be observed on ESR data also.

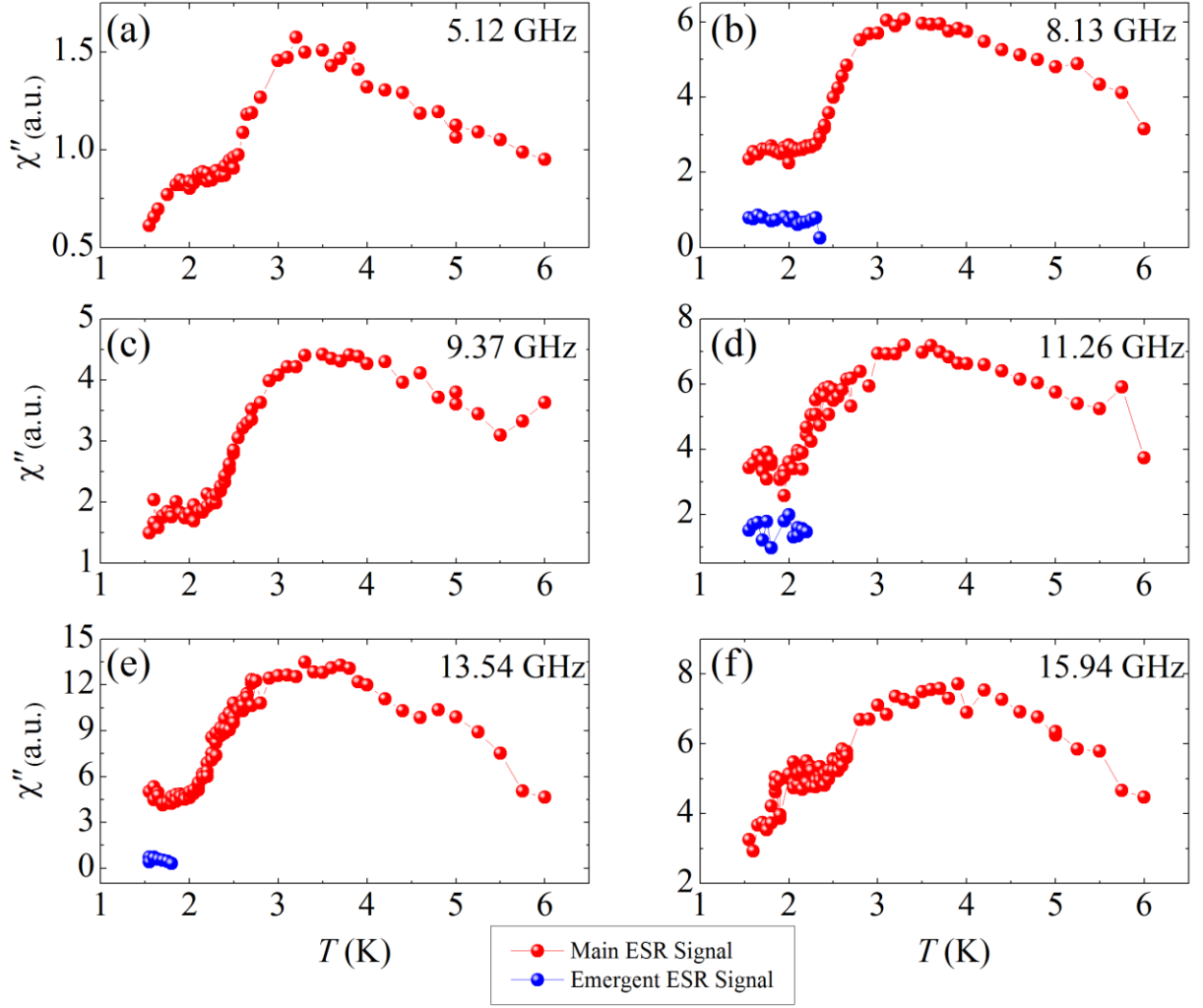


FIG. 7.5. The susceptibility obtained of the ESR lines vs. temperature for the main and the emergent ESR signals at various frequencies. The used sputtered resonator had a $w = 60 \mu\text{m}$ and a $G = 40 \mu\text{m}$.

This is shown in practice in the following: The position of the maximum for χ'' in Figure 7.6 (a) shifts towards lower temperature when the field is changed from 0 T to 4 T and further to 8 T, whereas, the maximum ESR intensity in this work (Figure 7.5) moves toward higher temperatures by increasing the field from 180 mT to 570 mT. This observation may be explained by the fact that the maximum ESR intensity depends more on the frequency rather than magnetic field. When we change the field from 180 mT to 570 mT, the frequency changes from 5.12 GHz to 15.94 GHz either.

Nevertheless, as long as we compare the ESR intensity (χ'') response to temperature at a single frequency (data of Figure 7.5), the trend of the obtained susceptibility from the ESR measurements of this work and the data of Figure 7.6 (black curve of χ'') confirm each other very well in terms of the maximum occurrence and the kink features.

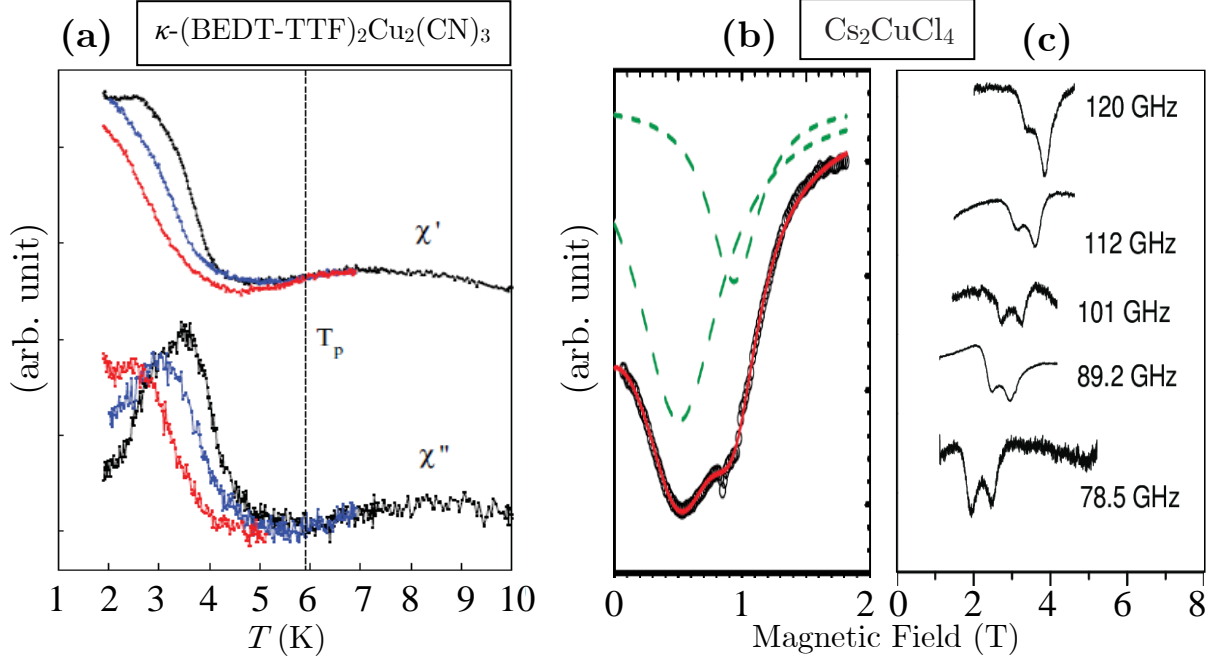


FIG. 7.6. (a) The real (χ') and imaginary (χ'') part of the susceptibility of κ -(BEDT-TTF)₂Cu₂(CN)₃ at 16.5 GHz taken from [201]. Magnetic field is applied in-plane: black: 0 T, blue: 4 T, and red: 8 T. (b) The double Lorentzian ESR line of the spin-liquid Cs₂CuCl₄ at 1.3 K at 27 GHz [202]. The dashed lines show the two Lorentzian ESR lines extracted from the experimental data (circles and the red line). (c) The ESR lines doublets of the spin-liquid Cs₂CuCl₄ at 0.5 K at different frequencies [203].

A substantial alteration in the data of $\chi''(0 \text{ T})$ in Figure 7.6 is not expected up to 600 mT when we compare $\chi''(0 \text{ T})$ with $\chi''(4 \text{ T})$.

One important question here is that why does the ESR signal intensity (χ'') is decreasing at temperatures lower than $\approx 3.3 \text{ K}$? Is it the lower magnetization which is causing the fall of ESR intensity or is this happening because the lower number of (oriented) spins are showing ESR? The answer of this question could be the latter since the real part of the susceptibility, as shown in Figure 7.6 (a), is still increasing by further cooling down and this is the imaginary part which is decreasing in magnitude. In fact, what we see as the decreasing of the ESR signal intensity is not because of the lower magnetization of the sample but a lower number of oriented spins which are able to show the ESR resonance.

It is hard to say if there is any signature of the emergent ESR in the shown data of Figure 7.6 (a).

Alteration of the ESR signal by temperature to two ESR signals is once observed in this compound around 8 K by Ref. [166]. The observed behavior of two Lorentzians in ESR field and their splitting from each other, could be a signature of the simultaneous presence of two various magnetic contributions or magnetic sublattices (spin domains).

Since they respond differently to the external magnetic field because of different spin relaxation mechanisms and locally different internal magnetic fields, two separated ESR lines and g -factors become observable in the ESR spectra. Figure 7.7 and Figure 7.8 show the ESR linewidth and g -factor of the primary sample. The emergent ESR signal for the frequencies of 9.37 GHz and 15.94 GHz was unfortunately too noisy for analyzing. At 5.12 GHz no emergent ESR was revealed.

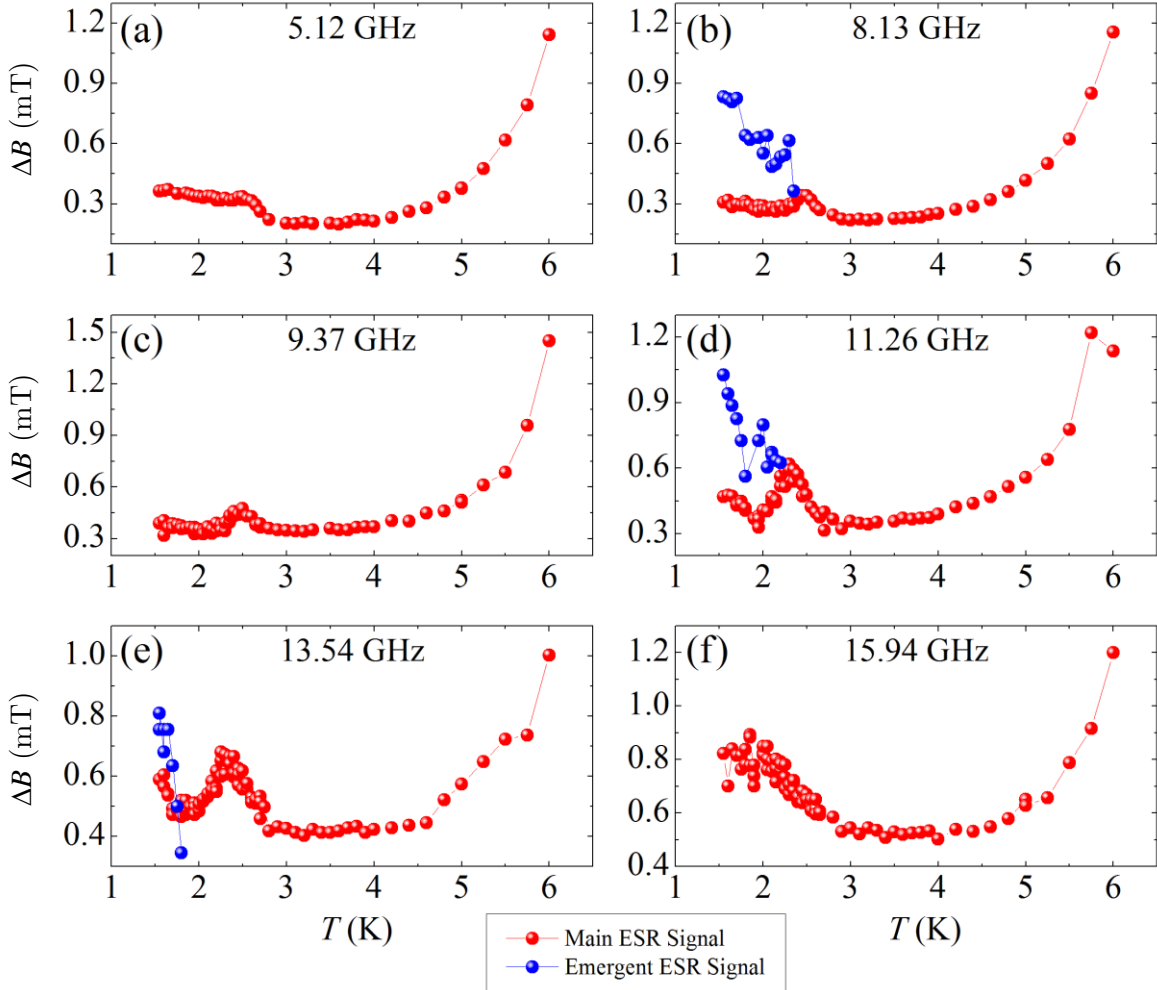


FIG. 7.7. The ESR linewidth of κ -(BEDT-TTF) $_2$ Cu $_2$ (CN) $_3$ obtained of the ESR measurements by a sputtered CPW metallic resonator with $w = 60 \mu\text{m}$ and a $G = 40 \mu\text{m}$.

As can be seen in Figure 7.7, by lowering the temperature, right before the emergent ESR starts to appear, the ESR linewidth ΔB broadens slightly. This is a clear sign for the formation of a new coherence in a part of magnetic moments (spins) which differs in g -factor (Larmor frequency) and gets magnetically “separated” from the main batch of the spins; Figure 7.8. Generally, the higher the variation of Larmor frequencies in a spin ensemble, the wider the ESR linewidth. These become fully “separated” later by further cooling down and form a new collective magnetization with its own magnetic resonance which generates the so called (in this thesis) “emergent” ESR.

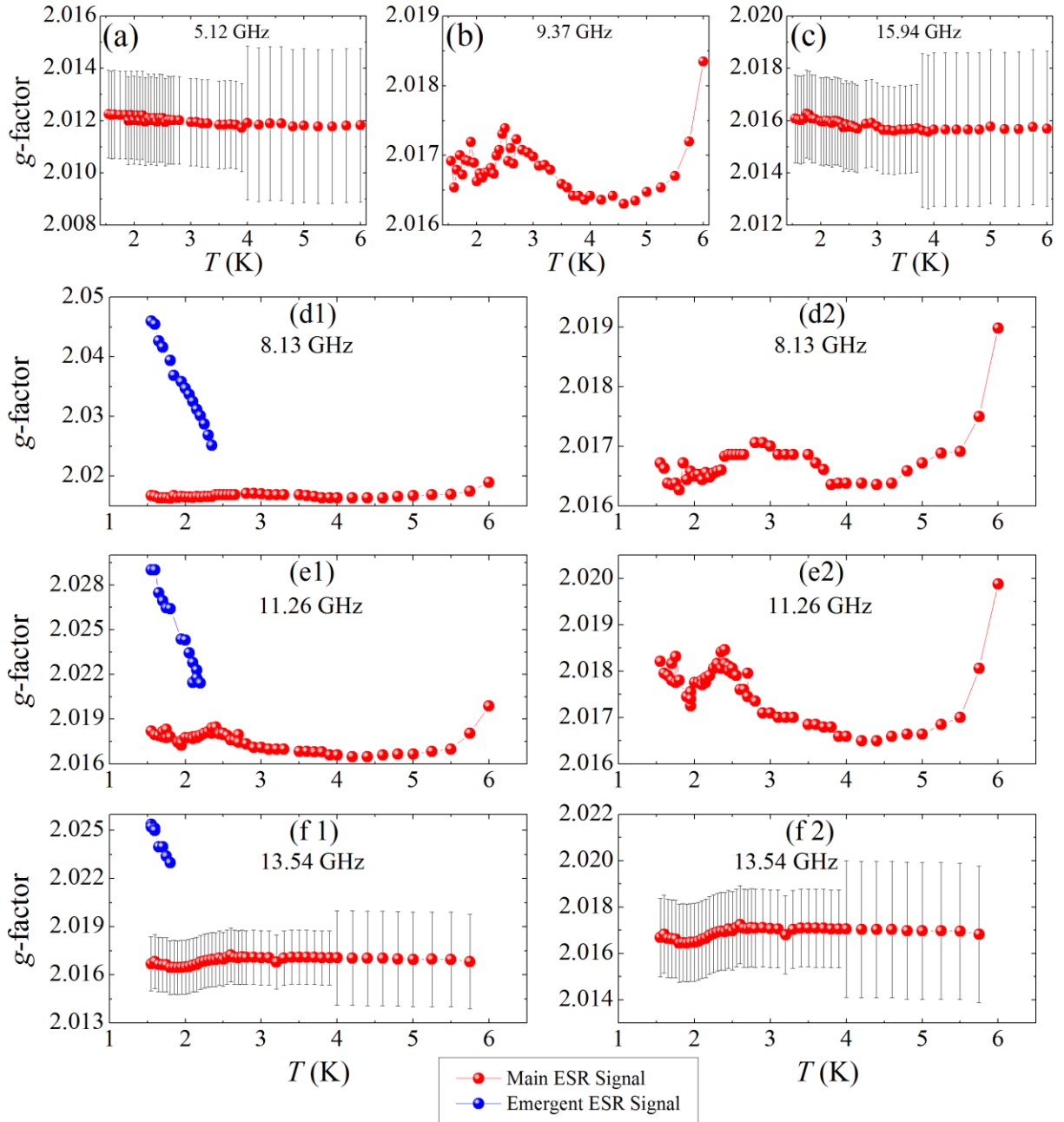


FIG. 7.8. The g -factor of κ -(BEDT-TTF) $_2$ Cu $_2$ (CN) $_3$ obtained of the ESR measurements by a CPW metallic resonator. (d2), (e2) and (f2) contain the same data of (d1), (e1) and (f1) but without the data points of the emergent ESR to see the data of the main ESR signal in a bigger scale with more details. The error bars are determined by the uncertainty in determination of the resonance fields stemming from a slight noise in the data so that finding the exact point as the resonance field was not possible. This was not a problem in the case of the data at 8.13 GHz, 9.37 GHz and 11.26 GHz and the fitting procedure of the ESR signal could always yield a given point as the resonance field.

The g -factor of the emergent ESR raises by further cooling down which leads to the moving of the emergent ESR leftward as shown in Figure 7.4. As will be discussed later

in the text, the g -factor may decrease for the emergent ESR because of the probable anisotropy in the magnetic lattice of this spin liquid compound.

The doublet of the ESR signal is an obvious sign of coexisting of various spin “groups” in the system and now the question is what kind of spin groups they are? The ESR doublet shows that there are two correlated spin continuums in the system, because, if they were more than two, we would have most probably seen more than one emergent ESR signal. Therefore, it could intuitively be concluded that the hypothesis of spin domains formations and domain walls is not correct since, first, the formation of spin domains is in contrast to the nature of a frustrated spin system and thus it is very unlikely, and second, in all the measured samples with different sizes and growth methods only one emergent signal was observed and no more. If spin domains had been formed, why must there only be two domains in all the samples? Thus, the formation of spin domains cannot describe the ESR doublet with all details.

The most likely reason for the doublet of the ESR signal is introduced to be spinon continuums and their inherent interactions in the spin chains in triangular spin liquid systems [202] [203]. The spinon continuums must not be mistaken with dimer spinons shown in e.g. Figure 3.11.

Spinon continuums formation and emerging new collective magnetic interactions is discussed in Ref. [202] and [203] in which, the inorganic spin-liquid compound Cs_2CuCl_4 showed a double Lorentzian ESR lineshape. Cs_2CuCl_4 is spin liquid between 0.62 K and 4 K. Figure 7.6 (b) and (c) show the experimental data of Cs_2CuCl_4 from [202] and [203] at 1.3 K and 0.5 K respectively. The distorted lattice of this compound is described by a quasi-two-dimensional model of spin- $\frac{1}{2}$ Heisenberg antiferromagnetic model. However, the elementary excitations of this spin liquid are like the one-dimensional fermionic spinon excitations [202] [203] [204]. Thus, it could be viewed as quasi-one-dimensional lattice. This is due to the presence of a uniform Dzyaloshinskii–Moriya (DM) interaction between the in-plane copper spins [202] [203] [204]. The DM interactions are a result of frustration in such Heisenberg antiferromagnetic lattice. These interactions weakly couples the singlet spin in the 1D chains of Cu. The DM couplings are responsible for the emergence of long-range magnetic order at sufficiently low temperatures [202]. They cause the formation of Spinon continuums. The appearance of Spinon continuums is in fact the formation of bosonic spin pairs from a fraction of the fermionic spins (chapter 3, section 3.3). In the case of Cs_2CuCl_4 two Spinon continuums are formed which is a result of 1D Cu chains in the quasi-2D lattice of this compound.

The presence of DM interaction has theoretically been discussed in the organic compound with weak ferromagnetic phase κ -(BEDT-TTF)₂Cu[N(CN)₂]Cl also [205]. Hence, the presence of the DM interactions in κ -(BEDT-TTF)₂Cu₂(CN)₃ is not an unexpected phenomenon. The cavity resonator ESR measurements of κ -(BEDT-TTF)₂Cu₂(CN)₃ in 1. Physikalisches Institut always showed that the intensity of the ESR signal is in one given in-plane direction the highest. This can be interpreted as the 1D preference in the correlation of the spins in this spin-liquid compound. Existing the DM interactions between the κ -(BEDT-TTF)₂ dimers at low temperatures (≈ 2.3 K as shown in Figure 7.8) can be the reason for the double ESR observation in this material as well. DM interactions in κ -(BEDT-TTF)₂Cu₂(CN)₃ has been discussed and proposed in Ref. [166] as well.

A helpful experiment to provide information for confirming the DM interactions among κ -(BEDT-TTF)₂ dimers is checking the sample isotropy/anisotropy for the emergent ESR signal. The κ -(BEDT-TTF)₂ dimers are placed canted beside each other and the antiferromagnet order and the spinon continuum magnetizations could also be canted. Thus, a change in the ESR signal could be expected if the external magnetic field is applied in other directions.

For this purpose, the secondary sample (the sample which was grown by Kanoda's group in University of Tokyo) was measured twice. In the second measurement the sample was rotated 90 degree relative to its position in the first measurement. With this the relative orientation of the sample and the external magnetic field was rotated also. Both the measurements were performed in-plane (the external magnetic field was applied parallel to the *bc*-plane).

The ESR lines of the first measurement are shown in Figure 7.9 (a). The curves in 7.9 (b) are the ESR lines of the same sample after 90 degree in-plane rotation. As seen in the figure, the new ESR signal appears on the right side of the main signal and evolves toward higher fields on decreasing the temperature. After rotating the sample 90 degree and repeating the measurement, interestingly, the new ESR appears this time on the left side of the main ESR and evolves toward smaller fields by decreasing the temperature as shown in Figure 7.9 (b).

This result could hint at belonging the emergent ESR signal to κ -(BEDT-TTF)₂ dimers since, as mentioned above, their canted standing up orientations relative to the external magnetic field is changed after a 90 degree rotation. Therefore, the probability that the anions, Cu₂(CN)₃, are the corresponding magnetic moments of the emergent ESR is low compared to (BEDT-TTF)₂ dimers.

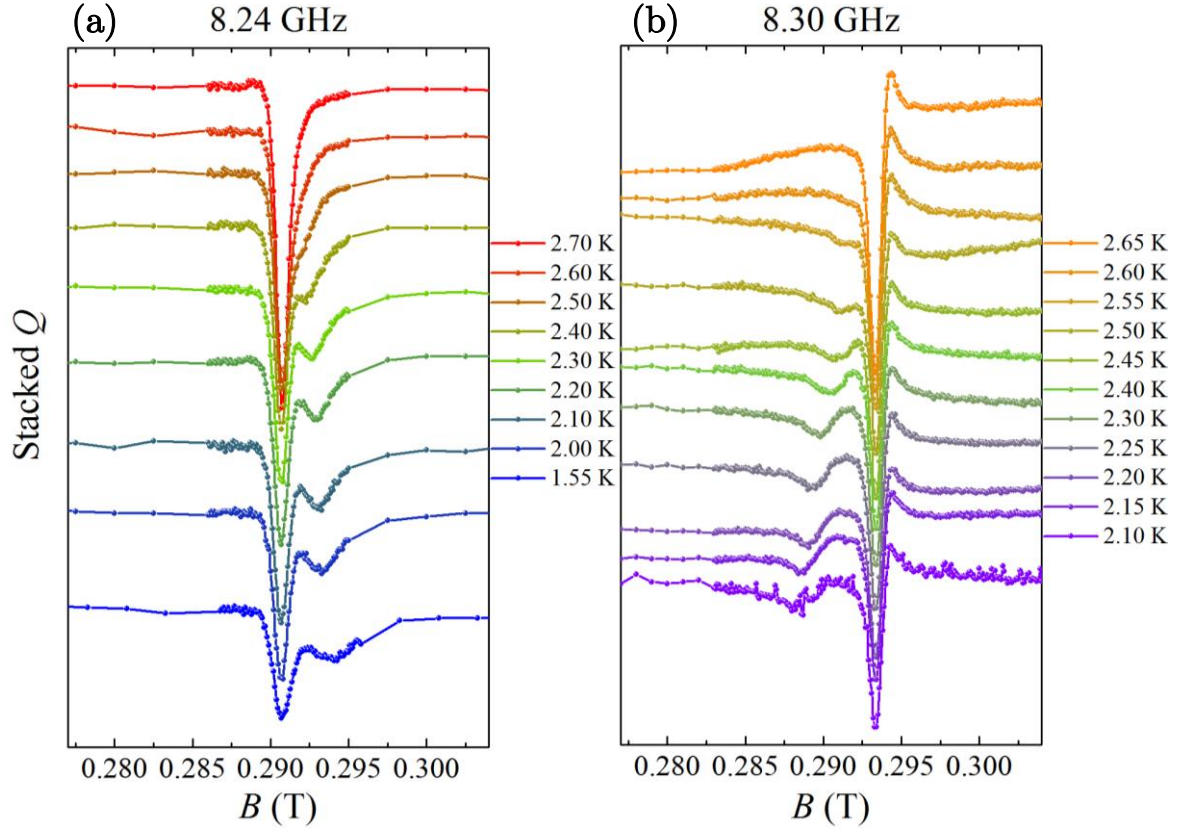


FIG. 7.9. The ESR lines of the secondary sample for (a) before and (b) after 90° rotation of the sample on the resonator surface. The slight difference in the resonance frequency (8.24 GHz vs. 8.30 GHz) comes from the different positioning of the sample on the resonator and a slight change in the effective permittivity of the resonator.

Since the achieved data of κ -(BEDT-TTF) $_2$ Cu $_2$ (CN) $_3$ in this work cover a relatively large range of temperature and magnetic field, the proposed $T - H$ phase diagram in Ref. [160] can now be modified and elaborated. The modified phase diagram is shown in Figure 7.10.

The QC (Quantum Critical) and WAF (Weak Antiferromagnetic) phases of the old phase diagram of Ref. [160] are now divided to three distinct regions. “ESR Incr.” phase is the region in which the ESR intensity increases monotonically. “ESR Decr.” shows the phase in which the ESR intensity decreases monotonically. “Dbl. ESR” represents the region in which the new ESR signal emerges and evolves further. It must note that at 5.12 GHz (corresponding to 0.182 T) no emergent ESR was observed down to 1.55 K, thus, the real beginning of the region “Dbl. ESR” may be different as what is shown here.

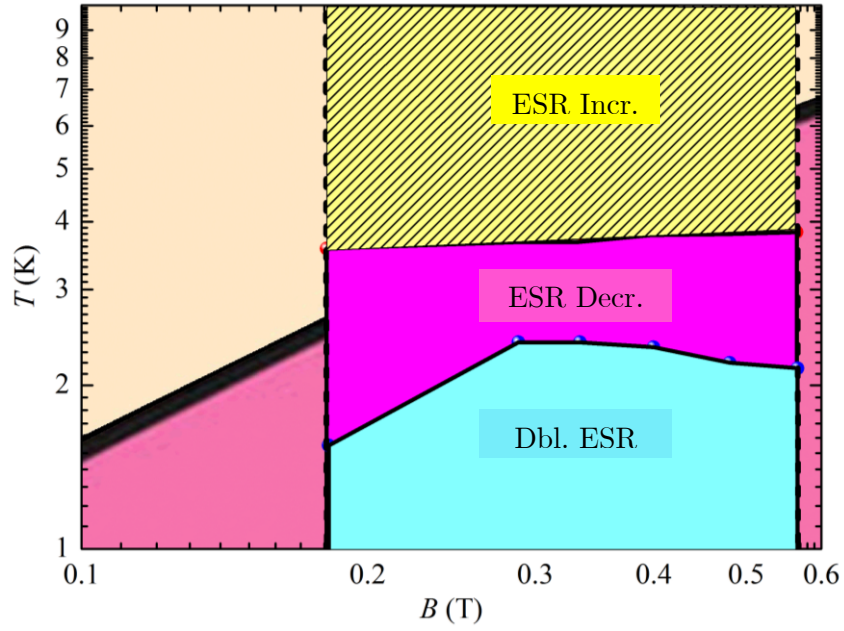


FIG. 7.10. The partial modification of the $T - H$ ($T - B$) phase diagram of κ -(BEDT-TTF) $_2$ Cu $_2$ (CN) $_3$ from Ref. [160] by the obtained data of this work. The scales are logarithmic on the both axes.

8. Summary and Outlook

In this work a new tool for electron spin resonance (ESR) spectroscopy was developed by which some strongly correlated materials were investigated. The obtained data were comparable with the ones of the conventional methods. In some cases, the new developed system was able to uncover and yield even new states and phases in the examined samples. This would not be feasible by the other so far utilized ESR systems and methods.

The advantages and efficiency of coplanar waveguides and resonators (CPW resonators) in comparison with conventional cavity resonators could be noted by considering the points at the following:

- Higher capability of ESR measurements since a CPW resonator has several resonances (resonator modes) in contrast to single resonance performance of the cavity resonators,
- Achieving desired resonance frequencies easily by modifying the geometrical parameters or manufacturing materials of the CPW resonator,
- Increasing the feasibility of ESR measurements at ultra-low temperatures since a CPW can be produced with a relatively small size and hence they are well compatible with dilution refrigerators,
- The small size help achieving higher filling factors,
- Achieving very high quality factors since they could be made of superconducting materials,

The advantageous performance of CPW resonators in the ESR measurements, in the case of a conventional superconducting CPW, could be affected by the severe distortion of the obtained signal since the quality factor of the resonator dramatically falls by application of magnetic fields. This could, however, be eliminated by using normal metallic CPW resonator, although, the quality factor values are smaller.

Furthermore, one of the most important characteristics of a measurement tool or method is the high stability and having artefacts as low as possible. In the superconducting CPWs the quality factor alteration is quite significant by changing the temperature even in the range of far below the critical temperature (T_c). This means, the change in the intensity of the ESR signal at various temperatures is not a pure effect of the sample under study since the resonator loss changes also.

In addition, Superconductors have Meissner effect also which repels the magnetic field and can cause local magnetic field intensity to increase on around the material. This can lead to have a field intensity on the sample higher than the aimed one.

To overcome the drawbacks of superconducting CPWs, the metallic CPW resonators were designed, fabricated, measured and optimized by redesign through the first phase of this work [206]. The quality factors as high as 470 were achieved at low temperatures which was a remarkable value for such miniaturized resonators. They showed constant quality factor values from almost 20 K down to the lowest achieved temperatures. This means, the observed variations in the ESR signal intensity by changing the temperature in the measurements of under 20 K could be well attributed directly to the properties of the sample under test.

The mentioned and achieved advantages of the metallic CPW resonators compared to the superconducting ones are listed below:

- No severe drop of quality factor even up to 7 T. Around 0.1% of quality factor change from 0 to 0.5 T compared to almost 90% of quality factor loss of a conventional superconducting CPW for the same field range. This avoids the tedious numerical analysis and regression analysis to remove the distortions in the ESR signals,
- Stability of the quality factor value for all the temperatures below 20 K whereas the T_c of Niobium is ≈ 9 K,
- No repelling of the magnetic field and local increase of the field which causes the aimed field magnitude and the sensed field magnitude by the sample to be closed together as much as possible,
- Simplicity of the system since no vortex loss mechanism of superconductivity is involved.

As a part of the qualification process and checking the reliability of the fabricated resonators performance in yielding reliable data, the first ESR experiments were performed by measuring the well-known calibrating material for ESR tools: 2,2-diphenyl-1-picrylhydrazyl (DPPH). Sharp ESR lines from DPPH were observed at various frequencies. These data were very helpful to understand one important artefact

of metallic CPW resonator in ESR measurements. That was the emergence of two bumps right after and before the ESR trough in the case of having a material whose ESR linewidth is narrower than the resonator resonance linewidth. This is explained in chapter 5.

The materials of interest in this work were, however, the exotic materials with quantum phase transitions. In these compounds observing and alteration of ESRs have always been a surprising and interesting phenomenon. The materials were:

- Two heavy fermions (HFs): YbRh_2Si_2 and YbNi_4P_2
- One spin-liquid: $\kappa\text{-(BEDT-TTF)}_2\text{Cu}_2(\text{CN})_3$

The ESR measurements of YbRh_2Si_2 with the metallic CPWs of this work revealed new data which confirmed and partly challenged the conclusions which were made based on the ESR experiments with superconducting CPW resonators. One of the new observations with metallic CPWs was the increase of g -factor in the Landau Fermi Liquid regime of this compound whereas the data obtained from superconducting resonators experiments did not show it at all.

Another result was a non-linear dependence between ESR linewidth and $\log(T)$ in the transition range from Landau Fermi Liquid to non-Fermi Liquid phase. In Ref. [194], such a dependence is introduced in NFL region, however, for temperatures above 4 K.

In the obtained ESR data by the metallic resonators (as well as by the superconducting ones) no probable effect of T^* line (range) on the ESR linewidth could be observed.

One of the hypothesizes about the observance of the ESR signals in HF Kondo lattices is the presence of short-range FM correlations between the screened moments. YbNi_4P_2 as a HF compound with FM order and polarizations might yield data which could be helpful in elaborating this theory. Therefore, two different samples of YbNi_4P_2 were measured. Despite trying several different measurement conditions like changing sample position in the resonator box and as just mentioned using different samples with totally different sizes and growth method, no sharp and well-defined ESR signal like in the case of YbRh_2Si_2 was obtained. This could be due to the quasi-one-dimensional Yb^{3+} ions along c -direction of the crystal and avoiding the motional narrowing mechanism among the moments with FM correlation.

The ESR measurements of $\kappa\text{-(BEDT-TTF)}_2\text{Cu}_2(\text{CN})_3$ were very rich in yielding new and (so far) unseen results. The motivation to measure it was to investigate the ESR observability at lower temperatures and ESR alteration in a highly correlated spin system with a geometrical magnetic order frustration.

The intensity of the ESR signal on decreasing the temperature from 6 to ≈ 3.2 K at all measured frequencies (≈ 5 to ≈ 16 GHz) increases as it is expected for every system. However, on cooling down further from ≈ 3.2 K the signal begins to get reduced in intensity down to 1.55 K which was the lowest available temperature at the used variable temperature insert (VTI) setup. This agrees the imaginary part of the susceptibility which is reported in Ref. [201]. In the same reference the real part of the susceptibility is shown to be increasing monotonically by decreasing the temperature down to under 2 K, whereas, as just mentioned, the imaginary part starts to fall down from ≈ 3 K or 4 K depending on the applied magnetic field. Thus, it seems that the major reason for the weaker ESR intensity for the temperatures lower than ≈ 3.2 K is the lower number of the spins which show ESR and it is not because of a lower magnetization.

On decreasing the temperature further from around 2.3 K, a new ESR signal evolves from the main signal. This reveals the formation of a new magnetic correlation as a kind of sub-magnetic-lattice. Theoretical and experimental studies have shown that these new magnetic correlations in spin liquid compounds are spinon continuums. In fact, the observed double ESR is because of the two spinon continuums in the spin liquid sample. The Dzyaloshinskii-Moriya (DM) interactions are introduced as 1D correlations between spins in each of the mentioned spinon continuums or, in other words, the spinon continuums are formed by the DM interactions.

Where the signal in Q - B diagram appears and in which direction it evolves is depends on the relative orientation of the sample and the external magnetic field so that by rotating the sample 90 degree the new emerging ESR trough appeared on the left (lower fields) side of the main signal although it emerged on the right side (higher fields) before the rotation. Thereby, one could probably conclude that the emergent signal belongs to and evolves from κ -(BEDT-TTF)₂ dimers since their canted standing up orientation relative to the external magnetic field is the only parameter in the lattice which will not be the same after a 90 degree rotation.

The advantageous metallic CPWs could help us find a more detailed view about the investigated materials of this work. The obtained results could in some cases elaborate our information about the existing phases of the materials which were obtained by other investigations and in some other cases revealed quite new existing phases.

ESR measurements by using metallic CPWs can be continued and there are several possibilities for further modifications and improvements in gaining data with these tools. Achieving high quality factors of resonators can always help the quality and the precision of the obtained data improve. Some measures which can still be considered in future relevant works to obtain higher quality factors could be:

- Further structural manipulation: widening the center conductors and ground planes further, as shown in this work, can improve the quality factor of the resonators,
- Utilizing (or Developing) mixed resonators: one idea to have high quality factors is to substitute either the center conductor or the ground planes by high temperature or normal superconducting materials.
- Utilizing of the resonators made of high temperature superconductors which typically have a high first critical field and thus the lower background effects.

In addition, the interesting observed data in this work can definitely be complemented by more experiments.

In the case of YbRh_2Si_2 more data points in the transition region from LFL to NFL could help show the T^2 Trend of the ESR linewidth better.

Obtaining data of $\kappa\text{-(BEDT-TTF)}_2\text{Cu}_2(\text{CN})_3$ with measurements at millikelvin range can help elaborate the phase diagram further. In addition, an in-situ rotation of the sample can yield more information about the anisotropy of the (magnetic) lattice which is probably the reason for the occurrence of the emergent ESR signal at opposite positions after 90 degree rotation of the sample.

8. Zusammenfassung und Ausblick

In dieser Arbeit wurde ein neues Instrument für die Elektronenspinresonanz-Spektroskopie (ESR) entwickelt, mit dem stark korrelierte Materialien untersucht wurden. Die gewonnenen Daten waren mit denjenigen konventioneller Methoden vergleichbar. Es konnten jedoch in einigen Fällen neue Phasen und Zustände der Materialien entdeckt werden. Dies war mit den anderen bisher angewendeten ESR-Systemen und -Methoden nicht möglich.

Die Vorteile und die Effizienz koplanarer Wellenleiter und Resonatoren (CPW-Resonatoren) im Vergleich zu konventionellen Hohlraumresonatoren können wie folgt zusammengefasst werden:

- Höhere Leistungsfähigkeit einer ESR-Messung bei Verwendung eines CPW-Resonators, da in diesem Fall mehrere Resonanzen (Resonatoren-Moden) im Vergleich zu der einzigen Resonanz eines konventionellen Hohlraumresonators zur Verfügung stehen,
- Einfache Konfiguration der gewünschten Resonanz-Frequenzen durch Modifizierung der geometrischen Parameter oder der Materialien des CPW-Resonators,
- Erhöhte Machbarkeit von ESR-Messungen bei extrem niedrigen Temperaturen, weil ein CPW mit vergleichsweise kleiner Größe hergestellt werden kann und er daher besser kompatibel mit Mischungskryostaten ist,
- Höhere Füllfaktoren aufgrund der geringen Größe,
- Höherer Gütefaktor der Resonatoren, da sie aus supraleitenden Materialien hergestellt werden können.

Die hohe Leistung der koplanaren Resonatoren in ESR-Messungen kann im Falle konventioneller supraleitender CPWs von extremen Signalverzerrungen beeinflusst sein, da der Gütefaktor eines solchen Resonators bei Anwendung eines externen Magnetfeldes stark abfällt. Dies kann zwar durch den Gebrauch von CPWs aus normalen Metallen verhindert werden, doch deren Gütefaktoren sind kleiner.

Eines der wichtigsten Merkmale einer Messeinrichtung oder einer Messmethode ist eine hohe Stabilität und so wenig wie möglich Artefakte. Bei supraleitenden CPWs ist die Änderung des Gütefaktors sogar bei Temperaturänderungen weit unter der kritischen Temperatur (T_c) sehr deutlich. Das bedeutet, die Änderung der ESR-Signalstärke bei unterschiedlichen Temperaturen ist nicht nur ein Effekt der zu untersuchenden Probe, sondern auch aufgrund der Verluste des Resonators.

Außerdem zeigen Supraleiter den Meißner-Ochsenfeld-Effekt, aufgrund dessen ein extern angelegtes Magnetfeld abgestoßen wird und eine erhöhte lokale Magnetfeldstärke um die Probe verursacht werden kann. Das kann dazu führen, dass die Feldstärke an der Probe höher als die am Versuchsstand eingestellte Feldstärke ist.

Aufgrund der Nachteile der supraleitenden CPWs wurden in der ersten Phase dieser Forschungsarbeit metallische CPW-Resonatoren entworfen, gefertigt, gemessen und optimiert [206]. Es wurden hohe Gütefaktoren wie 470 bei tiefen Temperaturen erreicht. Das ist ein beachtlicher Wert für diese miniaturisierten Resonatoren. Der Gütefaktor blieb ab Temperaturen um 20 K unverändert und konstant bis zu den niedrigsten erreichten Temperaturen. Das heißt, die beobachteten Veränderungen der ESR-Signalstärke durch die Temperaturänderung in den Messungen unter 20 K können direkt den Materialeigenschaften zugeschrieben werden.

Die Vorteile der metallischen CPW-Resonatoren im Vergleich zu supraleitenden CPW-Resonatoren können wie folgt zusammengefasst werden:

- Kein erwähnenswerter Verlust des Gütefaktors bis zu einer magnetischen Flussdichte von 7 T. Der Änderung des Gütefaktors im Promillebereich bei Änderung der magnetischen Flussdichte von 0 zu 0,5 T steht der fast 90%ige Gütefaktor-Verlust bei konventionellen supraleitenden CPWs in derselben Spanne gegenüber. Das vermeidet die mühsamen numerischen Analysen und Regression-Analysen zum Entfernen der Verzerrungen in den ESR-Signalen.
- Hohe Gütefaktor-Stabilität bei Temperaturen unter 20 K, wohingegen die kritische Temperatur (T_c) von Niobium bei 9 K liegt,
- Keine Abstoßung und lokale Verstärkung des Magnetfeldes, was dazu führt, dass die gewünschte Feldstärke und die von der Probe anliegende Feldstärke nahezu gleich sind,
- Einfachheit des Systems, da es keinen Vortex-Verlust aufgrund der Supraleitung gibt.

Zur Validierung und Überprüfung der Zuverlässigkeit der gefertigten Resonatoren bei der Datenausgabe wurden die ersten ESR-Experimente mit dem üblichen ESR-Kalibrierungsmaterial 2,2-Diphenyl-1-Picrylhydrazyl (DPPH) durchgeführt. Scharfe Resonanzkurven von DPPH wurden bei verschiedenen Frequenzen beobachtet. Diese

Daten waren hilfreich, um ein wichtiges Artefakt von solchen metallischen CPW-Resonatoren in ESR-Messungen zu verstehen. Falls die ESR-Linienbreite eines Materials schmaler als die Resonator-Resonanz-Linienbreite ist, treten zwei kleine Peaks unmittelbar rechts und links des ESR-Wellentals auf. Dieses Phänomen wurde im Kapitel 5 erläutert.

Von besonderem Interesse in dieser Arbeit waren allerdings die außergewöhnlichen Materialien mit Quantenphasenübergängen. In diesen Verbindungen sind die Beobachtung und die Änderung der ESRs immer ein überraschendes und interessantes Phänomen gewesen. Die Materialien waren:

- Zwei Schwere-Fermionen (HF): YbRh_2Si_2 und YbNi_4P_2
- Eine Quantenspinflüssigkeit: $\kappa\text{-(BEDT-TTF)}_2\text{Cu}_2(\text{CN})_3$

Die ESR-Messungen von YbRh_2Si_2 mit den metallischen CPWs aus dieser Arbeit ergaben neue Ergebnisse, welche die durch die supraleitenden CPWs erhaltenen Ergebnissen bestätigt und auch teilweise angefochten haben. Eine von den neuen Beobachtungen war die Steigerung des g -Faktors im Landau-Fermi-Flüssigkeits-Bereich dieser Verbindung, wohingegen die Daten der Experimente mit den supraleitenden Resonatoren diese Steigerung überhaupt nicht gezeigt haben.

Ein weiteres Ergebnis war eine nicht-lineare Abhängigkeit zwischen der ESR-Linienbreite und $\log(T)$ im Bereich des Übergangs von der Landau-Fermi-Flüssigkeit zur nicht-Fermi-Flüssigkeitsphase. In Referenz [194] wurde eine lineare Abhängigkeit in der nicht-Fermi-Flüssigkeitsphase bei Temperaturen größer 4 K vorgestellt.

In den ESR-Daten der metallischen Resonatoren (ebenso wie bei den supraleitenden) konnte kein Effekt der T^* -Linie (bzw. -Spanne) auf die ESR-Linienbreite beobachtet werden.

Eine der Hypothesen zur Beobachtung der ESR-Signale in HF-Kondo-Gittern ist das Vorhandensein von kurzreichweitigen ferromagnetischen (FM) Korrelationen zwischen den abgeschirmten magnetischen Momenten. YbNi_4P_2 als eine HF-Verbindung mit FM-Anordnung und -Polarisationen sollte Daten ergeben, welche diese Theorie unterstützen. Daher wurden Versuche mit zwei verschiedenen YbNi_4P_2 -Proben durchgeführt. Trotz mehrerer Messungen mit verschiedenen Konfigurationen wie Proben-Position im Resonator-Gehäuse, unterschiedlichen Probengrößen und Wachstumsmethoden wurde kein scharfes ESR-Signal wie bei YbRh_2Si_2 festgestellt. Ein Grund dafür könnten die quasi-eindimensionalen Yb^{3+} -Ionen entlang der c -Richtung des Kristalls und das Vermeiden der Bewegungsverschmälerung (Motional Narrowing) unter den magnetischen Momenten mit FM-Korrelationen sein.

Die ESR-Messungen der Quantenspinflüssigkeit $\kappa\text{-(BEDT-TTF)}_2\text{Cu}_2(\text{CN})_3$ ergaben völlig neue und bislang unbeobachtete Ergebnisse. Die Motivation zur Erforschung

dieses Materials ergab sich aus der Beobachtung der ESR bei tiefen Temperaturen und das Erforschen der ESR-Veränderungen in einem stark korrelierten Spin-System mit geometrisch frustrierter magnetischer Anordnung.

Die ESR-Signalstärke steigt bei Verringerung der Temperatur von 6 K bis $\approx 3,2$ K bei allen Frequenzen (≈ 5 GHz bis ≈ 16 GHz) an, wie es für jedes System zu erwarten ist. Allerdings reduziert sich die Signalstärke beim weiteren Abkühlen von $\approx 3,2$ K auf 1,55 K (die niedrigste verfügbare Temperatur bei dem verwendeten variablen Temperatureinsatz (VTI-Anlage)). Das entspricht dem Imaginärteil der magnetischen Suszeptibilität, wie in Referenz [201] berichtet worden ist. In derselben Quelle wurde gezeigt, dass der Realteil der Suszeptibilität bei Temperaturen bis kleiner 2 K monoton steigend ist, wohingegen - wie gerade erwähnt - der Imaginärteil ab ≈ 3 K oder ≈ 4 K je nach angelegter Magnetfeldstärke kleiner wird. Somit scheint es, dass der Hauptgrund der schwächeren ESR-Signalstärke bei Temperaturen unter $\approx 3,2$ K in der geringeren Anzahl der Spins liegt, die eine ESR zeigen, und nicht in der geringeren Magnetisierung des Materials.

Beim weiteren Abkühlen kleiner $\approx 2,3$ K erscheint neben dem Hauptsignal ein neues ESR-Signal. Dieses könnte die Entstehung einer neuen magnetischen Korrelation, ein magnetisches Untergitter, anzeigen. Theoretische und experimentelle Untersuchungen haben gezeigt, dass diese neuen magnetischen Korrelationen Spinon-Kontinuen sind. Genau genommen ergibt sich die Doppel-ESR infolge der zwei Spinon-Kontinuen in der Spinflüssigkeitsprobe. Die Dzyaloshinskii-Moriya (DM)-Wechselwirkungen sind eindimensionale Korrelationen zwischen den Spins in jedem Spinon-Kontinuum oder anders ausgedrückt, die Spinon-Kontinuen werden durch die DM-Wechselwirkungen gebildet.

An welcher Stelle das neue Signal im Q - B -Diagramm auftritt und in welche Richtung es sich entwickelt, ist abhängig von der relativen Ausrichtung der Probe und des angelegten externen Magnetfeldes. Bei einer um 90 Grad gedrehten Ausrichtung der Probe erscheint das neue Signal auf der linken Seite (niedrigeres Feld) des ESR-Hauptsignals und bewegt sich nach links, obwohl es ursprünglich auf der rechten Seite des ESR-Hauptsignals (höheres Feld) lag und sich nach rechts bewegt hat. Daraus lässt sich folgern, dass das neue Signal aufgrund der κ -(BEDT-TTF)₂-Dimere entsteht, da deren relativ zum Magnetfeld schräggestehende Ausrichtung der einzige richtungsabhängige Parameter in diesem Gitter ist.

Die vorteilhaften metallischen CPWs trugen zu einer detaillierten Betrachtung der untersuchten Materialien in dieser Arbeit bei. Die in den Messungen erhaltenen Ergebnisse vertieften in einigen Fällen die bestehenden Kenntnisse zu den existierenden Phasen der Materialien, welche durch andere Untersuchungen herausgearbeitet wurden. In einigen Fällen konnten neue Phasen in den Materialien aufgezeigt werden.

ESR-Messungen unter Verwendung metallischer CPWs sollten in zukünftigen Forschungen fortgeführt werden und es gibt einige Möglichkeiten für weitere Modifizierungen und Verbesserungen zur Datengewinnung durch diese Module. Höhere Gütefaktoren der Resonatoren verbessern die Datenqualität und -genauigkeit weiter. Einige Aspekte zur Erzielung höherer Gütefaktoren, welche in zukünftigen Arbeiten noch betrachtet werden können, sind:

- Weitere strukturelle Modifikation: Erweiterung des Innenleiters und der Grundplatte kann, wie in dieser Arbeit gezeigt wurde, den Gütefaktor verbessern.
- Verwendung (oder Entwicklung) von Misch-Resonatoren: Eine Möglichkeit für höhere Gütefaktoren sind Resonatoren, in denen entweder der Innenleiter oder die Grundplatte aus supraleitenden Materialien besteht.
- Verwendung von Resonatoren, welche aus Hochtemperatur-Supraleiter bestehen. Hochtemperatur-Supraleiter haben in der Regel ein höheres kritisches Magnetfeld, so dass weniger Hintergrund-Effekte von den Resonatoren erzeugt werden.

Außerdem können die in diese Arbeit erhaltenen interessanten Daten durch weitere Experimente vertieft werden.

Weitere Daten im Übergangsbereich von Landau-Fermi-Flüssigkeit (LFL) zu nicht-Fermi-Flüssigkeit (NFL) können im Fall von YbRh_2Si_2 den T^2 -Trend der ESR-Linienbreite deutlicher herausstellen.

Daten durch Messungen im Millikelvin-Bereich der Quantenspinflüssigkeit κ -(BEDT-TTF) $_2\text{Cu}_2(\text{CN})_3$ können das Phasendiagramm erweitern. Darüber hinaus könnte eine In-situ-Drehung der Probe mehr Informationen zu der Anisotropie in dem (magnetischen) Gitter, die wahrscheinlich der Grund für das Auftreten des neuen ESR-Signals bei entgegengesetzter Ausrichtung ist, ergeben.

Appendices

Appendix I

Q loss Background Analysis:

A. Problem description:

Our ESR measurements were based on a resonator technique. In the measurements, superconducting coplanar resonators were used above which a sample (YbRh_2Si_2) was mounted. At a particular magnetic field, electromagnetic signal with a given range of the frequency was sent to the resonators. If signal energy is suitable to perform spin resonance between the splitting spin states (Zeeman Effect), the signal is absorbed by the sample. The signal absorption by the sample will be demonstrated by a significant decrease of the quality factor if one plot the quality factor versus external magnetic field. This is due to the concept of quality factor which is the amount of energy loss relative to the stored energy of the resonator. If some parts of the signal are absorbed by the sample, the situation is analogous to a situation in which more energy is lost in the resonator. Thus, the quality factor decreases. So, we can realize the resonance frequency and with further analysis the corresponding band width. This is possible by sweeping the magnetic field through on and off resonance values (FIG. 1). On the other hand, increasing magnetic field has another direct effect on the quality factor. By exceeding the superconducting critical field, the normal state (non-superconducting) vortices start to form in a superconductor. The higher the field, the higher the number of vortices. Therefore, due to the damping effect of the vortices the energy loss enhances and consequently the quality factor monotonically decreases [26] [47] [206]. This background effect is to model and get subtracted from the ESR resonance data.

Beside the resonator effects (artefacts), materials properties dependence on experiment conditions like magnetic field or frequency can also deviate the ESR line. Here the properties are meant which are not the purpose of the investigation for example magnetoresistance in an ESR experiment [118] [191], Drude behavior of conductivity (resistivity) [195], magnetic field dependence of Drude behavior [207]. However, one should consider to which extent may these sample dependent effects influence an ESR line. The ESR of the materials/samples of this and similar works occur in a range of 150 mT (for each resonance frequency) at the most, and on the other hand, the frequency range of each resonance (of the resonator) is maximum 300 MHz wide. In such spans of field and frequency, the highest alteration of e.g. resistivity or conductivity, even at low field in Ref. [118] or the Drude model roll off [195] where the change rates are the highest, does not exceed $\sim 5\%$. One should note that this maximum 5% is happening in the sample itself and not in the ESR data. It would reduce with a

factor(s) of ten(s) in changing the quality factor of the CPW resonator¹. Therefore, in comparison with the ESR line distortion stemming from the superconductivity of the CPWs, the sample effects are negligible.

B. Measurements:

The measurements were carried out using 3 different resonators (nominated by R01, R02 and R03) each of which was used for particular resonance frequencies. The temperature range was from 40 mK to 4 K; more details will be offered further. The measurements were done in a dilution refrigerator to be able to reach to milli-Kelvin temperatures.

For the data of each resonator we formed an exclusive formula (R02 and R03 had the same formulae) to perform the background analysis.

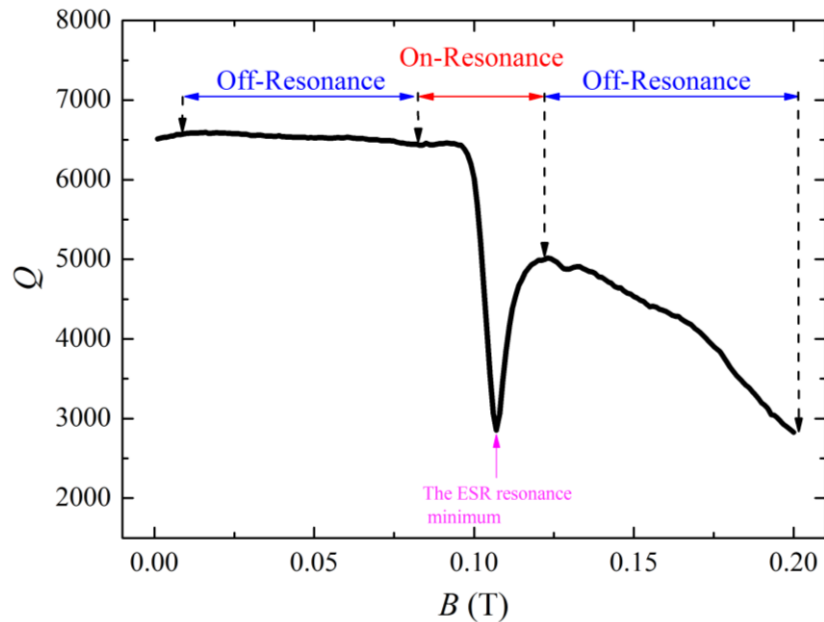


FIG. 1. One typical Q (Quality factor) vs. B (Magnetic field in Tesla unit) plot. The deep minimum is caused by the ESR resonance field. The area of the ESR effect (On resonance) and the off-resonance areas are shown.

C. Temperature Analysis:

The temperature analysis of the data was required to determine the actual temperature at which the sample was during the measurements. The actual sample temperature was determined by reading out the measured resistance of the temperature sensor and converting it via a corresponding formula. It must be noted

¹ This is observable by comparing Figure 3.7 (b) and 6.11 (a) and (c). Note: in this work no superconducting resonator was used.

that, the sample temperature was determined only by the recorded data through the time period of the ESR range. This means, if the ESR resonance field range was from 75 mT to 125 mT, only the sensor data of this 50 mT range was taken to account, although, maybe the measurement was performed from 0 mT to 200 mT.

For the data above 800 mK, the sample temperature was considered as the mixing chamber (of the dilution refrigerator by which the measurements were performed) temperature.

1. Resonator R01:

The measurements with R01 are briefed in Table 1.

Table 1. The temperature range and the ESR resonance field change of resonator R01.

	Temperature Range (mK) (Sample Temperature)	Resonance Field for Lowest/Highest Temperature (mT)
Mode 1, 1.48 GHz (Fundamental)	52.3 - 4000	34/38 in the AFM phase. 38/34 in the PM phase.
Mode 2, 2.95 GHz	53.7 - 4000	75/64
Mode 3, 4.41 GHz	54.0 - 4000	107/95
Mode 4, 5.86 GHz	54.2 - 4000	137/124
Mode 5, 7.30 GHz	54.4 - 4000	168/152
Mode 6, 8.73 GHz	54.9 - 4000	199/185
Mode 7, 10.22 GHz	61.9 - 4000	227/213
Mode 8, 11.85 GHz	55.5 - 4000	263/250
Mode 9, 13.11 GHz	55.5 - 4000	295/280

One of the typical data curves of R01 is shown in FIG. 2. The surrounded area by the solid line oval is the ESR part. This part is temporarily omitted from the spectrum and the rest of the points, in which apparently there is no trace of the ESR, are fitted with the formula at the following:

$$Q = \underbrace{\text{St.Fn} * \left(\text{Pr1} + \frac{\text{Pr2}}{1 + \exp(\text{Pr3} * (B - \text{Pr4}))} \right)}_A + \underbrace{(1 - \text{St.Fn}) \left(\text{Pr5} + \frac{\text{Pr6}}{1 + \exp(\text{Pr7} * (B - \text{Pr8}))} \right)}_B \quad (1.1)$$

Pr1 to Pr8 as well as Pr9 and Pr10 in St.Fn (relationship (1.2)) are the fitting parameters. The B unit is Tesla. Relationship (1.1) is a combination of two smaller parts of A and B. The St.Fn (1.2) which is a kind of step function (FIG. 3) has the duty of transferring from A to B by increasing the magnetic field.

$$\text{St.Fn} = \left(\frac{1}{1 + \exp(\text{Pr9} * (B - \text{Pr10}))} \right) \quad (1.2)$$

In fact, this transferring from A to B is due to the bump-like part of the curve (shown with the dashed oval in FIG.1) that is a feature which must be considered in the model formula for this resonator. The fitting parameter Pr9 determines how narrow the transferring range from A to B is. In other words, in how large magnetic field domain the both parts of A and B have considerable shares in fitting value of Q . For example if Pr9=200 and Pr10=0.175, the function St.Fn changes from 0.99 to 0.01 in 0.046 T (46 mT) span around the center of 0.175 T (175 mT) as shown in FIG. 3.

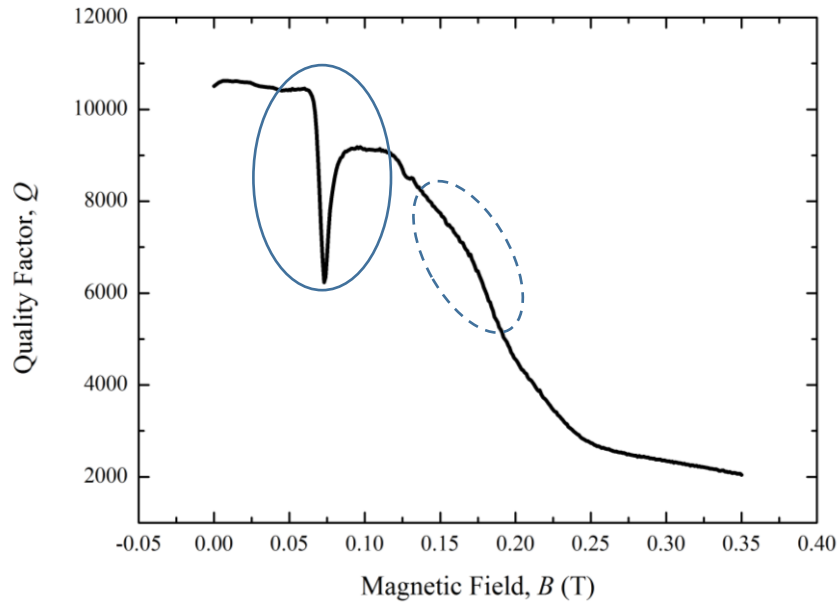


FIG. 2. The plot of Q vs. B for mode 2 at the mixing chamber temperature of 60 mK (Sample temperature of 76.7 mK). The dotted circle shows the ESR data and the dashed oval shows the bump-like feature which appears almost in the all modes.

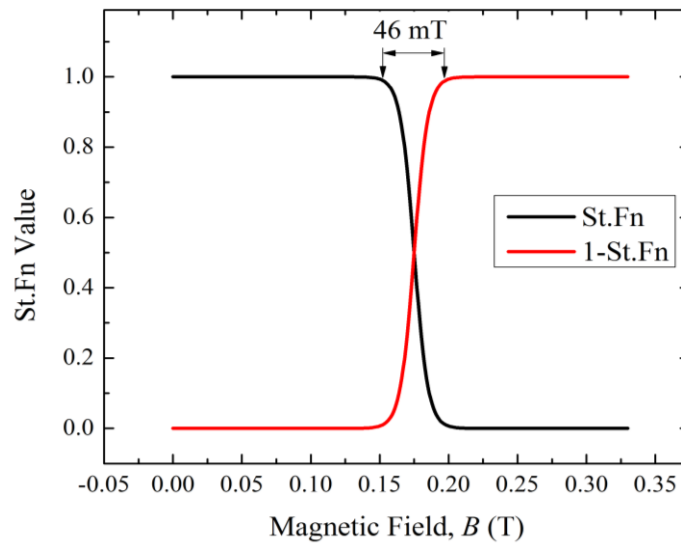


FIG. 3. The value of St.Fn changes from 1 to 0 in a given width which is defined by Pr9.

A list of some additional proposed formula (out of 35 formulae) and the corresponding issues are briefed in Table 2.

Table 2. Some of the proposed relationships for resonator R01 to fit the data.

Relationship:	Description:
$Q = Pr1 + \frac{Pr2}{(1 + \exp((B - Pr3) * Pr4))} + \frac{Pr5}{\exp((Pr6 * (B - Pr7))^2)}$	7 parameters. An exponential roll off + a Gaussian peak to fulfill the bump
$Q = Pr1 + \frac{Pr2}{1 + \exp((Pr3 * (B - Pr4))^{Pr5})} + \frac{Pr6}{1 + \exp((Pr7 * (B - Pr8))^{Pr9})}$	9 parameters. An exponential roll off + a Gaussian peak to fulfill the bump
$Q = Pr1 + \frac{Pr2}{1 + \exp(Pr3 * (B - Pr4)^{Pr5})} + \frac{Pr6}{\exp(Pr7 * (B - Pr8)^{Pr9})}$	9 parameters. An exponential roll off + a Gaussian peak to fulfill the bump
$Q = Pr1 + \frac{Pr2}{1 + \exp((Pr3 * (B - Pr4))^{Pr5})} + \frac{Pr6}{1 + (Pr7 * (B - Pr8))^{Pr9}}$	9 parameters. An exponential roll off + a rational peak to fulfill the bump
$Q = Pr1 + \frac{Pr2}{1 + (Pr3 * (B - Pr4))^{Pr5}} + \frac{Pr6}{1 + (Pr7 * (B - Pr8))^{Pr9}}$	9 parameters. An rational roll off + a rational peak to fulfill the bump
$Q = \left(\frac{1}{1 + \exp(CP * (B - TP))} \right) * \left(Pr1 + \frac{Pr2}{1 + \exp(Pr3 * (B - Pr4)^{Pr5})} \right) + \left(1 - \frac{1}{1 + \exp(CP * (x - TP))} \right) * \frac{Pr6}{1 + \exp(Pr7 * (B - Pr8)^{Pr9})} + \frac{Pr6}{\exp(Pr7 * (B - Pr8)^{Pr9})}$	11 parameters. 2 exponential roll offs + a step function + a Gaussian peak to fulfill the bump
$Q = (\tanh((x - TP) * CP)) * \left(Pr1 + \frac{Pr2}{1 + \exp(Pr3 * (B - Pr4)^{Pr5})} \right) + (1 - \tanh((x - TP) * CP)) * \frac{Pr6}{1 + \exp(Pr7 * (B - Pr8)^{Pr9})} + \frac{Pr6}{\exp(Pr7 * (B - Pr8)^{Pr9})}$	11 parameters. 2 exponential roll offs + a step function + a Gaussian peak to fulfill the bump
$Q = Pr1 + \frac{Pr2}{(B + Pr3) * Pr4} + \frac{Pr5}{\exp(Pr6 * (B - Pr7)^{Pr8})}$	8 parameters. An rational roll off + a Gaussian peak to fulfill the bump
$Q = Pr1 * \cos\left(\frac{B}{Pr2}\right) + \frac{Pr3}{\exp((Pr4 * (B - Pr5))^{Pr6})} + \frac{Pr7}{\exp((Pr8 * (B - Pr9))^{Pr10})}$	10 parameters. A cosine roll off + An rational roll off + a Gaussian peak to fulfill the bump

For each mode, the ESR range was determined and deleted from the data set. The remnant points were then fitted, and so, the cut piece of data was numerically fitted by a constructed formula in the absence of ESR effect. This is shown as an example in FIG. 4.

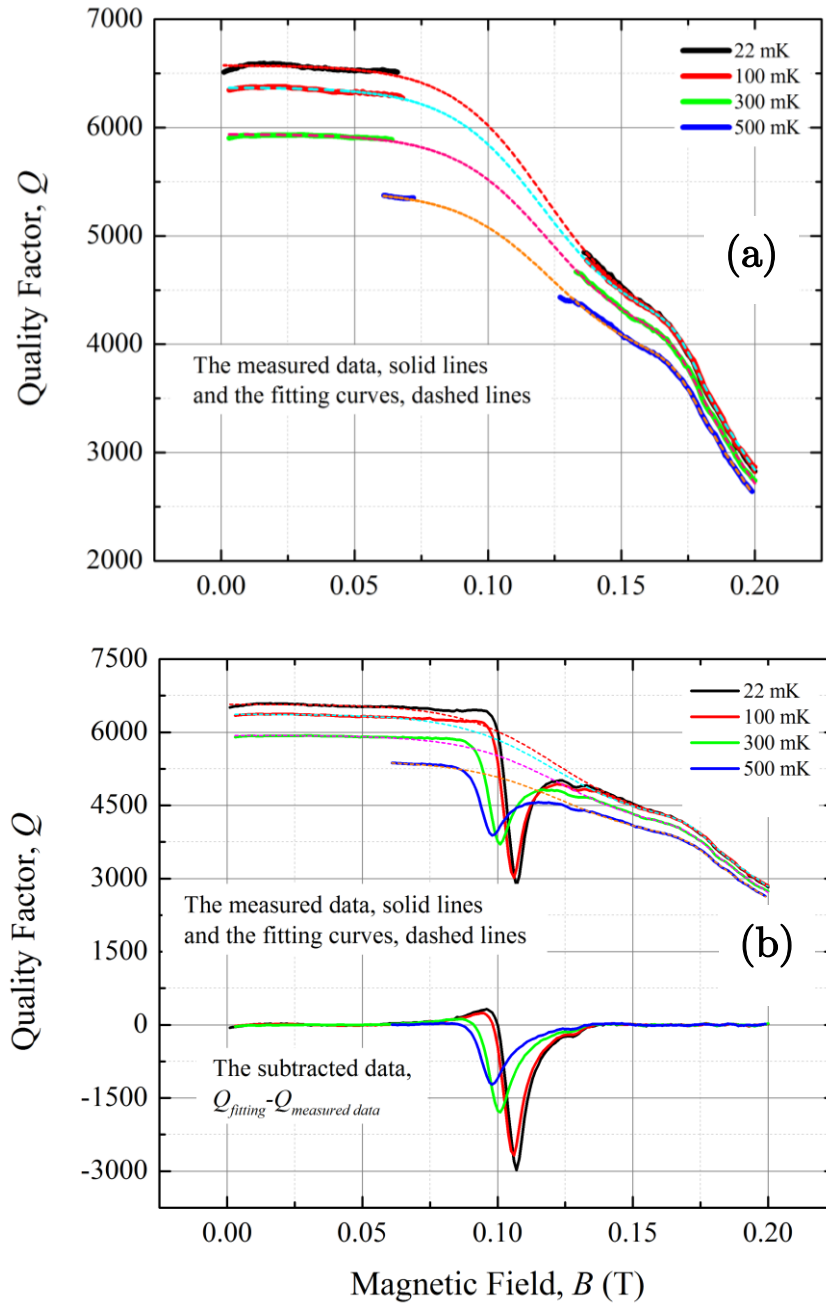


FIG. 4. (a) The data points of the ESR are omitted from the measured data and the remnant points are fitted. The curves belong to mode 3. (b) The upper curves show the measured data (solid lines) and their corresponding fitting curves (dashed lines). The lower curves are fitted data subtracted from the measured data. The temperatures are the mixing chamber temperature of the dilution fridge.

1.1. Mode1:

In mode 1 data the fitting procedure was not applied. This is due to the fact that the resonator background effect at the lowest temperatures was not remarkable; probably due to the strongly dominating ESR signal. Hence, the data at all temperatures were not gone under any background fitting.

1.2. Mode 2:

Although (1.1) was prepared according to a full range spectrum (0 to 350 mT), most of the data of mode 2 were recorded until 150 mT which was enough to observe the ESR part. All the measurements were continued even after the ESR resonance to have the points for fitting procedure. For mode 2 only the first part of (1.1) was taken to account because for the field value lower than 150 mT, the values of the step function is equal to 1 by fixing parameter 9 at 200.

In the all fitting analysis of the data, regardless of the mode or the resonator, some parameters are fixed which means the parameter is not quite (or absolutely) free to change during the fitting procedure. Fixing has been either at a fixed number or with a formula. The initial hint for fixing value or formula was obtained by picking around 15 curves of each mode and fitting them manually using Origin[®] program. Then the parameters' values were plotted versus temperature and observed to find the best relationship to fit them. Afterwards, the formula was given to the MATLAB[®] program to perform the fitting. The results from MATLAB[®] program was again checked to find the required changes in the already introduced formula. So, the process was a kind of interactive procedure to reach to the optimum desired results.

The fitting parameters are monitored against temperature in FIG. 5 and Table 3. Pr5 to Pr10 were not regarded since Mode 2 ESR data were all completely located in A part of formula (1.1).

“RealTemp” is in fact the sample temperature during the measurements which is different than the mixing chamber temperature of the dilution refrigerator. In the formulae it is always in mK unit.

In the diagram of Pr3 two groups of the points (two separate curves) are seen. This comes from two different series of measurements which were taken at two various time periods. The vortex arrangement and hysteresis effects in Niobium [48] was probably changed by sweeping the magnetic fields to higher values (than the ones of runs up to 60) and thus it changed the background for the runs up to 60 from run 61 on. This change in the resonator behavior will be reported again in section 1.10 of this appendix.

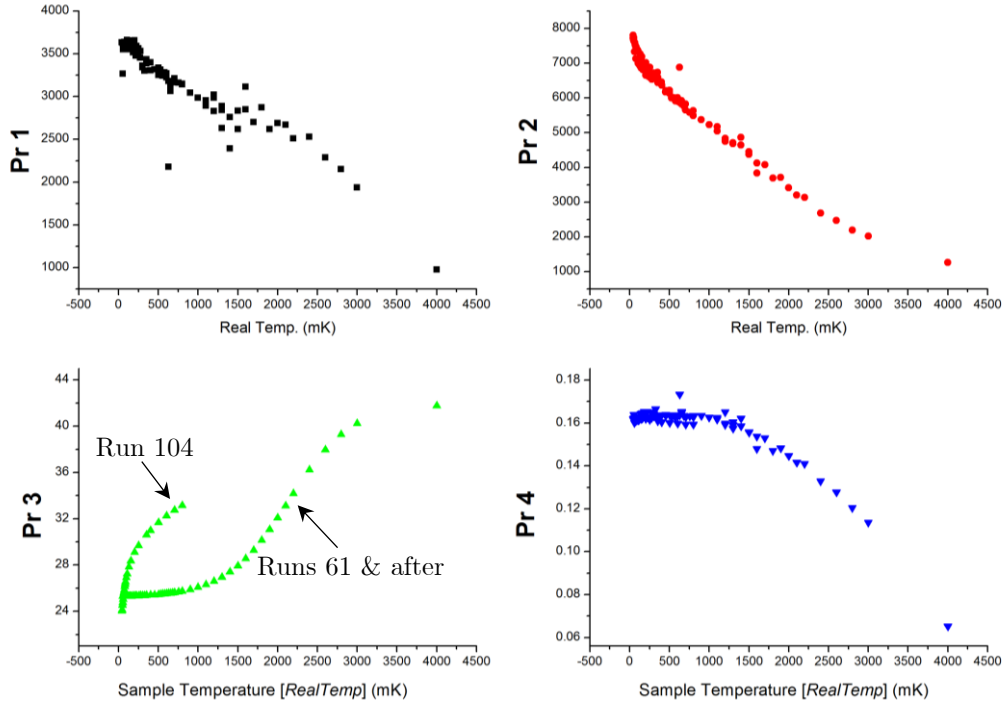


FIG. 5. Temperature dependence of the fitting parameters for mode 2.

Table 3. Mode 2 fixed parameters and fixing formulae. “*RealTemp*” values in mK.

Fixed Parameter	Fixing Formula	Description
3	$Pr3 = 41.89788 - \frac{16.7}{1 + \exp\left(\frac{RealTemp - 2141}{391}\right)}$	runs 61 & after
1	$Pr1 = 3663 - \frac{RealTemp}{1.5}$	unnumbered runs (Run 104)
3	$Pr3 = 160704 - 6.4 * \exp\left(\frac{RealTemp}{-145}\right) - 160675 * \exp\left(\frac{RealTemp}{-2.79751E7}\right)$	unnumbered runs (Run 104)

1.3. Mode 3:

Mode 3 data were treated with all 10 parameters since the position of the ESR part necessitated continuing the measurements further to the part B of (1.1). The fitting parameters are plotted in FIG. 6 and explained in Table 4.

The data which are outlier in their adjacent points, are due to problems like completely anomalous spectrum (compared to their neighboring spectra) or noisy data.

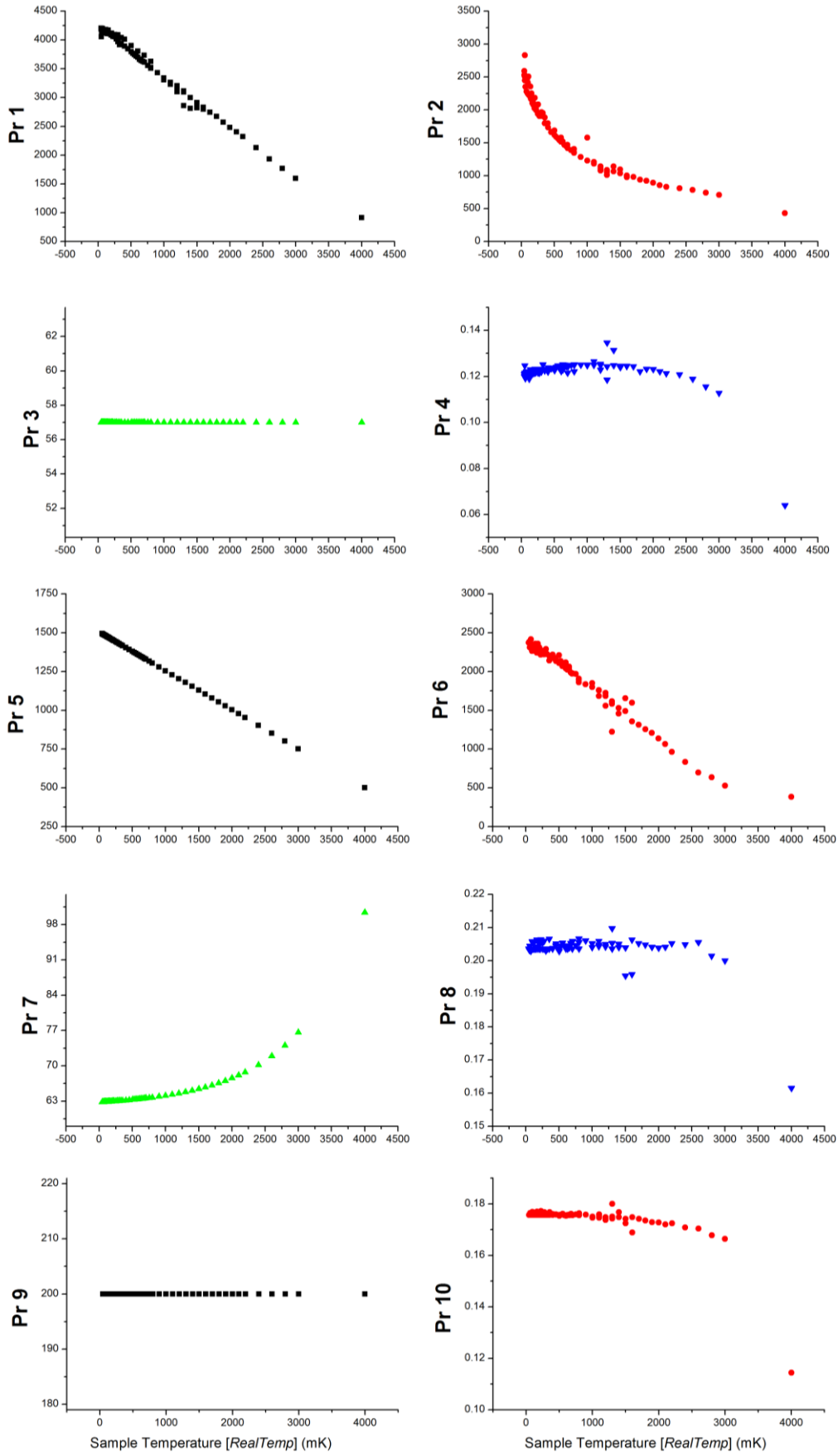


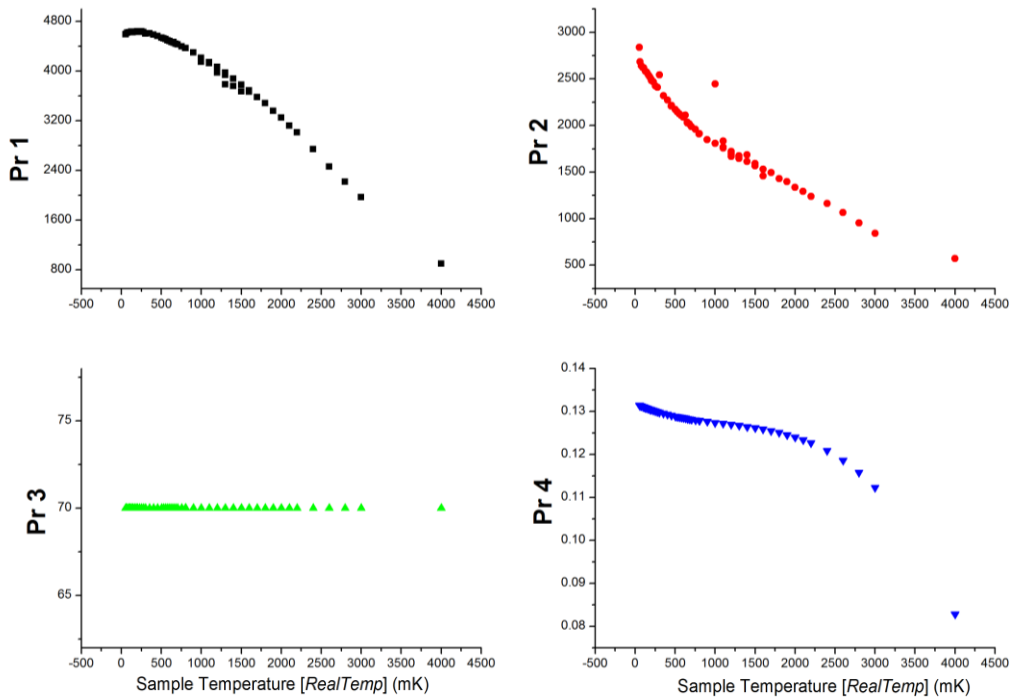
FIG. 6. Temperature dependence of the fitting parameters for mode 3.

Table 4. Mode 3 fixed parameters and fixing formulae. “*RealTemp*” values in mK.

Fixed Parameter	Fixing Formula	Description
3	$Pr3 = 57$	runs 61 & after & unnumbered runs (Run 104)
5	$Pr5 = 1505 - \frac{RealTemp}{3.98}$	runs 61 & after & unnumbered runs (Run 104)
7	$Pr7 = 62 + 0.2 * \exp\left(\frac{RealTemp + 1452}{1036}\right)$	runs 61 & after & unnumbered runs (Run 104)
9	$Pr9 = 200$	runs 61 & after & unnumbered runs (Run 104)
6	$Pr6 = 219 + \frac{2645}{1 + \exp\left(\frac{RealTemp - 1252}{816}\right)}$	unnumbered runs (Run 104)
8	$Pr8 = (-2.2e - 7) * \exp\left(\frac{RealTemp}{-329}\right) + 0.203$	unnumbered runs (Run 104)
10	$Pr10 = (-2.7e - 5) * \exp\left(\frac{RealTemp}{-513}\right) + 0.176$	unnumbered runs (Run 104)

1.4. Mode 4:

Similar to mode 3, mode 4 has also the complete formula (10 parameters). FIG. 7 and Table 5 show the temperature dependent fitting parameters.



Continue on the next page:

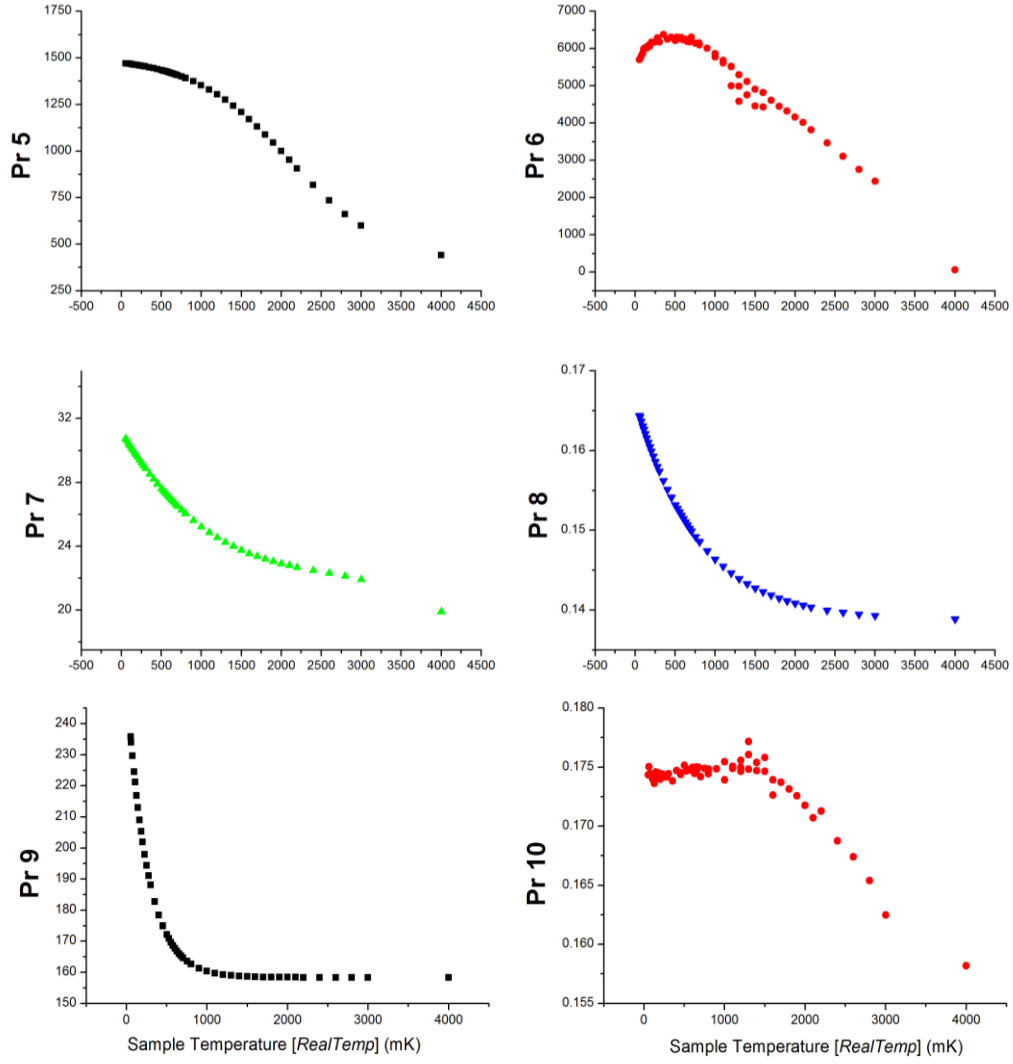


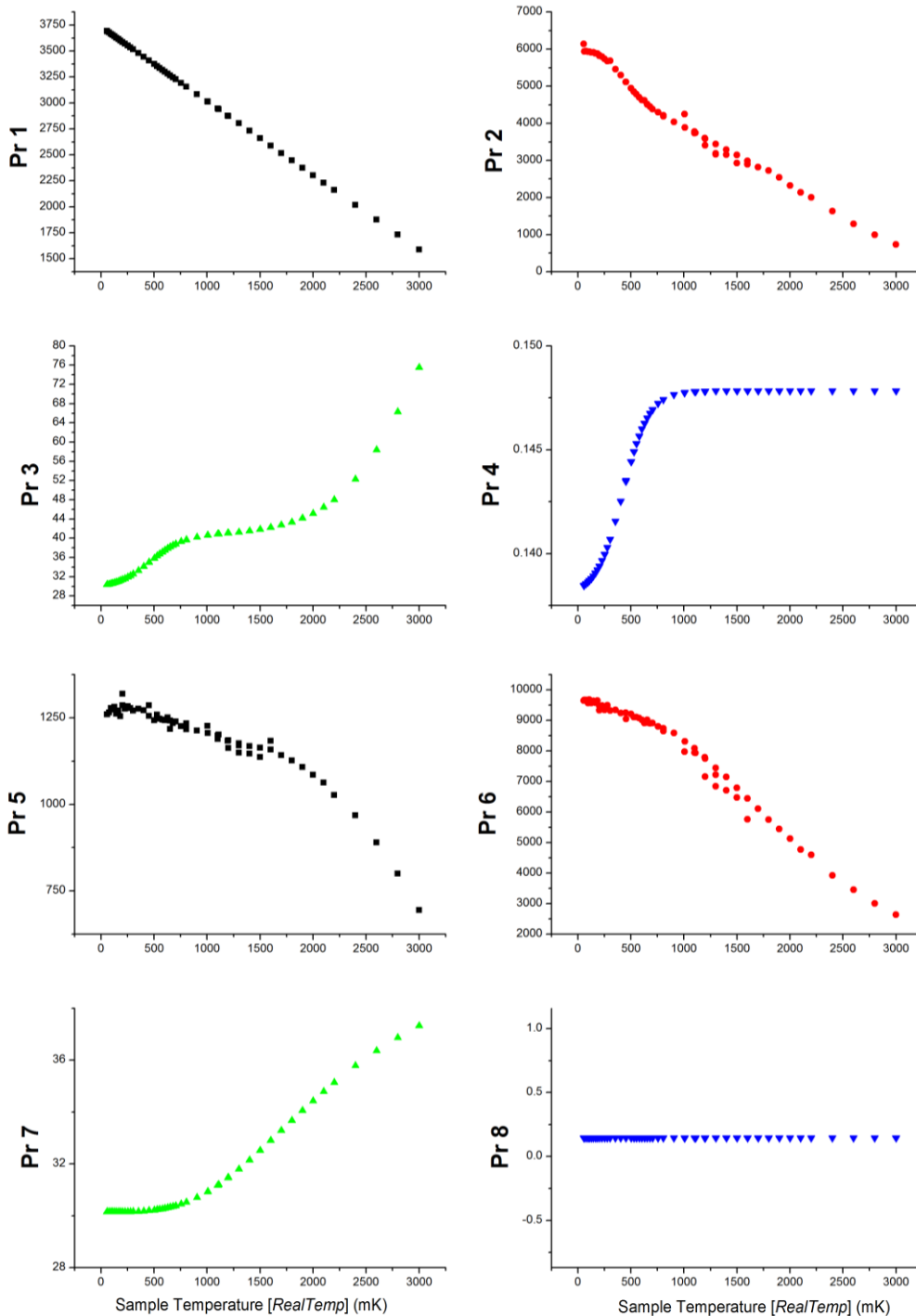
FIG. 7. Temperature dependence of the fitting parameters for mode 4.

Table 5. Mode 4 fixed parameters and fixing formulae. “*RealTemp*” values in mK.

Fixed Parameter	Fixing Formula	Description
3	$Pr3 = 70$	runs 61 & after
4	$Pr(4) = 0.1318 - (8.109e - 6) * RealTemp + (5.24383E - 9) * RealTemp^2 - (1.56972E - 12) * RealTemp^3$	runs 61 & after
5	$Pr5 = 396 + \frac{1109}{1 + \exp(\frac{RealTemp - 2103}{601})}$	runs 61 & after
7	$Pr7 = 31 - 0.0086 * RealTemp + (3.00865e - 6) * RealTemp^2 - (3.91235e - 10) * RealTemp^3$	runs 61 & after
8	$Pr8 = 0.02747 * \exp\left(\frac{-RealTemp}{783}\right) + 0.13871$	runs 61 & after
9	$Pr9 = 95.5 * \exp\left(\frac{-RealTemp}{259}\right) + 158$	runs 61 & after

1.5. Mode 5:

The fitting parameters are presented in the FIG. 8 and Table 6. The ESR range in mode 5 measurements was located exactly in the bump part of the lines (FIG. 2). This made the analysis more difficult than the first 3 modes (modes 2, 3 and 4) because parameter 9 had no clue to get directed during the fitting procedure. Thus, by considering the last analyzed modes and the approximate Pr9 values in them, Pr9 in mode 5 analysis was fixed at 250.



Continue on the next page:

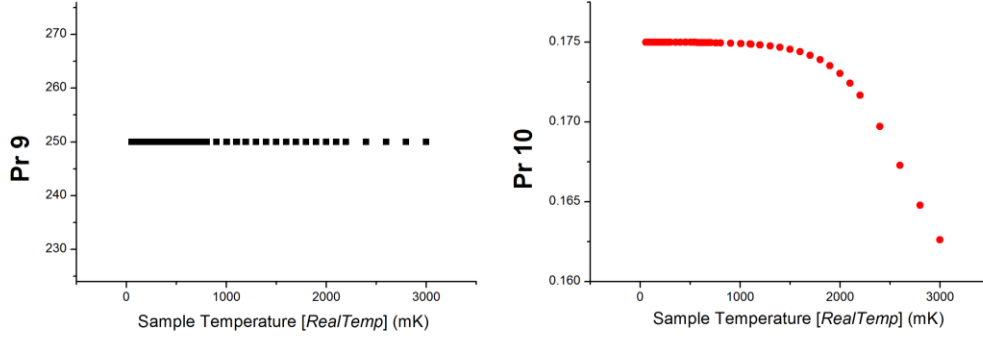


FIG. 8. Temperature dependence of the fitting parameters for mode 5.

Table 6. Mode 5 fixed parameters and fixing formulae. “*RealTemp*” values in mK.

Fixed Parameter Number	Fixing Formula	Description
1	$Pr1 = 3730 - 0.714 * RealTemp$	runs 61 & after
3	$Pr3 = 29.55 + 83 * \left(\frac{0.13267}{1 + 10^{(461.7 - RealTemp) * 0.00277}} + \frac{0.86733}{1 + 10^{(3023 - RealTemp) * 0.00114}} \right)$	runs 61 & after
4	$Pr4 = 0.148 - \frac{0.00984}{1 + \exp\left(\frac{RealTemp - 423}{123}\right)}$	runs 61 & after
7	$Pr7 = 30 + \frac{11}{\left(1 + \left(\frac{1816}{RealTemp}\right)^{2.45}\right)^{1.58}}$	runs 61 & after
8	$Pr8 = 0.145$	runs 61 & after
9	$Pr9 = 250$	runs 61 & after
10	$Pr10 = 0.159 + \frac{0.016}{1 + \exp\left(\frac{RealTemp - 2634}{319}\right)}$	runs 61 & after

1.6. Mode 6:

The fitting parameters of mode 6 are offered in FIG. 9 and Table 7.

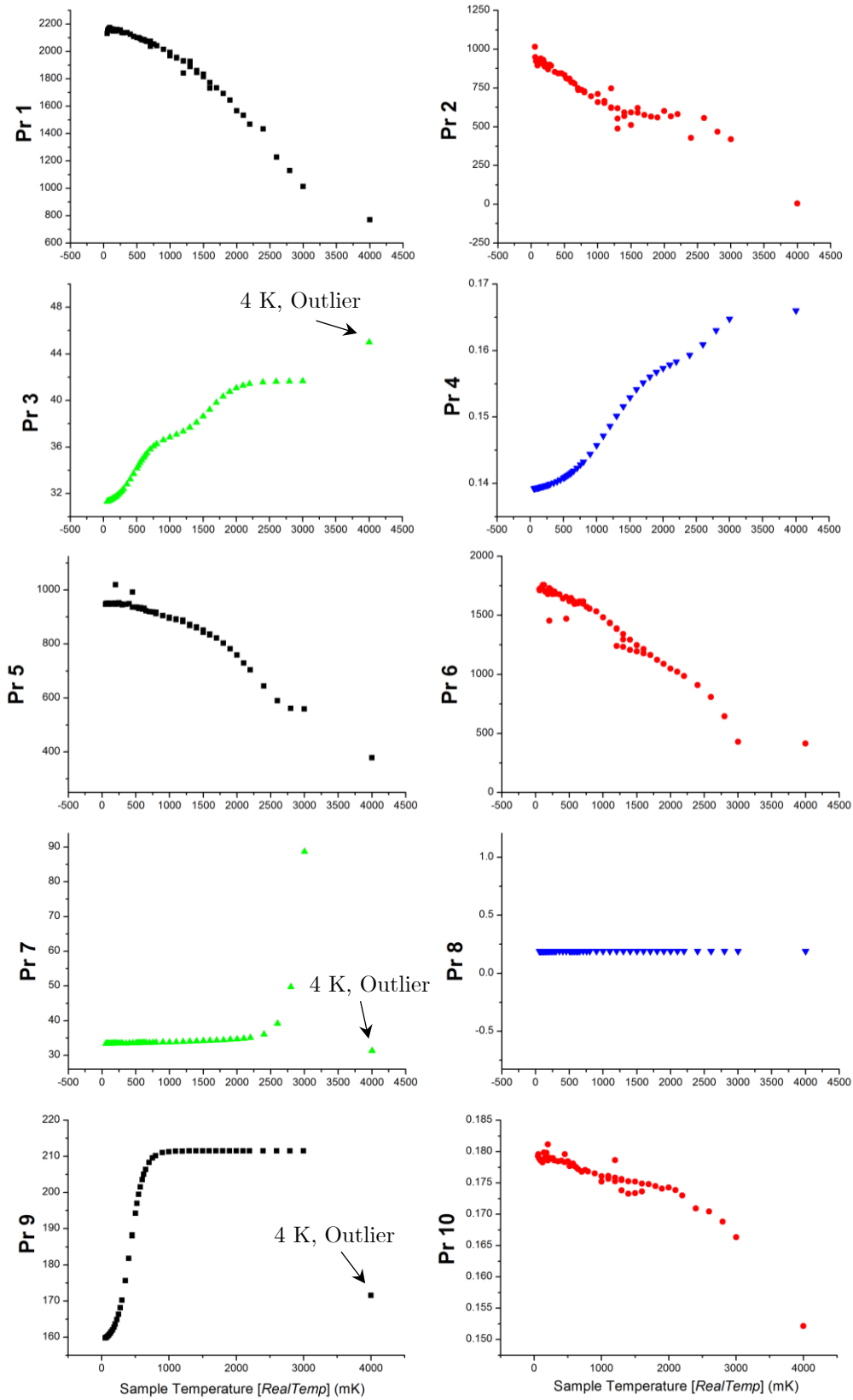


FIG. 9. Temperature dependence of the fitting parameters for mode 6. 4 K line is outlier and not included in the fixing parameter process for Pr3, Pr7 and Pr9.

Table 7. Mode 6 fixed parameters and fixing formulae. “*RealTemp*” values in mK.

Fixed Parameter	Fixing Formula	Description
3	$Pr3 = 31 + 10.7 * \left(\frac{0.5413}{1 + 10^{(471 - RealTemp) * 0.00289}} + \frac{0.4587}{1 + 10^{(1597 - RealTemp) * 0.00212}} \right)$	runs 61 & after
4	$Pr4 = 0.1386 + 0.0274 * \left(\frac{0.7473}{1 + 10^{(1214 - RealTemp) * 0.00128}} + \frac{0.2527}{1 + 10^{(2734 - RealTemp) * 0.00258}} \right)$	runs 61 & after
7	$Pr7 = 32.8 + 0.78 * \exp\left(\frac{RealTemp - 473}{1745}\right) + (2.88e - 6) * \exp\left(\frac{RealTemp - 473}{151}\right)$	runs 61 & after
8	$Pr8 = 0.19$	runs 61 & after
9	$Pr9 = 211 - \frac{53}{1 + \exp\left(\frac{RealTemp - 428}{100}\right)}$	runs 61 & after

1.7.Mode 7:

The measured ranges of 7th mode were enough short to analyze with only 4 parameters. However, resonator behavior alteration due to vortices and hysteresis caused the data to line up in three different sets. FIG. 10 and Table 8 show the parameters.

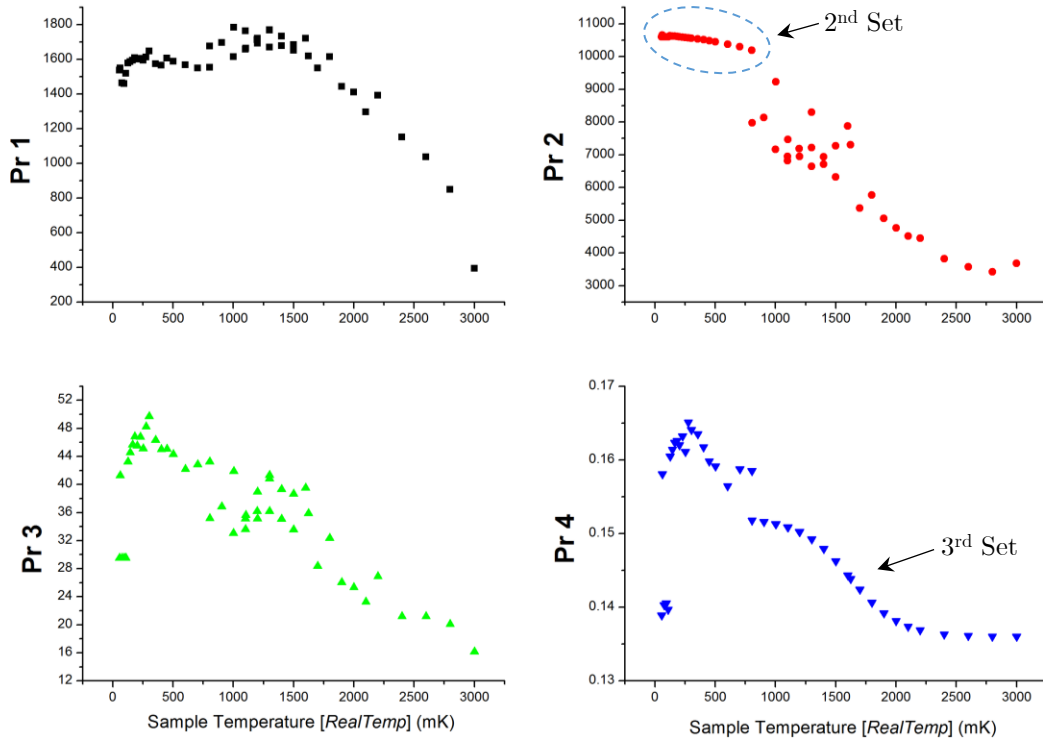


FIG. 10. Temperature dependence of the fitting parameters for mode 7.

Table 8. Mode 7 fixed parameters and fixing formulae for different sets of the data. “*RealTemp*” values in mK.

Fixed Parameter	Fixing Formula	Description
2	$Pr2 = 10600$	1 st Set*
3	$Pr3 = 29.5$	1 st Set*
2	$Pr2 = 10829 - 161 * \exp\left(\frac{RealTemp}{585}\right)$	2 nd Set**
4	$Pr4 = 0.136 + \frac{0.017}{1 + \exp\left(\frac{RealTemp - 1615}{204}\right)}$	3 rd Set***

*1st set: The data in Table 9.

**2nd Set: The data upto 800 mK of run 67.

***3rd data: The data of 800 mK (Run 89) and higher temperatures.

Table 9. 1st set of the data

Run Number	MC Temperature (mK)
77	22
62	60
62	80
63	100

1.8. Mode 8:

Mode 8 was also analyzed by 4 parameters. The data of higher than 1800 mK in mode 8 were not seemed to be reliable since the ESR range was no recognizable due to the up going data after 270 mT (FIG. 11).

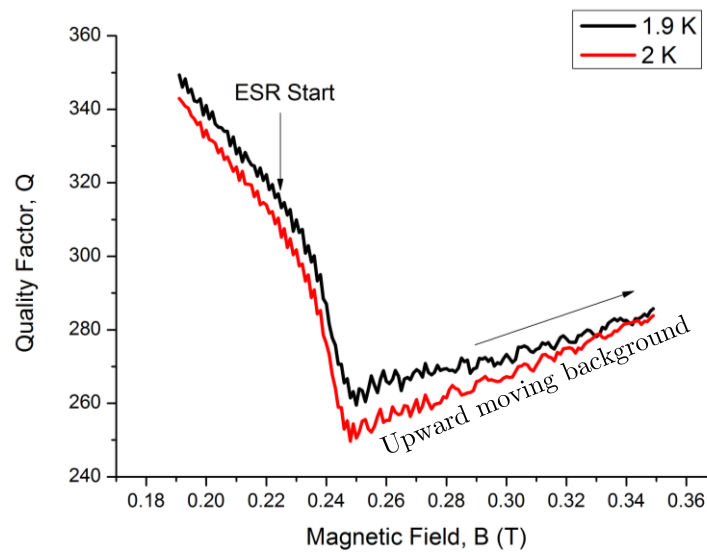


FIG. 11. The upward moving background in mode 8 data avoids recognition of the ESR range.

Thus, mode 8 curves were analyzed only up to 1800 mK and the rest of the data were left. They will probably get discussed and analyzed to gain some hints about the resonator behavior changes. The fitting parameters are plotted in figure 12.

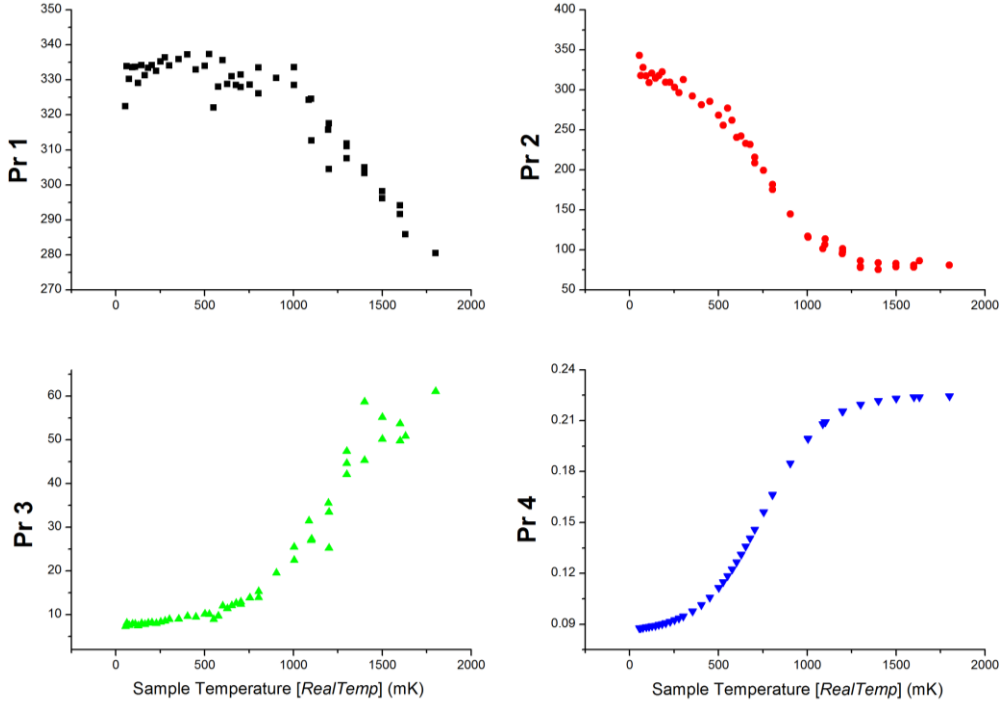


FIG. 12. Temperature dependence of the fitting parameters for mode 8.

There was only parameter number 4 which became formulated (fixed) and the rest of them were free to change during the fitting process (Table 10).

Table 10. Mode 8 fixed parameter and fixing formula. “*RealTemp*” values in mK.

Fixed Parameter	Fixing Formula	Description
4	$Pr4 = 0.225 + \frac{-0.140}{1 + \exp\left(\frac{RealTemp - 749}{169}\right)}$	runs 61 & after upto 1800 mK

1.9. Mode 9:

Mode 9 was also analyzed by 4 parameters.

Another mismatching had occurred in the data of mode 9 between 1400 mK and 1500 mK. This has directly affected the fitting parameters distribution as some abrupt changes in the parameter plots of FIG. 13.

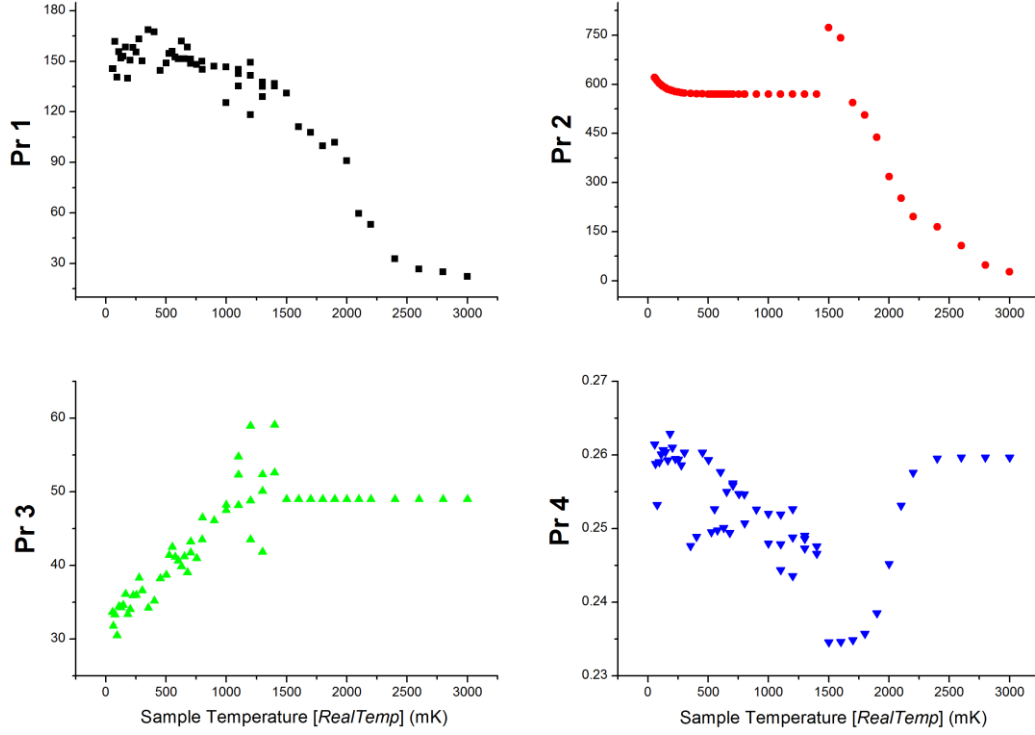


FIG. 13. Temperature dependence of the fitting parameters for mode 9. The different groups of data (e.g. at Pr4 data points) are due to the anomalous alterations in the resonator behavior. The fixed parameters are described in Table 11.

Table 11. Mode 9 fixed parameter and fixing formula. “*RealTemp*” values in mK.

Fixed Parameter	Fixing Formula	Description
2	$Pr2 = 570 + 93 * \exp\left(\frac{-RealTemp}{92}\right)$	upto 1400 mK
3	$Pr3 = 49$	from 1500 mK
4	$Pr4 = 0.260 - \frac{0.025}{1 + \exp\left(\frac{RealTemp - 2023}{74}\right)}$	from 1500 mK

1.10. The shift in the ESR resonance field:

During the measurements of the R01, it was noticed that after a time point in the measurements, a shift of the ESR resonance frequency has happened. This means, the ESR resonance field in the all data which were obtained before the mentioned time point was slightly different than the resonance field of the measured data (at the equal temperatures) after that. The point at which the shift had happened was the run

number 61 in which for the first time the magnetic field was increased to 350 mT in order to measure the higher modes of 4 to 9. In FIG. 14 one sample of the shifted data is presented.

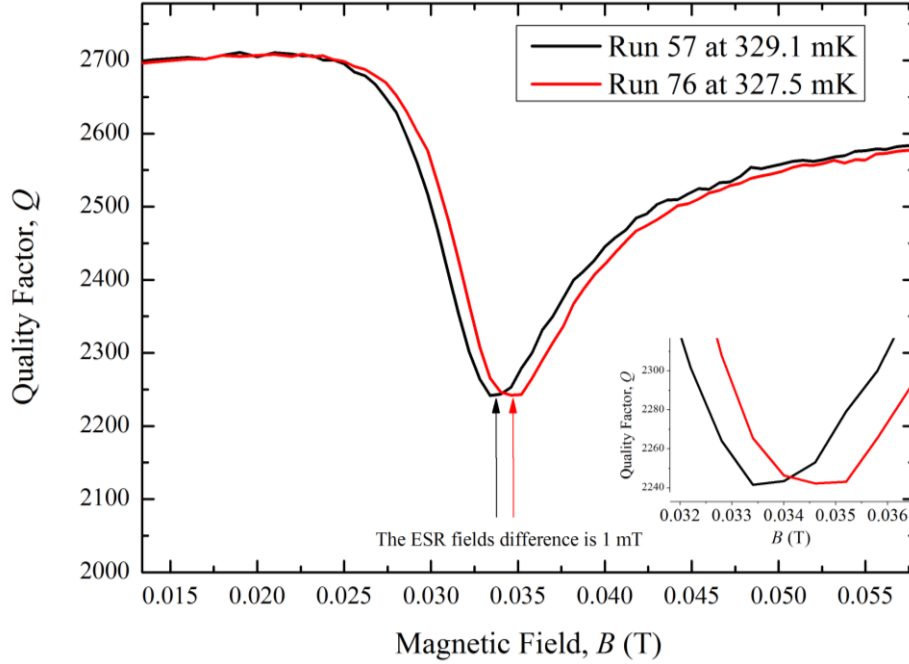


FIG. 14. The observed shift of the ESR field in mode 1 data. The inset magnifies the ESR resonance field regions.

We attributed this shift to the hysteretic behavior of the resonator under applying and sweeping magnetic field [48] since the background (off-resonance part of the line) was altered too. The shift was between 0.6 to 0.8 mT. As seen in the analysis above (from 1.2 to 1.9), due to this shift, all the data were categorized into two categories of before and after shift and analyzed separately to avoid a probable misinterpretation.

It should be noted that, the resonance frequency of the used resonator (R01) for the runs up to 60 and the runs from 61 on, was not different (at same temperatures) so that it leads to such a shift. For example, the resonance frequency of Mode 2 in Run 60 was 2.958... GHz at 56.5 mK and in Run 61 was 2.958... GHz at 53.7 mK which means the difference was less than 1 MHz. Such a difference could even be seen in the data of each run itself from the beginning to the end of the ESR line.

2. Resonator R02:

2.1. Circumstances and challenges:

Table 12 presents the measurements performed by R02.

Table 12. The temperature range and the ESR resonance field change of resonator R02.

	Temperature Range; Lowest/Highest (mK)	Resonance Field for Lowest/Highest Temperature (mT)
Mode 1, 2.07 GHz	43.7/2100	53/45
Mode 2, 4.09 GHz	43.5/2100	99/85
Mode 3, 6.14 GHz	44.2/2100	143/128
Mode 4, 8.12 GHz	48.5/2100	185/170
Mode 5, 10.12 GHz	50.6/2100	226/209
Mode 6, 12.14 GHz	51.7/2100	269/253

In the analyzing of the obtained data from R02, the biggest challenge was too low number of data after omitting the ESR range. This means we did not have so much background information to guide the fitting procedure to act as it is desired. FIG. 15 (a) shows the problem clearer. Like the fitting procedure of R01, for each mode, the ESR range was determined and deleted from the data set. The remnant points were then fitted, and so, the cut piece of data was numerically fitted by a constructed formula in the absence of ESR effect. This is shown as an example in FIG. 15.

The low number of the data to fit causes the fitting process stops (and consequently, different resulting fitting curves come out) as soon as the fitting criteria are satisfied. However, we want to reach to the best possible fitting curves which are close as much as possible to the very limited number of the existing data with the full range. This means, the parameters were fixed so that the extrapolated fitting curves were as similar as possible to the mentioned full range data. Extrapolations of the fitting curves were done toward 0 mT and toward 350 mT from the first and last recorded data of the measured ranges. Having this as the goal, the fitting procedure must be under purposeful fitting parameter fixing.

The proposed relationship for R02 (and R03, Section 3) is:

$$Q = Pr1 + \frac{Pr2}{1 + \exp(Pr3 * (B - Pr4))} \quad (2.1)$$

Fitting information of the all modes of R02 (except mode 1, due to the same reason for mode 1 of R01) is presented at the following.

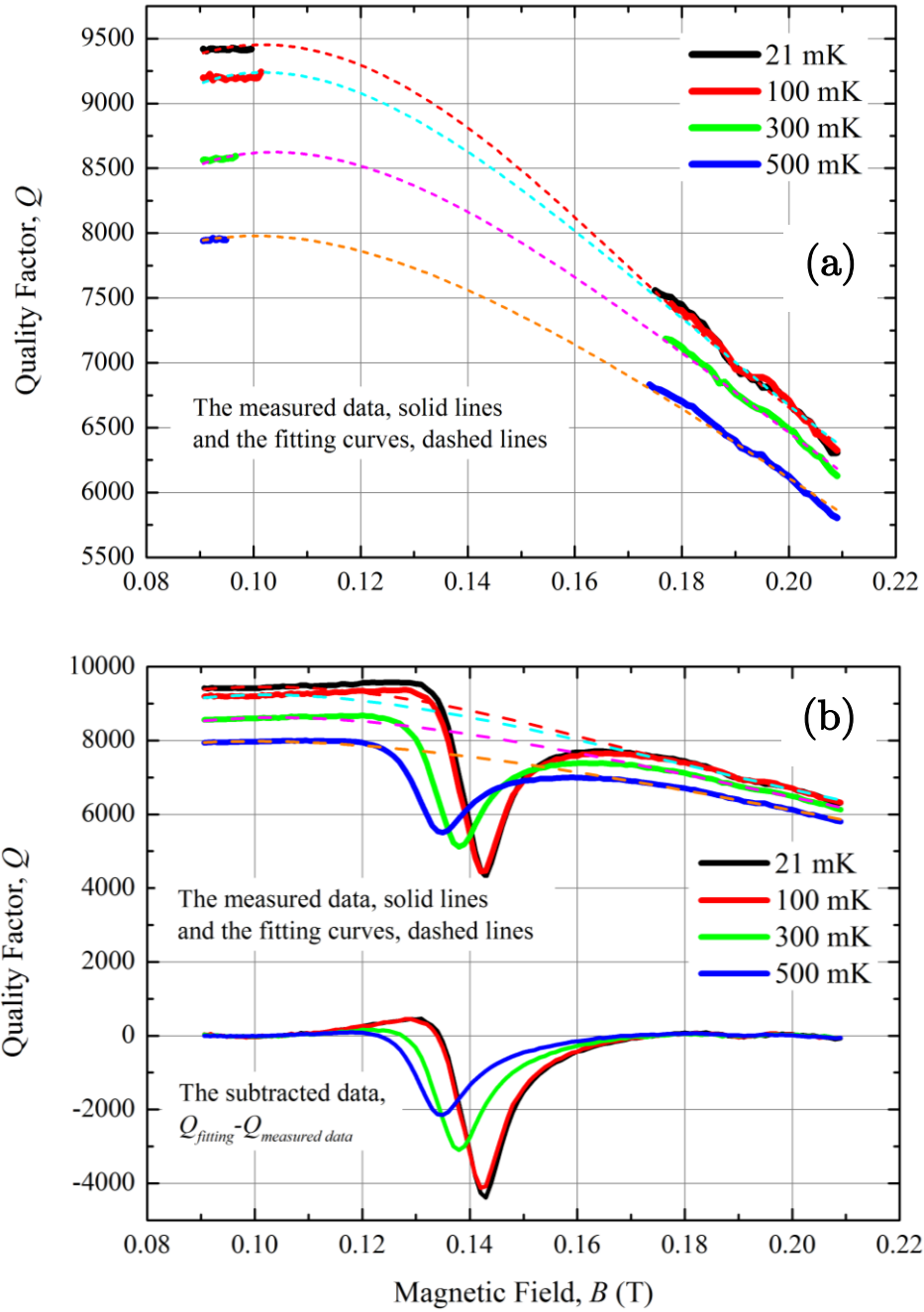


FIG. 15. (a) The data points of the ESR are omitted from the measured data and the remnant points are fitted. The curves belong to mode 3. (b) The upper curves show the measured data (solid lines) and their corresponding fitting curves (dashed lines). The lower curves are fitted data subtracted from the measured data. The temperatures are the mixing chamber temperature of the dilution fridge.

2.2. Mode 2:

FIG. 16 and Table 13 show the curves and fitting parameters plots of mode 2.

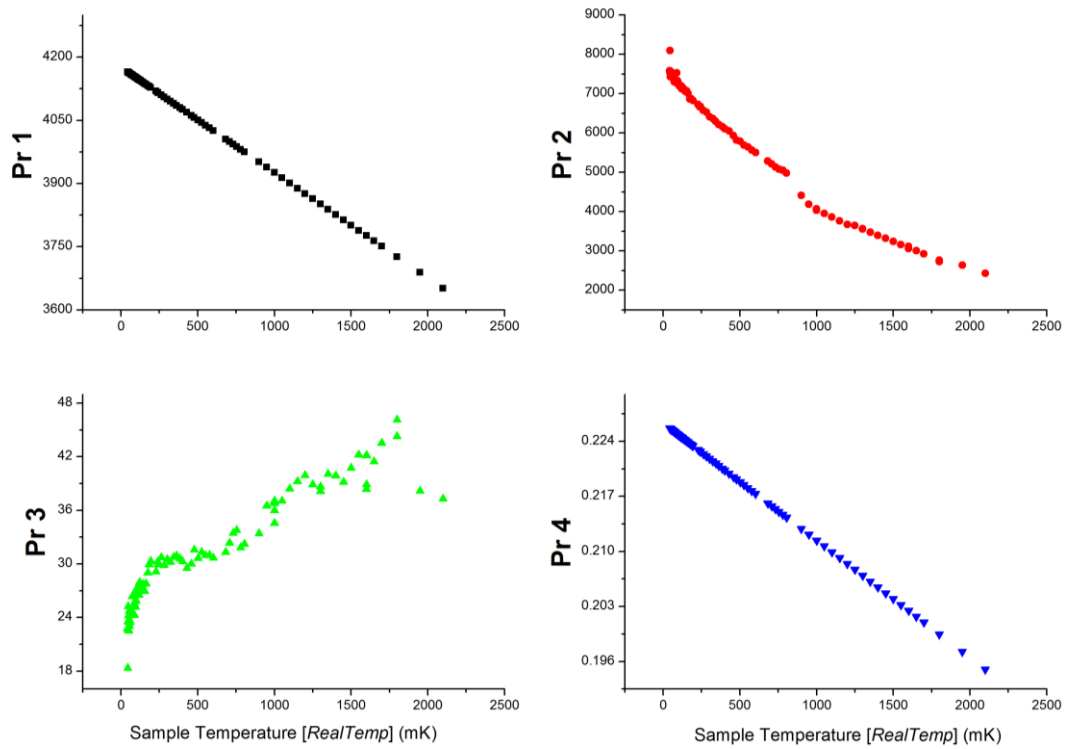


FIG. 16. Temperature dependence of the fitting parameters for mode 2.

Table 13. Mode 2 fixed parameter and fixing formula. “*RealTemp*” values in mK.

Fixed Parameter	Fixing Formula
1	$Pr1 = 4176 - 0.25 * RealTemp$
4	$Pr4 = 0.2263 - (1.49043E - 5) * RealTemp$

2.3. Mode 3:

FIG. 17 and Table 14 show the curves and fitting parameters plots of mode 3.

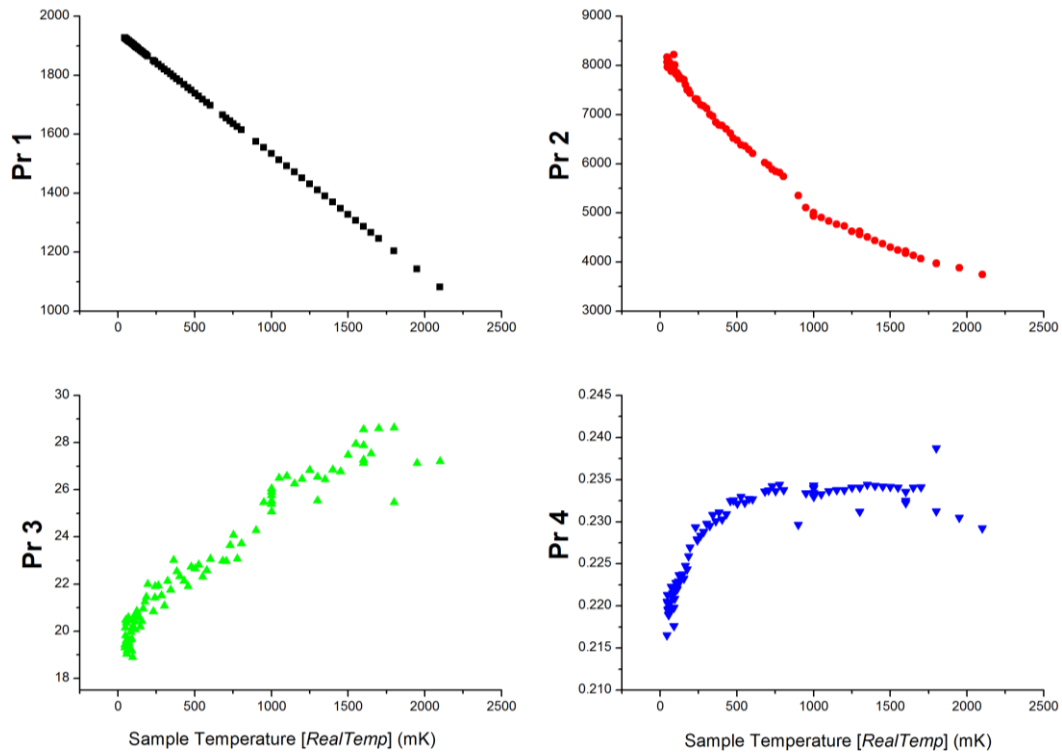


FIG. 17. Temperature dependence of the fitting parameters for mode 3.

Table 14. Mode 3 fixed parameter and fixing formula. “*RealTemp*” values in mK.

Fixed Parameter Number	Fixing Formula
1	$Pr1 = 1945 - 0.412 * RealTemp$

2.4. Mode 4:

FIG. 18 show the curves and fitting parameters plots of mode 4.

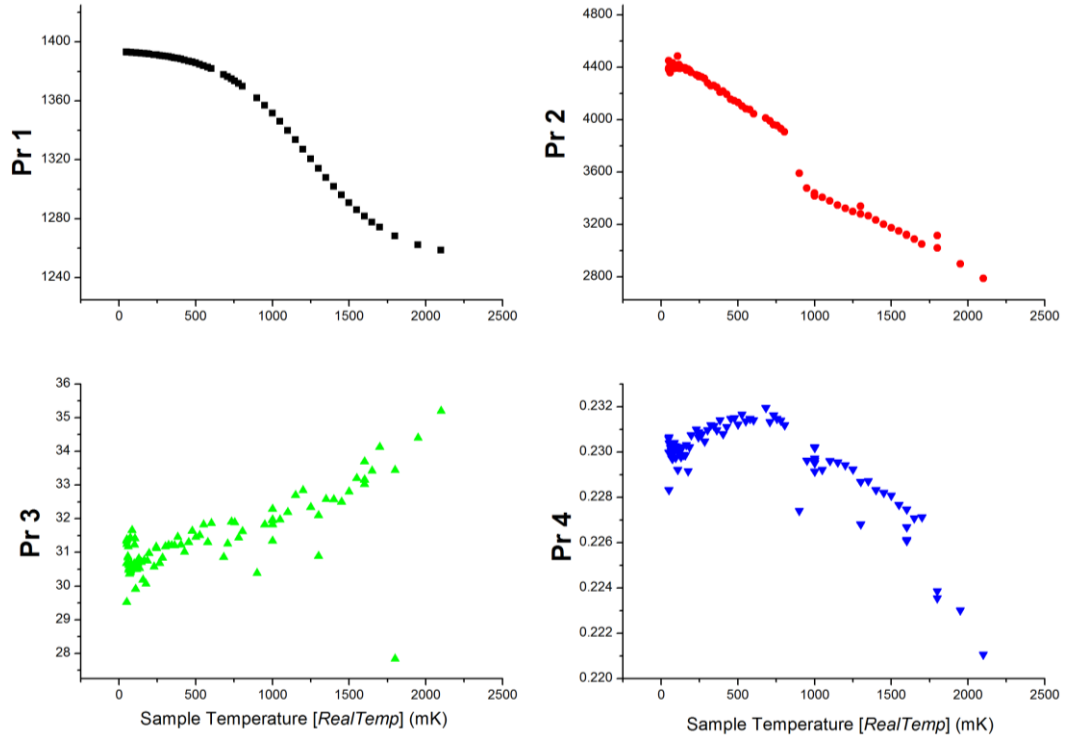


FIG. 18. Temperature dependence of the fitting parameters for mode 4. The jump between 800 mK and 900 mK in parameter 2 is because of the resonator performance change.

The significant gap between 800 mK and 900 mK data points in Pr2 diagram is because of a sudden decrease of the quality factor of the resonator which is not only because of 100 mK temperature increase. FIG. 19 shows the first data point of the entire obtained curve. This problem is found in modes 2 and 3 also; however, it is not as remarkable as the other modes.

The only fixed parameter in this mode is listed in Table 15.

Table 15. Mode 4 fixed parameter and fixing formula. “*RealTemp*” values in mK.

Fixed Parameter Number	Fixing Formula
1	$Pr1 = 1252.97238 + \frac{141.89777}{1 + \exp(0.00367 * (RealTemp - 1224.76772))}$

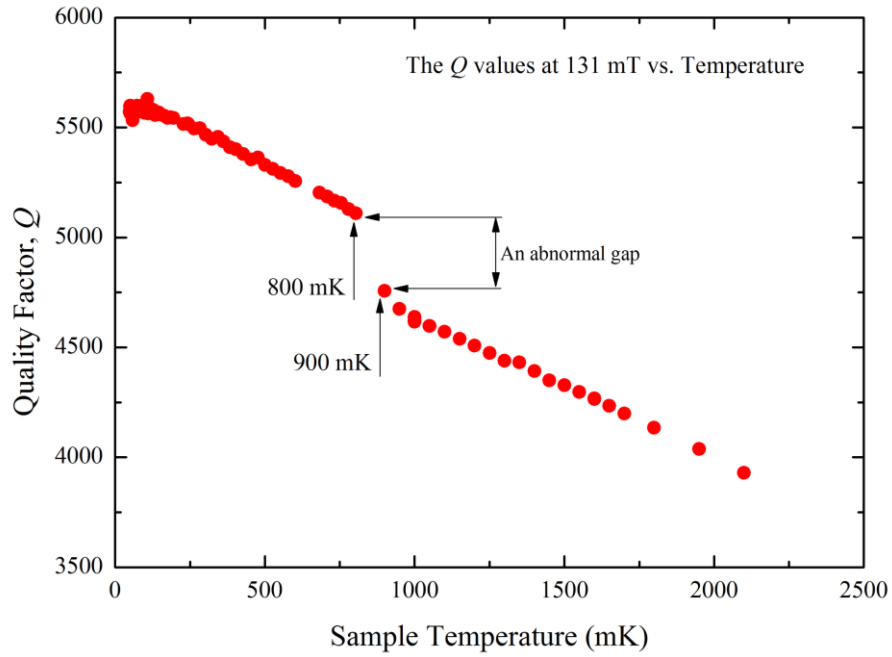


FIG. 19. The data points are the quality factor values at 131 mT (the first recorded field point) of mode 4 data. The dramatic decrease between 800 mK and 900 mK data points is not solely due to the temperature increase. The analogous between FIG. 19 and FIG. 18 Pr2 is remarkable.

2.5. Mode 5:

FIG. 20 and Table 16 shows the curves and fitting parameters of mode 5.

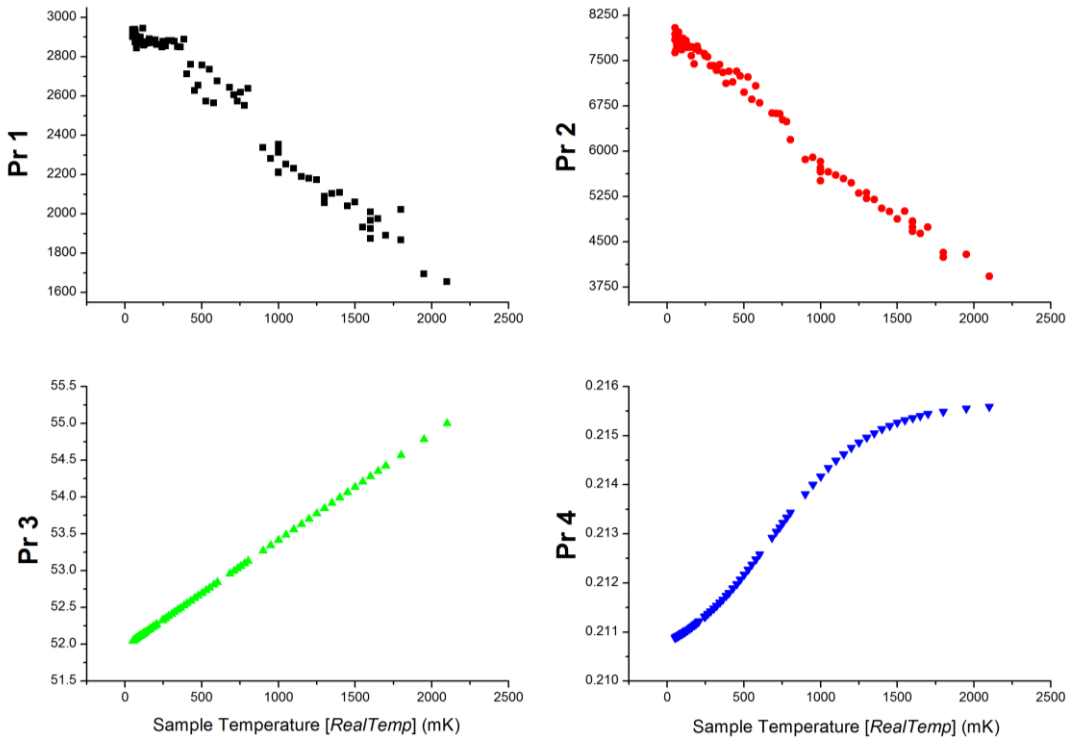


FIG. 20. Temperature dependence of the fitting parameters for mode 5.

The data of Mode 5 contained an abnormal jump for the fields above 240 mT. This jump and the following data were shifted down by an amount to make the two parts coincident.

Table 16. Mode 5 fixed parameter and fixing formula. “*RealTemp*” values in mK.

Fixed Parameter	Fixing Formula
3	$Pr3 = 52 + 0.00144 * RealTemp$
4	$P4 = 0.21025 + \frac{0.0054}{1 + \exp(0.00315 * (690.2 - RealTemp))}$

2.6. Mode 6:

FIG. 21 and Table 17 shows the curves and fitting parameters of mode 6.

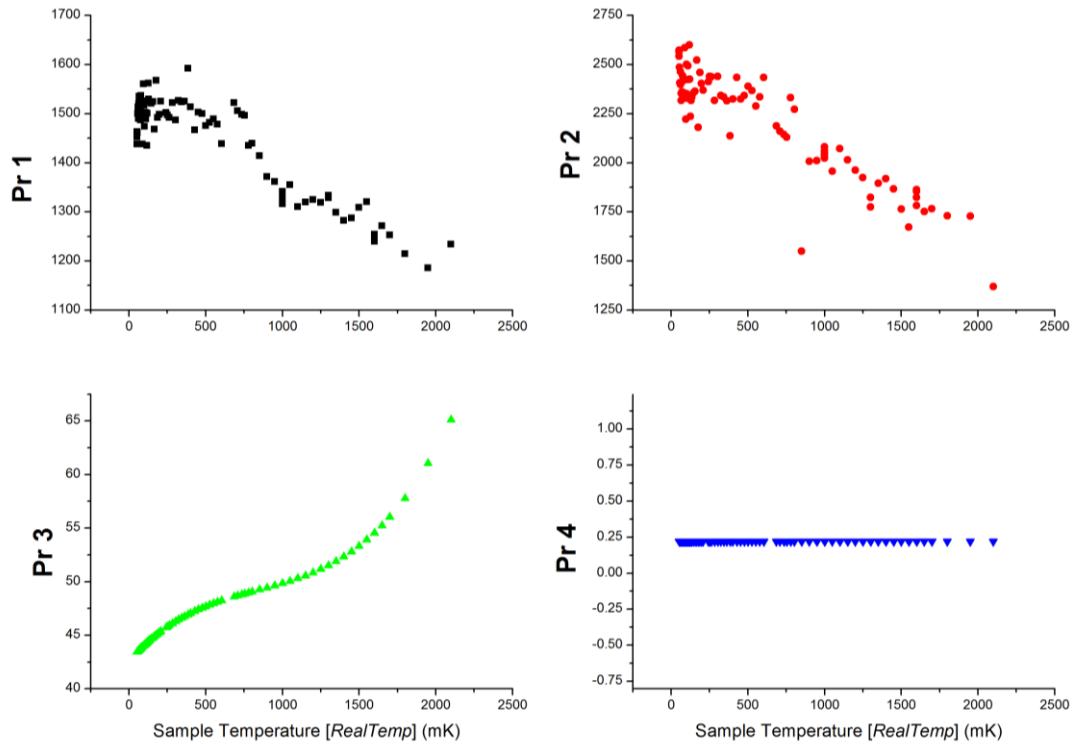


FIG. 21. Temperature dependence of the fitting parameters for mode 6.

Table 17. Mode 6 fixed parameter and fixing formula. “*RealTemp*” values in mK.

Fixed Parameter	Fixing Formula
3	$P3 = 42.65648 + 0.01568 * RealTemp - 1.40584E - 5 * RealTemp^2 + 5.56444E - 9 * RealTemp^3$
4	$P4 = 0.21977$

3. Resonator R03:

Table 18 presents the measurements performed by R03:

Table 18. The temperature range and the ESR resonance field change of resonator R03.

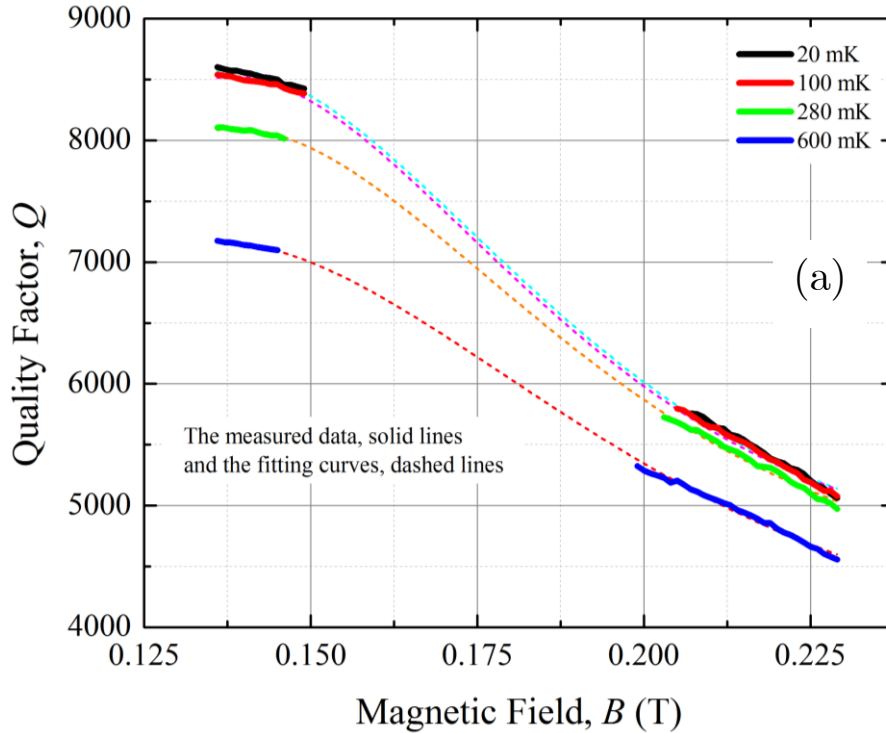
	Temperature Range (mK)	Resonance Field for Lowest/Highest Temperature (mT)
Mode 1, 2.65 GHz	43.6 - 4000	67/57
Mode 2, 5.25 GHz	43.6 - 4000	124/109
Mode 3, 7.90 GHz	47.7 - 4000	179/162
Mode 4, 10.52 GHz	50.4 - 4000	234/216

The proposed relationship for R03 is:

$$Q = Pr1 + \frac{Pr2}{1 + \exp(Pr3*(B - Pr4))} \quad (3.1)$$

The measurements of resonator R03 were also, like R02, with a short range of magnetic field and had the same procedures and challenges.

Like the fitting procedure of R01 and R02, for each mode, the ESR range was determined and deleted from the data set. The remnant points were then fitted, and so, the cut piece of data was numerically fitted by a constructed formula in the absence of ESR effect. This is shown as an example in FIG. 22.



Continue on the next page

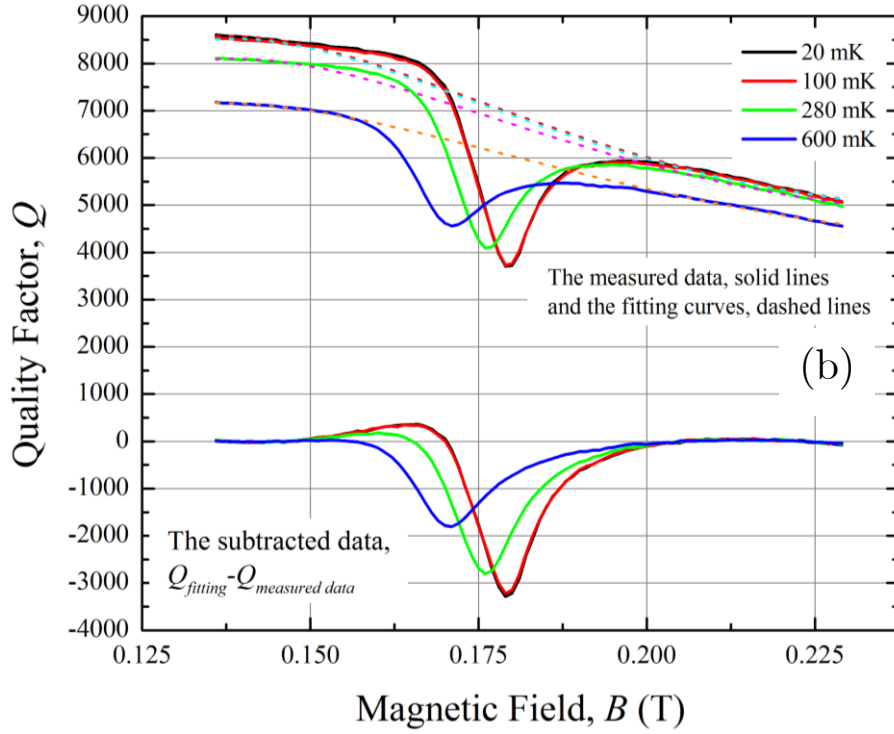


FIG. 22. (a) The data points of the ESR are omitted from the measured data and the remnant points are fitted. The curves belong to mode 3. (b) The upper curves show the measured data (solid lines) and their corresponding fitting curves (dashed lines). The lower curves are fitted data subtracted from the measured data. The temperatures are the mixing chamber temperature of the dilution fridge.

3.1. Mode 2:

FIG. 23 and Table 19 contain the fitting parameters of mode 2.

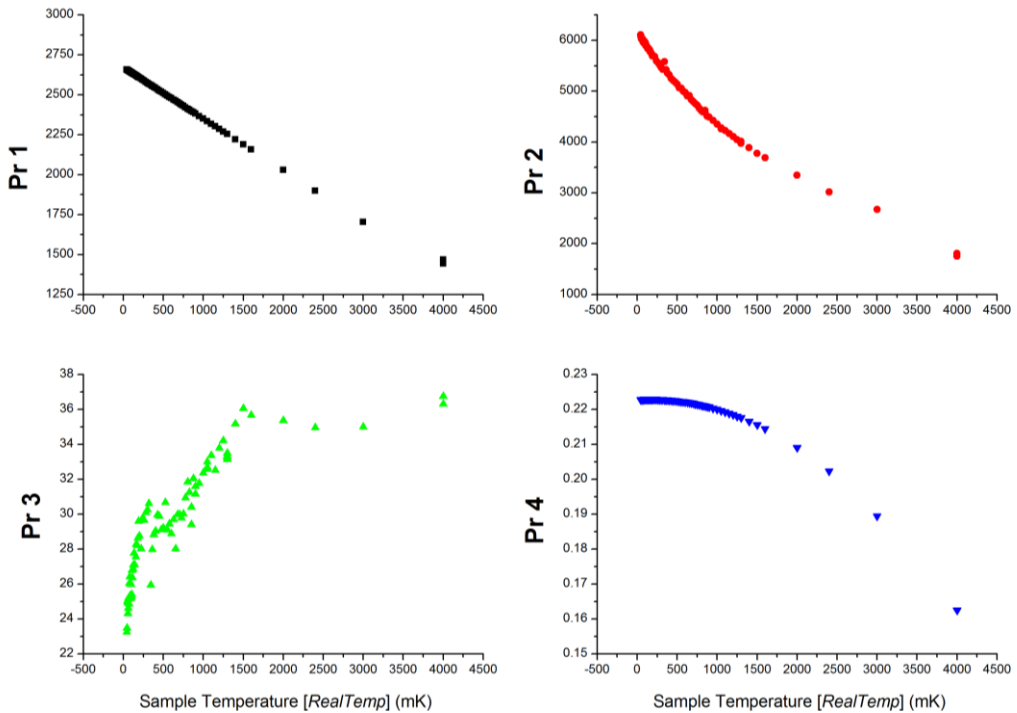


FIG. 23. Temperature dependence of the fitting parameters for mode 2.

Table 19. Mode 2 fixed parameter and fixing formula. “*RealTemp*” values in mK.

Fixed Parameter	Fixing Formula
1	$Pr1 = 2667 - 0.31209 * RealTemp$
4	$Pr4 = 0.22272 + (1.43655E - 6) * RealTemp - (4.16612E - 9) * RealTemp^2$

3.2. Mode 3:

FIG. 24 and Table 20 show the fitting parameters of mode 3.

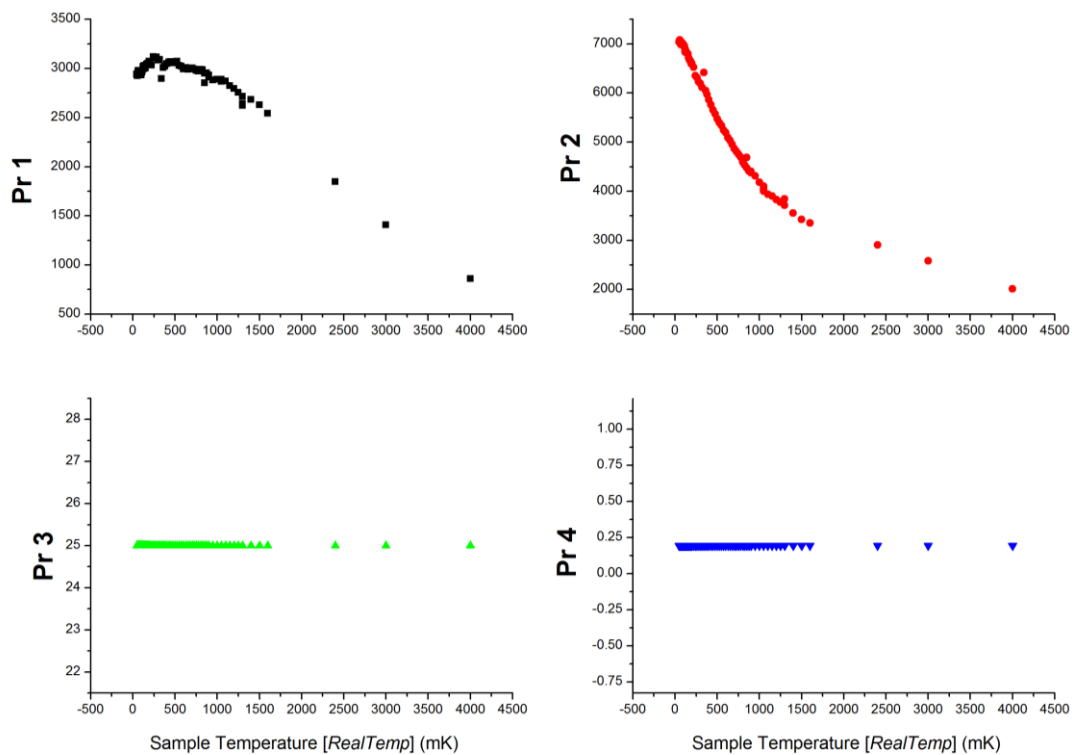


FIG. 24. Temperature dependence of the fitting parameters for mode 3.

Table 20. Mode 3 fixed parameter and fixing formula. “*RealTemp*” values in mK.

Fixed Parameter	Fixing Formula
3	$Pr3 = 25$
4	$Pr4 = 0.19358$

3.3. Mode 4:

FIG. 25 and Table 21 show the fitting parameters plots of mode 4.

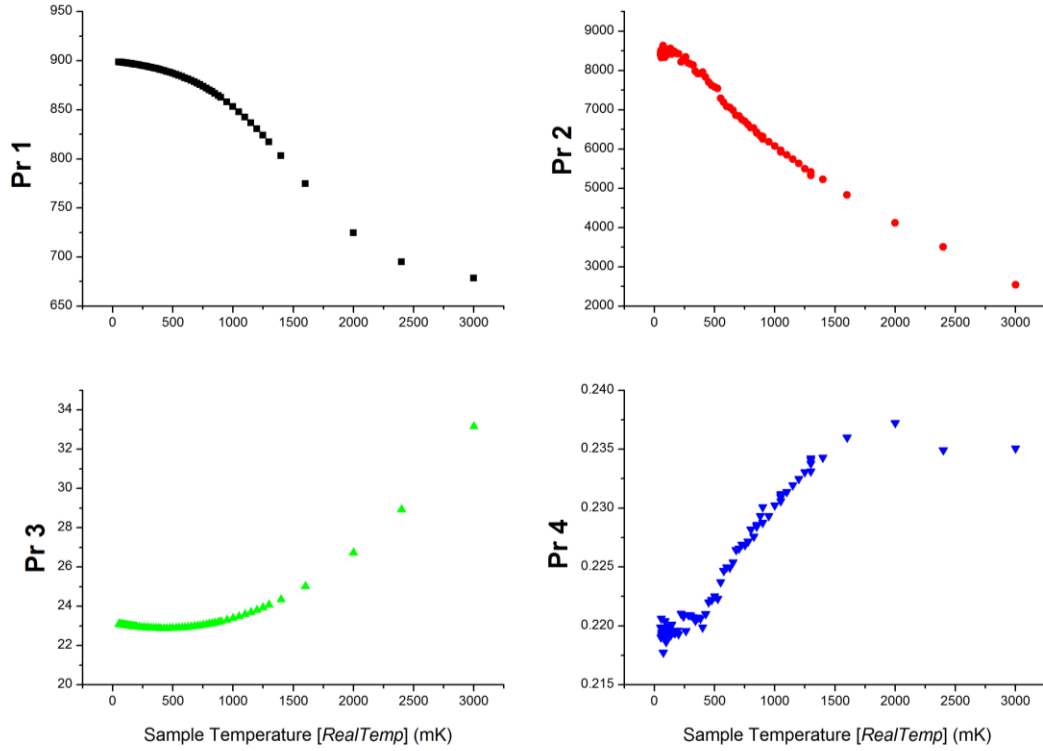


FIG. 25. Temperature dependence of the fitting parameters for mode 4.

The fixed parameters in this mode are listed in Table 21.

Table 21. Mode 4 fixed parameter and fixing formula. “*RealTemp*” values in mK.

Fixed Parameter	Fixing Formula
1	$Pr1 = 673.0234 + \frac{231.62057}{1 + \exp(0.0025 * (RealTemp - 1500))}$
3	$Pr3 = 23.15423 - 0.00131 * RealTemp + (1.54816E - 6) * RealTemp^2$

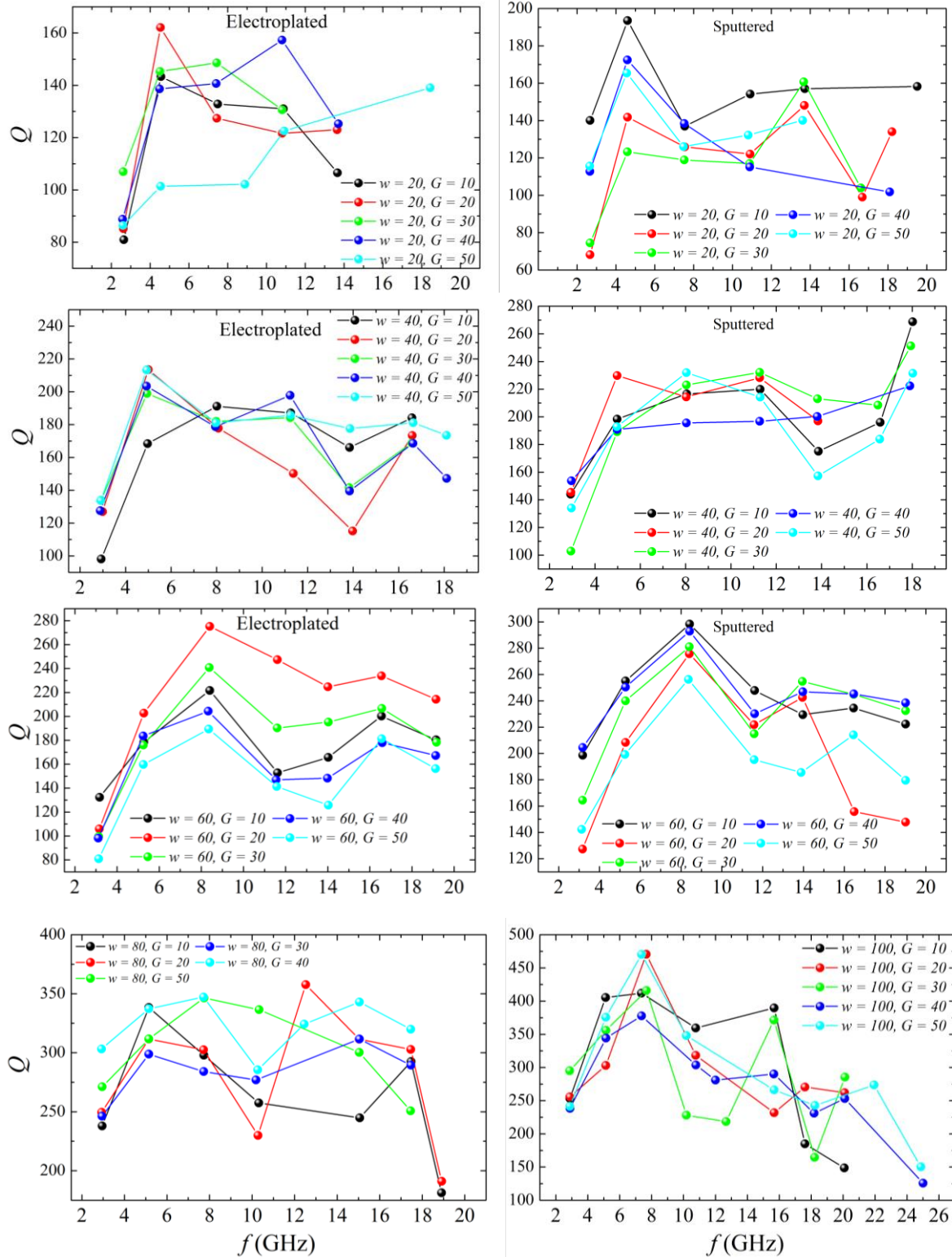
Appendix II

The list of the obtained quality factors at 5 K of the measured resonators with the structures of Nr. 3 and 4 in Table 4.2, chapter 4. The red-letter data are at some cases plotted in the diagrams and at some cases which were not fitting suitably are not.

w (μm)	G (μm)	Mode & Q
20	10	Electroplated: 1 & 81, 2 & 143, 3 & 132, 4 & 131, 5 & 106, 7 & 172 Sputtered: 1 & 140, 2 & 194, 3 & 137, 4 & 154, 5 & 157, 7 & 158
	20	Electroplated: 1 & 85, 2 & 162, 3 & 127, 4 & 122, 5 & 123, 6 & 131, 7 & 190 Sputtered: 1 & 68, 2 & 142, 3 & 126, 4 & 122, 5 & 148, 6 & 99, 7 & 134
	30	Electroplated: 1 & 107, 2 & 145, 3 & 148, 4 & 131, 5 & 161, 6 & 160, 7 & 113 Sputtered: 1 & 74, 2 & 123, 3 & 119, 4 & 117, 5 & 161, 6 & 103
	40	Electroplated: 1 & 89, 2 & 139, 3 & 141, 4 & 157, 5 & 125 Sputtered: 1 & 85, 2 & 162, 3 & 127, 4 & 122, 5 & 123, 6 & 131, 7 & 190
	50	Electroplated: 1 & 56, 2 & 101, 3 & 102, 4 & 122, 7 & 140 Sputtered: 1 & 112, 2 & 172, 3 & 138, 4 & 115, 7 & 101
40	10	Electroplated: 1 & 98, 2 & 168, 3 & 191, 4 & 187, 5 & 166, 6 & 184 Sputtered: 1 & 144, 2 & 198, 3 & 216, 4 & 220, 5 & 175, 6 & 196, 7 & 268
	20	Electroplated: 1 & 127, 2 & 213, 3 & 178, 4 & 150, 5 & 115, 6 & 173 Sputtered: 1 & 145, 2 & 230, 3 & 214, 4 & 228, 5 & 197
	30	Electroplated: 1 & 134, 2 & 199, 3 & 182, 4 & 184, 5 & 142, 6 & 169 Sputtered: 1 & 103, 2 & 189, 3 & 223, 4 & 232, 5 & 213, 6 & 208, 7 & 251
	40	Electroplated: 1 & 127, 2 & 203, 3 & 179, 4 & 198, 5 & 140, 6 & 169, 7 & 147 Sputtered: 1 & 154, 2 & 191, 3 & 196, 4 & 196, 5 & 200, 7 & 222
	50	Electroplated: 1 & 134, 2 & 213, 3 & 181, 4 & 186, 5 & 178, 6 & 181, 7 & 173 Sputtered: 1 & 134, 2 & 193, 3 & 232, 4 & 214, 5 & 157, 6 & 183, 7 & 231
60	10	Electroplated: 1 & 132, 2 & 178, 3 & 222, 4 & 153, 5 & 166, 6 & 200, 7 & 180 Sputtered: 1 & 199, 2 & 255, 3 & 298, 4 & 248, 5 & 230, 6 & 234, 7 & 222
	20	Electroplated: 1 & 106, 2 & 203, 3 & 275, 4 & 247, 5 & 225, 6 & 234, 7 & 214 Sputtered: 1 & 127, 2 & 208, 3 & 275, 4 & 222, 5 & 242, 6 & 158, 7 & 147
	30	Electroplated: 1 & 100, 2 & 176, 3 & 240, 4 & 190, 5 & 195, 6 & 207, 7 & 178 Sputtered: 1 & 164, 2 & 240, 3 & 281, 4 & 215, 5 & 255, 6 & 245, 7 & 232
	40	Electroplated: 1 & 98, 2 & 184, 3 & 204, 4 & 147, 5 & 148, 6 & 178, 7 & 167 Sputtered: 1 & 205, 2 & 251, 3 & 293, 4 & 230, 5 & 247, 6 & 245, 7 & 238
	50	Electroplated: 1 & 81, 2 & 160, 3 & 190, 4 & 141, 5 & 126, 6 & 181, 7 & 156 Sputtered: 1 & 142, 2 & 199, 3 & 256, 4 & 195, 5 & 185, 6 & 214, 7 & 179
80	10	Electroplated: 1 & 237, 2 & 338, 3 & 298, 4 & 257, 5 & 103, 6 & 245, 7 & 292
	20	Electroplated: 1 & 250, 2 & 311, 3 & 302, 4 & 229, 5 & 357, 6 & 311, 7 & 302
	30	Electroplated: 1 & 246, 2 & 298, 3 & 284, 4 & 276, 5 & 423, 6 & 311, 7 & 289
	40	Electroplated: 1 & 303, 2 & 337, 3 & 347, 4 & 285, 5 & 324, 6 & 343, 7 & 319
	50	Electroplated: 1 & 271, 2 & 311, 3 & 346, 4 & 336, 6 & 300, 7 & 250
100	10	Electroplated: 1 & 253, 2 & 405, 3 & 412, 4 & 360, 6 & 390, 7 & 184, 8 & 148
	20	Electroplated: 1 & 255, 2 & 303, 3 & 471, 4 & 318, 6 & 231, 7 & 270, 8 & 262

30	Electroplated: 1 & 295, 2 & 356, 3 & 416, 4 & 228, 5 & 218, 6 & 164, 7 & 285
40	Electroplated: 1 & 238, 2 & 344, 3 & 378, 4 & 303, 5 & 280, 6 & 253, 7 & 176
50	Electroplated: 1 & 241, 2 & 376, 3 & 470, 4 & 347, 5 & 266, 6 & 242, 7 & 273

In the following, the plotted diagrams of the quality factor of the resonators of above table.



Appendix III

Figure 1 shows the variation of ESR line asymmetry, $\frac{A}{B}$, by change of $\frac{T_D}{T_2}$ [134]. The variables are defined in Figure 1 below. The ESR line is shown as absorbed power P vs. H and $\frac{dP}{dH}$ vs. H , while, the ESR signal in this work is always realized by plotting Q vs. B . Nevertheless, one can still use the interpretations of Figure 1 since in our ESR measurement the opposite of Q , $-Q$, represents the absorbed power P (insets). The ratio of $\frac{A}{B}$ is not expected to alter by changing the variable from P to $-Q$ since the both A and B will change in the same way and thus $\frac{A}{B}$ will stay unchanged. The horizontal axes of the insets of Figure 1 can also be replaced by B since the stretch of the curves as well as shifting the curves to right or left side will not influence A and B values.

Figure 2 shows $-Q$ vs. B and Figure 3 shows $\frac{d(-Q)}{dB}$ vs. B for the data of Figure 6.5 (e1); 19.77 GHz.

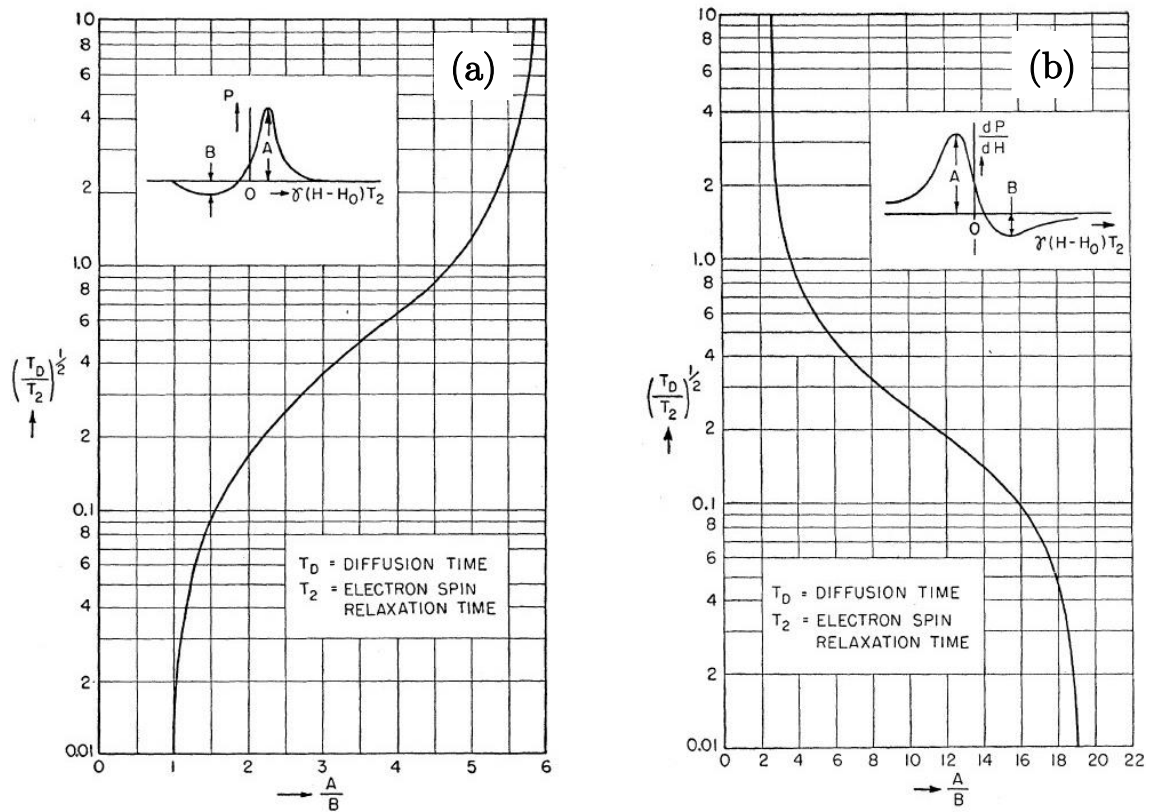


FIG. 1. $\frac{A}{B}$ vs. $\left(\frac{T_D}{T_2}\right)^{\frac{1}{2}}$ for (a) the power absorption and (b) the first derivative of the power absorption due to ESR in a thick metallic sample [134]. It is to note that the “A”s and “B”s in (a) and (b) represent totally different values and interpretations although have the same sign.

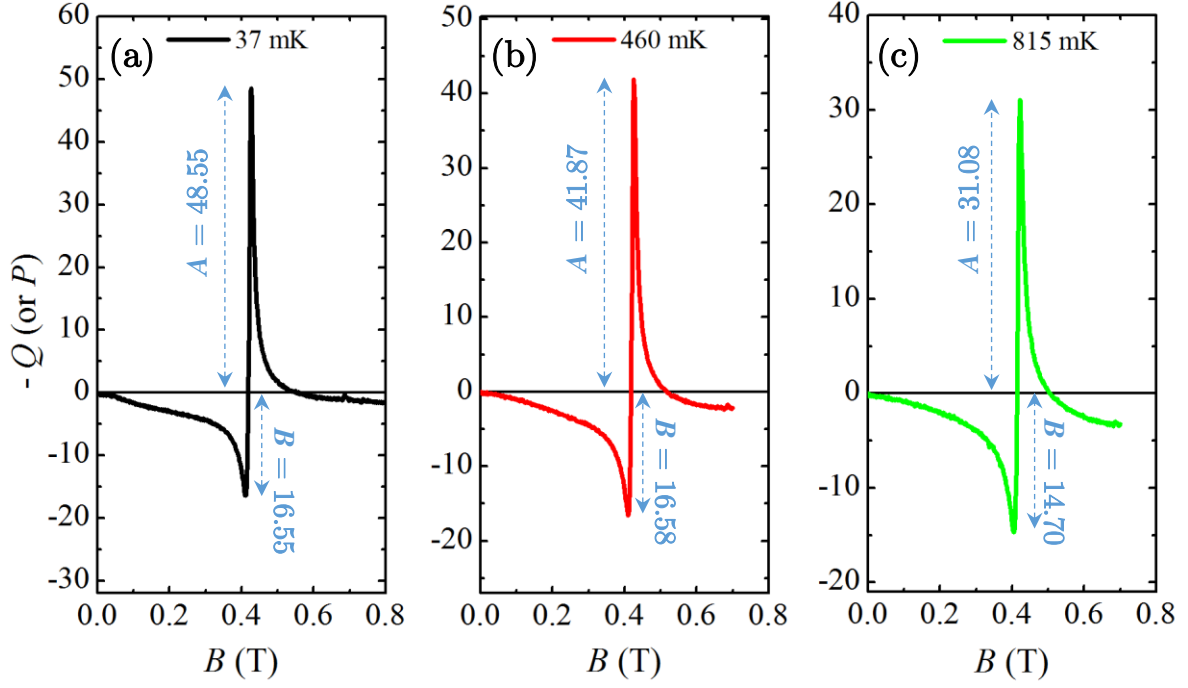


FIG. 2. $-Q$ vs. B at 19.77 GHz for (a) 37 mK (b) 460 mK and (c) 815 mK. A and B values are brought next to the corresponding parts.

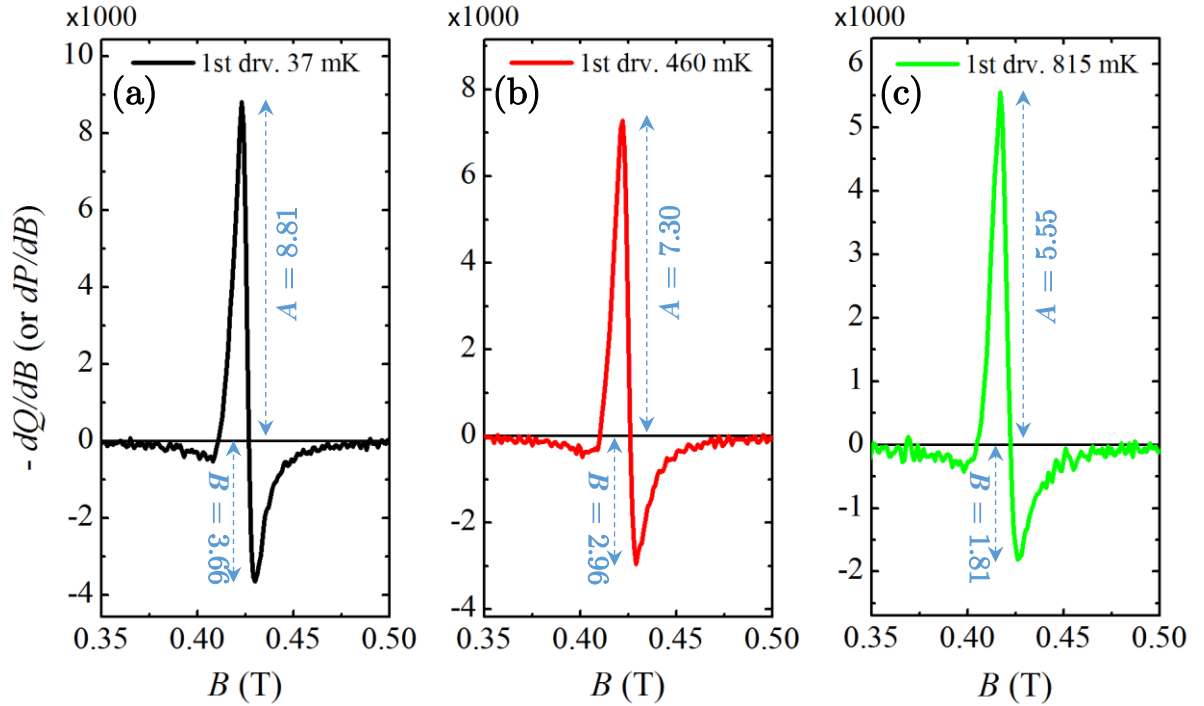


FIG. 3. $\frac{d(-Q)}{dB}$ vs. B at 19.77 GHz for (a) 37 mK (b) 460 mK and (c) 815 mK. A and B values are brought next to the corresponding parts.

The same plots for Figure 6.5 (a1), 2.65 GHz, are offered below in Figure 4. Table 1 contains the $\frac{A}{B}$ for all the data shown in Figure 6.5.

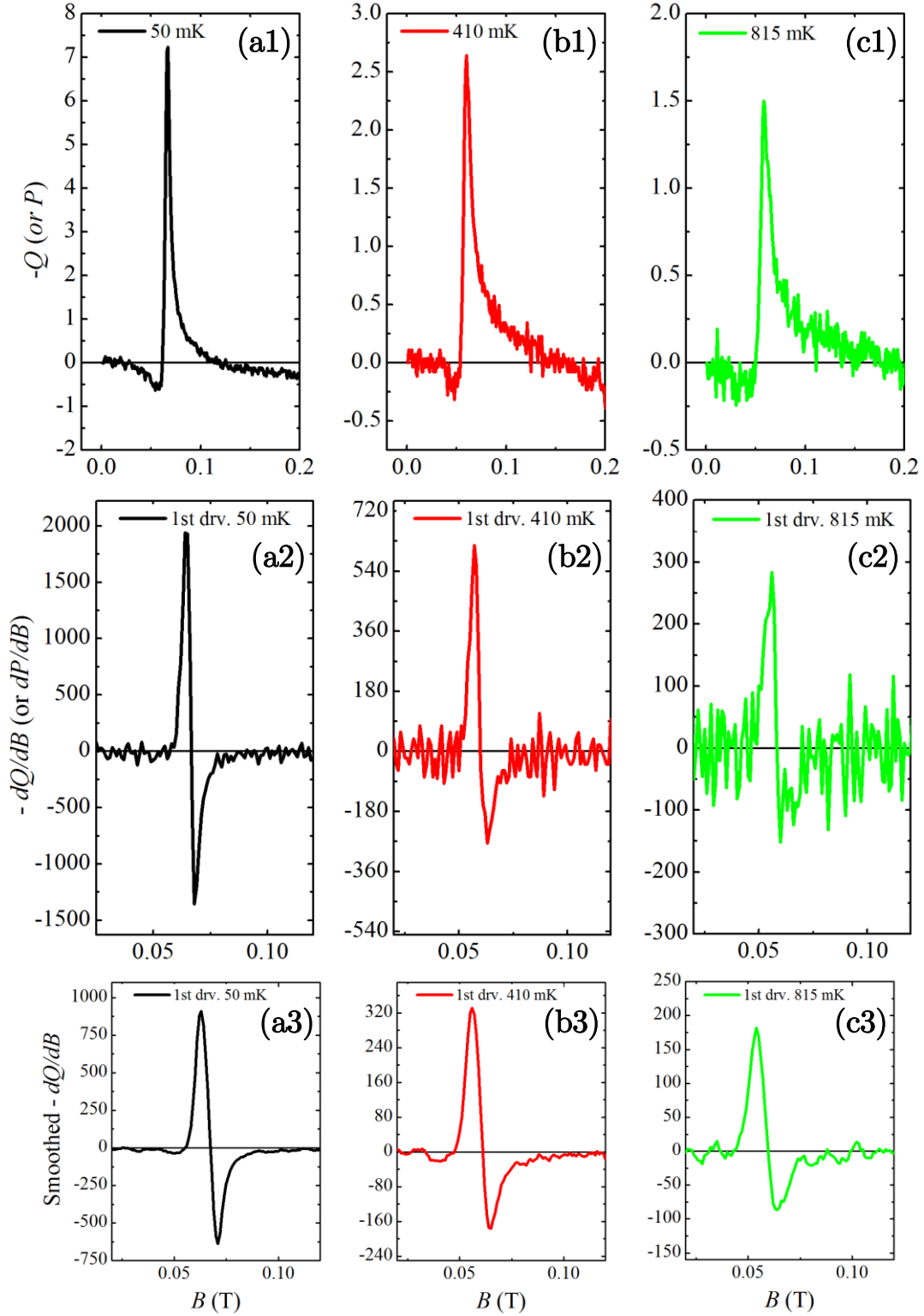


FIG. 4. (a) 37 mK (b) 460 mK and (c) 815 mK lines for Q vs. B at 2.65 GHz. (a1) 37 mK (b1) 460 mK and (c1) 815 mK lines for $\frac{d(-Q)}{dB}$ vs. B at 2.65 GHz and their corresponding smoothed curves in (a3), (b3) and (c3) respectively. The “Smoothed $\frac{d(-Q)}{dB}$ ” plots are smoothed quadratic with 10 points using Origin[®].

Table 1. $\frac{A}{B}$ for all the data shown in Figure 6.5. All data are calculated of the original data without smoothing. “Black”, “Red” and “Green” are the color of the curves in Figure 6.5 each of which has a given temperature in the range of 40, 400 and 800 mK respectively.

	Black		Red		Green	
	$-Q$	$-dQ/dB$	$-Q$	$-dQ/dB$	$-Q$	$-dQ/dB$
2.65 GHz	A=7.23 B=0.62 $A/B=11.66$	A=1940 B=1354 $A/B=1.43$	A=2.64 B=0.32 $A/B=8.25$	A=618 B=275 $A/B=2.25$	A=1.50 B=0.22 $A/B=6.82$	A=283 B=152 $A/B=1.86$
5.74 GHz	A=5.65 B=0.87 $A/B=6.49$	A=1232 B=952 $A/B=1.29$	A=2.71 B=0.44 $A/B=6.16$	A=508 B=266 $A/B=1.91$	A=1.70 B=0.16 $A/B=10.63$	A=273 B=135 $A/B=2.02$
9.35 GHz	A=26.39 B=1.79 $A/B=14.74$	A=4167 B=3992 $A/B=1.04$	A=17.89 B=1.99 $A/B=8.99$	A=2713 B=2061 $A/B=1.32$	A=11.13 B=0.97 $A/B=11.47$	A=1530 B=953 $A/B=1.61$
15.08 GHz	A=25.11 B=3.16 $A/B=7.95$	A=3281 B=2691 $A/B=1.22$	A=20.96 B=3.45 $A/B=6.08$	A=2811 B=1972 $A/B=1.43$	A=15.11 B=2.38 $A/B=6.35$	A=2004 B=1172 $A/B=1.71$
19.77 GHz	A=48.55 B=16.55 $A/B=2.93$	A=8819 B=3657 $A/B=2.41$	A=41.87 B=16.58 $A/B=2.52$	A=7296 B=2957 $A/B=2.47$	A=31.08 B=14.7 $A/B=2.11$	A=5549 B=1812 $A/B=3.06$

As discussed in Ref. [20], [134], [135] and [190], Figure 1 (b) shows $\frac{A}{B}$ has an approach to 2.7 for $\frac{dp}{dH}$ for $\frac{T_D}{T_2} \rightarrow \infty$. This is the case for “an undesired resonance due to impurities” with a Lorentzian ESR line if they are distributed throughout the volume of the sample. In a case that stationary paramagnetic impurities are placed only at the surface of the metallic sample, $\frac{A}{B}=1$ and the line is Gaussian [134].

In a case of a completely anomalous skin effect the ESR line asymmetry results to a $\frac{A}{B} = 5$ [134].

All these theoretical predictions and even their practical proving in Ref. [134], [135] have been done for alkali or in other words normal metals. By comparing these with the obtained $\frac{A}{B}$ ratios for YbRh₂Si₂ in this work (Table 1, from $\frac{d(-Q)}{dB}$; highlighted by Cyan) as well as the similar data of the other ESR studies on YbRh₂Si₂ [2] [126], one notes immediately that, there are still needs to develop theories for interpretation of the ESR data of a strongly correlated system like a Kondo lattice.

References

- [1] P. Gegenwart, Q. Si, F. Steglich, "Quantum criticality in heavy-fermion metals," *Nature Physics*, vol. 4, p. 186, 2008.
- [2] J. Sichelschmidt, V. A. Ivanshin, J. Ferstl, C. Geibel, F. Steglich, "Low Temperature Electron Spin Resonance of the Kondo Ion in a Heavy Fermion Metal: YbRh₂Si₂," *Physical Review Letters*, vol. 91, p. 156401, 2003.
- [3] C. Krellner, S. Lausberg, A. Steppke, M. Brando, L. Pedrero, H. Pfau, S. Tence, H. Rosner, F. Steglich, C. Geibel, "Ferromagnetic quantum criticality in the quasi-one-dimensional heavy fermion metal YbNi₄P₂," *New Journal of Physics*, vol. 13, p. 103014, 2011.
- [4] T. Isono, T. Terashima, K. Miyagawa, K. Kanoda, S. Uji, "Quantum criticality in an organic spin-liquid insulator κ -(BEDT-TTF)₂Cu₂(CN)₃," *Nature Communications*, vol. 7, p. Article Nr. 13494, 2016.
- [5] M. Dressel, P. Lazic, A. Pustogow, E. Zhukova, B. Gorshunov, J. A. Schlueter, O. Milat, B. Gumhalter, S. Tomic, "Lattice vibrations of the charge-transfer salt κ -(BEDT-TTF)₂Cu₂(CN)₃: Comprehensive explanation of the electrodynamic response in a spin-liquid compound," *Physical Review B*, vol. 93, p. 081201, 2016.
- [6] M. Pinteric, M. Culo, O. Milat, M. Basletic, B. Korin-Hamzic, E. Tafra, A. Hamzic, T. Ivek, T. Peterseim, K. Miyagawa, K. Kanoda, J. A. Schlueter, M. Dressel, S. Tomic, "Anisotropic charge dynamics in the quantum spin-liquid candidate κ -(BEDT-TTF)₂Cu₂(CN)₃," *Physical Review B*, vol. 90, p. 195139, 2014.
- [7] J. von Fraunhofer, "Bestimmung des Brechungs- und des Farbenzerstreungs-Vermögens verschiedener Glasarten, in Bezug auf die Vervollkommnung achromatischer Fernröhre," *Annalen der Physik*, vol. 56, p. 264, 1817.
- [8] G. Kirchhof, R. Bunsen, " Chemische Analyse durch Spectralbeobachtungen," *Annalen der Physik und der Chemie*, vol. 110, p. 161, 1860.
- [9] J. J. Balmer, "Notiz über die Spectrallinien des Wasserstoffs," *Annalen der Physik*, vol. 261, p. 80, 1885.
- [10] N. Bohr, "On the constitution of atoms and molecules," *Philosophical Magazine*, vol. 26, p. 1, 1913.
- [11] R. C. Hilborn, "Einstein coefficients, cross sections, f values, dipole moments, and all that," *American Journal of Physics*, vol. 50, p. 982, 1982.

- [12] S. N. Bose, "Plancks Gesetz und Lichtquantenhypothese," *Zeitschrift für Physik*, vol. 26, p. 178, 1924.
- [13] W. Gerlach, O. Stern, "Der experimentelle Nachweis der Richtungsquantelung im Magnetfeld," *Zeitschrift für Physik*, vol. 8, p. 349, 1922.
- [14] W. Gerlach, O. Stern, "Das magnetische Moment des Silberatoms," *Zeitschrift für Physik*, vol. 9, p. 353, 1922.
- [15] W. Gerlach, O. Stern, "Der experimentelle Nachweis des magnetischen Moments des Silberatoms," *Zeitschrift für Physik*, vol. 8, p. 110, 1922.
- [16] S. Goudsmit, R. de L. Kronig, "Die Intensität der Zeemankomponenten," *Naturwissenschaften*, vol. 13, p. 90, 1925.
- [17] W. Pauli, "Über den Zusammenhang des Abschlusses der Elektronengruppen im Atom mit der Komplexstruktur der Spektren," *Zeitschrift für Physik*, vol. 31, p. 765, 1925.
- [18] G.E. Uhlenbeck, S. Goudsmit, "Ersetzung der Hypothese vom unmechanischen Zwang durch eine Forderung bezüglich des inneren Verhaltens jedes einzelnen Elektrons," *Naturwissenschaften*, vol. 13, p. 953, 1925.
- [19] "CODATA values of the fundamental constants, NIST".
- [20] C. P. Poole, *Electron Spin Resonance; A Comprehensive Treatise on Experimental Techniques*, Dover Publications, Inc., 1997.
- [21] C. C. Rowlands, D.M. Murphy, "EPR Spectroscopy, Theory, in *Encyclopedia of Spectroscopy and Spectrometry* (ed J. Lindon)," 445, Elsevier, Oxford, 1999.
- [22] <http://www.drmmr.dk/MR>.
- [23] <http://www.chem.wisc.edu/areas/reich/nmr/08-tech-01-relax.htm>.
- [24] D. M. Pozar, *Microwave Engineering*, 4 ed., John Wiley & Sons Ltd , 2011.
- [25] B. Johansson, S. Haraldson, L. Pettersson, O. Beckman, "A stripline resonator for ESR," *Review of Scientific Instruments*, vol. 45, p. 1445, 1974.
- [26] D. Bothner, T. Gaber, M. Kemmler, D. Koelle, R. Kleiner, "Improving the performance of superconducting microwave resonators in magnetic fields," *Applied Physics Letters*, vol. 98, p. 102504, (2011).
- [27] K. Geerlings, S. Shankar, E. Edwards, L. Frunzio, R. J. Schoelkopf, M. H. Devoret, "Improving the quality factor of microwave compact resonators by optimizing their geometrical parameters," *Applied Physics Letters*, vol. 100, p. 192601, 2012.

- [28] J-Y. Ke, C. H. Chen, "Dispersion and Attenuation Characteristics of Coplanar Waveguides with Finite Metallization Thickness and Conductivity," *IEEE Transactions on Microwave Theory and Techniques*, vol. 43, no. 5, p. 1128, 1995.
- [29] A. K. Rastogi, S. Mishra, "Coplanar Waveguide Characterization with Thick Metal Coating," *International Journal of Infrared and Millimeter Waves*, vol. 20, no. 3, p. 505, 1999.
- [30] M. R. Namordi, A. Mogro-Campero, L. G. Turner, D. W. Hogue, "Comparison of high-temperature-superconductor and metal-based resonators," *IEEE Transactions on Microwave Theory and Techniques*, vol. 39, no. 9, p. 1468, 1991.
- [31] A. Dehe, H. Klingbeil, C. Weil, H. L. Hartnagel, "Membrane-supported coplanar waveguides for MMIC and sensor application," *IEEE Microwave and Guided Wave Letters*, vol. 8, no. 5, p. 185, 1998.
- [32] H. Wang, L. Zhu, "Ultra-wideband bandpass filter using back-to-back microstrip-to-CPW transition structure," *IEEE Microwave and Wireless Components Letters*, vol. 15, no. 12, p. 1337, 2005.
- [33] D. Bothner, M. Knufinke, H. Hattermann, R. Wölbing, B. Ferdinand, P. Weiss, S. Bernon, J. Fortágh, D. Koelle, R. Kleiner, "Inductively coupled superconducting half wavelength resonators as persistent current traps for ultracold atoms," *New Journal of Physics*, vol. 15, p. 093024, 2013.
- [34] H. Wang, M. Mariani, R. C. Bialczak, M. Lenander, E. Lucero, M. Neeley, A. D. O'Connell, D. Sank, M. Weides, J. Wenner, T. Yamamoto, Y. Yin, J. Zhao, J. M. Martinis, A. N. Cleland, "Deterministic Entanglement of Photons in Two Superconducting Microwave Resonators," *Physical Review Letters*, vol. 106, p. 060401, 2011.
- [35] Y. Wiemann, J. Simmendinger, C. Clauss, L. Bogani, D. Bothner, D. Koelle, R. Kleiner, M. Dressel, M. Scheffler, "Observing electron spin resonance between 0.1 and 67 GHz at temperatures between 50 mK and 300 K using broadband metallic coplanar waveguides," *Applied Physics Letters*, vol. 106, p. 193505, 2015.
- [36] W. J. Wallace, R. H. Silsbee, "Microstrip resonators for electron-spin resonance," *Review of Scientific Instruments*, vol. 62, p. 1754, 1991.
- [37] H. J. Mamin, R. Budakian, D. Rugar, "Superconducting microwave resonator for millikelvin magnetic resonance force microscopy," *Review of Scientific Instruments*, vol. 74, p. 2749, 2003.
- [38] R. Narkowicz, D. Suter, R. Stonies, "Planar microresonators for EPR experiments," *Journal of Magnetic Resonance*, vol. 175, p. 275, 2005.

- [39] R. Narkowicz, D. Suter, I. Niemeyer, "Scaling of sensitivity and efficiency in planar microresonators for electron spin resonance," *Review of Scientific Instruments*, vol. 79, p. 084702, 2008.
- [40] A. C. Torrezan, T. P. Mayer Alegre, G. Medeiros-Ribeiro, "Microstrip resonators for electron paramagnetic resonance experiments," *Review of Scientific Instruments*, vol. 80, p. 075111, 2009.
- [41] Y. Twig, E. Dikarov, W. D. Hutchison, A. Blank, "Note: High sensitivity pulsed electron spin resonance spectroscopy with induction detection," *Review of Scientific Instruments*, vol. 82, p. 076105, 2011.
- [42] H. Malissa, D. I. Schuster, A. M. Tyryshkin, A. A. Houck, S. A. Lyon, "Superconducting coplanar waveguide resonators for low temperature pulsed electron spin resonance spectroscopy," *Review of Scientific Instruments*, vol. 84, p. 025116, 2013.
- [43] C. Clauss, D. Bothner, D. Koelle, R. Kleiner, L. Bogani, M. Scheffler, M. Dressel, "Broadband electron spin resonance from 500 MHz to 40 GHz using superconducting coplanar waveguides," *Applied Physics Letters*, vol. 102, p. 162601, 2013.
- [44] M. Scheffler, K. Schlegel, C. Clauss, D. Hafner, C. Fella, M. Dressel, M. Jourdan, J. Sichelschmidt, C. Krellner, C. Geibel, F. Steglich, "Microwave spectroscopy on heavy-fermion systems: Probing the dynamics of charges and magnetic moments," *Physica Status Solidi B*, vol. 250, p. 439, 2013.
- [45] A. Ghirri, C. Bonizzoni, D. Gerace, S. Sanna, A. Cassinese, M. Affronte, "YBa₂Cu₃O₇ microwave resonators for strong collective coupling with spin ensembles," *Applied Physics Letters*, vol. 106, p. 184101, 2015.
- [46] R. Narkowicz, H. Ogata, E. Reijerse, D. Suter, "A cryogenic receiver for EPR," *Journal of Magnetic Resonance*, vol. 237, p. 79, 2013.
- [47] D. Bothner, C. Clauss, E. Koroknay, M. Kemmler, T. Gaber, M. Jetter, M. Scheffler, P. Michler, M. Dressel, D. Koelle, R. Kleiner, "Reducing vortex losses in superconducting microwave resonators with microsphere patterned antidot arrays," *Applied Physics Letters*, vol. 100, p. 12601, 2012.
- [48] D. Bothner, T. Gaber, M. Kemmler, D. Koelle, R. Kleiner, S. Wünsch, M. Siegel, "Magnetic hysteresis effects in superconducting coplanar microwave resonators," *Physical Review B*, vol. 86, p. 14517, 2012.
- [49] M. Dressel, G. Grüner, *Electrodynamics of Solids: Optical Properties of Electrons in Matter*, Cambridge University Press, 2002.
- [50] "MIT Open Course Ware," 2006. [Online]. Available: <https://ocw.mit.edu/courses/electrical-engineering-and-computer-science>.

- [51] L. Moura, I. Darwazeh, Introduction to Linear Circuit Analysis and Modelling: From DC to RF, Elsevier, Newness, 2005.
- [52] W. Hilberg, "From Approximations to Exact Relations for Characteristic Impedances," *IEEE Transactions on Microwave Theory and Techniques*, vol. 17, no. 5, p. 259, 1969.
- [53] A. K. Rastogi, N. J. McEwan, I. U. Khairuddin, A. Z. Jakai, "Effect of substrate thickness and metallization thickness on dispersion characteristics of CPW," *International Journal of Infrared and Millimeter Waves*, vol. 16, p. 1393, 1995.
- [54] K. C. Gupta, R. Garg, I. J. Bahl, P. Bhartia, Microstrip Lines and Slotlines, vol. 2, Artech House, Inc., 1996.
- [55] R. E. Collin, Foundations for Microwave Engineering, vol. 2, New York: Mc Graw-Hill, 1992.
- [56] "<http://qucs.sourceforge.net/tech/>," [Online].
- [57] T. Konaka, M. Sato, H. Asano, S. Kubo, "Relative permittivity and dielectric loss tangent of substrate materials for high-Tc superconducting film," *Journal of Superconductivity*, vol. 4, p. 283, 1991.
- [58] W. H. Hydl, "Experimentally observed frequency variation of the attenuation of millimeter-wave coplanar transmission lines with thin metallization," *IEEE Microwave and Guided Wave Letters*, vol. 2, p. 322, 1992.
- [59] S. Gevorgian, T. Martinsson, A. Deleniv, E. Kollberg, I. Vendik, "Simple and accurate dispersion expression for the effective dielectric constant of coplanar waveguides," *IEEE Proceedings - Microwaves, Antennas and Propagation*, vol. 144, no. 2, p. 145, 1997.
- [60] X. Zhang, J. Fang, K. K. Mei, Y. Liu, "Calculations of the Dispersive Characteristics of Microstrips by the Time-Domain Finite Difference Method," *IEEE Transactions on Microwave Theory and Techniques*, vol. 36, no. 2, p. 263, 1988.
- [61] M. S. Islam, E. Tuncer, D. P. Neikirk, "Calculation of conductor loss in coplanar waveguide using conformal mapping," *Electronics Letters*, vol. 29, no. 13, p. 1189, 1993.
- [62] I. Wolff, Coplanar Microwave Integrated Circuits, John Wiley & Sonc, Inc., 2006, pp. 63, 74.
- [63] T. Kaitazawa, C. W. Kuo, K. S. Kong, T. Itoh, "Planar transmission lines with finitely thick conductors and lossy substrates," *MTT-S Digest*, p. 769, 1991.
- [64] G. Ghione, C. U. Naldi, "Coplanar Waveguides for MMIC Applications: Effect of Upper Shielding, Conductor Backing, Finite-Extent Ground Planes, and Line-to-Line Coupling," *IEEE Transactions on Microwave Theory and Techniques*, vol. MTT 35, p. 260, 1987.

- [65] J-Y. Ke, I-S. Tsai, C. H. Chen, "Dispersion and Leakage Characteristics of Coplanar," *IEEE Transactions on Microwave Theory and Techniques* , vol. 40, no. 10, p. 1970, 1992.
- [66] D. Bhattacharya , "Characteristic impedance of coplanar waveguide," *Electronics Letters* , vol. 21, no. 13, p. 557, 1985.
- [67] R. Hoffmann, *Microwave Integrated Circuit Handbook*, Boston, MA: Artech House Publishers, 1987 .
- [68] J. S. McLean, A. D. Wieck, K. Ploog, T. Itoh, "Fullwave Analysis of Open-End Discontinuities in Coplanar Stripline and Finite Ground Plane Coplanar Waveguide in Open Environments using a Deterministic Spectral Domain Approach," in *Microwave Conference* , 1991.
- [69] M. Wang, B. Gao, Y. Tian, L. Tong, "Analysis of Characteristics of Coplanar Waveguide with Finite Ground-planes by the Method of Lines," *PIERS Online*, vol. 6, p. 46, 2010.
- [70] G. E. Ponchak, L. P. B. Katehi, E. M. Tentzeris, "Finite Ground Coplanar (FGC) Waveguide: It's Characteristics and Advantages for use in RF and Wireless Communication Circuits," in *International Wireless Communications Conference (WCC '98)*, 1998.
- [71] J. Zhang, S. Alexandrou, T. Y. Hsiang, "Attenuation Characteristics of Coplanar Waveguides at Subterahertz Frequencies," *IEEE Transactions on Microwave Theory and Techniques*, vol. 53, no. 11, p. 3281, 2005.
- [72] A. K. Rastogi, S. Mishra, "Coplanar Waveguide Characterization with Thick Metal Coating," *International Journal of Infrared and Millimeter Waves*, vol. 20, no. 3, p. 505, 1999.
- [73] T. Kitazawa, Y. Hayashi , "Quasistatic characteristics of a coplanar waveguide with thick metal coating," *IEEE Transactions on Microwave Theory and Techniques*, vol. 24, p. 604, 1976.
- [74] K. Koshiji, E. Shu, S. Miki, "Simplified computation of coplanar waveguide with finite conductor thickness," *Microwaves, Optics and Antennas, IEEE Proceedings H*, vol. 130, p. 315, 1983.
- [75] R. Delrue, C. Seguinot, P. Pribetich, P. Kennis, "The effects of a dielectric capacitor layer and metallization on the propagation parameters of coplanar waveguide for MMIC," *IEEE Transactions on Microwave Theory and Techniques*, vol. 36, p. 1285, 1988.
- [76] X. Gong, B. Gao, Y. Tian, L. Tong, "An Analysis of Characteristics of Coplanar Transmission Lines with Finite Conductivity and Finite Strip Thickness by the Method of Lines," *Journal of Infrared, Millimeter, and Terahertz Waves*, vol. 30, p. 792, 2009.

- [77] W. H. Haydl, T. Kitazawa, J. Braunstein, R. Bosch, M. Schlechtweg, "Millimeterwave coplanar transmission lines on gallium arsenide, indium phosphide and quartz with finite metalization thickness," in *IEEE MTT-S International Microwave Symposium Digest*, 1991.
- [78] D. A. Rowe, B. Y. Lao, "Numerical Analysis of Shielded Coplanar Waveguides," *IEEE Transactions on Microwave Theory and Techniques*, Vols. MTT-31, p. 911, 1983.
- [79] M. Tsuji, H. Shigesawa, A. A. Oliner, "New interesting leakage behavior on coplanar waveguides of finite and infinite widths," *IEEE Transactions on Microwave Theory and Techniques*, vol. 39, no. 12, p. 2130, 1991.
- [80] G. A. Garcia, C. T. Chang, "Crosstalk Between Two Coplanar Waveguides," *Defence Technical Information Center*, vol. 43, p. 55, 1989.
- [81] K. -K. M. Cheng, "Analysis and Synthesis of Coplanar Coupled Lines on Substrates of Finite Thicknesses," *IEEE Transactions on Microwave Theory and Techniques*, vol. 44, no. 4, p. 636, 1996.
- [82] N. D. Yordanov, A. Christova, "DPPH as a primary standard for quantitative EPR spectrometry," *Applied Magnetic Resonance*, vol. 6, p. 341, 1994.
- [83] J. X. Boucherle, B. Gillon, J. Maruani, J. Schweizer, "Crystal structure determination by neutron diffraction of 2,2-diphenyl-1-picrylhydrazyl (DPPH) benzene solvate (1/1)," *Acta Crystallographica Section C*, vol. 43, no. 9, p. 1769, 1987.
- [84] H. J. M. Slangen, "Determination of the spin concentration by electron spin resonance," *Journal of Physics E: Scientific Instruments*, vol. 3, p. 775, 1970.
- [85] J. Krzystek, A. Sienkiewicz, L. Pardi, L. C. Brunel, "DPPH as a Standard for High-Field EPR," *Journal of Magnetic Resonance*, vol. 125, p. 207, 1997.
- [86] T. Fujito, "Magnetic Interaction in Solvent-free DPPH and DPPH–Solvent Complexes," *Bulletin of the Chemical Society of Japan*, vol. 54, p. 3110, 1981.
- [87] D. Žilić, D. Pajić, M. Jurić, K. Molčanov, B. Rakvin, P. Planinić, K. Zadro, "Single crystals of DPPH grown from diethyl ether and carbon disulfide solutions – Crystal structures, IR, EPR and magnetization studies," *Journal of Magnetic Resonance*, vol. 207, no. 1, p. 34, 2010.
- [88] G. B. Teitelbaum, E. G. Kharakhashyan, S. Ya. Khlebnikov, A. G. Zenin, "Observation of antiferromagnetic resonance in the DPPH free radical," *JETP Letters*, vol. 34, p. 555, 1981.
- [89] "<https://en.wikipedia.org/wiki/DPPH>," [Online].
- [90] P. Grobet, L. Van Gerven, A. Van Den Bosch, J. Vansummeren, "Low temperature magnetic properties of solid DPPH," *Physica B+C*, Vols. 86-88B, p. 1132, 1977.

- [91] R. Verlinden, P. Grobet, L. Van Gerven, "Low temperature magnetic properties of DPPH.(C₆D₆)_x studied by NMR and EPR," *Chemical Physics Letters*, vol. 27, p. 535, 1974.
- [92] J. S. Chalmers, P. W. France, "*g*-Tensor anisotropy of DPPH in DPPH₂," *Journal of Magnetic Resonance*, vol. 23, no. 1, p. 51, 1969.
- [93] W. Voesch, M. Thiemann, D. Bothner, M. Dressel, M. Scheffler, "On-Chip ESR Measurements of DPPH at mK Temperatures," *Physics Procedia, 20th International Conference on Magnetism, ICM 2015*, vol. 75, p. 503, 2015.
- [94] M. Amusia, K. Popov, V. Shaginyan, W. Stefanowicz, *Theory of Heavy-Fermion Compounds*, Switzerland: Springer, 2015.
- [95] L.D. Landau, "The Theory of a Fermi Liquid," *Journal of Experimental and Theoretical Physics*, vol. 30, p. 1058, 1956.
- [96] I.Y. Pomeranchuk, "On the Stability of a Fermi Liquid," *Journal of Experimental and Theoretical Physics*, vol. 35, p. 324, 1959.
- [97] W. R. Abel, A. C. Anderson, W. C. Black, J. C. Wheatley, "Low-Temperature Heat Capacity of Liquid ³He," *Physical Review*, vol. 147, p. 111, 1966.
- [98] Q. D. Osheroff, R. C. Richardson, D. M. Lee, "Evidence for a New Phase of Solid ³He," *Physical Review Letters*, vol. 28, p. 885, 1972.
- [99] D. D. Osheroff, W. J. Gully, R. C. Richardson, D. M. Lee, "New Magnetic Phenomena in Liquid ³He below 3 mK," *Physical Review Letters*, vol. 29, p. 920, 1972.
- [100] A. Low Thomson, H. Meyer, E. Dwight Adams, "Nuclear Susceptibility of Liquid Helium-3 under Pressure," *Physical Review*, vol. 128, p. 509, 1962.
- [101] P. Gegenwart, J. Custers, C. Geibel, K. Neumaier, T. Tayama, K. Tenya, O. Trovarelli, F. Steglich, "Magnetic-Field Induced Quantum Critical Point in YbRh₂Si₂," *Physical Review Letters*, vol. 89, p. 56402, 2002.
- [102] K. Kadowaki, S. B. Woods, "Universal relationship of the resistivity and specific heat in heavy-Fermion compounds," *Solid State Communications*, vol. 58, p. 507, 1986.
- [103] V. R. Shaginyan, J. G. Han, J. Lee, "Fermion condensation quantum phase transition versus conventional quantum phase transitions," *Physics Letters A*, vol. 329, p. 108, 2004.
- [104] J. A. Hertz, "Quantum critical phenomena," *Physical Review B*, vol. 14, p. 1165, 1976.
- [105] A. J. Millis, "Effect of a nonzero temperature on quantum critical points in itinerant fermion systems," *Physical Review B*, vol. 48, p. 7183, 1993.

- [106] Q. Si, S. Rabello, K. Ingersent, J. L. Smith, "Locally critical quantum phase transitions in strongly correlated metals," *Nature*, vol. 413, p. 804, 2001.
- [107] N. Oeschler, S. Hartmann, A. P. Pikul, C. Krellner, C. Geibel, F. Steglich, "Low-temperature specific heat of YbRh_2Si_2 ," *Physica B*, vol. 403, p. 1254, 2008.
- [108] W. J. De Haas, G. J. Van Den Berg, "The electrical resistance of gold and silver at low temperatures," *Physica*, vol. 3, p. 440, 1936.
- [109] C. Kittel, *Solid State Physics*, New York: Wiley, 1983, p. Chapter 6.
- [110] J. Kondo, "Resistance Minimum in Dilute Magnetic Alloys," *Progress of Theoretical Physics*, vol. 23, p. 37, 1964.
- [111] A. C. Hewson, J. Kondo, "Kondo effect," Scholarpedia, 2009.
- [112] T. K. Ng, P. A. Lee, "On-Site Coulomb Repulsion and Resonant Tunneling," *Physical Review Letters*, vol. 61, p. 1768, 1988.
- [113] K. G. Wilson, "The renormalization group: Critical phenomena and the Kondo problem," *Reviews of Modern Physics*, vol. 47, p. 773, 1975.
- [114] U. Schaufuß, V. Kataev, A. A. Zvyagin, B. Büchner, J. Sichelschmidt, J. Wykhoff, C. Krellner, C. Geibel, F. Steglich, "Evolution of the Kondo State of YbRh_2Si_2 Probed by High-Field ESR," *Physical Review Letters*, vol. 102, p. 76405, 2009.
- [115] P. Gegenwart, T. Westerkamp, C. Krellner, M. Brando, Y. Tokiwa, C. Geibel, F. Steglich, "Unconventional quantum criticality in YbRh_2Si_2 ," *Physica B*, vol. 403, p. 1184, 2008.
- [116] O. Trovarelli, C. Geibel, S. Mederle, C. Langhammer, F. M. Grosche, P. Gegenwart, M. Lang, G. Sparn, F. Steglich, " YbRh_2Si_2 : Pronounced Non-Fermi-Liquid Effects above a Low-Lying Magnetic Phase Transition," *Physical Review Letters*, vol. 85, p. 626, 2000.
- [117] P. Gegenwart, Y. Tokiwa, T. Westerkamp, F. Weickert, J. Custers, J. Ferstl, C. Krellner, C. Geibel, P. Kersch, K. -H. Müller, F. Steglich, "High-field phase diagram of the heavy-fermion metal YbRh_2Si_2 ," *New Journal of Physics*, vol. 8, p. 171, 2006.
- [118] H. R. Naren, S. Friedemann, G. Zwicknagl, C. Krellner, C. Geibel, F. Steglich, S. Wirth, "Lifshitz transitions and quasiparticle de-renormalization in YbRh_2Si_2 ," *New Journal of Physics*, vol. 15, p. 093032, 2013.
- [119] J. Custers, P. Gegenwart, H. Wilhelm, K. Neumaier, Y. Tokiwa, O. Trovarelli, C. Geibel, F. Steglich, C. Pépin, P. Coleman, "The break-up of heavy electrons at a quantum critical point," *Nature*, vol. 424, p. 524, 2003.

- [120] S. Paschen, T. Lühmann, S. Wirth, P. Gegenwart, O. Trovarelli, C. Geibel, F. Steglich, P. Coleman, Q. Si, "Hall-effect evolution across a heavy-fermion quantum critical point," *Nature*, vol. 432, p. 881, 2004.
- [121] P. Wölfle, E. Abrahams, "Spin-flip scattering of critical quasiparticles and the phase diagram of YbRh_2Si_2 ," *Physical Review B*, vol. 92, p. 155111, 2015.
- [122] C. Krellner, S. Taube, T. Westerkamp, Z. Hossain, C. Geibela, "Single crystal growth of YbRh_2Si_2 and YbIr_2Si_2 ," *Philosophical Magazine*, Vols. 19-21: Symposium on Design, Discovery and Growth of Novel Materials, p. 2508, 2012.
- [123] U. Köhler, N. Oeschler, F. Steglich, S. Maquilon, Z. Fisk, "Energy scales of $\text{Lu}_{1-x}\text{Yb}_x\text{Rh}_2\text{Si}_2$ by means of thermopower investigations," *Physical Review B*, vol. 77, p. 104412, 2008.
- [124] L. M. Holanda, J. G. S. Duque, E. M. Bittar, C. Adriano, P. G. Pagliuso, C. Rettori, R. W. Hu, C. Petrovic, S. Maquilon, Z. Fisk, D. L. Huber, S. B. Oserof, "Field-dependent collective ESR mode in YbRh_2Si_2 ," *Physica B: Condensed Matter*, vol. 404, p. 2964, 2009.
- [125] T. Gruner, J. Sichelschmidt, C. Klingner, C. Krellner, C. Geibel, F. Steglich, "Electron spin resonance of the Yb 4f moment in $\text{Yb}(\text{Rh}_{1-x}\text{Co}_x)_2\text{Si}_2$," *Physical Review B*, vol. 85, p. 035119, 2012.
- [126] J. Sichelschmidt, J. Wykhoff, H-A. Krug von Nidda, J. Ferstl, C. Geibel, F. Steglich, "Spin dynamics of YbRh_2Si_2 observed by electron spin resonance," *Journal of Physics: Condensed Matter*, vol. 19, p. 116204, 2007.
- [127] V. A. Ivanshin, A. A. Sukhanov, D. A. Sokolov, M. C. Aronson, S. Jia, S. L. Budko, P. C. Canfield, "Electron spin resonance of dense Yb-based heavy-fermion compounds: New experimental data," *Journal of Alloys and Compounds*, vol. 480, p. 126, 2009.
- [128] T. Forster, J. Sichelschmidt, C. Krellner, C. Geibel, F. Steglich, "Electron spin resonance of the ferromagnetic Kondo lattice CeRuPO ," *Journal of Physics: Condensed Matter*, vol. 22, p. 435603, 2010.
- [129] T. Gruner, J. Wykhoff, J. Sichelschmidt, C. Krellner, C. Geibel, F. Steglich, "Anisotropic electron spin resonance of YbIr_2Si_2 ," *Journal of Physics: Condensed Matter*, vol. 22, p. 135602, 2010.
- [130] P. Schlottmann, "Electron spin resonance in CeB_6 ," *Journal of Applied Physics*, vol. 113, p. 17E109, 2013.
- [131] J. Sichelschmidt, J. Wykhoff, T. Gruner, C. Krellner, C. Klingner, C. Geibel, F. Steglich, H-A. Krug von Nidda, D. V. Zakharov, A. Loidl, I. Fazlizhanov, "Effect of pressure on the electron spin resonance of a heavy-fermion metal," *Physical Review B*, vol. 2001, p. 205116, 2010.

- [132] V. A. Ivanshin, E. M. Gataullin, A. A. Sukhanov, "ESR study of spin dynamics in the ternary phosphide YbRh_6P_4 ," *Journal of Physics: Conference*, vol. 324, p. 012019, 2011.
- [133] L. M. Holanda, J. M. Vargas, W. Iwamoto, C. Rettori, S. Nakatsuji, K. Kuga, Z. Fisk, S. B. Oseroff, P. G. Pagliuso, "Quantum Critical Kondo Quasiparticles Probed by ESR in $\beta\text{-YbAlB}_4$," *Physical Review Letters*, vol. 107, p. 026402, 2007.
- [134] G. Feher, A. F. Kip, "Electron Spin Resonance Absorption in Metals. I. Experimental," *Physical Review*, vol. 98, p. 337, 1955.
- [135] F. J. Dyson, "Electron Spin Resonance Absorption in Metals. II. Theory of Electron Diffusion and the Skin Effect," *Physical Review*, vol. 98, p. 349, 1955.
- [136] C. Rettori, D. Davidov, R. Orbach, E. P. Chock, B. Ricks, "Electron-Spin Resonance of Rare Earths in Aluminum," *Physical Review B*, vol. 7, p. 1, 1973.
- [137] C. Rettori, D. Davidov, H. M. Kim, "Crystalline-Field Effects in the EPR of Er in Various Cubic Metals," *Physical Review B*, vol. 8, p. 5335, 1973.
- [138] C. Rettori, H. M. Kim, E. P. Chock, D. Davidov, "Dynamic behavior of paramagnetic ions and conduction electrons in intermetallic compounds: $\text{Gd}_x\text{Lu}_{1-x}\text{Al}_2$," *Physical Review B*, vol. 10, p. 1826, 1974.
- [139] P. Schlottmann, "Electron spin resonance in heavy-fermion systems," *Physical Review B*, vol. 79, p. 045104, 2009.
- [140] J. Sichelschmidt, T. Kambe, I. Fazlishanov, D. Zakharov, H-A. Krug von Nidda, J. Wykhoff, A. Skvortsova, S. Belov, A. Kutuzov, B.I. Kochelaev, V. Pashchenko, M. Lang, C. Krellner, C. Geibel, F. Steglich, "Low temperature properties of the electron spin resonance in YbRh_2Si_2 ," *Physica Status Solidi B*, vol. 247, p. 747, 2010.
- [141] E. Abrahams, P. Wölfle, "Electron spin resonance in Kondo systems," *Physical Review B*, vol. 78, p. 104423, 2008.
- [142] B. I. Kochelaev, S. I. Belov, A. M. Skvortsova, A. S. Kutuzov, J. Sichelschmidt, J. Wykhoff, C. Geibel, F. Steglich, "Why could electron spin resonance be observed in a heavy fermion Kondo lattice?," *The European Physical Journal B*, vol. 72, p. 485, 2009.
- [143] P. Gegenwart, J. Custers, Y. Tokiwa, C. Geibel, F. Steglich, "Ferromagnetic Quantum Critical Fluctuations in $\text{YbRh}_2(\text{Si}_{0.95}\text{Ge}_{0.05})_2$," *Physical Review Letters*, vol. 94, p. 076402, 2005.
- [144] C. Krellner, T. Förster, H. Jeevan, C. Geibel, J. Sichelschmidt, "Relevance of Ferromagnetic Correlations for the Electron Spin Resonance in Kondo Lattice Systems," *Physical Review Letters*, vol. 100, p. 066401, 2008.
- [145] P. Monod, F. Beuneu, "Conduction-electron spin flip by phonons in metals: Analysis of experimental data," *Physical Review B*, vol. 19, p. 911, 1979.

- [146] J. G. S. Duque, E. M. Bittar, C. Adriano, C. Giles, L. M. Holanda, R. Lora-Serrano, P. G. Pagliuso, C. Rettori, C. A. Pérez, R. Hu, C. Petrovic, S. Maquilon, Z. Fisk, D. L. Huber, S. B. Oseroff, "Magnetic field dependence and bottlenecklike behavior of the ESR spectra in YbRh_2Si_2 ," *Physical Review B*, vol. 79, p. 035122, 2009.
- [147] A. Steppke, R. KÜchler, S. Lausberg, Edit Lengyel, L. Steinke, R. Borth, T. Lühmann, C. Krellner, M. Nicklas, C. Geibel, F. Steglich, M. Brando, "Ferromagnetic Quantum Critical Point in the Heavy-Fermion Metal $\text{YbNi}_4(\text{P}_{1-x}\text{As}_x)_2$," *Science*, vol. 339, p. 933, 2013.
- [148] R. Sarkar, P. Khuntia, J. Spehling, C. Krellner, C. Geibel, H. Klaus, M. Baenitz, "Static and dynamic susceptibility in the putative ferromagnetic quantum critical system YbNi_4P_2 probed by ^{31}P NMR," *Physica Status Solidi B*, vol. 250, p. 519, 2013.
- [149] S. J. Yamamoto, Q. Si, "Metallic ferromagnetism in the Kondo lattice," *Proceedings of the National Academy of Sciences*, vol. 107, p. 15704, 2010.
- [150] S. Deputier, O. Pena, T. Le Bihan, J. Y. Pivan, R. Guerin, "Magnetic properties of the lanthanoid nickel arsenides and phosphides LnNi_4X_2 with ZrFe_4Si_2 -type structure," *Physica B*, vol. 233, p. 26, 1997.
- [151] C. Krellner, C. Geibel, "Magnetic anisotropy of YbNi_4P_2 ," *Journal of Physics: Conference Series*, vol. 391, p. 012032, 2012.
- [152] Z. Huesges, O. Stockert, M. M. Koza, C. Krellner, C. Geibel, F. Steglich, "Crystalline electric field splitting in YbNi_4P_2 measured by inelastic neutron scattering," *Physica Status Solidi B*, vol. 250, p. 522, 2013.
- [153] S. Sachdev, Quantum Phase Transitions, Cambridge Univ. Press, 2011.
- [154] L. Balents, "Spin liquids in frustrated magnets," *Nature*, vol. 464, p. 199, 2010.
- [155] P. W. Anderson, "Resonating valence bonds: A new kind of insulator?," *Materials Research Bulletin*, vol. 8, p. 153, 1973.
- [156] T. Senthil, M. Vojta, S. Sachdev, "Weak magnetism and non-Fermi liquids near heavy-fermion critical points," *Physical Review B*, vol. 69, p. 35111, 2004.
- [157] W. Zheng, J. O. Fjærrestad, R. R. P. Singh, R. H. McKenzie, R. Coldea, "Excitation spectra of the spin-1/2 triangular-lattice Heisenberg antiferromagnet," *Physical Review B*, vol. 74, p. 224420, 2006.
- [158] F. Mila, "Quantum spin liquids," *European Journal of Physics*, vol. 21, p. 499, 2000.
- [159] Y. Shimizu, K. Miyagawa, K. Kanoda, M. Maesato, G. Saito, "Spin Liquid State in an Organic Mott Insulator with a Triangular Lattice," *Physical Review Letters*, vol. 91, p. 107001, 2003.

- [160] F. L. Pratt, P. J. Baker, S. J. Blundell, T. Lancaster, S. Ohira-Kawamura, C. Baines, Y. Shimizu, K. Kanoda, I. Watanabe, G. Saito, "Magnetic and non-magnetic phases of a quantum spin liquid," *Nature*, vol. 471, p. 612, 2011.
- [161] "<http://www.chemspider.com/Chemical-Structure.549911.html>," [Online].
- [162] J. Singelton, Band theory and electronic properties of solids, Oxford master series in condensed matter physics, 2014.
- [163] S. Ohira, Y. Shimizu, K. Kanoda, G. Saito, "Spin liquid state in κ -(BEDT-TTF)₂Cu₂(CN)₃ studied by muon spin relaxation method," *Journal of Low Temperature Physics*, vol. 142, p. 153, 2006.
- [164] M. Yamashita, N. Nakata, Y. Kasahara, T. Sasaki, N. Yoneyama, N. Kobayashi, S. Fujimoto, T. Shibauchi, Y. Matsuda, "Thermal-transport measurements in a quantum spin-liquid state of the frustrated triangular magnet κ -(BEDT-TTF)₂Cu₂(CN)₃," *Nature Physics*, vol. 5, p. 44, 2009.
- [165] T. Komatsu, N. Matsukawa, T. Inoue, G. Saito, "Realization of superconductivity at ambient pressure by band-filling control in κ -(BEDT-TTF)₂Cu₂(CN)₃," *Journal of the Physical Society of Japan*, vol. 65, p. 1340, 1996.
- [166] K. G. Padmalekha, M. Blankenhorn, T. Ivek, L. Bogani, J. A. Schlueter, M. Dressel, "ESR studies on the spin-liquid candidate κ -(BEDT-TTF)₂Cu₂(CN)₃: Anomalous response below T=8 K," *Physica B*, vol. 460, p. 211, 2015.
- [167] S. Lee, P. A. Lee, T. Senthil, "Amperean pairing instability in the U(1) spin liquid state with Fermi surface and application to κ -(BEDT-TTF)₂Cu₂(CN)₃," *Physical Review Letters*, vol. 98, p. 067006, 2007.
- [168] V. Galitski, Y. B. Kim, "Spin-triplet pairing instability of the spinon Fermi surface in a U(1) spin liquid," *Physical Review Letters*, vol. 99, p. 266403, 2007.
- [169] R. S. Manna, M. de Souza, A. Brühl, J. A. Schlueter, M. Lang, "Lattice effects and entropy release at the low-temperature phase transition in the spin-liquid candidate κ -(BEDT-TTF)₂Cu₂(CN)₃," *Physical Review Letters*, vol. 104, p. 016403, 2010.
- [170] M. Poirier, M. de Lafontaine, K. Miyagawa, K. Kanoda, Y. Shimizu, "Ultrasonic investigation of the transition at 6 K in the spin-liquid candidate κ -(BEDT-TTF)₂Cu₂(CN)₃," *Physical Review B*, vol. 89, p. 045138, 2014.
- [171] P. Wißmann, Electrical Resistivity of Thin Metal Films, Springer Berlin Heidelberg, 2007.
- [172] H. Marom, M. Eizenberg, "The temperature dependence of resistivity in thin metal films," *Journal of Applied Physics*, vol. 96, p. 3319, 2004.

- [173] A. Mallikarjunan, S. Sharma, S. P. Murarka, "Resistivity of Copper Films at Thicknesses Near the Mean Free Path of Electrons in Copper," *Electrochemical and Solid-State Letters*, vol. 3, p. 437, 2000.
- [174] M. Naghed, I. Wolff, "Equivalent capacitances of coplanar waveguide discontinuities and interdigitated capacitors using a three-dimensional finite difference method," *IEEE Transactions on Microwave Theory and Techniques*, vol. 38, p. 1808, 1990.
- [175] M. Göppl, A. Fragner, M. Baur, R. Bianchetti, S. Filipp, J. M. Fink, P. J. Leek, G. Puebla, L. Steffen, A. Wallraff, "Coplanar Waveguide Resonators for Circuit Quantum Electrodynamics," *Journal of Applied Physics*, vol. 104, p. 113904, 2008.
- [176] A. Abuelgasim, K. Mallik, P. Ashburn, D. M. Jordan, P. R. Wilshaw, R. J. Falster, C. H. de Groot, "Reduced microwave attenuation in coplanar waveguides using deep level impurity compensated Czochralski-silicon substrates," *Semiconductor Science and Technology*, vol. 26, p. 72001, 2011.
- [177] M. Ramazani, H. Miladi, M. Shahabadi, S. Mohajerzadeh, "Loss Measurement of Aluminum Thin-Film Coplanar Waveguide (CPW) Lines at Microwave Frequencies," *IEEE Transactions on Electron Devices*, vol. 57, p. 2037, 2010.
- [178] J. Ramy, M. Cotte, J. Bolloch, R. Schnitzler, J. Guena, C. Thebault, "Optimization of the Thick-and Thin-Film Technologies for Microwave Circuits on Alumina and Fused Silica Substrates," *IEEE Transactions on Microwave Theory and Techniques*, vol. 26, p. 814, 1978.
- [179] K. P. Müller, J. Pelka, "Redeposition in ion milling," *Microelectronic Engineering*, vol. 7, p. 91, 1987.
- [180] L. Frunzio, A. Wallraff, D. Schuster, J. Majer, R. Schoelkopf, "Fabrication and characterization of superconducting circuit QED devices for quantum computation," *IEEE Transactions on Applied Superconductivity*, vol. 15, p. 860, 2005.
- [181] H. Wang, M. Hofheinz, J. Wenner, M. Ansmann, R. C. Bialczak, M. Lenander, E. Lucero, M. Neeley, A. D. O'Connell, D. Sank, M. Weides, A. N. Cleland, J. M. Martinis, "Improving the Coherence Time of Superconducting Coplanar Resonators," *Applied Physics Letters*, vol. 95, p. 233508, 2009.
- [182] J. de Launay, R. L. Dolecek, R. T. Webber, "Magnetoresistance of copper," *Journal of Physics and Chemistry of Solids*, vol. 11, p. 37, 1959.
- [183] A. Ghirri, C. Bonizzoni, M. Righi, F. Fedele, G. Timco, R. Winpenney, M. Affronte, "Microstrip Resonators and Broadband Lines for X-band EPR Spectroscopy of Molecular Nanomagnets," *Applied Magnetic Resonance*, vol. 46, p. 706, 2015.

- [184] N. D. Yordanov, "Is Our Knowledge about the Chemical and Physical Properties of DPPH Enough to Consider It as a Primary Standard for Quantitative EPR Spectrometry," *Applied Magnetic Resonance*, vol. 10, p. 339, 1996.
- [185] C. Clauss, "Ph.D Thesis," University of Stuttgart, December 2014.
- [186] K. Baberschke, E. Tsang, "ESR Study of the Kondo Effect in Au: Yb," *Physical Review Letters*, vol. 45, p. 1512, 1980.
- [187] J. P. Joshi, S. V. Bhat, "On the analysis of broad Dysonian electron paramagnetic resonance spectra," *Journal of Magnetic Resonance*, vol. 168, p. 284, 2004.
- [188] S. E. Barnes, "Theory of electron spin resonance of magnetic ions in metals," *Advances in Physics*, vol. 30, p. 801, 1981.
- [189] R. J. Gale, *Spectroelectrochemistry: Theory and Practice*, Springer Science & Business Media, 2012.
- [190] J. C. W. Chien, *Polyacetylene: Chemistry, Physics, and Material Science*, Orlando, Florida: ACADEMIC PRESS, INC , 1984.
- [191] H. Pfau, S. Hartmann, U. Stockert, P. Sun, S. Lausberg, M. Brande, S. Friedemann, C. Krellner, C. Geibel, S. Wirth, S. Kirchner, E. Abrahams, Q. Si, F. Steglich, "Thermal and Electrical Transport across a Magnetic Quantum Critical Point," *Nature*, vol. 484, p. 493, 2012.
- [192] P. Gegenwart, T. Westerkamp, C. Krellner, Y. Tokiwa, S. Paschen, C. Geibel, F. Steglich, E. Abrahams, Q. Si, "Multiple Energy Scales at a Quantum Critical Point," *Science*, vol. 315, p. 969, 2007.
- [193] K. Kummer, S. Patil, A. Chikina, M. Güttler, M. Höppner, A. Generalov, S. Danzenbächer, S. Seiro, A. Hannaske, C. Krellner, Y. Kucherenko, M. Shi, M. Radovic, E. Rienks, G. Zwicknagl, K. Matho, J. W. Allen, C. Laubschat, C. Geibel, D. V. Vyalikh, "Temperature-Independent Fermi Surface in the Kondo Lattice YbRh₂Si₂," *Physical Review X*, vol. 5, p. 11028, 2015.
- [194] P. Wölfle, E. Abrahams, "Phenomenology of ESR in heavy-fermion systems: Fermi-liquid and non-Fermi-liquid regimes," *Physical Review B*, vol. 80, p. 235112, 2009.
- [195] M. Scheffler, M. Dressel, M. Jourdan, H. Adrian, "Extremely slow Drude relaxation of correlated electrons," *Nature*, vol. 438, p. 1135, 2005.
- [196] K. Kliemt, C. Krellner, "Crystal growth by Bridgman and Czochralski method of the ferromagnetic quantum critical material YbNi₄P₂," *Journal of Crystal Growth*, vol. 449, p. 129, 2016.

- [197] K. Parkkinen, M. Dressel, K. Kliemt, C. Krellner, C. Geibel, F. Steglich, M. Scheffler, "Signatures of Phase Transitions in the Microwave Response of YbRh_2Si_2 ," *Physics Procedia*, vol. 75, p. 340, 2015.
- [198] H. Pfau, R. Daou, S. Friedemann, S. Karbassi, S. Ghannadzadeh, R. K uchler, S. Hamann, A. Steppke, D. Sun, M. K onig, A. P. Mackenzie, K. Kliemt, C. Krellner, M. Brand, "Cascade of Magnetic-Field-Induced Lifshitz Transitions in the Ferromagnetic Kondo Lattice Material YbNi_4P_2 ," *Physical Review Letters*, vol. 119, p. 126402, 2017.
- [199] S. Els asser, D. Wu, M. Dressel, J. A. Schlueter, "Power-law dependence of the optical conductivity observed in the quantum spin-liquid compound $\kappa\text{-(BEDT-TTF)}_2\text{Cu}_2(\text{CN})_3$," *Physical Review B*, vol. 86, p. 155150, 2012.
- [200] S. Yamashita, Y. Nakazawa, M. Oguni, Y. Oshima, H. Nojiri, Y. Shimizu, K. Miyagawa, K. Kanoda, "Thermodynamic properties of a spin-1/2 spin-liquid state in a κ -type organic salt," *Nature Physics*, vol. 4, p. 459, 2008.
- [201] M. Poirier, S. Parent, A. Cote, K. Miyagawa, K. Kanoda, Y. Shimizu, "Magnetodielectric effects and spin-charge coupling in the spin-liquid candidate $\kappa\text{-(BEDT-TTF)}_2\text{Cu}_2(\text{CN})_3$," *Physical Review B*, vol. 85, p. 134444, 2012.
- [202] K. Yu. Povarov, A. I. Smirnov, O. A. Starykh, S. V. Petrov, A. Y. Shapiro, "Modes of Magnetic Resonance in the Spin-Liquid Phase of Cs_2CuCl_4 ," *Physical Review Letters*, vol. 107, p. 037204, 2011.
- [203] A. I. Smirnov, T. A. Soldatov, K. Yu. Povarov, A. Ya. Shapiro, "High-field magnetic resonance of spinons and magnons in the triangular lattice $S=1/2$ antiferromagnet Cs_2CuCl_4 ," *Physical Review B*, vol. 91, p. 174412, 2015.
- [204] O. A. Starykh, L. Balents, "Ordering in Spatially Anisotropic Triangular Antiferromagnets," *Physical Review Letters*, vol. 98, p. 077205, 2007.
- [205] M. Pinteri c, M. Miljak, N. Bi skup, O. Milat, I. Aviani, S. Tomi c, D. Schweitzer, W. Strunz, I. Heinen, "Magnetic anisotropy and low-frequency dielectric response of weak ferromagnetic phase in $\kappa\text{-(BEDT-TTF)}_2\text{Cu}[\text{N}(\text{CN})_2]\text{Cl}$, where BEDT-TTF is Bis(ethylenedithio)tetrathiafulvalene," *The European Physical Journal B*, vol. 11, p. 217, 1999.
- [206] J. E. Healey, T. Lindstr om, M. S. Colclough, C. M. Muirhead, A. Y. Tzalenchuk, "Magnetic field tuning of coplanar waveguide resonators," *Applied Physics Letters*, vol. 93, p. 043513, 2008.
- [207] S. V. Dordevic, K. S. D. Beach, N. Takeda, Y. J. Wang, M. B. Maple, D. N. Basov, "Heavy Fermion Fluid in High Magnetic Fields: An Infrared Study of $\text{CeRu}_4\text{Sb}_{12}$," *Physical Review Letters*, vol. 96, p. 017403, 2006.

- [208] M. Javaheri Rahim, T. Lehleiter, D. Bothner, C. Krellner, D. Koelle, R. Kleiner, M. Dressel, M. Scheffler, "Metallic coplanar resonators optimized for low-temperature measurements," *Journal of Physics D: Applied Physics*, vol. 49, p. 395501, 2016.
- [209] K. Yu. Povarov, A. I. Smirnov, O. A. Starykh, S. V. Petrov, A. Ya. Shapiro, "Modes of Magnetic Resonance in the Spin-Liquid Phase of Cs_2CuCl_4 ," *Physical Review Letters*, vol. 107, p. 037204, 2011.

Acknowledgements

This work would have not been possible without the support of many others. In order to acknowledge the people who provided me their supports I would like to express my gratitude, first of all, to Prof. Martin Dressel for giving me the opportunity to perform my PhD work at the 1. Physikalisches Institut. I appreciate his general support during the work and special helps at writing the paper and the thesis.

I thank my direct supervisor Dr. Marc Scheffler for his support and good pieces of advice in the whole time of my PhD work. He always answered the questions with a special patience and was always ready for even very long scientific discussions. I definitely profited much from his substantial amount of knowledge and expertise in research fields and experimental techniques.

I sincerely thank Prof. Jörg Wrachtrup who kindly allowed me to work in different laboratories of 3. Physikalisches Institut during the PhD work and accepted to co-referee my Thesis. Many thanks to Dr. Rainer Stöhr and Dr. Roman Kolesov because of their kind and outstanding technical support during the resonators' fabrication.

A great thanks to Prof. Harald Giessen for giving me the permission of using the MSL. Without using the MSL the fabrication of the resonators would definitely have not been possible. I thank Monika Ubl and Ramon Walter for their technical support in the MSL.

I would like to express my gratitude to the low temperature department, namely Joachim Lefèvre, Bernd Schobel, Andreas Manz, Florian Münzenmayer and Dario Profetto for their excellent performance. The supply of full helium cans was even during vacation time and holidays always guaranteed.

Another special thanks to the people who provided me the samples. Prof. Cornelius Krellner and Dr. Kristin Kliemt for Heavy Fermion samples. Dr. Ralph Hübner and Prof. Kanoda's group for the Spin Liquid sample.

I thank the Technical Faculty of the university of Kiel and specially Dr. Ali Tavassolizadeh for providing me the sputtered thin films which were used in the fabrication of the resonators.

I needed several new designed mechanical parts at different phases of my PhD and I always received the unique support of the mechanical workshop whose members I thank all. I learned plenty of hints and points in engineering drawing of the parts each time of my presence in their office.

The great support and collaboration with the Physikalisches Institut in Tübingen in the beginning phase of the fabrication process is unforgettable. I am very grateful for the help provided by Prof. Dieter Koelle and Prof. Reinhold Kleiner's group. Thanks to Dr. Daniel Bothner who gave me his time several days in the clean room of the University of Tübingen for fabricating the first metallic resonators. The valuable discussions with him about the theoretical and experimental aspects of the microwave waveguides helped me a lot.

Gabriele Untereiner, one of the most important persons at the institute has my thanks for her outstanding precision and support in various parts of my work. She not only performed a lot of works herself but taught me how to use some devices and machines also. I got sometimes some answers to my questions even after our discussions!

A great thanks to Agnieszka Cienkowska-Schmidt whose kindness, performance and motivation are indescribable! Sometimes so kind just like a mother! Thanks Agni!

Thanks to my dear friends in Stuttgart University physics department, Dr. Shahin Bagheri, Dr. Ali Momenzadeh and Mohammad Rezaei and of Max Planck's Institute Dr. Mostafa Enayat for the scientific discussions and friendships.

Thanks to all PI1 members then and now! Some special thanks to Dr. Conrad Klaus, Dr. Takuya Iizuka, Dr. Sadegh Ebrahimi, Dr. Uwe Pracht and Dr. Markus Thiemann for their supports and discussions. I would like to thank the people who worked directly and indirectly with me; Thomas Lehleiter, Dominik Störzer, Lars Wandel, Markus Bader, Mario Zinser, Yvonne Wiemann, Desiree Rausch, Manfred Beutel, Vincent Engl, Wolfgang Voesch and all other ones whom I may forgot to mention.

I would like to express my deepest thanks to the lady in my life Daniela Bayer. Her mental supports during this time have undoubtedly been of the biggest help for me to proceed further and fight against the most stressful moments in my personal and professional lives! Thanks a lot you!

Many thanks to my dear friends Dr. Mohsen Nemati, Mahdi Mottahedi, Dr. Mojtaba Mashmool, Morteza Najafi, Babak Mozooni, Amir Shirrangi, Dr. Mohammad Jalalirad and all the other friends whose presence was and is always a big motivation and encouragement for me.

Last but not least, my heartfelt thanks and gratitude to my very dear parents, sisters, brother and their families who helped me of thousands of kilometers away by their prayers, good wishes and positive energies! Thank you all!